



National Library
of Canada

Acquisitions and
Bibliographic Services Branch

395 Wellington Street
Ottawa, Ontario
K1A 0N4

Bibliothèque nationale
du Canada

Direction des acquisitions et
des services bibliographiques

395, rue Wellington
Ottawa (Ontario)
K1A 0N4

Your file *Votre référence*

Our file *Notre référence*

NOTICE

AVIS

The quality of this microform is heavily dependent upon the quality of the original thesis submitted for microfilming. Every effort has been made to ensure the highest quality of reproduction possible.

If pages are missing, contact the university which granted the degree.

Some pages may have indistinct print especially if the original pages were typed with a poor typewriter ribbon or if the university sent us an inferior photocopy.

Reproduction in full or in part of this microform is governed by the Canadian Copyright Act, R.S.C. 1970, c. C-30, and subsequent amendments.

La qualité de cette microforme dépend grandement de la qualité de la thèse soumise au microfilmage. Nous avons tout fait pour assurer une qualité supérieure de reproduction.

S'il manque des pages, veuillez communiquer avec l'université qui a conféré le grade.

La qualité d'impression de certaines pages peut laisser à désirer, surtout si les pages originales ont été dactylographiées à l'aide d'un ruban usé ou si l'université nous a fait parvenir une photocopie de qualité inférieure.

La reproduction, même partielle, de cette microforme est soumise à la Loi canadienne sur le droit d'auteur, SRC 1970, c. C-30, et ses amendements subséquents.

University of Alberta

Spanwise Secondary Instability of Dean & Görtler Vortices

by

Yan Guo



A thesis submitted to the Faculty of Graduate Studies and Research in partial fulfillment of the requirements for the degree of Doctor of Philosophy.

Department of Mechanical Engineering

Edmonton, Alberta

Fall / 1992



National Library
of Canada

Acquisitions and
Bibliographic Services Branch

395 Wellington Street
Ottawa, Ontario
K1A 0N4

Bibliothèque nationale
du Canada

Direction des acquisitions et
des services bibliographiques

395, rue Wellington
Ottawa (Ontario)
K1A 0N4

Your file *Votre référence*

Our file *Notre référence*

The author has granted an irrevocable non-exclusive licence allowing the National Library of Canada to reproduce, loan, distribute or sell copies of his/her thesis by any means and in any form or format, making this thesis available to interested persons.

L'auteur a accordé une licence irrévocable et non exclusive permettant à la Bibliothèque nationale du Canada de reproduire, prêter, distribuer ou vendre des copies de sa thèse de quelque manière et sous quelque forme que ce soit pour mettre des exemplaires de cette thèse à la disposition des personnes intéressées.

The author retains ownership of the copyright in his/her thesis. Neither the thesis nor substantial extracts from it may be printed or otherwise reproduced without his/her permission.

L'auteur conserve la propriété du droit d'auteur qui protège sa thèse. Ni la thèse ni des extraits substantiels de celle-ci ne doivent être imprimés ou autrement reproduits sans son autorisation.

ISBN 0-315-77400-2

INTER-DEPARTMENTAL



CORRESPONDENCE

TO Faculty of Graduate Studies & Research
2-8 University Hall

DATE July 9, 1992

FROM Warren Finlay, Assoc. Professor
Dept. of Mechanical Engineering

I am writing this memo to indicate that Yan Guo has my permission to include in his Ph.D. thesis the material from the paper listed below on which I am a joint author.

Guo, Y. and Finlay, W.H., 1992, "Spanwise Secondary Instability of Spatially Developing Vortices", Parts 1 and 2, submitted to Journal of Fluid Mechanics.

Guo, Y. and Finlay, W.H., 1991 "Splitting, Merging and Wavelength Selection of Vortices in Curved and/or Rotating Channels Due to Eckhaus Instability", Journal of Fluid Mechanics **228**: 661-991.

Handwritten signature of Warren Finlay.

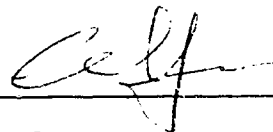
University of Alberta

Release Form

Name of Author: **Yan Guo**
Title of Thesis: **Spanwise Secondary Instability of Dean & Görtler
Vortices**
Degree: **Doctor of Philosophy**
Year this degree granted: **1992**

Permission is hereby granted to **The University of Alberta Library** to reproduce single copies of this thesis and to lend or sell such copies for private, scholarly, or scientific research purposes only.

The author reserves all other publication and other rights in association with the copyright in the thesis, and except as hereinbefore provided neither the thesis nor any substantial portion thereof may be printed or otherwise reproduced in any material form whatever without the author's prior written permission.



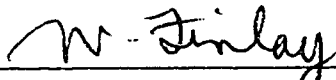
Yan Guo
608 10145 121St.
Edmonton, Alberta
Canada, T6G 2G8

Date : July 15, 1992


University of Alberta

Faculty of Graduate Studies and Research

The undersigned certify that they have read, and recommend to the Faculty of Graduate Studies and Research for acceptance, a thesis entitled **Spanwise secondary Instability of Dean & Görler Vortices** submitted by **Yan Guo** in partial fulfillment of the requirements for the degree of **Ph.D.**



Dr. Warren H. Finlay (Supervisor)



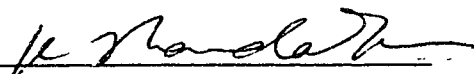
Dr. K. C. Cheng



Dr. Th. Herbert



Dr. J. H. Masliyah



Dr. K. Nandakumar

Date: July 15, 1992

Abstract

Streamwise vortices found in curved channels (Dean vortices), rotating channels, curved-rotating channels and in a concave boundary layer (Görtler vortices) are simulated numerically using spectral methods and Legendre spectral-element methods. Both linear and nonlinear aspects of the secondary instability of these vortices with respect to spanwise (transverse) perturbations are examined using temporal and spatial stability theories. When the energy level of Dean or Görtler vortices in the flow is low, the spatial growth of the vortices is governed by primary instability. At this stage, the vortices with different wavelengths can develop at the same time and do not interact with each other significantly. When certain vortices reach the nonlinear stage first and become the dominant wavelength, spanwise secondary instability sets in. For all cases studied, spatially developing Dean and Görtler vortices are found to be most unstable to spanwise disturbances with wavelength twice that of the dominant one. For Görtler vortices, the nonlinear growth of these perturbations generates a small vortex pair in between two pairs of vortices with long wavelength, but forces two pairs of vortices with short wavelength to develop into one pair. As a result, the structures of the dominant Görtler vortices become irregular. For Dean vortices, these disturbances distort the dominant vortices during their developing stage; when the dominant vortices reach the fully developed stage, the stability boundary is a small closed loop in a Reynolds number-wavenumber plane. Outside this loop, the nonlinear development of these disturbances causes two dominant vortex pairs to merge into one pair if the dominant wavelength is short, but generates a new vortex pair in between two dominant pairs if the dominant wavelength is long. Thus spanwise secondary instability plays an important role in wavenumber selection process for Dean vortices.

Acknowledgements

I would like to thank my advisor Dr. Warren H. Finlay for all the guidance and material support he gave me throughout this work. I thank Dr. K. Nandakumar for helpful advice and discussions. My sincere thanks also go to my fellow graduate students in the Department of Mechanical Engineering for creating a good social and working environment. Finally, I would like to express my deep appreciation for all the encouragement and support of my mother and sisters, which make it possible to see the completion of this work today.

Contents

chapter	page
1. Introduction	1
References	4
2. Splitting, merging and wavelength selection of vortices in curved and/or rotating channel flow	5
2.1 Introduction	5
2.2 Theory and numerical methods	9
2.3 Eckhaus stability boundary	13
2.4 Splitting and merging of vortices	16
2.5 Wavenumber selection	24
2.6 Recurrent splitting and merging	28
2.7 Nonlinear vortex splitting and merging	29
2.8 Conclusion	34
References	58
3. Spanwise secondary instability of spatially developing vortices.	
Part 1. Theory and application to Dean vortices	61
3.1 Introduction	61
3.2 Theory and numerical methods	65
3.3 Code verification	75
3.4 Primary instability and development of nonlinear Dean vortices ...	79
3.5 Spanwise secondary instability of fully developed Dean vortices ...	80
3.6 Spanwise secondary instability of developing Dean vortices	82
3.7 Simulation of splitting and merging of Dean vortices	88

3.8	Wavenumber selection and irregularity of Dean vortices	93
3.9	Conclusion	95
	References	123
4.	Spanwise secondary instability of spatially developing vortices.	
Part 2.	Irregularity and wavenumber selection of Görtler vortices ..	127
4.1	Introduction	127
4.2	Primary instability of Görtler vortices	132
4.3	Spatial development of nonlinear Görtler vortices	133
4.4	Spanwise secondary instability of developing Görtler vortices	135
4.5	Simulation of splitting and merging of Görtler vortices	144
4.6	Wavenumber selection and irregularity of Görtler vortices	152
4.7	Conclusion	156
	References	191
5.	Final remarks	194
Appendix A	195
Appendix B	196
Appendix C	199

List of Tables

	page
Table 2.1. Growth rates of primary and spanwise secondary instabilities in a curved channel.	97

List of Figures

	page
Figure 2.1. The geometry of curved and/or rotating channel.	36
Figure 2.2. Eckhaus stability boundaries in curved/rotating channels.	37
Figure 2.3. Eckhaus eigenvalue on the left side of Eckhaus boundary.	39
Figure 2.4. Eckhaus eigenvalue on the right side of Eckhaus boundary. ...	40
Figure 2.5. The most unstable wavenumber on Eckhaus boundary.	41
Figure 2.6. Eckhaus stability criterion and Eckhaus stability boundary. ..	41
Figure 2.7. Taylor vortices and the most unstable mode at $\alpha = 1.17$	42
Figure 2.8. Taylor vortices and the most unstable mode at $\alpha = 2.475$	43
Figure 2.9. Dean vortices and the most unstable mode at $\alpha = 2.0$	44
Figure 2.10. Dean vortices and the most unstable mode at $\alpha = 4.0$	45
Figure 2.11. The most unstable perturbations in a curved channel.	46
Figure 2.12. Dean vortices with/without secondary vortices.	48
Figure 2.13. Eckhaus growth rates with/without secondary vortices.	49
Figure 2.14. Maximum Eckhaus growth rate in a curved channel.	50
Figure 2.15. Eckhaus valley in a curved channel.	51
Figure 2.16. Eckhaus valley in a rotating channel.	52
Figure 2.17. Eckhaus growth rate in a curved-rotating channel.	53
Figure 2.18. Eckhaus valley in a curved-rotating channel.	54
Figure 2.19. Nonlinear vortex splitting and merging.	55
Figure 2.20. Pressure gradient at $Re = 2.2Re_c$, $\gamma = 0.975$, $\Gamma = 3\pi : 1$	56
Figure 2.21. Streamfunction at $Re = 2.2Re_c$, $\gamma = 0.975$, $\Gamma = 3\pi : 1$	57
Figure 3.1. The geometry of curved channel.	99

Figure 3.2.	Boundary layer flow over a concave surface.	100
Figure 3.3.	Linear growth rate of Görtler vortices with $\Lambda = 62$	101
Figure 3.4.	Eigenfunction of Görtler vortices with $\Lambda = 62$	102
Figure 3.5.	Contours of the spatial primary growth rate at $\gamma = 0.975$	103
Figure 3.6.	Energy of Dean vortices in a curved channel with $\gamma = 0.975$	104
Figure 3.7.	Spatial vortex spitting/merging of Dean vortices.	105
Figure 3.8.	Energy of the Dean vortices $\alpha = 4.0$ & their perturbation. ..	106
Figure 3.9.	Spanwise velocities of the flows in figure 3.8.	107
Figure 3.10.	Flow patterns of figure 3.8.	108
Figure 3.11.	Energy of the Dean vortices $\alpha = 2.0$ and their perturbation. ...	110
Figure 3.12.	Spanwise velocities of the flows in figure 3.11.	111
Figure 3.13.	Flow patterns of figure 3.11.	113
Figure 3.14.	Spanwise velocity of the dominant Dean vortices $\alpha = 4.0$	115
Figure 3.15.	Energy of figure 3.14 in spanwise Fourier modes.	116
Figure 3.16.	Flow pattern of the Dean vortices in figure 3.14.	117
Figure 3.17.	Energy of the dominant Dean vortices with $\alpha = 4.0$	119
Figure 3.18.	The dominant Dean vortices with $\alpha = 2.0$	120
Figure 3.19.	Flow pattern of the Dean vortices in figure 3.18.	121
Figure 3.20.	Interaction between the Dean vortices with different α	122
Figure 4.1.	Boundary layer flow over a concave surface.	159
Figure 4.2.	Primary growth rate of Görtler vortices.	160
Figure 4.3.	Streamwise velocity of the Görtler vortices with $\lambda = 1.8\text{cm}$. .	161
Figure 4.4.	Velocity profile of the Görtler vortices with $\lambda = 1.8\text{cm}$	163
Figure 4.5.	Spatial growth of the Görtler vortices in figure 4.4.	165
Figure 4.6.	Wall shear of the Görtler vortices in figure 4.4.	166

Figure 4.7.	Energy of Görtler vortices $\lambda = 2.13\text{cm}$ & their perturbation.	167
Figure 4.8.	Spatial developments of the flows in figure 4.7.	168
Figure 4.9.	Flow patterns of the flows in figure 4.7.	170
Figure 4.10.	Same as in figure 4.9 but with a different initial condition. ..	172
Figure 4.11.	Energy of Görtler vortices $\lambda = .745\text{cm}$ & their perturbation.	173
Figure 4.12.	Spatial development of the flows in figure 4.11.	174
Figure 4.13.	Flow patterns of the flows in figure 4.11.	175
Figure 4.14.	Same as in figure 4.13 but with a different initial condition. ..	177
Figure 4.15.	Energy of the flows in figure 4.14.	179
Figure 4.16.	Flow pattern of the dominant Görtler vortices $\lambda = 0.749\text{cm}$.	180
Figure 4.17.	Energy of figure 4.16 in spanwise Fourier modes.	182
Figure 4.18.	Streamwise velocity of the vortices in figure 4.16.	183
Figure 4.19.	Flow pattern of the dominant Görtler vortices $\lambda = 2.13\text{cm}$. ..	184
Figure 4.20.	Streamwise velocity of the vortices in figure 4.19.	186
Figure 4.21.	Same as in figure 4.19 but with a different initial condition. ..	187
Figure 4.22.	Görtler vortices in a large spanwise box.	188
Figure 4.23.	Interaction between Görtler vortices with different λ	189
Figure 4.24.	Flow pattern of figure 4.23.	190

Symbols And Nomenclature

Roman Symbols

A	Laplace matrix.
b	λ/λ_1 , Dimensionless wavenumber of spanwise perturbation.
B, B_p	Mass matrices.
B_x^n	Mass matrix of u_x at step n .
C_i	$i = x, y, z$. Discretized convection terms.
d	Channel spacing .
D_x, D_y	Gradient matrices.
e	Energy.
e_r	Unit vector of radial coordinate.
e_z	Unit vector of spanwise coordinate.
f	(f_x, f_y, f_z) , force term.
F_i	$i = x, y, z$. Discretized force terms.
$Gö$	$U_\infty \delta_m (\delta_m / R)^{1/2} / \nu$, Görtler number.
k_z	Spanwise Fourier wavenumber.
l	Length scale used to nondimensionalize growth rate σ .
p	Pressure of base flow.
p'	Pressure of perturbation.
\bar{p}	Mean streamwise pressure.
p^n	Discretized pressure p at step n .
\bar{p}^n	Discretized mean streamwise pressure \bar{p} at step n .
Q	Channel flow rate.
r	Radial coordinate.
r_o	Radius of concave (outer channel) wall.
r_i	Radius of convex wall (inner channel) wall.

R	Radius of concave surface.
Ro	$\Omega d/2\nu$, Rotation number.
Re	$\bar{U}d/2\nu$, Reynolds number of channel flow.
Re_c	Critical Reynolds number of Dean vortices.
s	$\sigma + i\omega$, complex eigenvalue.
t	Time.
t^*	Dimensional time.
\mathbf{u}^0	(u_x, u_y, u_z) or (u_r, u_θ, u_z) , velocity of base flow.
\mathbf{u}'	(u'_x, u'_y, u'_z) or (u'_r, u'_θ, u'_z) , velocity of spanwise perturbation.
$\tilde{\mathbf{u}}$	$(\tilde{u}_x, \tilde{u}_y, \tilde{u}_z)$ or $(\tilde{u}_r, \tilde{u}_\theta, \tilde{u}_z)$, eigenfunction of spanwise perturbation.
u_{1D}	Velocity of curved channel Poiseuille flow.
u_B	Streamwise velocity of Blasius boundary layer flow.
\bar{U}	Mean streamwise velocity.
U_∞	Freestream velocity.
\mathbf{U}^n	(U_x^n, U_y^n, U_z^n) , discretized velocity \mathbf{u} at step n .
v_B	Vertical velocity of Blasius boundary layer flow.
x	Cartesian streamwise coordinate .
y	Cartesian radial coordinate.
z	Spanwise coordinate.
z^*	Dimensional spanwise coordinate.

Greek Symbols

α	Wavenumber of base vortices. For Dean vortices, $\alpha = \pi d/\lambda$.
α_c	Critical wavenumber of Dean vortices.
β	Wavenumber of spanwise perturbation.
β_t	Coefficient used by a third-order Adam-Bashforth scheme.
γ	r_i/r_o for a curved channel; $(R - \delta_{.99})/R$ for a concave boundary layer.

Γ	Aspect ratio of computational box.
$\delta_{.99}$	Blasius boundary layer thickness at $0.99U_\infty$.
δ_m	Momentum thickness of Blasius boundary layer.
Δp	Streamwise pressure gradient parameter.
Δx	Step size in the x direction.
$\Delta \theta$	Step size in the θ direction.
λ	Dimensional spanwise wavelength of base vortices.
λ_1	Dimensional spanwise wavelength of perturbation.
Λ	$U_\infty \lambda (\lambda/R)^{1/2} / \nu$, Wavelength parameter of Görtler vortices.
θ	Streamwise coordinate.
ν	Kinematic viscosity.
ϕ_r	ru_r .
ϕ_θ	ru_θ .
ϕ_z	ru_z .
σ	Growth rate.
σ_{1D}	Spatial growth rate of primary instability.
σ_{2D}	Spatial growth rate of spanwise secondary instability.
ψ	Stokes stream function.
ω	Imaginary part of eigenvalue s .
Ω	Rotation of a channel.

CHAPTER 1

Introduction

Counter-rotating streamwise vortices caused by streamwise curvature have been attracting many researchers' attention for years. They can be found in many applications and play an important role in the transition toward turbulence. For open fluid systems where fluid particles are advected through the systems, Dean vortices found in curved channels (Dean, 1928) and Görtler vortices near a concave surface (Görtler, 1940) are two classical examples of such vortices. In this study, we will examine numerically the secondary instabilities of these types of vortices with respect to spanwise perturbations and their effects on wavenumber selection and nonlinear development of these vortices.

In curved channels, steady two-dimensional vortices (Dean vortices) develop above a critical Reynolds number Re_c owing to centrifugal effects. The same type of vortices are also found in channels with rotation or both curvature and rotation. Dean vortices significantly change the flow pattern, boundary layer structure, and the transition to turbulence. In a concave boundary layer, a similar vortex-type of secondary flow develops due to a centrifugal instability as the boundary layer grows thicker downstream. When the wall curvature is small, Görtler vortices provide disturbances for three dimensional Tollmien-Schlichting waves and thus cause early

transition. When the wall curvature is strong, Görtler vortices develop significantly faster than Tollmien-Schlichting waves. The boundary layer is then dominated by streamwise counter-rotating vortices and the transition toward turbulence is characterized by the breakdown of these vortices. A better understanding of these vortices may lead us a better understanding of many flows including the flows near the concave surfaces of turbine blades and aerofoils, and coolant flows inside turbine blades. Because of the analogies between the effects of curvature, rotation and buoyancy, the study of Dean vortices and Görtler vortices may also give some insight into the effects of rotation and buoyancy on transitions in the flow on a rotating plate and inside a rotating channel. Recently, some attention has been paid to the similarity between the counter-rotating streamwise vortices found in most transitional and turbulent wall bounded shear flows and Görtler vortices (cf. Swearingen & Blackwelder 1987 for a review). Some studies suggest that these vortices may be due to a Görtler instability resulting from streamwise curvature (Cantwell, Coles & Dimotakis, 1978). Thus, Görtler vortices offer a simple model to study the dynamics which govern the vortices in transitional and turbulent wall bounded shear layers.

Ever since Dean (1928) and Görtler (1940) predicted the existence of a secondary vortex-type motion in curved channels and boundary layers over concave surfaces, many efforts have been made both experimentally and theoretically to understand these vortices. Reviews of these efforts can be found in §2.1, §3.1 and §4.1. Most previous research deals with primary instabilities (Dean or Görtler instability), nonlinear evolutions of these vortices and secondary instabilities with respect to streamwise disturbances. Though the instabilities predicted by theoretical works over the years have been observed in experiments, many of the rich features revealed experimentally are still unexplained for. The secondary instability of these vortices with respect to spanwise disturbances (spanwise secondary instabilities) has never been addressed before.

In this study, using both temporal and spatial instability theories and three dimensional numerical simulations, we study the spatial development of Dean vortices and Görtler vortices and their secondary instabilities with respect to spanwise perturbations. We examine the roles of primary instability and spanwise secondary instability in the wavenumber selection process and their effects on the nonlinear evolution of Dean and Görtler vortices. Since both Görtler vortices and Dean vortices are caused by centrifugal instabilities and share various similarities, we compare and contrast the features of these two types of vortices.

In chapter 2, we study the spanwise secondary instability of the vortices found in curved and/or rotating channels using a temporal approach and spectral methods. In chapter 3, we develop a Legendre spectral-element method to study the spanwise secondary instability of spatially developing nonlinear vortices. As an application, we examine the linear and nonlinear aspects of the spanwise secondary instability of spatially developing Dean vortices. The same aspects of Görtler vortices are given in chapter 4. Chapters 2, 3 and 4 are reasonably self-contained and the references for each chapter are given at the end of the chapter. Final remarks are in chapter 5.

References

Cantwell, B.J., Coles, D.E. & Dimotakis, P.E. 1978 Structure and entrainment in the plane of symmetry of a turbulent spot. *J. Fluid Mech.* **87**, 641-672.

Dean, W.R. 1928 Fluid motion in a curved channel. *Pro. Roy. Soc. London A*, **121**, 402-420.

Görtler, H. 1940 Über eine drei- dimensionale instabilität laminarer Grenzschichten an konkaven wanden. *Math Phys Kl* **2**, 1, also *NASA TM*. 1375 (1954).

Swearingen J.D. & Blackwelder R.F. 1987 The growth and breakdown of streamwise vortices in the presence of a wall. *J. Fluid Mech.* **182**, 255-290.

CHAPTER 2

Splitting, merging and wavelength selection of vortices in curved and/or rotating channel flow due to Eckhaus instability

2.1 Introduction

¹As the Reynolds number, Re , is increased, the flow in channels with either curvature or rotation or both undergoes a supercritical transition from spanwise uniform one-dimensional ($1D$) Poiseuille type flow to a state with spanwise periodicity containing two-dimensional ($2D$) streamwise-oriented vortices. This transition is characterized by the $1D$ flow losing its stability to spanwise perturbations, due to an imbalance of centrifugal, Coriolis and pressure forces. For fixed curvature or rotation rate, the transition occurs when Re exceeds some critical value Re_c . When $Re = Re_c$, there is only one possible spanwise wavenumber α_c

¹A version of this chapter has been published in J. Fluid Mech. (1991), vol. 228, pp.661-691.

for the $2D$ vortices (cf. Tritton & Davies 1985, Finlay, Keller & Ferziger 1988, Alfredsson & Persson 1989, Finlay 1990 for a literature review on the primary instability of $1D$ Poiseuille type flow to $2D$ vortices in channels with either curvature or rotation, and Matsson & Alfredsson 1990 for channels with both curvature and rotation). At higher Re , a continuous band of stable wavenumbers for the $2D$ vortices is expected. The limits of this band are given by several different instabilities of the $2D$ vortices. For channels with infinite span, one of the most important instabilities of the $2D$ vortices is due to spanwise perturbations. In this paper, linear stability theory and flow simulation are used to examine this type of instability numerically for the flow in channels with curvature or rotation or both.

The channel geometry is given in figure 2.1. The channel spacing is $d = r_o - r_i$. The streamwise and spanwise directions of the flow are given by θ and z . The Reynolds number is $Re = \bar{U}d/2\nu$, where \bar{U} is the mean (bulk) streamwise velocity. The radius ratio of the two walls is $\gamma = r_i/r_o$. The rotation number is defined as $Ro = \Omega d/2\nu$, where Ω is the rotation speed of the system about the z -axis. The term rotating channel will be used to mean $Ro \neq 0$ and $\gamma = 1.0$, while the term curved channel refers to $Ro = 0$ and $\gamma < 1.0$. Otherwise the channel has both curvature and rotation. The spanwise wavenumber of the vortices is defined as $\alpha = \pi d/\lambda$, where λ is the spanwise vortex spacing. The term "two-dimensional vortices" indicates that each velocity component depends only on the two directions r and z . The flow is three-dimensional in the sense of having three velocity components. In channel flow experiments, the spanwise dimension of the channel is h and the aspect ratio $\Gamma = h/d$ is a finite number.

Instabilities induced by centrifugal and Coriolis forces have been studied for many years. One classical example is Taylor-Couette flow. Years of effort by many researchers (cf. DiPrima & Swinney 1985) has led to considerable knowledge about the physics of the transition to turbulence in this geometry. Similar work is needed for the flow in channels with curvature or rotation or both. A better understanding

of transition in these channel geometries may lead us to a better understanding of many flows including the flow inside impellers of centrifugal pumps or compressors, coolant flow in turbine blades, and deep sea currents partitioned by submarine ridges.

There has been some work done on the instabilities of $2D$ vortices in channels with either curvature or rotation or both. Recently, Finlay *et al.* (1988) and Finlay (1990) have examined numerically the instability with respect to perturbations that cause the vortices to become wavy in the streamwise direction. This instability does not restrict the spanwise wavenumber of the flow. These wavy vortices are similar to oscillatory Rayleigh-Bénard convection or wavy Taylor vortices. Though the flow in channels with either curvature or rotation or both bears some similarity to Taylor-Couette flow, recent experimental studies in channels with large aspect ratio ($\Gamma \geq 40$) show there is considerable unsteadiness that is not present in Taylor vortex flow (cf. Ligrani & Niver 1988 for the curved channel, Alfredsson & Persson 1989 for the rotating channel and Matsson & Alfredsson 1990 for the curved-rotating channel). When viewed in a spanwise-streamwise plane, the vortices cause long streaks in experimental flow visualizations. These streaks are occasionally split apart by new streaks or merge together (Alfredsson & Persson 1989, Matsson & Alfredsson 1990). We will refer to these phenomena as the splitting and merging of vortex pairs in this paper. These terms are always used to describe the behaviour of two or more vortex pairs, not individual vortex tubes. In the curved channel, spanwise motion, modulation and oscillation of vortices are also observed (Ligrani & Niver 1988). These phenomena are not well understood. Studies on the instability of $2D$ vortices to spanwise perturbations in Rayleigh-Bénard convection and Taylor-Couette flow show that an Eckhaus instability restricts the band of stable wavenumbers (Clever & Busse 1974, Riecke & Paap 1986). For Taylor vortices good agreement exists between theoretical and experimental results for the band of stable wavenumbers (Riecke & Paap 1986, Dominguez-Lerma, Cannel & Ahler 1986). If

vortices are created with wavenumber outside the stable region, Eckhaus instability causes the vortices to change their wavelength so that it lies in the stable region. But in channels with either curvature or rotation or both, little of such work has been done.

The instability with respect to spanwise perturbations bears the name of Eckhaus, since the first study of this type of instability was done by Eckhaus (1965, Eckhaus's work first appeared in 1963 in French in *J. de Physique*) for Tollmien-Schlichting waves, using an amplitude expansion method. His result shows that for a system of real eigenvalues and parameters, the band of stable wavenumbers α is given by $(\alpha_c - \alpha_-)/\sqrt{3} < \alpha - \alpha_c < (\alpha_+ - \alpha_c)/\sqrt{3}$, where α_- and α_+ are the wavenumbers on each branch of the neutral curve of primary instability for a given Re . The Eckhaus criterion has been proven valid in Rayleigh-Bénard convection and Taylor-Couette flow for Re close to Re_c . Stuart & DiPrima (1978) have corrected the above criterion for a general periodic flow and demonstrated the equivalence between the Eckhaus instability and the sideband instability of Benjamin & Feir (1967). To our knowledge, the stability criterion they give is the only available criterion for the flow in curved and/or rotating channels. However this criterion is only valid in the region close to Re_c .

At low Re in curved and/or rotating channels, the wavenumbers of experimentally observed vortices are close to those with the maximum growth rate of primary instability (i.e. maximum primary growth rate, cf. Finlay *et al.* 1988, Alfredsson & Persson 1989, Ligrani & Niver 1988). This suggests that perturbations with these wavenumbers develop faster than others from the $1D$ flow, thus becoming the dominant wavenumbers in the fully developed vortex flow. This is the only available comment in the literature regarding a mechanism for spanwise wavenumber selection in channels with either curvature or rotation. Yet this comment does not apply to high Re where the observed wavenumbers are considerably smaller than those with maximum primary growth rate (Finlay *et al.* 1988, Alfredsson & Persson

1989, Ligrani & Niver 1988).

In this chapter, the Eckhaus instability of the flow in channels with either curvature or rotation or both is studied. The formulation of the problem and numerical method we use are briefly described in §2.2. In §2.3, we present Eckhaus boundaries for channels with either curvature or rotation or both. We discuss the splitting and merging of vortices in §2.4. A spanwise wavenumber selection mechanism is discussed in §2.5 and recurrent splitting and merging in §2.6. Nonlinear flow simulations of splitting, merging and wavelength selection are given in §2.7.

2.2 Theory and numerical methods

For steady, two-dimensional, streamwise-oriented vortices, the pressure gradient ∇p is a constant and the velocity of the flow can be represented by

$$\mathbf{u}^0 = \left(-\frac{1}{r} \frac{\partial \psi}{\partial z}, u_\theta, \frac{1}{r} \frac{\partial \psi}{\partial r} \right) \quad (2.1)$$

where ψ is the stream function. The governing equations are the incompressible, steady, Navier-Stokes equations:

$$\begin{aligned} \mathbf{u}^0 \cdot \nabla \mathbf{u}^0 &= -\frac{1}{\rho} \nabla p + \nu \nabla^2 \mathbf{u}^0 - 2\Omega \mathbf{e}_z \times \mathbf{u}^0 \\ \nabla \cdot \mathbf{u}^0 &= 0. \end{aligned} \quad (2.2)$$

Periodic boundary conditions are imposed in the z direction, since the flow is assumed to have infinite span. Spectral methods are used to solve the above equations. We use a Fourier Galerkin method in the z direction and a Chebyshev tau method in the r direction. To eliminate aliasing error, the 3/2 rule is used to evaluate the nonlinear terms (cf. Canuto, Hussaini, Quarteroni, & Zang 1988). Adequate resolution is insured by monitoring the energies in the highest modes. In our computation, the numbers of Fourier modes N and Chebyshev modes M

vary from 16×16 to 20×26 ($N \times M$) depending on Re, γ, Ro and the spanwise wavenumber α of the vortices. Normally we include only one pair of vortices in the computational box.

Once the 2D vortex flow \mathbf{u}^0 is found, its stability can be examined using linear stability analysis. For small disturbances \mathbf{u}' , the perturbation equation can be linearized as

$$\begin{aligned} \frac{\partial \mathbf{u}'}{\partial t} + \mathbf{u}^0 \cdot \nabla \mathbf{u}' + \mathbf{u}' \cdot \nabla \mathbf{u}^0 &= -\frac{1}{\rho} \nabla p' + \nu \nabla^2 \mathbf{u}' - 2\Omega \mathbf{e}_z \times \mathbf{u}' \\ \nabla \cdot \mathbf{u}' &= 0. \end{aligned} \quad (2.3)$$

In general the perturbation \mathbf{u}' can be expressed as

$$\mathbf{u}'(r, \theta, z) = \bar{\mathbf{u}}(r, z) \exp [st + i(c\theta + bz)] \quad (2.4)$$

where c and b are the streamwise and spanwise wavenumbers of the perturbation. Since we are only interested in the spanwise perturbation, we set $c = 0$. Inserting the above expression into (2.3), the stability problem becomes an eigenvalue problem: the stability of \mathbf{u}^0 is determined by σ , the real part of the eigenvalue $s = \sigma + i\omega$. The flow pattern of the perturbation is given by

$$\text{Real} \{ \bar{\mathbf{u}}(r, z) \exp(ibz) \}. \quad (2.5)$$

Fourier Galerkin and Chebyshev tau spectral methods are used to solve the above eigenvalue problem. To reduce the number of unknown variables, the following representation of the perturbation is used:

$$\mathbf{u}' = \nabla \times \varphi \mathbf{e}_r + \frac{1}{2}(1 - \gamma) \nabla \times \nabla \times \chi \mathbf{e}_r. \quad (2.6)$$

Equation (2.3) then is reduced to two scalar equations: $\mathbf{e}_r \cdot \nabla \times (2.3)$ and $\mathbf{e}_r \cdot \nabla \times \nabla \times (2.3)$. If the resolution of \mathbf{u}^0 is $N \times M$, the dimension of the resulting complex eigenvalue problem is $2 \times (M - 2)(N + 1)$, compared with $(M - 1)(N/2 + 1) + (M - 3)(N/2)$ for the wavy type instability where only the out-phase (or in-phase) modes

are needed (Finlay *et al.* 1988, Jones 1981, 1985). Computation of the Eckhaus instability is thus much more expensive than in the wavy instability, especially when $N \times M$ is large. Among $2 \times (M - 2)(N + 1)$ eigenvalues, we are only interested in the eigenvalue with largest real part. We will use the term "Eckhaus eigenvalue" to refer to this eigenvalue and "Eckhaus growth rate" to refer to the real part of this eigenvalue. A similar method for solving the eigenvalue problem was used successfully by Clever & Busse (1974) for Rayleigh-Bénard convection and by Nagata (1986, 1988) and Jones (1985) for Taylor-Couette flows. More details of this method can be found in their papers.

To avoid a singularity when $\gamma = 1.0$ the nondimensional variables must be chosen carefully. The following nondimensional variables (x, y, z, t) are used in our formulation:

$$\begin{aligned} r/r_o &= \frac{1}{2}(1 + \gamma) + \frac{1}{2}(1 - \gamma)x \\ \theta &= \frac{1}{2}(1 - \gamma)y \\ z^*/r_o &= \frac{1}{2\alpha}(1 - \gamma)z \\ t^* &= \frac{d^2}{4\nu}t \end{aligned}$$

where z^* and t^* are dimensional, $-1.0 \leq x \leq 1.0$ and $0 \leq z \leq 2\pi$. The perturbation wavenumber b is thus non-dimensionalized by the spanwise wavelength of the vortices $2\pi/\lambda$. The resulting codes were extensively verified by duplicating the results of previous authors, including the Eckhaus boundary for Taylor vortices obtained by Riecke and Paap (1986), the wavy instability ($b = 0, d \neq 0$) results for Taylor vortices obtained by Jones (1985), and the wavy instability results obtained in channel flows with curvature or rotation by Finlay *et al.* (1988) and Finlay (1990).

It has been reported (Zebib 1984, Gardner, Trogdon & Douglass 1989) that the Chebyshev tau method produces spurious eigenvalues and in some cases it is

difficult to distinguish true eigenvalues from spurious ones. In our problem, spurious eigenvalues are also found. However, because only one spurious eigenvalue with positive real part is produced by the Chebyshev tau method for each Fourier mode and these spurious eigenvalues always have much larger magnitude ($|s|$) than the true eigenvalues (cf. Fox & Parker 1968), it is not difficult to distinguish between the true and spurious eigenvalues. The spurious eigenvalues can also be found easily by changing the number of modes used, i.e. M and N ; this causes the spurious eigenvalues to change drastically whereas the true eigenvalues vary little with M and N for sufficiently large M and N .

It can be shown that for any spanwise periodic flow, the eigenvalue $s = \sigma + i\omega$ and the non-dimensional spanwise perturbation wavenumber b have the following relation:

$$s(b) = s(\pm k \pm b) \quad (2.7)$$

where $0.0 < b < 1.0$ and $k = 1, 2, 3, \dots$ (cf. Appendix A). This result reduces the values of b we need examine to $0 < b < 1/2$, since setting $k = 1$ shows that $s(b) = s(1 - b)$ (i.e. s is symmetric about $b = 1/2$) and setting $k = 2, 3, 4, \dots$ covers the remaining b .

Equation(2.7) applies for any spanwise periodic flow. Our numerical results verify (2.7) for both Taylor-Couette flow and the flow in channels with either curvature or rotation or both. The numerical results given by Nagata & Busse (1983, their figure 10) and by Paap & Riecke (1990, their figure 2) also demonstrate the symmetry property of σ about $b = 0.5$ for $0 < b < 1$ in buoyancy driven shear layer flow and Taylor-Couette flow. Some previous studies did not exploit this property (2.7). Its immediate significance is to drastically reduce the range of perturbation wavenumbers that need to be explored and thus to reduce computational expense. In our studies, since the numerical difference between the eigenvalues s for $0 < b < 0.5$ and $0.5 < b < 1.0$ is less than 0.1% for the stated resolution, we only calculate s

for $0 < b < 0.5$. The values of s for $0.5 < b < 1.0$ are obtained from the symmetry property in (2.7).

2.3 Eckhaus stability boundary

The Eckhaus stability boundary is determined by a sign change in the Eckhaus growth rate σ as the parameters of the system are varied. Within the Eckhaus boundary, the Eckhaus growth rate is always negative. In the region neighboring the Eckhaus boundary, our numerical results show the eigenvalue with the maximum Eckhaus growth rate is always real. The stability boundary is thus determined by non-oscillatory perturbations. Figure 2.2 shows the Eckhaus boundaries for several channels with either curvature or rotation or both. In a curved channel ($\gamma = 0.975$) with rotation, Matsson & Alfredsson (1990) find the primary instability occurs as a Hopf bifurcation when $-0.014 > Ro > -0.0164$. Thus for Ro in this range there are no steady $2D$ vortex solutions. The two cases we present in figure 2.2(c) at $Ro = -0.0125$ and -0.02 are just outside the range of Ro for the primary instability to appear as a Hopf bifurcation. Figure 2.2 shows that the Eckhaus stable region for the flow in curved and/or rotating channels is a small closed region tangent to the minimum of the neutral stability curve for the primary instability. In all cases calculated by us, the Eckhaus boundary is only a weak function of γ and Ro .

When compared to other spanwise periodic flows known to the authors, channel flows with either curvature or rotation or both exhibit significant differences. For example in Taylor-Couette flow, the Eckhaus boundary is an open region, i.e., for any Re , there is always a band of stable wavenumber α . On the Eckhaus boundary, the spanwise wavenumber of perturbations, b , approaches zero when Re is not very high (Riecke & Paap, 1986). When Re is high, the boundary is given by $b = 0.5$ (Paap & Riecke, 1990). Paap & Riecke (1990) refer to this as a short-wavelength instability, in order to distinguish it from the long-wavelength nature of the classical

Eckhaus instability. Numerical calculations done by us for Taylor-Couette flow show that as α moves away from the Eckhaus boundary, b approaches 0.5 when Re is not very high. As Re increases, this happens very quickly. This is consistent with the results given by Paap & Riecke (1990). Our results also show that for any Re , α and b , the eigenvalue with maximum real part is always real in the Taylor-Couette problem. All parameters of the system are thus real and the stability criterion given by Eckhaus (1965) is valid in the region near Re_c (Riecke & Paap 1986)

In channels with either curvature or rotation or both, the situation is much more complicated. We have studied the case of the curved channel with $\gamma = 0.975$ most carefully. Our results show that near the left side of the Eckhaus boundary, the eigenvalue with Eckhaus growth rate is real for any b . Figure 2.3 shows $\sigma(b)$ at $Re = 1.07Re_c$ (figure 2.3a) and $1.225Re_c$ (figure 2.3b) as α approaches the left side of the Eckhaus boundary. Figure 2.3(a) shows that at $Re = 1.07Re_c$, $b = 0.0$ determines the Eckhaus boundary. Figure 2.3(b), however, shows that at $Re = 1.225Re_c$, $b = 0.5$ determines the boundary.

In the neighborhood of the right side of the Eckhaus boundary, the eigenvalue with Eckhaus growth rate is not real for all b when $Re > 1.1Re_c$. For some b , a complex conjugate pair has the maximum real part. Figure 2.4 shows the eigenvalue $s(b)$ for various α near the right side of the Eckhaus boundary at $Re = 1.07Re_c$ (figure 2.4a) and $Re = 1.225Re_c$ (figure 2.4b). The eigenvalue has zero imaginary part at $Re = 1.07Re_c$ so only $\sigma(b)$ is shown in figure 2.4(a). In figure 2.4(b) only the positive imaginary part of the eigenvalue is shown. By using different numbers of Chebyshev modes and Fourier modes, we have verified that these complex eigenvalues are not spurious eigenvalues produced by the Chebyshev tau method. Figure 2.4(a) shows that at $Re = 1.07Re_c$, $b = 0.25$ on the boundary. Figure 2.4(b) shows that at $Re = 1.225Re_c$, $b = 0.5$ on the boundary. Figure 2.4 also shows that the imaginary part of the eigenvalue which determines the Eckhaus boundary is zero on the boundary.

The value of $b(Re)$ on the boundary is shown in figure 2.5. On both sides of the boundary, b reaches 0.5 when $Re \geq 1.175Re_c$. Clearly here the boundary defined by the instability of 2D vortices to spanwise perturbations is not the classical Eckhaus stability boundary ($b \rightarrow 0$) found in Taylor-Couette flow. When $Re \leq 1.125Re_c$, only the left side of the boundary is of the classical Eckhaus type. For simplicity, we still call the entire boundary an Eckhaus boundary. Figure 2.6 shows a comparison of the Eckhaus criterion (Eckhaus, 1965), primary stability boundary (Finlay *et al.* 1988) and the Eckhaus boundary we have determined, all for a curved channel with $\gamma = 0.975$. The Eckhaus stability criterion does not apply to the right side of the Eckhaus boundary even in the region close to Re_c . On the left side, it is valid with reasonable accuracy up to $Re < 1.04Re_c$. In Taylor-Couette flow, the Eckhaus stability criterion is valid with reasonable accuracy up to $1.1Re_c$ for both sides of the boundary (Riecke & Paap, 1986). We believe that $b \neq 0$ and non-real eigenvalues on the right side of the boundary are the reason why the Eckhaus criterion is not valid here. (Another case where the Eckhaus criterion does not apply is the inclined shear layer driven by wall heating (Nagata & Busse 1983). There, the Eckhaus criterion is invalid on both sides of the Eckhaus boundary even near Re_c). Although the perturbation equations for both Taylor-Couette flow and curved and/or rotating channel flow have the same form (2.3), the base flow \mathbf{u}^0 is not the same. In channel flow, the streamwise component of \mathbf{u}^0 decreases to zero away from a maximum near the center of the channel, whereas in Taylor-Couette flow, the streamwise velocity is maximum at a wall. We believe this may be responsible for the difference between the Eckhaus instabilities in these geometries.

Beyond the top of the Eckhaus boundary, if Re/Re_c is not too high and α is not too small or too large, the eigenvalue with the maximum Eckhaus growth rate is given by $b = 0.5$ and is real. In the curved channel with $\gamma = 0.975$, we find the eigenvalue with the maximum Eckhaus growth rate is entirely real in the region of $Re \leq 3.5Re_c$ and $1.8 \leq \alpha \leq 5.0$. But at given Re there does exist a spanwise

wavenumber α' such that when $\alpha > \alpha'$, Eckhaus eigenvalues are complex for some $b \neq 0.5$. For example, at $Re = 2.0Re_c$, $\alpha' = 3.5$.

When Re/Re_c is very high, for example $Re/Re_c > 3.2$ in rotating channels, the real part of a complex conjugate pair is the largest for some α and so the corresponding perturbation is oscillatory. For example, at $Re = 472.5$ ($Re/Re_c = 5.56$) in the rotating channel $Ro = 0.03$, we find that when $2.0 \leq \alpha \leq 3.0$, an oscillatory unstable mode has the largest σ , but for $\alpha \leq 2.0$ and $\alpha \geq 3.75$ the most unstable mode has zero imaginary part. Because the Eckhaus instability is likely less important at high Re than the wavy instability, and the computation becomes very expensive, only a few high Re cases have been explored. More work needs to be done before this type of oscillatory unstable mode can be understood.

Results similar to those discussed above are found in all channels we examined. In all cases, $2D$ vortices are unstable to spanwise perturbations when $Re > 1.7Re_c$ (they are often unstable at even lower Re). Since the Eckhaus stable region is small and most experiments have been done outside this region, the instability associated with the most unstable mode, which usually has $b = 0.5$, is an important instability in channel flows with curvature or rotation or both.

2.4 Splitting and merging of vortices

In channel flow experiments, vortex pairs are sometimes observed to merge together (reducing the number of vortices across the channel) or to be split apart by the formation of new vortex pairs (Ligrani & Niver 1988, Alfredsson & Persson 1989, Matsson & Alfredsson 1990). In some cases, the merging and splitting of vortex pairs happens repetitively (Ligrani & Niver, 1989). Similar phenomena have also been reported by Finlay *et al.* (1988), Finlay (1989) and Bland & Finlay (1990) in their numerical simulations of channel flows with curvature or rotation. We believe that the splitting and merging of vortex pairs are associated with the instability of

$2D$ vortices to spanwise perturbations. In §2.3 our linear stability results indicate that no $2D$ vortex flow is stable to spanwise perturbations when $Re > 1.7Re_c$. In order to understand how these $2D$ vortex pairs lose their stability to spanwise perturbations and split apart or merge together, we examine the flow pattern of the most unstable mode of linear stability theory. The flow pattern of the most unstable mode is given by the eigenfunction (2.5), which has the largest growth rate σ . It grows at the rate $\exp(\sigma t)$.

2.4.1 Taylor-Couette flow

First, Taylor vortex flows are studied, because here linear stability theory calculations (Riecke & Paap, 1986) and experimental observation (Dominguez-Lerma *et al.* 1986) of the Eckhaus boundary show good agreement. The pairing of vortices has been discussed by Paap & Riecke (1990) using bifurcation diagrams. Here we will discuss the splitting and merging of vortex pairs from the perspective of the flow patterns of the most unstable modes.

As mentioned before, as α moves away from the Eckhaus boundary in Taylor vortex flow, the value of b corresponding to the maximum Eckhaus growth rate increases from 0.0 to 0.5. Figure 2.7 and 2.8 show the Taylor vortices (figure 2.7a, 2.8a), their most unstable modes (figure 2.7b, 2.8b) and linear superpositions of these two (figure 2.7c, 2.8c, 2.8d) at $Re = 2.0Re_c$ outside each side of the Eckhaus boundary, where the maximum Eckhaus growth rate is given by $b = 0.5$ (the Eckhaus boundary has $\alpha_{left} = 1.188$, $\alpha_{right} = 2.425$). In figure 2.7(a) and 2.8(a), the centers of the Taylor vortex pairs are at $z/\lambda = 0.0, 1.0$ and 2.0 , where the fluid flows from the convex wall to the concave wall (the outflow region). The streamwise direction is out of the plane of the plot. In figure 2.7(b), the unstable mode has three pairs of vortices in the space of two pairs of base vortices. If the perturbation maintains this character in the nonlinear state, one extra pair of vortices would be produced

out of every two base pairs. Figure 2.7(c) is a plot of the base flow (figure 2.7a) superimposed with the most unstable eigenfunction (figure 2.7b). The kinetic energy of the eigenfunction in figure 2.7(c) has been set to 1.4% of the base flow's kinetic energy. A new pair of vortices is seen at $z/\lambda = 0.5$ near the convex wall that splits apart the pairs of vortices on either side of $z/\lambda = 0.5$ in the base flow. This indicates that splitting of vortices occurs upon exiting the left side of the Eckhaus boundary. Outside the right side of the Eckhaus boundary (figure 2.8b), one vortex pair of the unstable mode takes the space of two pairs of the base flow (except for small weak secondary vortices near the walls). Figure 2.8(c) shows the most unstable eigenfunction (figure 2.8b) superimposed on the base flow (figure 2.8a). The kinetic energy of the perturbation is 7% of the base flow's kinetic energy, which is not a linear perturbation but the large perturbation is used for visual clarity. (The effect of the perturbation on the base flow is qualitatively independent of the perturbation amplitude). The two vortex pairs centered at $z/\lambda = 1.0$ and 2.0 in the base flow are squeezed toward $z/\lambda = 1.5$ by the two single vortices at $z/\lambda = 1.0$ and 2.0 in the eigenfunction. The two base vortices on either side of $z/\lambda = 1.5$ are weakened. This is seen more clearly when the percentage of the perturbation increases to 50% in figure 2.8(d). If this character of the perturbation is maintained in the nonlinear state, we can expect that the two vortices on either side of $z/\lambda = 1.5$ in the base flow will disappear. Thus one out of every two pairs of vortices will be lost, i.e. merging of vortices occurs upon exiting the right side of Eckhaus boundary.

Our numerical results show that the number of vortices in the perturbation eigenfunction depends on b . Over a distance λ/b , there is one extra pair (left side of the boundary) or one less pair (right side of the boundary). For example when $\alpha = 2.3$ at $Re = 1.5Re_c$ (the right side of Eckhaus boundary has $\alpha_{right} = 2.28$ at this Re), the maximum Eckhaus growth rate is given by $b = 0.1$. The corresponding eigenfunction shows that nine pairs of the perturbation vortices occupy the space of ten pairs of the base flow, i.e. only one pair will be lost for every ten pairs of base

vortices. Thus when α is close to the Eckhaus boundary where the most unstable mode has small b , a relatively small number of vortices will be produced or lost for a given number of base vortices. Further away from the boundary where the most unstable disturbance has $b = 0.5$, a larger number of vortices will be produced or lost.

In Taylor-Couette flow experiments, the spanwise wavenumber of the base vortex flow can be controlled by using adjustable spanwise walls (Dominguez-Lerma *et al.* 1986). Once Taylor vortices of desired wavenumber are developed at high Re , the Eckhaus boundary can be found by decreasing Re until the flow loses its stability. Usually only one pair of vortices is produced or lost when the flow crosses the Eckhaus boundary. Based on our results, only a single pair appears or disappears because as the flow crosses the boundary into the unstable region, unstable perturbations occur with b slightly greater than zero. When unstable modes occur with b having a certain value, the finite span of the experimental device allows an extra pair of vortices to be produced or absorbed: splitting or merging of vortex pairs occurs. The resulting vortex flow will then have a wavenumber which is inside the stable region.

The perturbation flow patterns from the Eckhaus instability seem to explain the Taylor-Couette experiment observations. But one should be cautious when using the above results to explain the details of the splitting and merging processes because the actual effects of the perturbations on the base vortices could be highly nonlinear and dependent on finite span effects. For example, if certain pairs of vortices begin to split or merge earlier than others, the following readjustment of spanwise wavenumbers across the span will change the wavenumbers of other vortices and thus change the splitting or merging processes of these other vortex pairs. However, we can say that splitting always occurs out the left side of the boundary and merging out the right side.

2.4.2 Channels with either curvature or rotation or both

In channels with either curvature or rotation or both, most experiments have been done outside the Eckhaus stable region, where the maximum Eckhaus growth rate is positive and occurs at $b = 0.5$. Figure 2.9 and 2.10 show two vortex flows ($\alpha = 2.0$ in figure 2.9 and $\alpha = 4.0$ in figure 2.10), their most unstable modes and linear superpositions of base flows plus perturbations at $Re = 2.0Re_c$ in the curved channel with $\gamma = 0.975$. Other unstable modes for different α (at $Re = 2.0Re_c$) can be found in figure 2.11 (the small waviness in figure 2.11a, d along $z/\lambda = 0.5, 1.5$ is caused by extremely small velocities being plotted with a fixed arrow size). At this Re , all spanwise wavenumbers of the base flow are unstable to Eckhaus instability. In all three figures, $z/\lambda = 0, 1.0$ and 2.0 are the centers of the base vortex pairs, where the fluid flows from the concave wall to convex wall (the inflow region). There are three types of unstable modes shown in figure 2.9, 2.10 and 2.11 that occur for different ranges of α . In figure 2.11(a), when $\alpha = 1.25$, there are five vortex pairs of the unstable mode in the space of two base pairs and the corresponding eigenvalue ($b = 0.5$) is complex. For $2.0 \leq \alpha \leq 3.5$ (figure 2.9b, 2.11b – d), three vortex pairs of the unstable mode take the space of two base pairs, though they do not have equal intensity or spanwise wavenumber. For α in this range, the eigenvalue with Eckhaus growth rate is always real for any b . In the range $\alpha > 3.5$ (figure 2.10b and figure 2.11e), there is only one vortex pair of the unstable mode in the space of two base pairs. In this range, Eckhaus eigenvalues are not always real for $b \neq 0.5$. But the eigenvalue with the maximum Eckhaus growth rate is still given by $b = 0.5$ and is real. Similar results are found in channels with rotation and curvature.

Heuristic arguments based on the flow patterns of the unstable modes in figure 2.9, 2.10 and 2.11 suggest some vortices in the unstable modes will generate new vortex pairs, causing the splitting of base vortex pairs, and some will force base vortex pairs together, causing merging. For example, in figure 2.9(b), a simple

argument suggests it is more likely the vortex pair at $z/\lambda = 1.5$ will develop compared to the one at $z/\lambda = 0.5$. This is because the large perturbation vortices centered at $z/\lambda = 1.0$ and $z/\lambda = 2.0$ induce flow at the centers of the base vortices on either side of $z/\lambda = 1.5$ that causes them to spread apart. In contrast, near $z/\lambda = 0.5$ the large perturbation vortices induce motion at the centers of the base vortices straddling $z/\lambda = 0.5$ that causes them to move together, obstructing the formation of the secondary vortex pair at $z/\lambda = 0.5$ (or $z/\lambda = 2.5$). Figure 2.9(c) shows the base flow (figure 2.9a) superimposed with the unstable mode (figure 2.9b) whose kinetic energy has grown linearly to 7% of the base flow's kinetic energy. It can be seen that one new pair of secondary vortices begins to form at $z/\lambda = 1.5$ near the concave wall. The original vortex pairs centered at $z/\lambda = 1.0$ and 2.0 spread apart from $z/\lambda = 1.5$ and are squeezed toward $z/\lambda = 0.5$ and 2.5 . As the energy level of the perturbation increases to 20% in figure 2.9(d), the new vortex pair grows bigger and moves away from the concave wall. This is a splitting event, since a new vortex pair appears between the base vortex pairs centered at $z/\lambda = 1.0$ and 2.0 . The two base vortex pairs centered at $z/\lambda = 1.0$ and 2.0 will be split apart by the new pair, yielding three pairs. Thus the vortex pair at $z/\lambda = 1.5$ in the most unstable eigenfunction is responsible for generating a new vortex pair in the outflow region of the base flow. When examining the eigenfunctions, the vortex pair which generates the new pair can be identified easily by the fact that it is centered about an inflow plane in the eigenfunctions.

As the wavenumber α of the base flow increases, the intensity of the pair responsible for splitting becomes weaker, as is shown in figure 2.11(b – d). When $\alpha > 3.5$, this pair is absent, as shown in figure 2.10(b) and 2.11(e), and splitting cannot happen. In addition, as α increases, the single vortices centered at $z/\lambda = 0.0, 1.0$ and 2.0 in the most unstable eigenfunction become stronger. These vortices are responsible for merging two base pairs together, as is seen figure 2.10 at $\alpha = 4.0$. Figure 2.10(c) shows the base flow (figure 2.10a) perturbed by 50% (kinetic energy)

of the most unstable mode (figure 2.10b). Two neighboring vortices (centered at $z/\lambda = 1.5$) of the two base vortex pairs become smaller and weaker while the other two become bigger and stronger. As the amplitude of the perturbation is increased further, the two vortices on either side of $z/\lambda = 1.5$ eventually disappear while the other two vortices form into one pair. Thus two pairs merge into one pair. The large perturbation amplitudes used to produce figures 2.9(d) and 2.10(c) are not linear amplitudes, but are used for visual clarity. The qualitative effects of the perturbations are independent of their amplitude.

The most unstable modes thus have two different effects on the base vortex flow, associated either with splitting or merging. There is not a clear cut wavenumber α that divides the effects of the most unstable modes into vortex splitting or merging regions. For example at $\alpha = 3.0$ in figure 2.11(c), the small vortex pair at $z/\lambda = 0.5$ tends to cause the appearance of a new pair in the base flow at $z/\lambda = 0.5$, while the single vortices at $z/\lambda = 0.0, 1.0$ and 2.0 tend to cause merging of the two vortex pairs in the base flow on either side of $z/\lambda = 1.5$ and this merging effect in return allows room for the appearance of the new pair. Thus when this eigenfunction is imposed on the base flow, splitting and merging of vortex pairs are seen to occur at the same time, but at spanwise locations separated by one wavelength. For general α and b , we find no strict relation between b and the number of vortices in the most unstable modes. It depends on both b and α . But it is always true that base vortex pairs with large wavenumbers merge whereas small wavenumbers split. Since base vortices with $\alpha < 1.5$ are not likely to occur experimentally because of the low growth rate of the primary instability at this α , subharmonic splitting and merging mechanisms will be the dominant feature of splitting and merging of vortex pairs in channels with either curvature or rotation or both. Since all 2D vortices are unstable to spanwise perturbations at high enough Re , the splitting and merging of vortex pairs, as suggested by figure 2.9, 2.10 and 2.11, will continually occur.

Support for our above results can be found from existing flow visualizations in

channels with either curvature or rotation or both given by various authors (Niver & Ligrani 1990, Ligrani & Niver 1988, Alfredsson & Persson 1989, Matsson & Alfredsson 1990) as well as in nonlinear simulations (§2.7). Splitting and merging of vortex pairs is prevalent in these experiments. When visualized with reflective flakes, in plan view the splitting of vortex pairs is indicated by two new bright streaks which represents a vortex pair first appearing between two existing streaks. The existing streaks are then split (spread) apart by the two new streaks. This is seen for example in figure 2.6(*d*), (*f*) of Alfredsson & Persson (1989) in channels with rotation or in figure 2.14(*d*) of Matsson & Alfredsson (1990) in a channel with both curvature and rotation. The disappearance of vortex pairs is indicated by adjacent bright streaks which occasionally merge together (cf. figure 2.6*e* of Alfredsson & Persson 1989, figure 14*d* of Matsson & Alfredsson 1990). We suggest that subharmonic splitting and merging are the mechanisms behind these phenomena. Splitting and merging of vortex pairs can also be found in flat plate boundary layers with rotation (Masuda & Matsubara, 1989) and concave wall boundary layer (Bippes, 1978) experiments. A similar Eckhaus instability mechanism in these flows may cause the splitting and merging of vortex pairs.

The actual splitting and merging processes observed in experiments are complicated and nonlinear. Niver & Ligrani (1990) and Ligrani & Niver (1988) provide observations of these processes in a curved channel ($\gamma = 0.979$). During the splitting of vortex pairs, according to their observation, new vortex pairs are formed first near the concave wall between other pairs, then followed by a readjustment of spanwise wavenumber. When viewed in the radial-spanwise plane, the new vortex pairs appear to "pop" out of the concave wall. Ligrani & Niver called them secondary vortices. This observation is consistent with our result in figure 2.9(*c*) and (*d*). The formation of the secondary vortices observed by Ligrani & Niver (1988) may thus be due to Eckhaus instability.

Further numerical results show that base vortices which have secondary vortices

between them are much more unstable to spanwise perturbations. For certain α we find two base solutions exist, one with secondary vortices and one without. Such non-uniqueness also occurs in Taylor-Couette flow (e.g. Meyer-Spasche & Keller 1985). Figure 2.12 shows the stream functions of the flows without and with such secondary vortices in a channel with rotation ($Ro = 0.03$, $Re = 472.5$). The related Eckhaus growth rate jumps from 0.059 in the absence of the secondary vortices to 0.108 when the secondary vortices are present. Comparison for other α can be found in figure 2.13 where there is always a large increase in the Eckhaus growth rate when secondary vortices are present.

The above arguments are based on linear theory which only applies to the beginning of splitting and merging processes prior to the onset of nonlinearity. In experiments, spanwise periodicity is not imposed so that if any two vortex pairs start to merge with each other earlier or more rapidly than others, neighboring vortex pairs will move in, causing a decrease in spanwise wavenumber of these neighboring vortices (readjustment of α), and suppression of their merging. Similarly, if certain vortex pairs begin to split apart earlier or more rapidly than others, they will tend to squeeze neighboring vortices and obstruct the splitting of these neighboring vortex pairs. Thus it is not surprising that in experiments the splitting and merging processes produce many patterns once the base vortices begin to lose their symmetry and move toward or away from each other. However, two to three splitting and two to one merging mechanisms are likely one of the major features of the transition from vortex flow to turbulence in channels with either curvature or rotation or both.

2.5 Wavenumber selection

Our discussion in §2.4 suggests that the splitting and merging processes are sensitive to the rate at which local perturbations develop, i.e. to the local Eckhaus growth rate σ . Vortices which yield smaller σ produce a region where the

perturbations take a longer time to develop, so that splitting or merging processes occurring elsewhere will suppress the splitting or merging of vortex pairs with low Eckhaus growth rate. Thus vortices with relatively lower growth rate are more likely to be observed in experiments. Figure 2.14 shows a plot of the Eckhaus growth rate $\sigma(b = 0.5)$ vs. α at different Re in the curved channel with $\gamma = 0.975$. For $Re \geq 2.2Re_c$, $\sigma(\alpha)$ has a minimum. When contours of σ are plotted in a (α, Re) plane this minimum appears as a valley and we call it the Eckhaus valley. As Re increases, both sides of the valley become steeper. Based on our above discussion, observed wavenumbers should be close to this valley. For $Re < 2.2Re_c$, σ varies little with α and here Eckhaus instability does not play a major role in the wavenumber selection process. Thus when $Re < 2.2Re_c$, without any other nonlinear selection mechanism the observed wavenumbers should be close to the ones with maximum primary growth rate, since these vortices develop most rapidly from the $1D$ Poiseuille type flow. Figure 2.15 shows the Eckhaus valley for $\gamma = 0.975$ in comparison with the wavenumbers observed by Kelleher *et al.* (1980) in a curved channel with $\gamma = 0.979$. Also shown are the wavenumbers with maximum primary growth rate and maximum pressure gradient (Finlay *et al.* 1988). For $Re < 2.2Re_c$, the observed wavenumbers are close to the ones with maximum primary growth rate. For $Re \geq 2.2Re_c$, the observed wavenumbers are close to the Eckhaus valley. This is consistent with our discussion.

A similar comparison can be found in figure 2.16 at $Re = 175$ and 472.5 in channels with rotation. The wavenumbers were measured by Alfredsson & Persson (1989) at three different downstream locations $y/d = 40, 80$ and 120 . In figure 2.16(a) the observed wavenumbers at $y/d = 40$ are closer to those with maximum primary growth rate than the Eckhaus valley. As the downstream distance increases to 80 and 120 , the observed wavenumbers become much closer to the Eckhaus valley. This suggests that near the entrance of the channel where the flow is still developing from $1D$ Poiseuille type flow to $2D$ vortices, the primary instability

plays an important role in wavenumber selection process. Once the $2D$ vortices are more fully developed, the Eckhaus instability sets in and the wavenumbers of the vortices are selected by the Eckhaus valley. This is particularly noticeable for $Ro \geq 0.05$ ($Re/Re_c \geq 2.566$) in figure 2.16(a), where the Eckhaus valley and observed wavenumbers diverge significantly from the curve of maximum primary growth rate.

In channels with rotation $Ro < 0.25$, the critical Reynolds number Re_c decreases as the rotation number Ro increases (Alfredsson & Persson 1989). So for a given Re , Re/Re_c increases as Ro increases. Our results indicate the Eckhaus valley becomes deeper and narrower with increasing Re/Re_c , making it a more effective wavenumber selection mechanism at higher Re/Re_c . Figure 2.16(a) indeed shows that the effect of the Eckhaus instability on wavenumber selection becomes more obvious as Re/Re_c increases. Figure 2.16(b) shows that at high Re/Re_c ($3.37 < Re/Re_c < 6.3$ in figure 2.16b) the Eckhaus valley provides a much better prediction for the observed wavenumber than the primary instability.

Similar results are found in channels with both curvature and rotation. Figure 2.17 shows a plot of the maximum Eckhaus growth rate vs. α at different Ro in the curved channel with $\gamma = 0.975$ and $Re = 180$. As $|Ro|$ increases in figure 2.17, the slopes of the Eckhaus valley become steeper. Increasing $|Ro|$ is thus similar to increasing Re in curved channels in that both cause an increase in the slope of the side of the Eckhaus valley. Figure 2.18 shows the corresponding Eckhaus valley and the wavenumbers which have the maximum primary growth rate. Matsson & Alfredsson (1990) provide experimental flow visualizations of vortices in channels with both curvature and rotation but the wavenumbers of the vortices are not available in their publication, so no comparison is made here.

Matsson & Alfredsson (1990) observe a range of Ro where rotation opposes curvature and restabilizes the flow to a $1D$ state. When $Ro = 0$ at $Re = 180$, they observe $2D$ vortices. When Ro decreases to -0.015 , they observe a complete

cancellation of vortices by rotation. In our numerical computation, we cannot obtain any steady $2D$ vortices near this parameter range. As Ro decreases further, $2D$ vortices begin to develop again in line with Matsson & Alfredsson's results.

At sufficiently high Re/Re_c and at locations far enough downstream from the inlet, $2D$ vortices in curved and/or rotating channels lose their stability to streamwise perturbations and develop into three-dimensional wavy vortices (Finlay *et al.* 1988, Finlay 1990). The spanwise wavenumber selection process is then no longer just determined by the Eckhaus instability. For example in the curved channel with $\gamma = 0.975$, $2D$ vortices first lose their stability to streamwise perturbations at $Re'_c = 1.2Re_c$ and $\alpha'_c = 2.2$, developing into undulating wavy vortices (Finlay *et al.* 1988) and calculations by us show at $Re''_c = 1.92Re_c$ and $\alpha''_c = 2.58$, they develop into twisting vortices (other values of α require larger Re for wavy vortices to develop). Little is known about the stability of $3D$ vortices in channels with either curvature or rotation or both. The effect of the wavy instability on wavenumber selection is unknown. In their numerical simulations, Finlay *et al.* (1988) reported that streamwise waviness delayed the onset of vortex doubling to higher Re .

Competition between Eckhaus instability and wavy instability will be dominated by wavy instability when the corresponding growth rates of Eckhaus instability are much less than those of the wavy instability. For example, in figure 2.16(a), the ratio of the average Eckhaus growth rate to the wavy growth rate is about 0.7. Here good agreement is found between the observed wavenumbers and the Eckhaus valley. Thus, when the Eckhaus growth rate is not that much less than that of the wavy instability, it appears that splitting and merging occur before the vortices develop into $3D$ vortices and the Eckhaus instability plays an important role in wavenumber selection. In figure 2.16(b) this ratio is 0.2, much smaller than in figure 2.16(a). The difference between the Eckhaus valley and the observed wavenumbers suggests that there is some effect due to the three-dimensionality of the vortices.

However, little can be said on this issue without performing a stability analysis of 3D wavy vortex flow.

2.6 Recurrent splitting and merging

The repetitive appearance of splitting and merging was first reported by Ligrani & Niver (1988) in a curved channel ($\gamma = 0.979$). It only occurred at certain Re ($Re = 2.03Re_c$ and $2.14Re_c$). The flow visualization results obtained by Alfredsson & Persson (1989) in channels with rotation (cf. their figure 6e) and by Matsson & Alfredsson (1990) in channels with both curvature and rotation (cf. their figure 14d) suggest that such a phenomenon also exists in rotating or curved-rotating channels. For example in a curved-rotating channel at $Re = 180$, $\gamma = 0.975$, $Ro = -0.025$ (figure 14d of Matsson & Alfredsson 1990), we can see that a short time after two vortex pairs split apart into three pairs, two of these three pairs merge back into one and then split again with the other one into three pairs. The mechanism behind this is still the subharmonic two to one merging and two to three splitting. Our discussion in §2.4 indicates that when the flows resulting from splitting or merging have the same Eckhaus growth rate as before the split or merge, the repetitive appearance of splitting and merging will occur. This may happen in two cases: *a*) where the Eckhaus valley is very flat and *b*) when the wavenumbers of the flows resulting from splitting and merging alternate between opposite sides of the Eckhaus valley where the Eckhaus growth rates are nearly the same. It is difficult to predict when the second case will happen. Compared with the first case, the conditions required for the second case are much more restrictive, so the chance of it being observed is considerably less than case *a*). In the first case, the Eckhaus growth rate is approximately the same for any vortex pair, so no vortex wavenumber is significantly more stable than any other. There is thus a good chance for the recurrent appearance of splitting and merging. In the curved channel

with $\gamma = 0.975$, this range is $1.7 \leq Re/Re_c \leq 1.9$ (figure 2.14). Ligrani & Niver observed repetitive splitting and merging when close to this region. For Matsson & Alfredsson's case, the corresponding Eckhaus growth rate is shown in figure 2.17(a). In the range $-0.025 \leq Ro \leq -0.035$, the Eckhaus growth rate curve is relatively flat near its minimum value. Repetitive splitting and merging thus mostly appears to occur in parameter regimes where the Eckhaus valley is relatively flat.

2.7 Nonlinear vortex splitting and merging

The results on splitting and merging given in §2.4, 2.5 and 2.6 are based on linear stability theory. Nonlinearity sets in once a splitting or merging event develops past the initial linear stage. In order to study the nonlinear aspect of the problem and how it affects the validity of our linear theory results, we use the Galerkin spectral numerical method of Moser, Moin & Leonard (1983) to simulate the axisymmetric, time-dependent, incompressible Navier-Stokes equations in a curved channel. The code is a modification of the one used to study wavy Taylor vortices by Moser *et al.* (1983), wavy Dean vortices by Finlay *et al.* (1988), wavy vortices in rotating channel flow by Finlay (1990) and to perform a direct simulation of turbulence in the curved channel (Moser & Moin 1984, 1987). Periodic boundary conditions are used in the spanwise direction. We will discuss two simulations. The first of these demonstrates the nonlinear details of splitting and merging, while the second demonstrates wavelength selection due to Eckhaus instability.

According to the linear stability analysis of §2.4, the spanwise wavenumber of the most unstable disturbance is $\alpha/2$ (i.e. $b = 0.5$), where α is the spanwise wavenumber of base flow. In our first simulation, the spanwise computational domain is chosen to initially include two complete vortex pairs. Small, two-dimensional random disturbances ($< 0.1\% \bar{U}$) are used to perturb the initial 2D vortex flow. The solution progresses in time with constant mass flux imposed. The energies in the highest

modes are monitored to insure that adequate resolution is achieved. The simulation parameters are $Re = 1.776Re_c$ and $\gamma = 0.975$. The wavenumber of the initial vortices is $\alpha = 2.0$. At these parameters, we use 40 spanwise Fourier modes and 32 Chebyshev polynomials in the radial direction.

Figure 2.19 shows the flow velocity projected onto (r, z) plane at different time steps. The initial conditions for the simulation are shown in figure 2.19(a). The centers of the initial two pairs are at $z/\lambda = 0.5$ and 1.5 . At $t = 5700d/2\bar{U}$ in figure 2.19(b), a small new vortex pair has begun to form near $z/\lambda = 0.0$ (and $z/\lambda = 2.0$). The original pairs are squeezed toward $z/\lambda = 1.0$. During the early stage of the simulation when the disturbances are very small, the temporal growth rate of the disturbances is 0.0079, compared to 0.0080 for the most unstable mode from linear stability analysis. This shows that the most unstable eigenfunction from the linear theory is indeed the dominant unstable disturbance (and also further verifies our linear stability code). The appearance of the new pair of vortices in figure 2.19(b) is associated with a splitting event and is caused by the growth of the most unstable eigenfunction from the random initial disturbances. The flow patterns obtained in the nonlinear simulation up to this time are very similar to those obtained from the linear stability analysis by imposing the most unstable eigenfunction on the base flow, as depicted in figure 2.9(c) and (d). When $t = 6200d/2\bar{U}$ (figure 2.19c), the new pair is well developed and the computational box is filled with three strong pairs. At the same time, a merging process of the two original pairs has begun. This can be seen more clearly in figure 2.19(d). The merging process is similar to that depicted by linear stability analysis in figure 2.10(c): two neighboring vortices of the two original vortex pairs become weaker while the other two vortices become stronger. By the time $t = 8450d/2\bar{U}$ in figure 2.19(e), two vortices have completely disappeared and the two original vortex pairs have merged into one pair. The new pair of vortices that appeared due to splitting has adjusted itself so that the velocity field of the flow has returned exactly to its original pattern, but with a spanwise

shift of half a wavelength. The above splitting and merging processes continue periodically in time. Compared with the predictions from linear theory in figure 2.9 and 2.10, the similarity is striking. The simultaneous splitting and merging effects of the most unstable eigenfunction discussed in §2.4 are demonstrated clearly in figure 2.19. When splitting occurs, a new pair is always generated between two base pairs. When merging occurs, two base pairs merge into one pair.

Outside the Eckhaus stable region, all wavenumbers are unstable. However, our discussions in §2.5 indicate that vortices with wavenumber in the Eckhaus valley are the least unstable to splitting and merging and are likely to be observed more often in experiments. In order to study the validity of this result in the presence of nonlinear splitting and merging processes and the interactions between vortices with different wavenumbers, we select the aspect ratio of our computational box in our second simulation to be $3\pi : 1$. Periodic boundary conditions are again imposed in the spanwise direction, but now over a spanwise extent three times larger than in the first simulation. Since an integer number of pairs of vortices must appear in the simulation region, the average wavenumber of the vortices is restricted to $n/3$, where n is an integer. We use 96 spanwise Fourier modes and 16 Chebyshev polynomials (in the radial direction) in this simulation.

We start the simulation using curved channel Poiseuille flow with low amplitude random noise ($< 0.1\% \bar{U}$) superimposed and use $Re = 2.2Re_c$ in a curved channel having $\gamma = 0.975$. Figure 2.20 shows the time development of the pressure gradient parameter Δp , defined as (Finlay *et al.* 1988)

$$\Delta p \equiv \frac{\overline{\frac{\partial P}{\partial \theta}} - \frac{\partial P}{\partial \theta}}{\frac{\partial P}{\partial \theta}} \quad (2.8)$$

where $-(1/r)\frac{\partial P}{\partial \theta}$ is the streamwise pressure gradient of curved channel Poiseuille flow and $-(1/r)\frac{\partial P}{\partial \theta}$ is the streamwise pressure gradient of the vortex flow averaged over the computational box.

After $t = 500d/2\bar{U}$, finite amplitude $2D$ vortices develop rapidly. In figure 2.20,

the corresponding Δp increases dramatically. Figure 2.21(a) shows contours of the Stokes stream function at $t = 650d/2\bar{U}$. Excluding the three pairs near the center of the box where a splitting event is underway, the average wavenumber of the vortices at this time is 2.79. This is very close to the wavenumber $\alpha = 2.82$ which has the maximum primary instability growth rate (see figure 2.15). This demonstrates that during the early stage of the development of vortex flow, the primary instability does play an important role in wavenumber selection process, as suggested in §2.5.

As the solution proceeds in time, the flow goes through a sequence of splitting and merging processes and there is a decrease in the average wavenumber of the vortices until $t = 1300d/2\bar{U}$. For $t > 1300d/2\bar{U}$, the wavenumber of the vortices remains near the Eckhaus valley, which is rather flat and lies between $\alpha = 2.1$ and $\alpha = 2.35$ (see figure 2.14). But it continues to fluctuate due to splitting and merging events. The time record of Δp is useful for determining when splitting and merging events occur, since according to Finlay *et al.* (1988), for $\alpha < 3.7$ at $Re = 2.2Re_c$ and $\gamma = 0.975$, the smaller α is, the smaller Δp is. Examining $\Delta p(t)$ and the velocity field, we find that whenever Δp decreases, merging processes are underway, but whenever Δp increases, there are splitting processes dominating the flow. Figure 2.21(b – g) show a typical cycle of the flow development from $t = 1850d/2\bar{U}$ to $2099d/2\bar{U}$. In figure 2.21(b), the average wavenumber of the first 3 vortex pairs from the left side of the box is 2.37, while the rest of the vortices have a wavenumber of 2.19, which is in the Eckhaus valley. There is a merging process just underway between the first two pairs from the left. This merging process becomes clearer in figure 2.21(c). For the rest of the vortices, there is a very small decrease in wavenumber from 2.19 to 2.13. When $t = 1978d/2\bar{U}$ in figure 2.21(d), one vortex pair has completely disappeared. The pressure gradient Δp reaches a local minimum (cf. figure 2.20).

In figure 2.21(c), there is a new pair beginning to appear near the left end of the box. This becomes clearer in figure 2.21(d) and 21(e). Another new pair also begins

to develop near the center of the box where the vortices have smaller α . The rest of vortices remain essentially unchanged. When $t = 2069d/2\bar{U}$ in figure 2.21(*f*), the new pair near the left side is almost fully developed. The other one near the center continues to grow. The rest of vortices have been squeezed somewhat and there is an increase in their wavenumbers (from 2.17 in figure 2.21*d* to 2.57 in figure 2.21*f*). It can be seen the second and third pairs from the left in figure 2.21(*f*) have begun a merging process. In figure 2.21(*g*), the new pair near the center has completed its development. At this time, the wavenumber is nearly the same for all vortices and the average wavenumber is 2.67. This high wavenumber causes a local maximum in Δp . The merging of the second and third pairs from the left proceeds. As these two pairs continue to merge, the other vortices experience an adjustment in their wavenumbers which results in smaller wavenumbers. From figure 2.21 and similar results at other times in the simulation, we find that when the wavenumber of several pairs of neighboring vortices is close to the Eckhaus valley, the wavenumber of these pairs remains nearly constant for a long time and their adjustment due to splitting and merging events is very weak, as is the case in figure 2.21(*b - d*). But when the wavenumber of two or more neighboring pairs is not close to Eckhaus valley, there is a rapid and large change in wavenumber.

The simulation results also show that when the average wavenumber of the vortices is near the Eckhaus valley, the development of splitting and merging is relatively slow. When the wavenumbers of vortices are far from the Eckhaus valley, the pressure gradient experiences rapid and large fluctuations as a result of simultaneous multiple splitting or merging processes. A vortex flow with wavenumbers far from the Eckhaus valley does not last long. Thus, when averaged on time, the average wavenumber is close to the Eckhaus valley.

Figure 2.21 also demonstrates repetitive splitting and merging. In figure 2.21(*b - g*), the first 2 pairs from the left merge, and then this is followed by a splitting event with the neighboring vortex pair on the left side. The above

simulation results are consistent with our discussion in §2.5 and §2.6. For fully developed two-dimensional vortex flow, Eckhaus instability plays an important role in the wavelength selection process and splitting and merging of vortices occur continuously.

2.8 Conclusion

Eckhaus instability was examined for the flow in channels with either curvature or rotation or both, using linear stability theory and spectral methods. The results explain several experimental phenomena. Curvature and rotation both cause similar instabilities with respect to spanwise perturbations in these geometries. The Eckhaus stable region was found to be a small closed region, different from any other periodic flow known to the author. The stability criterion based on amplitude expansion given by Eckhaus (1965) does not always apply, even in the region close to Re_c . Outside the Eckhaus stable region, splitting and merging of vortex pairs occur and the spanwise wavenumbers are selected by the Eckhaus instability. Two pairs of vortices are split apart by a new pair to yield three pairs if the wavenumber of the vortices is small. If instead the wavenumber is large, the two pairs merge into one pair. Most experimentally observed wavenumbers are the ones which are least unstable to spanwise perturbations. At certain Re all vortices are equally unstable to spanwise perturbations and repetitive splitting and merging of vortex pairs occur. The wavenumber selection process as the flow proceeds downstream can be described as follows. Near the entrance of the channel, the flow is one-dimensional Poiseuille type flow. Further downstream, vortices with spanwise wavenumber near those with maximum primary growth rate develop first. At these locations, the primary instability plays an important role in the wavenumber selection process. Further downstream, as the flow approaches fully developed two-dimensional vortex flow, the Eckhaus instability or wavy instability sets in, depending on which has dominant

growth rate. When Re is not too high, the spanwise wavenumber of the flow lies in the Eckhaus valley, i.e. the region of low Eckhaus growth rate. When Re is very high, the stability of three-dimensional vortices must be examined to predict wavenumber selection.

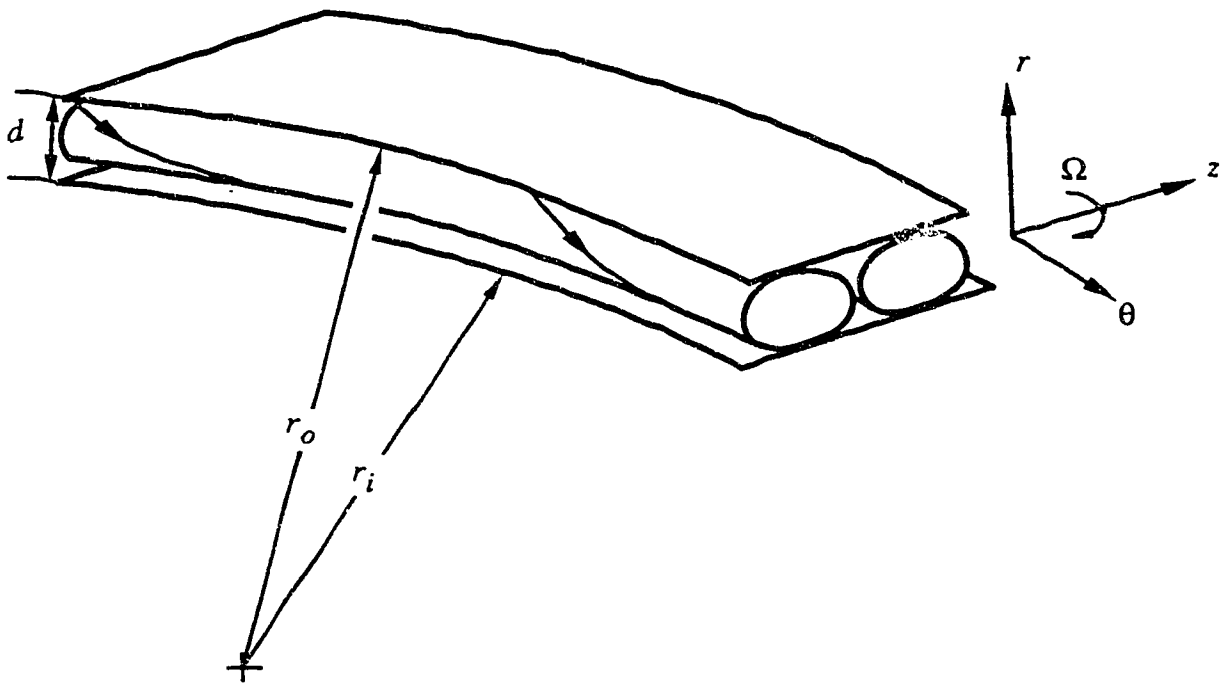


FIGURE 2.1. The geometry of curved and/or rotating channel is shown. The flow is periodic in z .

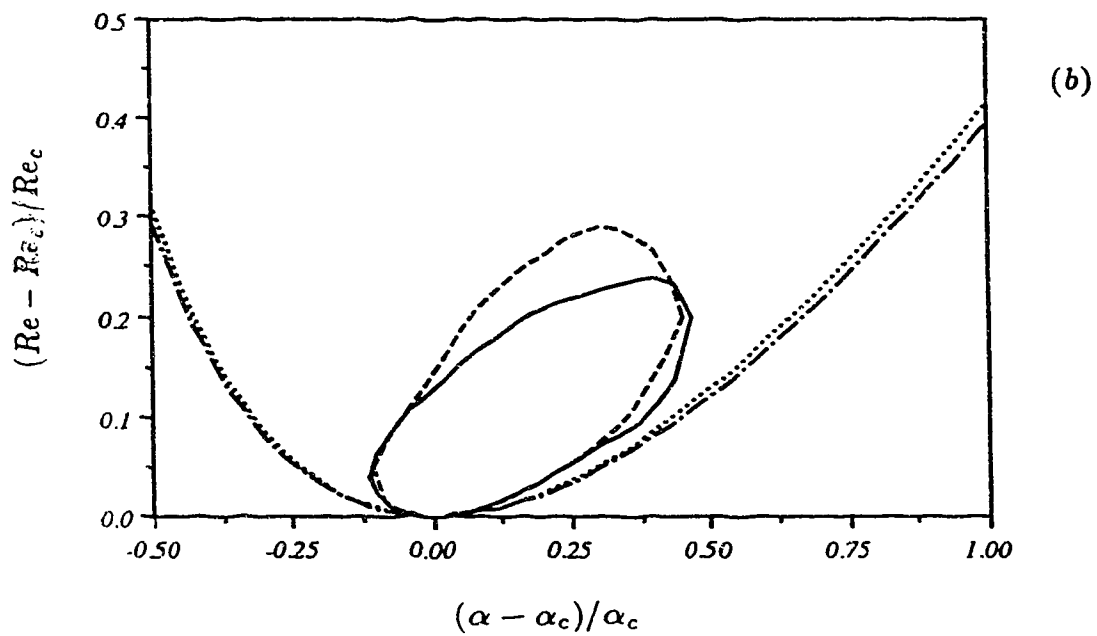
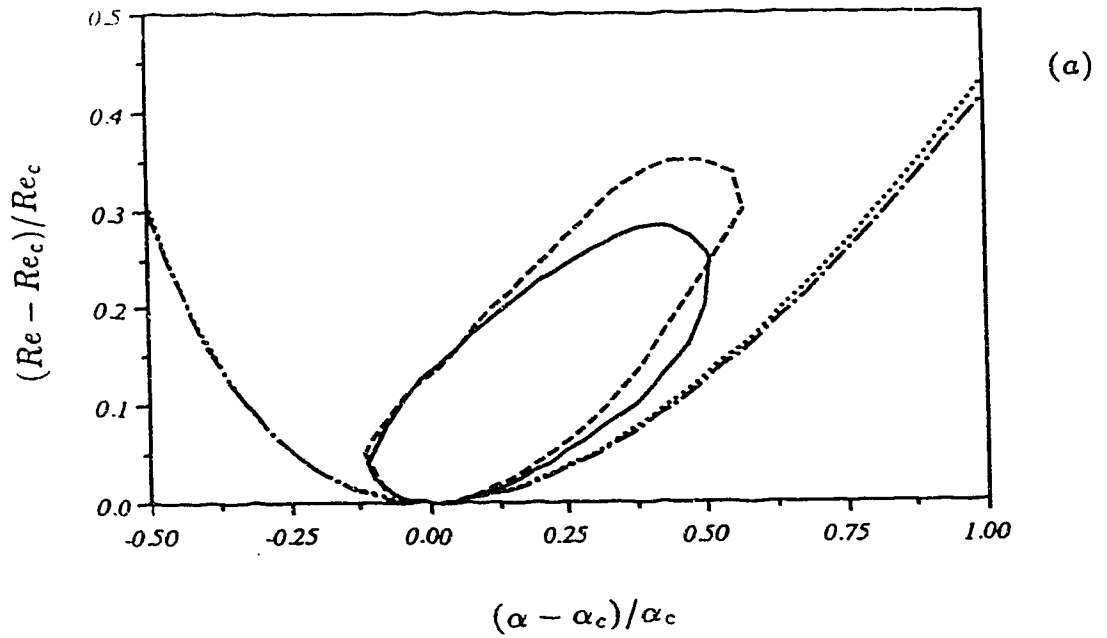


FIGURE 2.2. For caption see facing page.

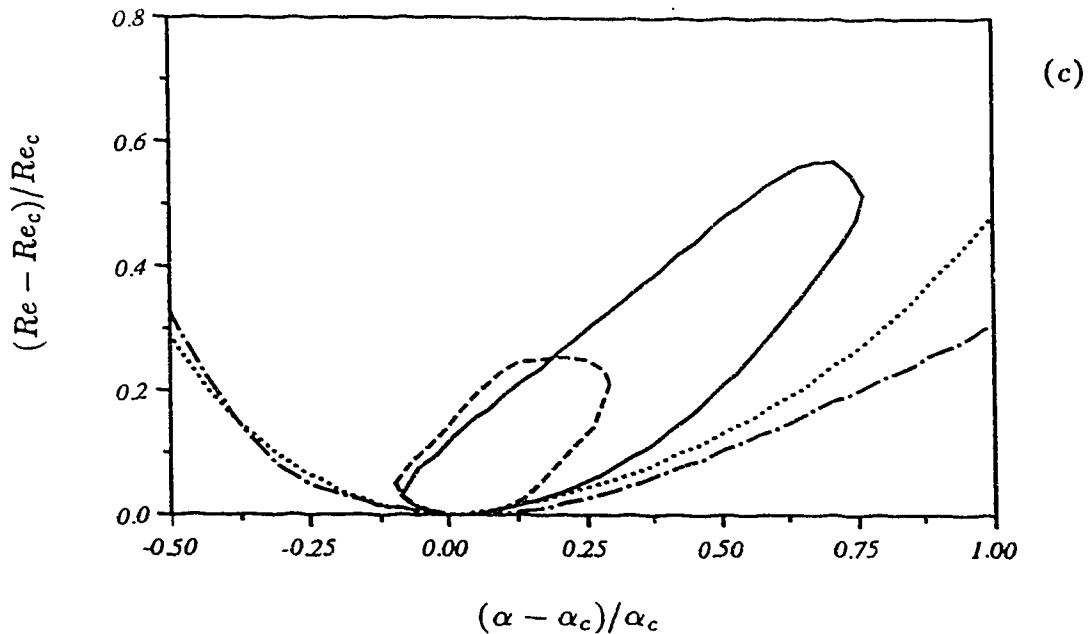


FIGURE 2.2. Eckhaus stability boundaries are shown for curved and/or rotating channel flow. The primary stability boundary is included for reference. (a) shown for curved channels are Eckhaus: —, $\gamma = 0.975$ ($Re_c = 114.26$, $\alpha_c = 1.98$); ----, $\gamma = 0.7$ ($Re_c = 35.83$, $\alpha_c = 2.07$); and primary: - - - , $\gamma = 0.975$; ·····, $\gamma = 0.7$. (b) shown for rotating channels are Eckhaus: —, $Ro = 0.005$ ($Re_c = 198.95$, $\alpha_c = 2.01$); ----, $Ro = 0.25$ ($Re_c = 44.30$, $\alpha_c = 2.46$); and primary: - - - , $Ro = 0.005$; ·····, $Ro = 0.25$. (c) shown for curved-rotating channels are Eckhaus: —, $\gamma = 0.975$, $Ro = -0.0125$ ($Re_c = 275.4$, $\alpha_c = 1.96$); ----, $\gamma = 0.975$, $Ro = -0.02$ ($Re_c = 195.0$, $\alpha_c = 2.16$); and primary: - - - , $\gamma = 0.975$, $Ro = -0.0125$; ·····, $\gamma = 0.975$, $Ro = -0.02$.

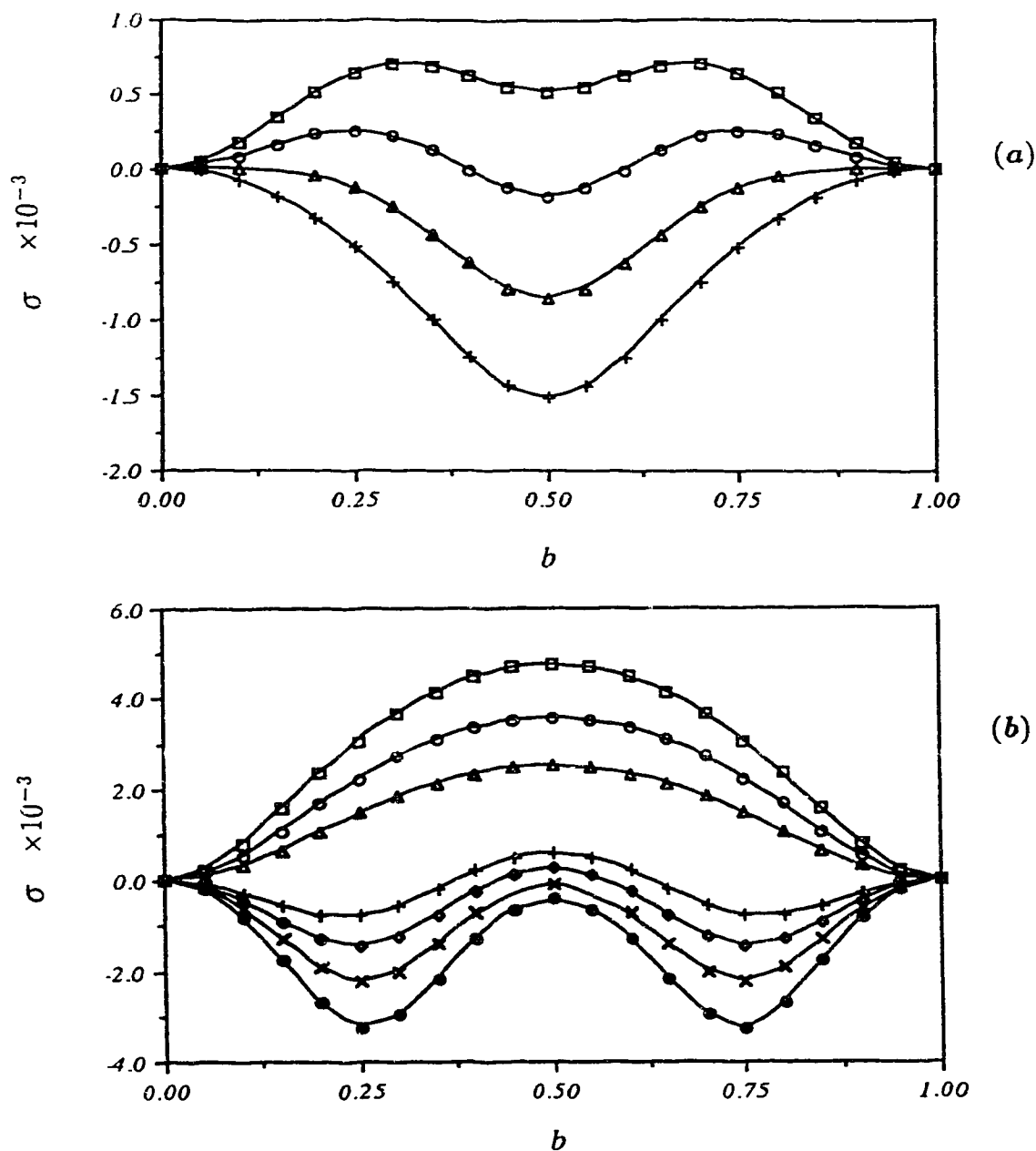


FIGURE 2.3. Eckhaus growth rate σ as a function of spanwise perturbation wavenumber b in a curved channel ($\gamma = 0.975$) as the spanwise wavenumber α of 2D vortices approaches the left side of the Eckhaus boundary (α_{left}) at (a) $Re = 1.07 Re_c$ and (b) $Re = 1.225 Re_c$. In (a): $\alpha_{left} = 1.8$; \square , $\alpha = 1.7$; \circ , $\alpha = 1.75$; \triangle , $\alpha = 1.8$; $+$, $\alpha = 1.85$. In (b): $\alpha_{left} = 2.355$; \square , $\alpha = 1.6$; \circ , $\alpha = 1.8$; \triangle , $\alpha = 2.0$; $+$, $\alpha = 2.3$; \diamond , $\alpha = 2.35$; \bullet , $\alpha = 2.45$.

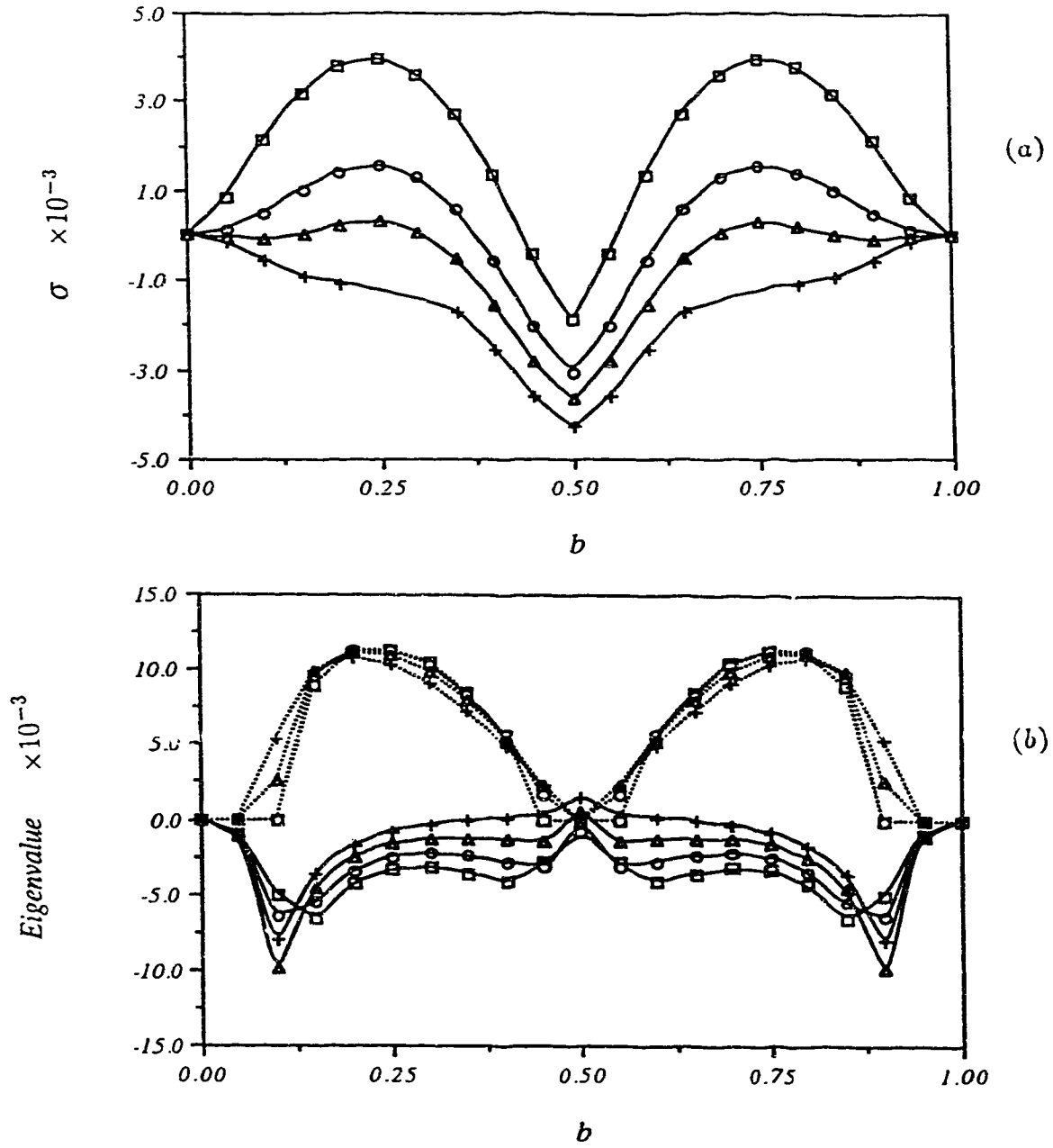


FIGURE 2.4. Eckhaus eigenvalue, $\sigma + i\omega$, as a function of spanwise perturbation wavenumber b as the spanwise wavenumber α of 2D vortices approaches the right side of the Eckhaus boundary (α_{right}) at (a) $Re = 1.07Re_c$ and (b) $Re = 1.225Re_c$. In (a), $\omega(b) = 0$; $\alpha_{right} = 2.565$; $+$, $\alpha = 2.55$; Δ , $\alpha = 2.575$; \circ , $\alpha = 2.6$; \square , $\alpha = 2.65$. In (b), $\alpha_{right} = 2.98$; \square , $\alpha = 2.9$; \circ , $\alpha = 2.95$; Δ , $\alpha = 3.0$; $+$, $\alpha = 3.05$; — for σ ; for ω .

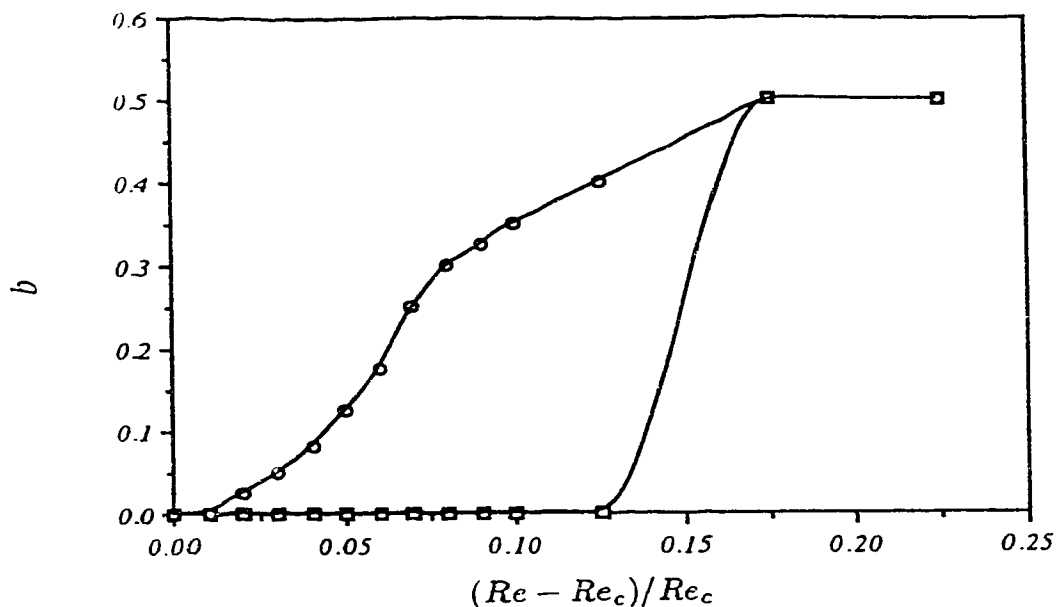


FIGURE 2.5. Spanwise perturbation wavenumber b as a function of Re on the Eckhaus boundary in a curved channel ($\gamma = 0.975$): \square for left side of the Eckhaus boundary; \circ for the right side of the boundary.

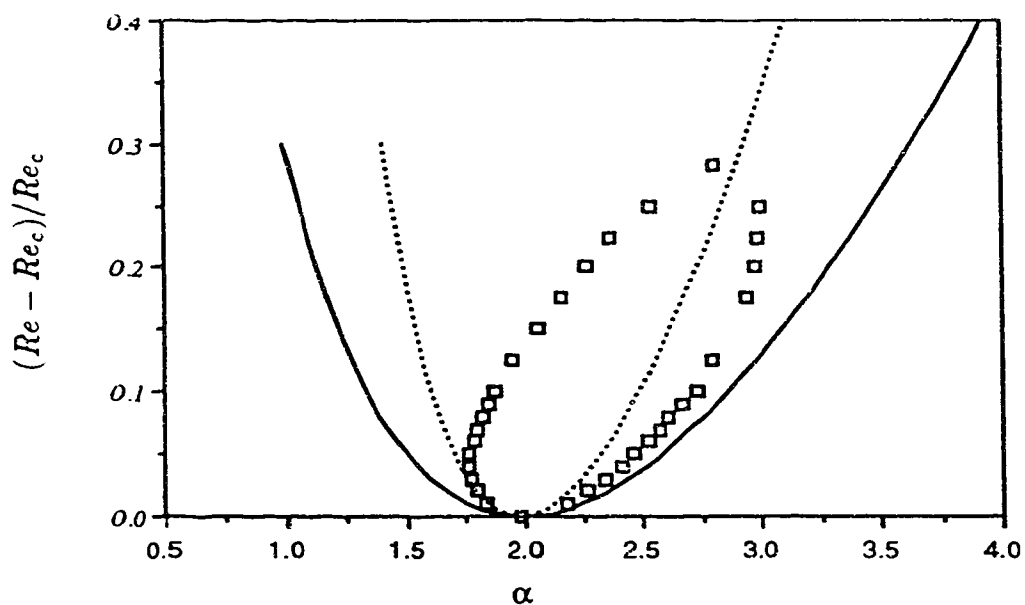


FIGURE 2.6. Stability criterion of Eckhaus (1965) (.....), the primary stability boundary of Finlay *et al.* (1989) (—) and the Eckhaus stability boundary (\square) in a curved channel with $\gamma = 0.975$.

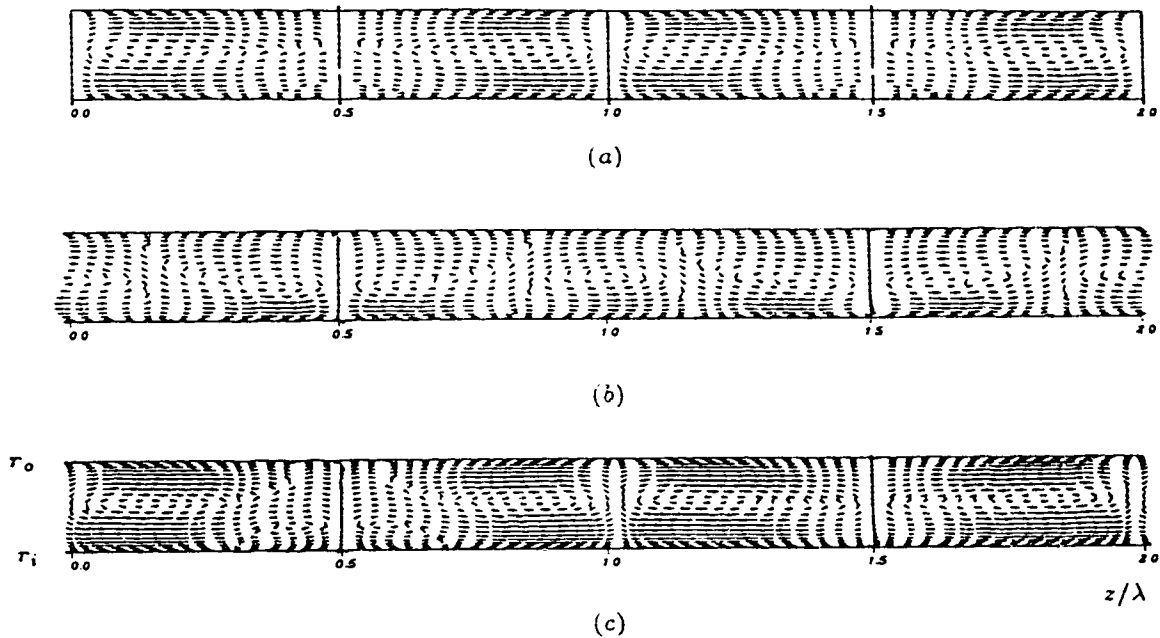


FIGURE 2.7. Taylor vortices (a), their most unstable mode (b), and Taylor vortices + the most unstable mode (c) projected onto the (r, z) plane at $Re = 2.0Re_c$, $\gamma = 0.75$ and $\alpha = 1.17$, outside the left side of the Eckhaus boundary ($\alpha_{left} = 1.188$); In (c), the kinetic energy of the most unstable mode is 1.4% of the base flow's kinetic energy. $b = 0.5$ for the most unstable mode.

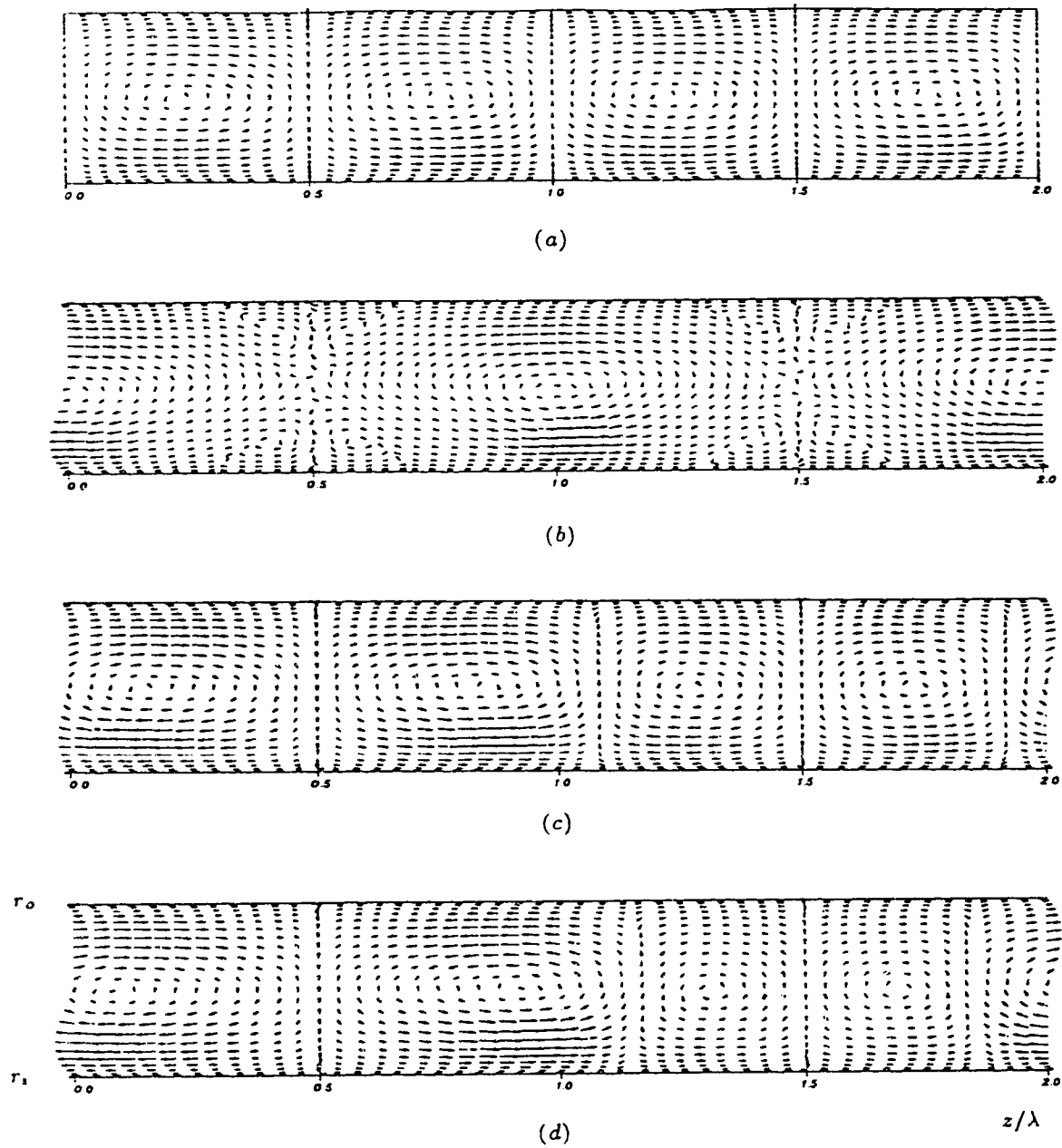


FIGURE 2.8. Same as figure 2.7 but at $\alpha=2.475$, outside the right of the Eckhaus boundary ($\alpha_{right} = 2.425$). In (c), the kinetic energy of the most unstable mode is 7% of the base flow's kinetic energy. In (d), the percentage of the most unstable mode is 50%.

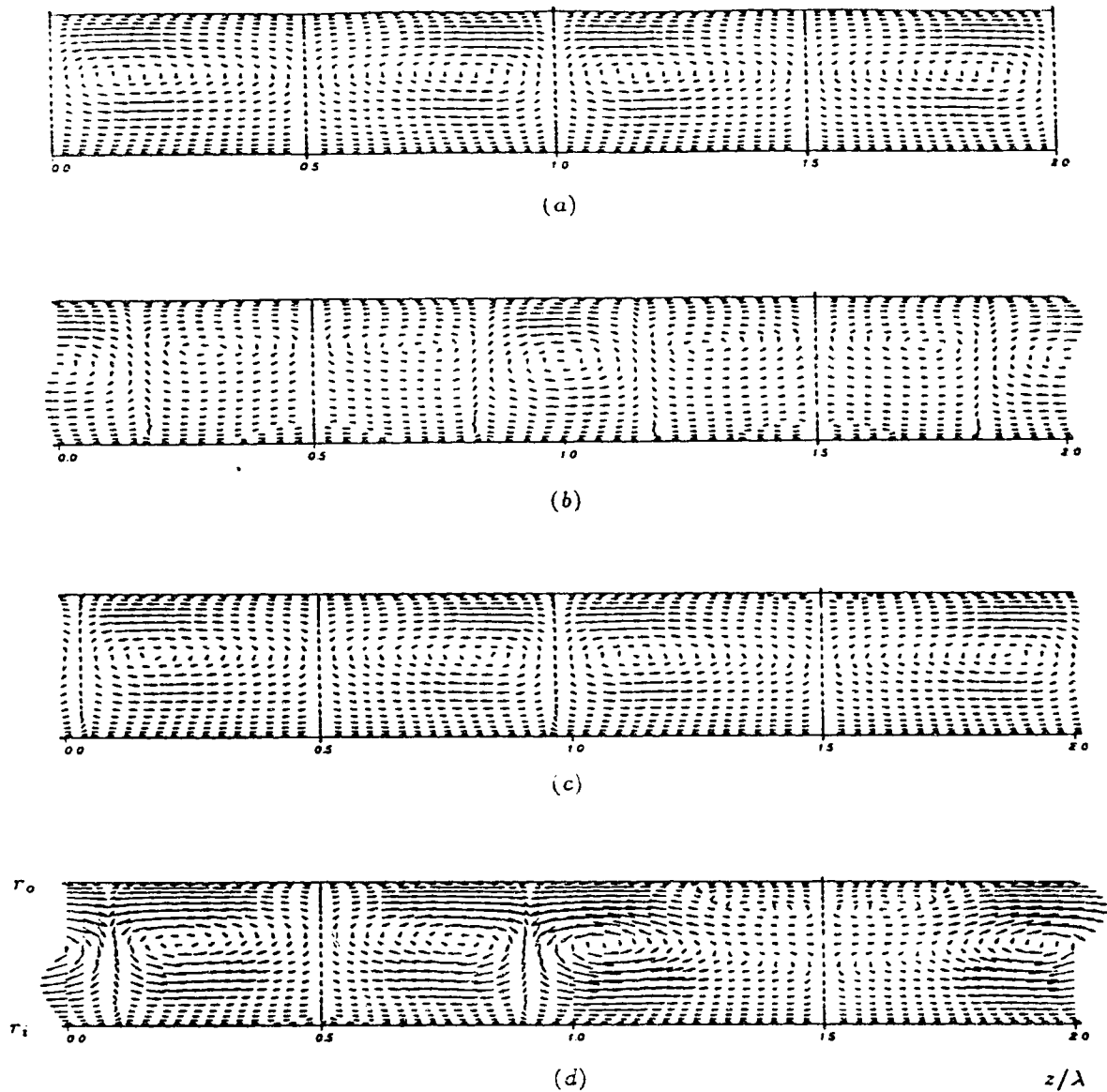


FIGURE 2.9. 2D vortices (a), their most unstable mode (b) and 2D vortices + the most unstable mode (c,d) in a curved channel ($\gamma = 0.975$) at $Re = 2.0Re_c$, $\alpha = 2.0$ projected onto the (r, z) plane. In (c), the kinetic energy of the most unstable mode is 7% of the base flow's kinetic energy. In (d), the percentage of the most unstable mode is 20%. The most unstable mode has $b = 0.5$.

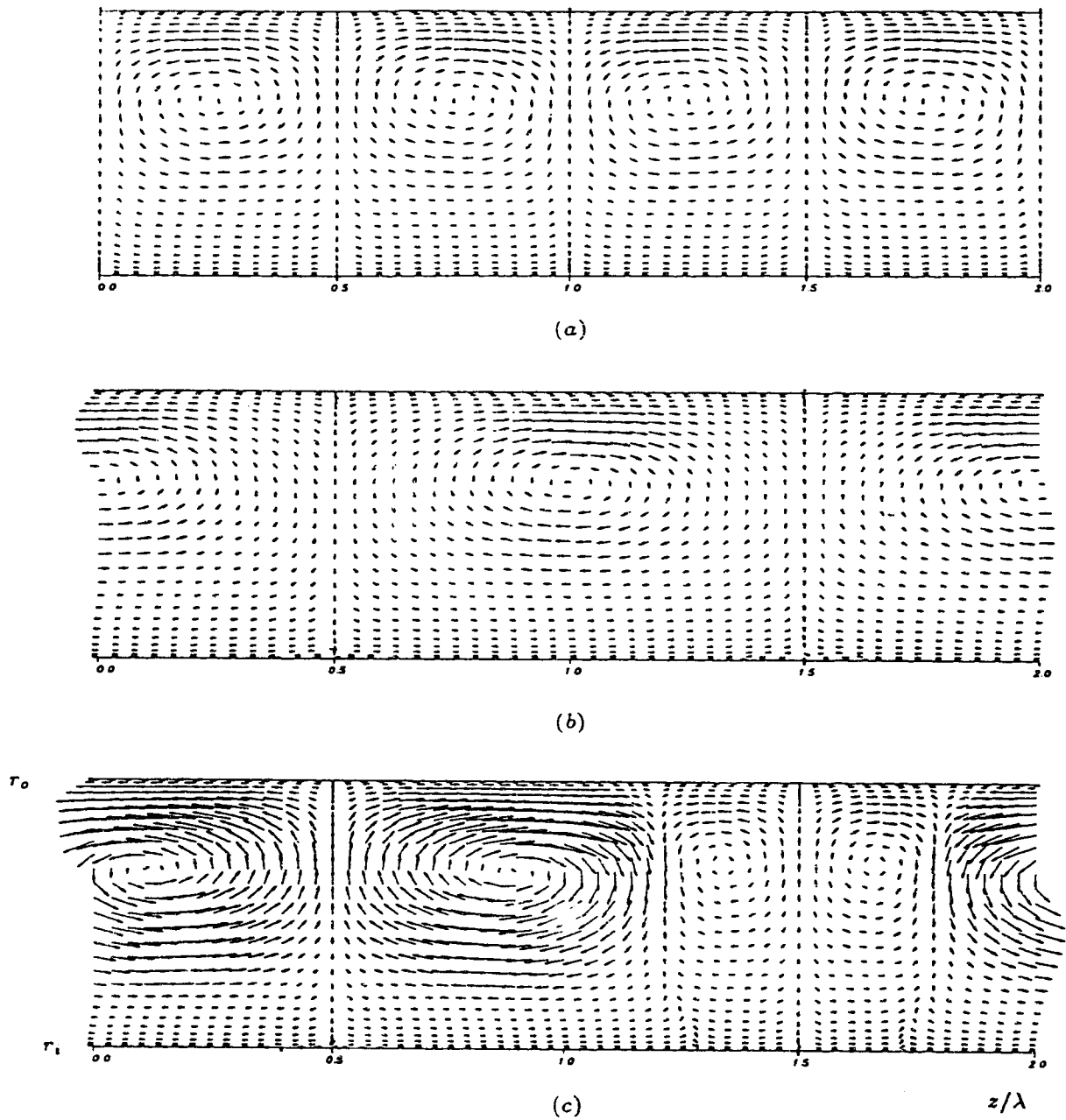
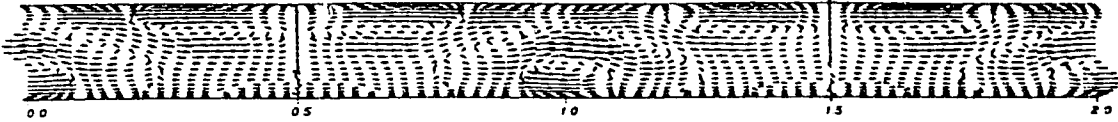
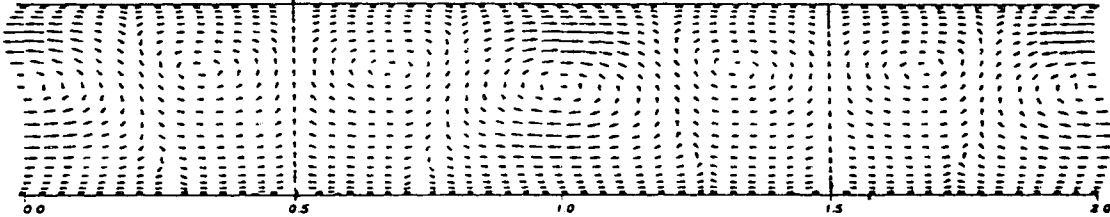


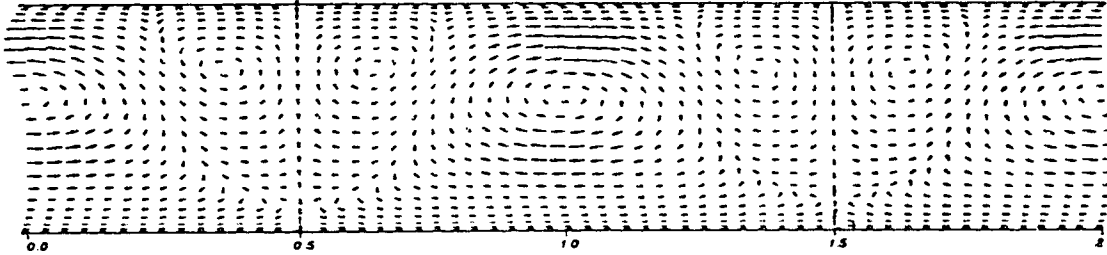
FIGURE 2.10. Same as in figure 2.9 but at $\alpha = 4.0$. In (c), the percentage of the most unstable mode is 50%.



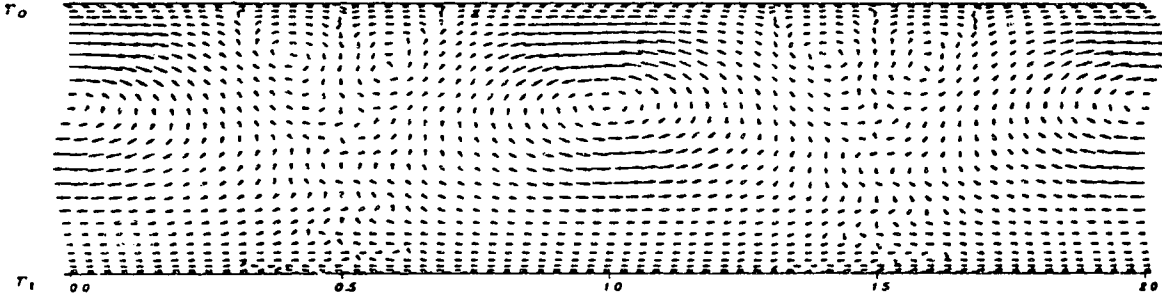
(a)



(b)



(c)



(d)

FIGURE 2.11. For caption see facing page.

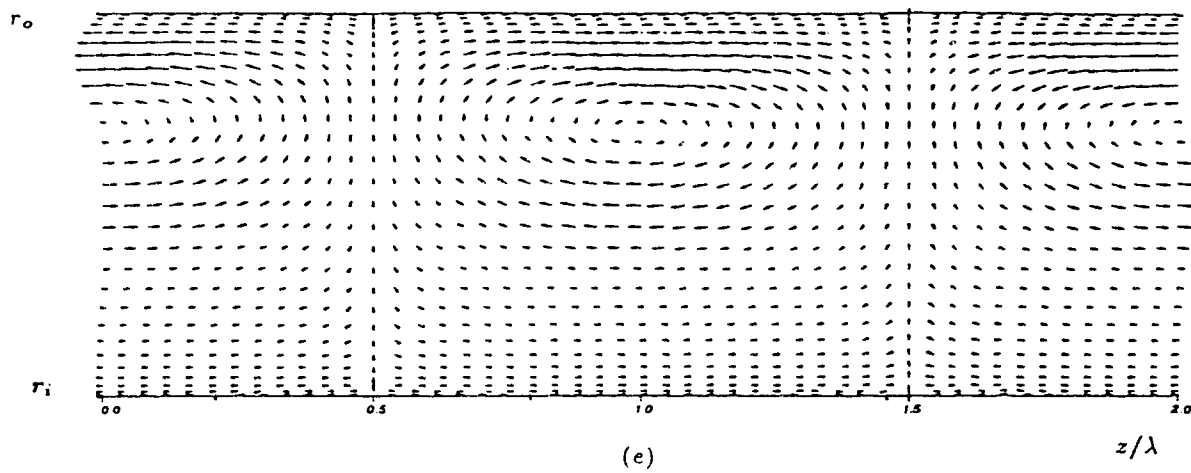


FIGURE 2.11. Most unstable modes (projected onto the (r, z) plane) in a curved channel ($\gamma = 0.975$) at $Re = 2.0Re_c$ and α : (a) $\alpha = 1.25$; (b) $\alpha = 2.5$; (c) $\alpha = 3.0$; (d) $\alpha = 3.5$; (e) $\alpha = 5.0$; $b = 0.5$ for all these modes.

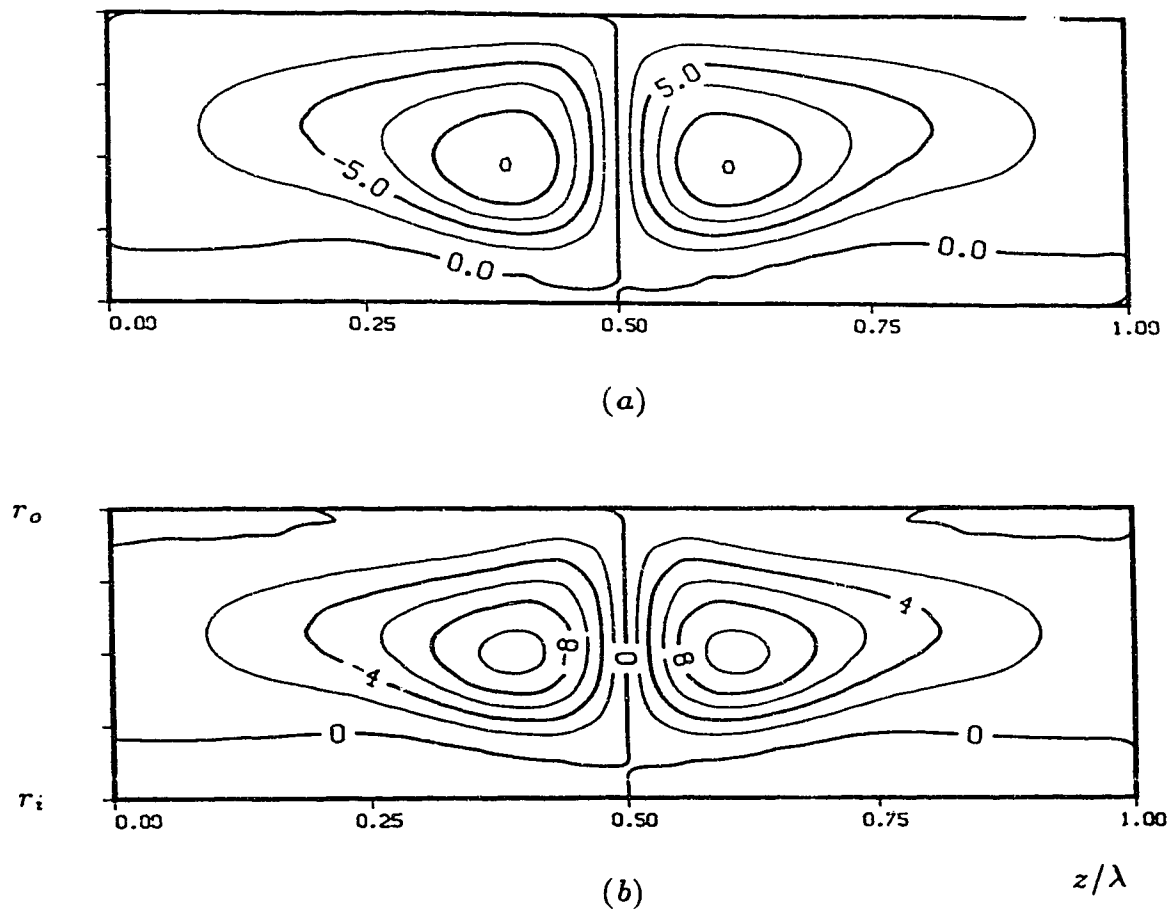


FIGURE 2.12. Streamfunctions of 2D vortices in a rotating channel ($Ro = 0.03$) at $Re = 472.5$, $\alpha = 2.0$: (a) without secondary vortices; (b) with secondary vortices. The Eckhaus growth rates are (a) $\sigma = 0.059$ and (b) $\sigma = 0.108$.

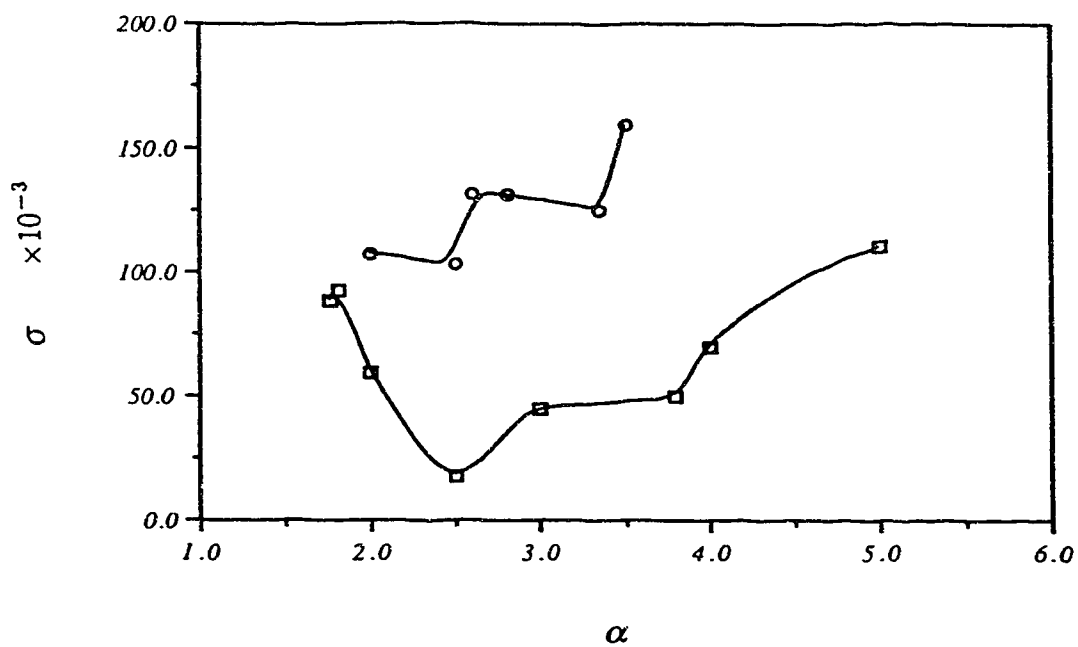


FIGURE 2.13. Comparison of the maximum Eckhaus growth rate σ of 2D vortices with secondary vortices (\circ) and without secondary vortices (\square) at $Re = 472.5$ in a rotating channel ($Ro = 0.03$) for $1.75 \leq \alpha \leq 5.0$; $b = 0.5$ yields the maximum Eckhaus growth rate for each α .

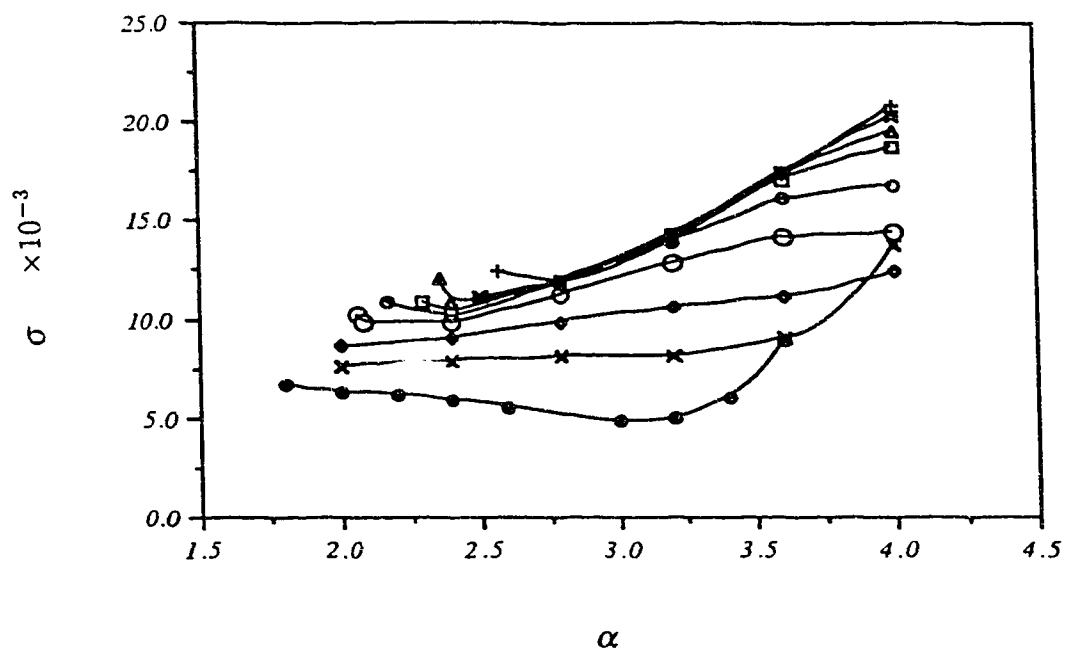


FIGURE 2.14. Maximum Eckhaus growth rate σ as a function of the spanwise wavenumber α of 2D vortices in a curved channel ($\gamma = 0.975$) at Re : \bullet , $Re = 1.5Re_c$; \times , $Re = 1.7Re_c$; \diamond , $Re = 1.9Re_c$; \circ , $Re = 2.2Re_c$; \circ , $Re = 2.5Re_c$; \square , $Re = 2.8Re_c$; Δ , $Re = 3.0Re_c$; \star , $Re = 3.25Re_c$; $+$, $Re = 3.5Re_c$.

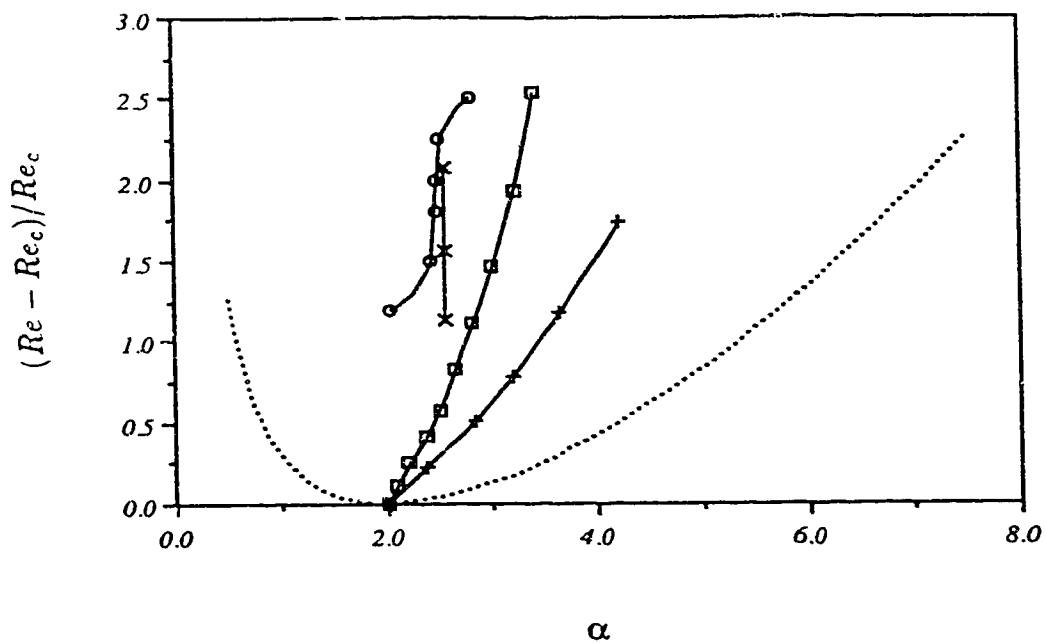


FIGURE 2.15. Eckhaus valley (\circ), the curves of maximum primary growth rate (\square) and maximum pressure gradient ($+$) of Finlay *et al.* (1988) in a curved channel with $\gamma = 0.975$, and the wavenumbers of 2D vortices observed by Kelleher *et al.* (1980) (\times) in $\gamma = 0.979$. The primary stability boundary (.....) of Finlay *et al.* is included for reference.

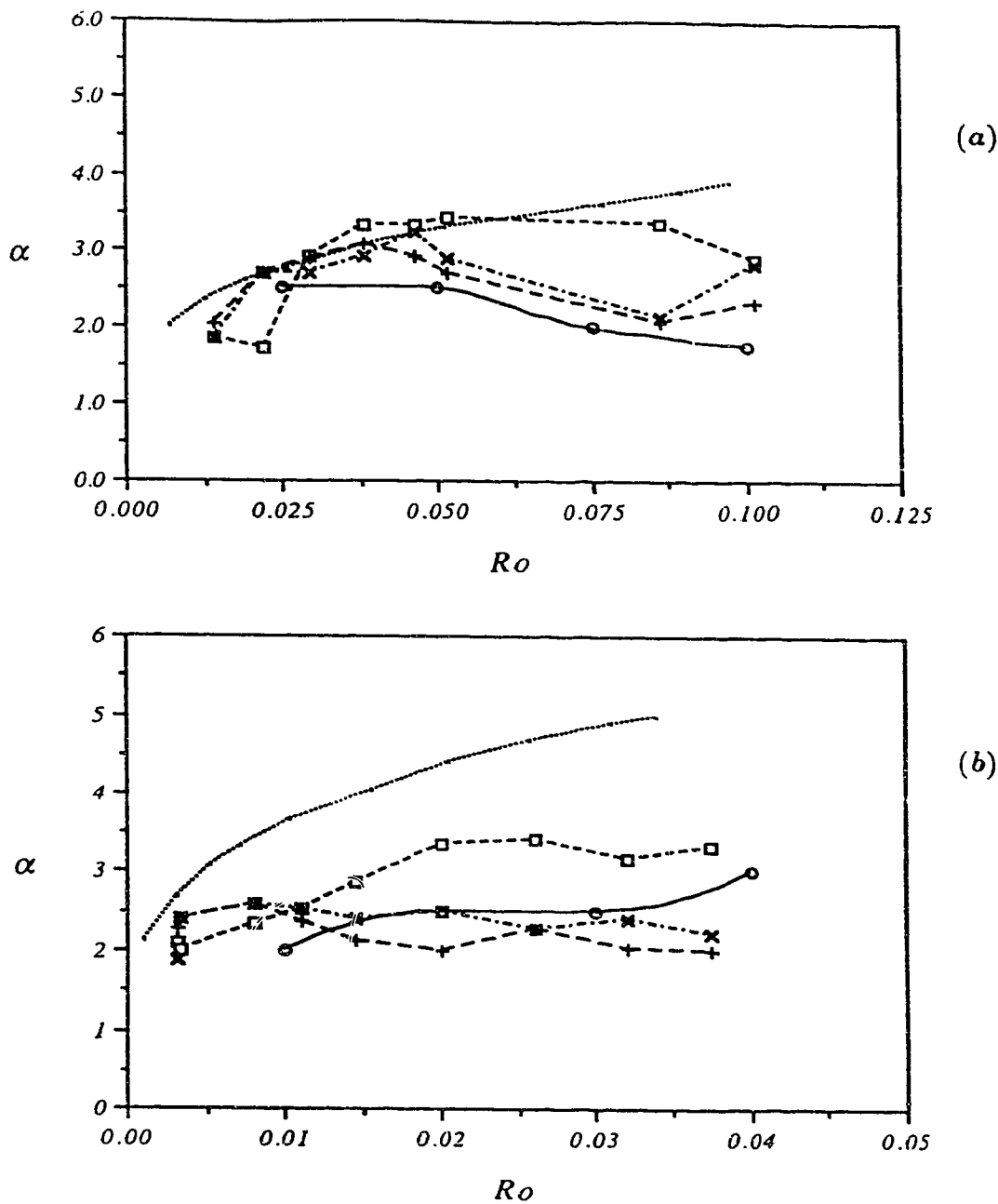


FIGURE 2.16. Eckhaus valley (\circ), the curve of maximum primary growth rate (.....) and the observed wavenumbers of 2D vortices of Alfredsson & Persson (1989) in a rotating channel at different downstream locations y/d : \square , $y/d=40$; \times , $y/d=80$; $+$, $y/d=120$. In (a), $Re = 175$; in (b), $Re = 472.5$.

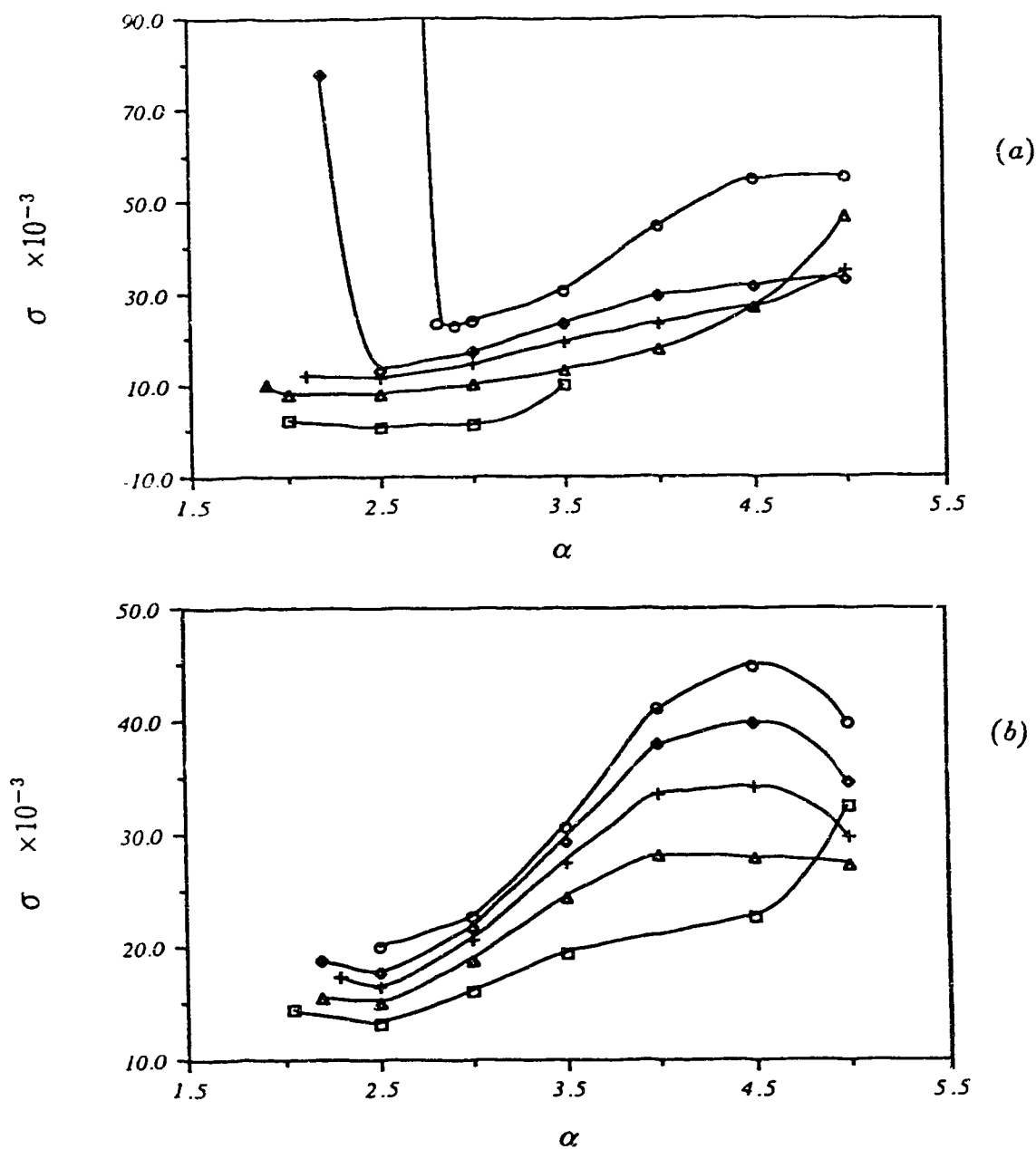


FIGURE 2.17. Maximum Eckhaus growth rate σ as a function of the spanwise wavenumber α of 2D vortices in a curved-rotating channel ($\gamma = 0.975$) at $Re = 180$. In (a), $Ro < 0$: \square , $Ro = -0.025$; \triangle , $Ro = -0.035$; $+$, $Ro = -0.045$; \diamond , $Ro = -0.055$; \circ , $Ro = -0.11$. In (b), $Ro > 0$: \square , $Ro = 0.015$; \triangle , $Ro = 0.025$; $+$, $Ro = 0.035$; \diamond , $Ro = 0.045$; \circ , $Ro = 0.055$.

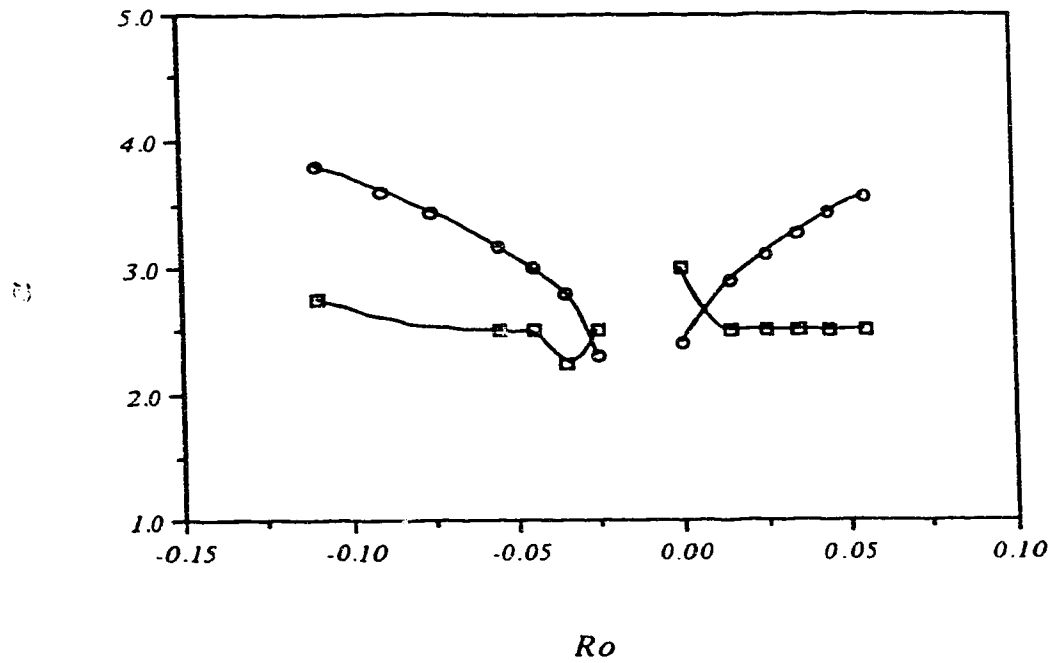


FIGURE 2.18. Eckhaus valley (\square) and the curve of maximum primary growth rate (\circ) for a curved-rotating channel ($\gamma = 0.975$) at $Re = 180$.

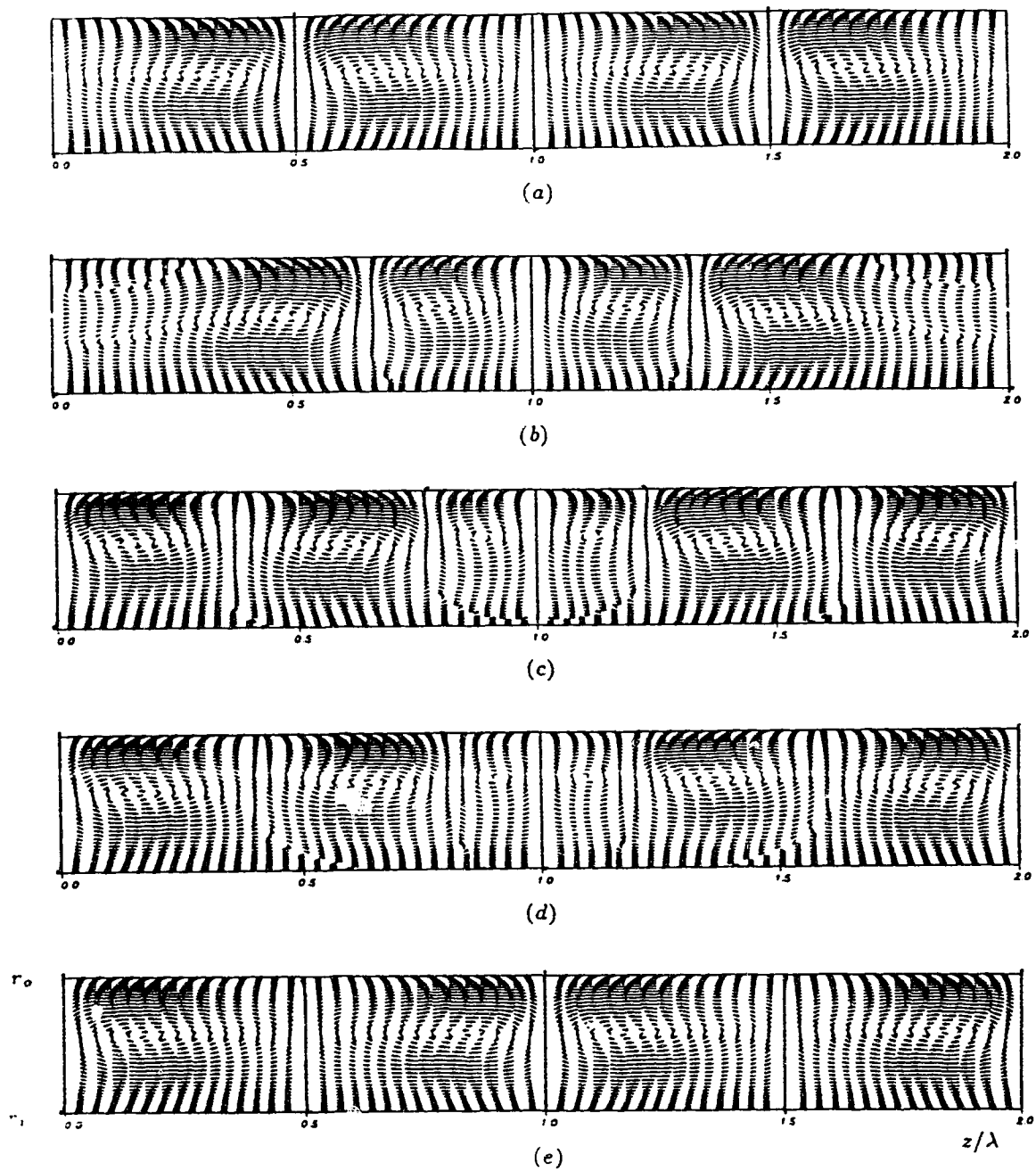


FIGURE 2.19. Nonlinear splitting and merging of vortex pairs at $Re = 1.776Re_c, \gamma = 0.975$. The flow is projected onto the (r, z) -plane at time (a) 0, (b) $5700d/2\bar{U}$, (c) $6200d/2\bar{U}$, (d) $6450d/2\bar{U}$ and (e) $8450d/2\bar{U}$. The vortices in a) and e) have $\alpha = 2.0$.

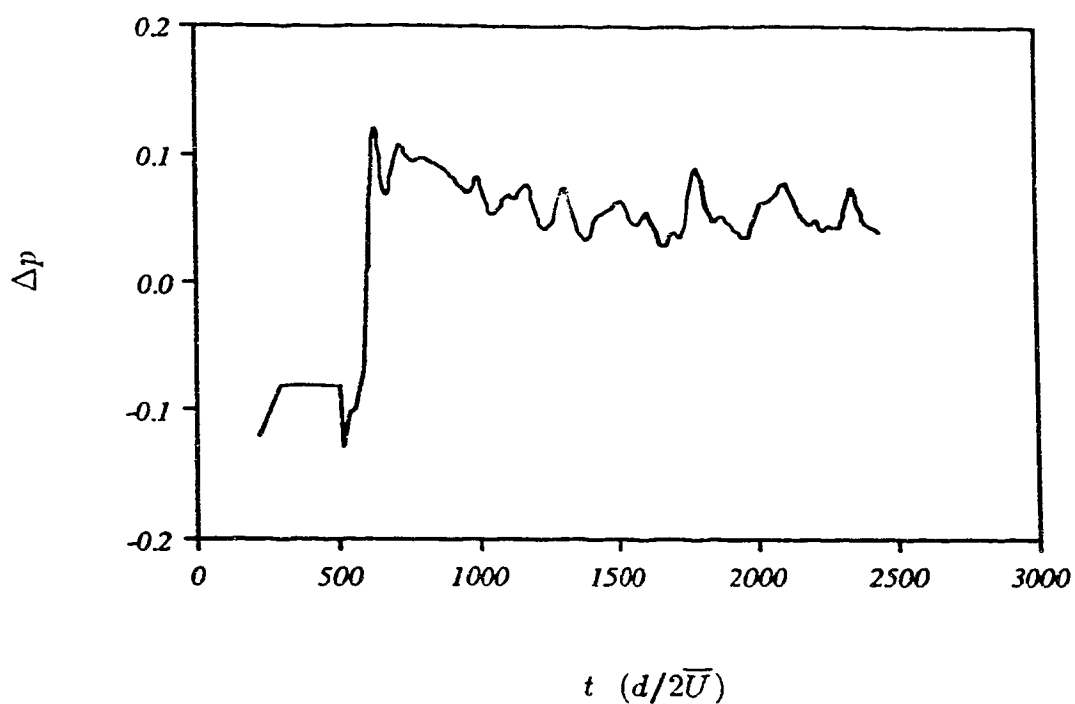


FIGURE 2.20. The pressure gradient parameter Δp as a function of time at $Re = 2.2Re_c$ in a curved channel $\gamma = 0.975$ with aspect ratio $\Gamma = 3\pi : 1$ and periodic spanwise boundary conditions.

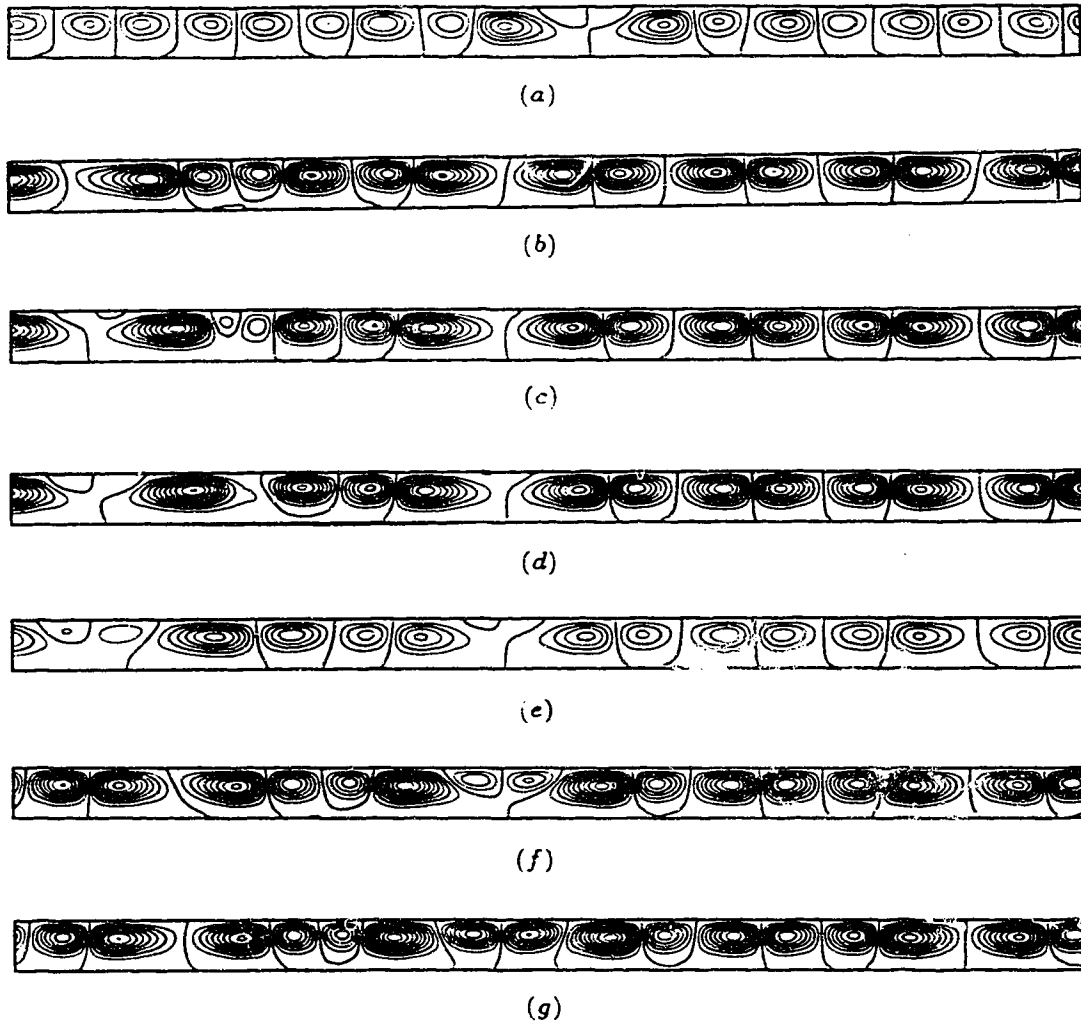


FIGURE 2.21. Contours of Stokes stream function for curved channel flow at $Re = 2.2Re_c$, $\gamma = 0.975$ are shown in the (r, z) -plane at time (a) $650d/2\bar{U}$, (b) $1850d/2\bar{U}$, (c) $1949d/2\bar{U}$, (d) $1978d/2\bar{U}$, (e) $2009d/2\bar{U}$, (f) $2069d/2\bar{U}$ and (g) $2099d/2\bar{U}$. The aspect ratio is $\Gamma = 3\pi : 1$, with periodic spanwise boundary conditions.

References

- Alfredsson, P.A. & Persson, H. 1989 Instabilities in channel flow with system rotation *J. Fluid Mech.* **202**, 543–557.
- Bippes, H. 1978 Experimental study of the laminar-turbulent transition of a concave wall in a parallel flow *NASA TM.* 75243.
- Bland S.B. & Finlay W.H. 1991 Transitions towards turbulence in a curved channel. *Phys. Fluids A*, **3**, 106–114.
- Canuto, C., Hussaini, M.Y., Quarteroni, A. & Zang, T.A. 1988 *Spectral Methods in Fluid Dynamics*. Springer-Verlag.
- Clever, R.M. & Busse, F.H. 1974 Transition to time-dependent convection. *J. Fluid Mech.* **65**, 625–645.
- DiPrima, R.C. & Swinney, H.L. 1985 Instabilities and transition in flow between concentric rotating cylinders In *Hydrodynamic Instabilities and the Transition to Turbulence*, 2nd edition (ed. H.L. Swinney & J.P. Gollub), Topics in Applied Physics vol. 45, pp.139–180. Springer-Verlag.
- Dominguez-Lerma, M.A., Cannell, D.S. & Ahler, G. 1986 Eckhaus boundary and wave-number selection in Rotating Couette-Taylor flow. *Physical Review A* **34**, 4956–4970.
- Eckhaus, W. 1965 *Studies in nonlinear stability theory*. Springer, New York.
- Finlay, W.H., Keller, J.B. & Ferziger, J.H. 1988 Instability and transition in curved channel flow. *J. Fluid Mech.* **194**, 417–456.
- Finlay, W.H. 1990 Transition to oscillatory motion in rotating channel flow.. *J. Fluid Mech.* **215** ,. 209–227
- Gardner, D.R., Trogon, S.A. & Douglass, R.W. 1989 A modified Tau spectral method that eliminates spurious eigenvalues. *J. Compt. Phys.* **80**, 133–167.

- Jones, C.A. 1981 Nonlinear Taylor vortices and their stability. *J. Fluid Mech.* **117**, 135-162.
- Jones, C.A. 1985 Numerical methods for the transition to wavy Taylor vortices. *J. Comput. Phys.* **61**, 32-344.
- Kelleher, M.D., Flentie, D.L. & McKee, R.J. 1980 An experimental study of the secondary flow in a curved rectangular channel. *Trans. ASME I: J. Fluids Engng.* **102**, 92-96.
- Ligrani, P. & Niver, R.D. 1988 Flow visualization of Dean vortices in a curved channel with 40 to 1 aspect ratio. *Phys. Fluids* **31**, 3605-3618.
- Ligrani, P. & Longest, J.E. 1990 Appearance, disappearance and spanwise wavenumber selection of Dean vortex pairs in a curved rectangular channel. submitted
- Masuda S. & Matsubara M. 1989 Visual study of boundary layer transition on rotating flat plate *IUTAM Symposium on Laminar-Turbulent Transition*. Springer.
- Matsson, J.O.E. & Alfredsson, P.H. 1990 Curvature- and rotation- induced instabilities in channel flow. *J. Fluid Mech.* **202**, 543-557.
- Meryer-Spasche, R. & Keller, H.B. 1985 Some bifurcation diagrams for Taylor vortex flows. *Phys. Fluids* **28**, 1248-1252.
- Moser, R.D., Moin, P. & Leonard, A. 1983 A spectral numerical method for the Navier-Stokes equations with applications to Taylor-Couette flow. *J. Comp. Phys.* **52**, 524-544.
- Moser, R.D. & Moin, P. 1984 Direct numerical simulation of curved turbulent channel flow. *NASA TM* 85974.
- Moser, R.D. & Moin, P. 1987 The effects of curvature in wall-bounded turbulent flow. *J. Fluid Mech.* **175**, 497-510.
- Nagata, M. 1986 Bifurcations in Couette flow between almost corotating cylinders. *J. Fluid Mech.* **169**, 229-250.

Nagata, M. 1988 On wavy instabilities of the Taylor-vortex flow between corotating cylinders. *J. Fluid Mech.* **188**, 585–598.

Nagata, M. & Busse, F. H. 1983 Three-dimensional tertiary motion in a plane shear layer. *J. Fluid Mech.* **135**, 1–26.

Paap, H. & Riecke, H. 1990 Wave-number restriction and mode interaction in Taylor vortex flow: Appearance of a short-wavelength instability. *Physical Review A* **41**, 1943–1951.

Riecke, H. & Paap, H. 1986 Stability and wave-vector restriction of axisymmetric Taylor vortex flow. *Physical Review A* **33**, 547–553.

Stuart, J. T., & DiPrima, R.C. 1978 The Eckhaus and Benjamin-Feir resonance mechanism. *Pro. R. Soc. Lond. A.* **362**, 27–41.

Tritton, D.J. & Davies, P.A. 1985 Instabilities in geophysical fluid dynamics. In *Hydrodynamic Instabilities and the Transition to Turbulence*, 2nd edn (ed. H.L. Swinney & J.P. Gollub), Topics in Applied Physics vol. 45, pp. 229–270. Springer-Verlag.

Zebib, A. 1984 A Chebyshev method for the solution of boundary value problems. *J. Compt. Phys.* **53**, 443–455.

CHAPTER 3

Spanwise secondary instability of spatially developing vortices.

Part 1. Theory and application to Dean vortices

3.1 Introduction

¹Counter-rotating streamwise vortices caused by streamwise curvature have attracted many researchers' attention, and can be found in many applications. Such vortices play an important role in the transition toward turbulence. Dean vortices found in curved channels, and Görtler vortices near a concave surface are two classical examples of such vortices.

In curved channels, Dean vortices significantly change the flow pattern, boundary layer structure, and the transition to turbulence. In the growing boundary layer on a concave wall with small curvature, Görtler vortices provide disturbances for

¹A version of this chapter has been submitted to J. Fluid Mech. for publication.

three dimensional Tollmien-Schlichting waves and thus promote early transition. When the wall curvature is strong, Görtler vortices develop significantly faster than Tollmien-Schlichting waves. The boundary layer is then dominated by streamwise counter-rotating vortices and the transition toward turbulence is characterized by the breakdown of these vortices. A better understanding of these vortices may lead to a better understanding of many flows including the flows near the concave surfaces of turbine blades and aerofoils. Because of the analogies between the effects of curvature, rotation and buoyancy, the study of Dean and Görtler vortices may also give some insight into the effects of rotation and buoyancy on transitions in the flow on a rotating plate and inside a rotating channel. In addition, recent attention has been paid to the similarity between Görtler vortices and the counter-rotating streamwise vortices found in most transitional and turbulent wall bounded shear flows (cf. Swearingen & Blackwelder 1987 for a review). Some studies suggest that these vortices may be due to a Görtler instability resulting from streamwise curvature (Cantwell, Coles & Dimotakis, 1978). Thus, Görtler vortices offer a simple model for studying the dynamics which govern the vortices in transitional and turbulent wall bounded shear layers.

In this study, we use a spectral-element numerical method to study the instability of spatially developing nonlinear streamwise vortices with respect to spanwise perturbations. The effect of this instability on wavenumber selection and nonlinear development of these vortices is examined. As a case study, we present our results on Dean vortices in this chapter. Results on Görtler vortices are presented in the next chapter as Part 2 of this study. Since some parts of the theory and numerical codes developed in this study can only be justified and verified in the Görtler problem, necessary information about Görtler vortices is introduced here.

The flow geometries for Dean vortices and Görtler vortices are shown in figures 3.1 and 3.2. The streamwise and spanwise directions of the flow are given by θ and z respectively. For Dean vortices the channel spacing is $d = r_o - r_i$. The Reynolds

number is $Re = \bar{U}d/2\nu$, where \bar{U} is the mean (bulk) streamwise velocity. The radius ratio of the two walls is $\gamma = r_i/r_o$, which is a measure of channel curvature. The spanwise dimensionless wavenumber of the vortices is defined as $\alpha = \pi d/\lambda$, where λ is the dimensional wavelength of the vortices.

For Görtler vortices, we will restrict ourselves to the case of constant wall curvature, i.e. the radius of the wall R is constant. The freestream velocity is U_∞ . The effect of the wall curvature is measured by the Görtler number

$$G\ddot{o} = \frac{U_\infty \delta_m}{\nu} \left(\frac{\delta_m}{R} \right)^{\frac{1}{2}}$$

where δ_m is the momentum thickness of a Blasius boundary layer at the downstream distance $x = R\theta$ from the leading edge. The wall curvature can also be measured by the ratio $\gamma = (R - \delta_{.99})/R$, where $\delta_{.99}$ is the Blasius boundary layer thickness at $u_\theta = 0.99U_\infty$. In this study, the wavelength of the Görtler vortices is measured by the dimensionless parameter

$$\Lambda = \frac{U_\infty \lambda}{\nu} \left(\frac{\lambda}{R} \right)^{\frac{1}{2}}$$

where λ is the dimensional wavelength in the spanwise direction. Both Λ and λ are constant in the streamwise direction.

Many studies have been done both experimentally and theoretically toward understanding the primary and secondary instabilities and nonlinear development of Dean vortices. Reviews can be found in Finlay, Keller & Ferziger (1988), Ligrani & Niver (1988) and Matsson & Alfredsson (1990). Most theoretical efforts are based on temporal theories. Finlay *et al.* (1988) examined theoretically and numerically the linear and nonlinear aspects of secondary instabilities with respect to streamwise perturbations using temporal theories and three-dimensional numerical simulations. Their results show that streamwise perturbations cause Dean vortices to develop travelling waves. Guo & Finlay (1991) studied the secondary instability with respect to spanwise perturbation using a temporal theory. They find that the stability

boundary is a closed loop in an (Re, α) plane. Outside the stability boundary, the most unstable wavenumber is usually half that of the base Dean vortices. The nonlinear development of these most unstable spanwise perturbations causes two pairs of Dean vortices to split into three pairs if the wavenumbers of the vortices are small and to merge into one pair if the wavenumbers are large. We referred to this type of secondary instability as Eckhaus instability to credit the first work of this kind done by Eckhaus (1965). The instability studied by Eckhaus is an instability with respect to long wavelength perturbations. However, the secondary instability studied by Guo & Finlay (1991) is more general, and in most cases is of short wavelength nature. This has led to some confusion. In order to avoid this confusion, we will refer to the secondary instability with respect to general spanwise perturbations as "spanwise secondary instability" (rather than Eckhaus instability) in this study.

One drawback of temporal theories is the difficulty in comparing with spatially developing experimental observations. Though the instabilities found by temporal theories (e.g. Finlay *et al.* 1988, Yang & Kim 1991, Guo & Finlay 1991, Ligrani *et al.* 1992) have been observed in experiments, many of the rich features revealed experimentally by Ligrani & Niver (1988), Alfredsson & Persson (1989), Matsson & Alfredsson (1990, 1992) and Ligrani *et al.* (1992) are still unaccounted for, particularly the spatial aspects of those instabilities. To overcome this drawback, Matsson & Alfredsson (1990) studied the spatial primary instability. The spatial development of Dean vortices and their secondary instabilities were studied by Bottaro, Matsson & Alfredsson (1991) using a time-dependent three-dimensional finite-volume code. But due to the high cost of three-dimensional simulations, the results they presented were limited. The details of the spatial evolution of the primary instabilities and secondary instabilities are still not clear.

So far, the secondary instability of spatially developing streamwise vortices with respect to spanwise disturbances has not been addressed in publications. In this

study, applying the concept of parabolization to spatial instability theory and three-dimensional numerical simulation, we develop a numerical method to study this type of instability. Because Dean vortices are less controversial due to their parallel nature, they are chosen to be our first case study. In this paper, we study the spatial development of Dean vortices and their secondary instability with respect to spanwise perturbations. In addition, we examine the roles of primary instability and spanwise secondary instability in the wavenumber selection process and their implications on the nonlinear evolution of Dean vortices.

In §3.2 we describe the theories and numerical approaches developed in this study. Code verifications are given in §3.3. We present in §3.4 our results on the primary instability and nonlinear evolution of spatially developing Dean vortices. The linear secondary instability of nonlinear Dean vortices with respect to spanwise perturbations is studied in §3.5 and §3.6. The nonlinear aspect of spanwise secondary instability is presented in §3.7 and the splitting and merging of vortices caused by this type of secondary instability and their effects on the wavenumber selection are discussed in §3.8. Concluding remarks are given in §3.9.

3.2 Theory and numerical methods

For an incompressible flow in which the streamwise velocity is dominant and has slow streamwise variation compared with cross-stream variation, the upstream influence of disturbances is negligible. The Navier-Stokes equations then have a parabolic nature in the streamwise direction. A disturbance generated locally is swept downstream from the source and only affects the downstream flow. If the disturbance grows downstream, then in the context of stability theory, these statements imply the flow is locally convectively unstable (Huerre & Monkewitz, 1990). Though the stability of a flow requires a rigorous study in order to classify it, we believe that if the use of parabolization can be justified, the stability of the

flow is locally convective.

In many applications, the developing vortices such as Dean and Görtler vortices are caused by relatively mild curvature (the ratio $\gamma > 0.9$). For such developing vortices, the length scales in the streamwise direction are much longer than those in the cross-stream directions, and the streamwise velocity component is much larger than in any other direction, even when the vortices become nonlinear (but before the onset of short wavelength wavy types of secondary instabilities such as twisting waves found by Finlay *et al.* 1988). Thus the use of parabolization is justified for Dean and Görtler vortices. The primary instabilities which cause these two types of vortices can be considered as locally convective instabilities.

The numerical simulations from both Guo & Finlay (1991) and this study show that when splitting or merging of Dean vortices and Görtler vortices occurs, the flows can still be treated as parabolic because of slow streamwise variations and dominant streamwise velocities. Thus the secondary instability of Dean and Görtler vortices with respect to spanwise perturbations, which causes the splitting and merging of vortices, can also be considered as a locally convective instability.

It has been shown by numerous theoretical studies that the primary instabilities associated with Dean and Görtler vortices are nonoscillatory. Many experimental observations also indicate that before the onset of any secondary instabilities, Dean and Görtler vortices are basically time-independent, spatially developing flows. Thus the primary instabilities of these two vortices are nonoscillatory spatial instabilities.

There are some differences in the experimental observations of the spanwise secondary instability which causes the splitting and merging of Dean vortices in curved channel flows. While Matsson & Alfredsson (1992) favour the steady spatial development of splitting and merging of vortices, Ligrani's experiments (1991) showed significant unsteadiness. Theoretically, there are many similarities between

primary instability and spanwise secondary instability. Using temporal theories, Guo & Finlay (1991) show that this type of secondary instability of fully developed Dean vortices is nonoscillatory. The difference between these two instabilities is that the base flow is one dimensional curved channel Poiseuille flow for primary instability and two dimensional fully developed Dean vortices for spanwise secondary instability. A similar situation can be found in Taylor-Couette flow (Riecke & Paap, 1986). Because of the similarity between primary and spanwise secondary instabilities, we believe that spanwise secondary instability of Dean vortices is a nonoscillatory spatial instability. The support for this conclusion can also be found from the experimental measurements done by Matsson & Alfredsson (1992) and Ligrani *et al.* (1992). The time-averaged flow patterns from both sources reveal the spatial developments of splitting and merging of vortices. If the splitting and merging of vortices are time-dependent, it is likely that the time-averaged flow patterns would not show any particular pattern. The unsteadiness observed by Ligrani (1991) was probably due to time-dependent perturbations at the entrance of the channel.

For Görtler vortices, no attention has been given to spanwise secondary instability either theoretically or experimentally. Whether this instability is time-dependent or not is unknown. Our results show it is not oscillatory. From our experience with Dean vortices and Taylor vortices (Guo & Finlay, 1991), we do not see any reason why it should be time-dependent. In this study, we will assume this instability is a non-oscillatory spatial instability. Even if it is time-dependent, the spatial aspect of this instability is still worth studying.

To summarize, the primary instabilities of both Dean and Görtler vortices can be treated as nonoscillatory spatial instabilities of locally convective nature. This allows us to represent developing Dean and Görtler vortices using the steady, three-dimensional, parabolized Navier-Stokes equations. It is also likely that the spanwise secondary instability of Dean and Görtler vortices is a nonoscillatory instability of

locally convective nature. Thus the spatial aspect of this instability can be studied by steady parabolized methods.

3.2.1 Three-dimensional parabolized Navier-Stokes equations and spectral-element methods

For steady flow with slow streamwise variation, the streamwise diffusion terms can be neglected and the pressure influence on the streamwise momentum equation can be considered as invariant in the cross-stream plane. With the above simplifications, the system of governing equations is non-elliptic in the streamwise direction and a marching strategy can be used. This version of the parabolized Navier-Stokes equations and its variations have been explored extensively by many researchers (cf. Fletcher 1988 for a review). Since the geometries we study here have radius ratio $\gamma > 0.9$, this version of the parabolized Navier-Stokes equations can be applied safely.

For simplicity, a Cartesian coordinate system is used to demonstrate the formulation of our numerical methods. Choosing x as the streamwise direction and z as the spanwise direction, the steady parabolized Navier-Stokes equations can be written in the streamwise direction as

$$2u_x \frac{\partial u_x}{\partial x} + \frac{\partial}{\partial y}(u_y u_x) + \frac{\partial}{\partial z}(u_z u_x) - f_x = -\frac{\partial \bar{p}}{\partial x} + \frac{1}{Re} \left(\frac{\partial^2 u_x}{\partial y^2} + \frac{\partial^2 u_x}{\partial z^2} \right) \quad (3.1)$$

and in the cross-stream plane (y, z) as

$$\begin{aligned} \frac{\partial}{\partial x}(u_x u_y) + \frac{\partial}{\partial y}(u_y u_y) + \frac{\partial}{\partial z}(u_z u_y) - f_y &= -\frac{\partial p}{\partial y} + \frac{1}{Re} \left(\frac{\partial^2 u_y}{\partial y^2} + \frac{\partial^2 u_y}{\partial z^2} \right) \\ \frac{\partial}{\partial x}(u_x u_z) + \frac{\partial}{\partial y}(u_y u_z) + \frac{\partial}{\partial z}(u_z u_z) - f_z &= -\frac{\partial p}{\partial z} + \frac{1}{Re} \left(\frac{\partial^2 u_z}{\partial y^2} + \frac{\partial^2 u_z}{\partial z^2} \right) \end{aligned} \quad (3.2)$$

The continuity equation is

$$-\frac{\partial u_y}{\partial y} - \frac{\partial u_z}{\partial z} = \frac{\partial u_x}{\partial x} \quad (3.3)$$

In equation (3.1), \bar{p} is the pressure averaged across the (y, z) plane. For channel flows, the velocity \mathbf{u} is non-dimensionalized by the mean streamwise velocity \bar{U} . For growing boundary layers, \mathbf{u} is non-dimensionalized by the free stream velocity U_∞ . In a (y, z) plane, the equations (3.1-3.3) are elliptic. In the streamwise direction, the variable x behaves like time t in a two-dimensional Navier-Stokes problem. Non-slip boundary conditions are used at walls. In the spanwise direction, z , periodic boundary conditions are used for both Dean and Görtler vortices. In the case of boundary layer flow on a concave wall, homogeneous Neumann boundary conditions are applied in the y direction far away from the wall.

Control volume methods (Patankar & Spalding 1972), finite difference methods (Rubin *et al.* 1977) and finite element methods (Baker, 1983) have been used to solve the equations (3.1-3.3). In this study, a Legendre spectral-element method is used (Rønquist, 1988 and Maday & Patera, 1989). The combination of the high accuracy of spectral methods with the geometry flexibility of finite element methods makes the spectral-element methods particularly suitable for this study. For example, in this study the matrix system resulting from the stability analysis (see §3.2.2) is complex and full, and a direct solver is needed. The numerical work associated with a direct solver is proportional to $O(K^3 N^6)$, where K is the number of elements and N is the order of polynomials within each element. The numerical truncation error ϵ of a finite element method decreases algebraically with K but exponentially with N . For a given ϵ , high order methods offer the best choice, since by using relatively high order polynomials within each element and relatively few elements, the problem can be tackled more efficiently. This is the advantage of spectral-element methods over h -type finite element methods for the stability problem.

The advantage of spectral-element methods over spectral methods is that to switch from Dean vortices to Görtler vortices, we only need to modify the boundary conditions, which requires only minor code changes. This advantage helps us to

verify the numerical codes developed in this study and gives us confidence in our results for the Görtler problem. Boundary layers can also be captured easily by using small elements near the wall. Thus there is no need to use a coordinate transformation.

In a (y, z) plane, the equations (3.1-3.3) are discretized by a Legendre spectral-element method. In the streamwise direction, a third order Adam-Bashforth scheme is used for the nonlinear convection terms and force terms, while a backward Euler scheme is used for the viscous terms. Though (3.1-3.3) are different from any examples given by Rønquist (1988) and Maday & Patera (1989), following the procedures they give and standard variational principles, the discretization of (3.1-3.3) in a (y, z) plane is straightforward. Within each element, the velocity \mathbf{u} is represented on $(N + 1)(N + 1)$ Gauss-Lobatto/Gauss-Lobatto Legendre nodes by Legendre Lagrange interpolating polynomials of degree N . The pressure p is represented on $(N - 1)(N - 1)$ Gauss/Gauss Legendre nodes by Legendre Lagrange interpolating polynomials of degree $(N - 2)$. The resulting matrix system can be written in the streamwise direction as

$$2B_x^n \frac{U_x^{n+1} - U_x^n}{\Delta x} + \sum_{l=0}^2 \beta_l (C_x - F_x)^{n-l} = -B \bar{P}_x^{n+1} - \frac{1}{Re} A U_x^{n+1} \quad (3.4)$$

and in the cross-stream directions as

$$\frac{B_x^{n+1} U_i^{n+1} - B_x^n U_i^n}{\Delta x} + \sum_{l=0}^2 \beta_l (C_i - F_i)^{n-l} = -D_i P^{n+1} - \frac{1}{Re} A U_i^{n+1} \quad (3.5)$$

The continuity equation is

$$-D_y^T U_y^{n+1} - D_z^T U_z^{n+1} = \frac{B_p^T}{\Delta x} (U_x^{n+1} - U_x^n) \quad (3.6)$$

Equation (3.5) contains two equations, obtained by setting $i = y$ and z . The symbol U_i^n is the vector consisting of the values of u_i at the Gauss-Lobatto/Gauss-Lobatto nodes at step n ; \bar{P}_x^{n+1} is the streamwise pressure gradient averaged across the (y, z) plane at step $n + 1$; P^{n+1} is the vector consisting of the values of the pressure p

at the Gauss/Gauss nodes at step $n + 1$. The symbols A, B and D_i are the standard Laplace matrix, mass matrix (lumped) and gradient matrices; B_x^n is the lumped mass matrix of u_x on the Gauss-Lobatto/Gauss-Lobatto nodes at step n , and B_p is the mass matrix on the Gauss/Gauss-Lobatto nodes. C_i and F_i ($i = x, y, z$) are from the convection and force terms. The coefficient $\beta_l = 23/12, -16/12$ and $5/12$ for $l = 0, 1$ and 2 . More details about the discretization of (3.1-3.3) can be found in Appendix B.

The following strategies are used to march the solutions of (3.4-3.6) in the streamwise direction. The streamwise momentum equation (3.4) is marched first from step n to step $n + 1$ to give U_x^{n+1} ; B_x^{n+1} is then calculated from U_x^{n+1} . For the flow on a concave wall, \bar{P}_x^{n+1} is set to zero. For channel flow, \bar{P}_x^{n+1} is found by forcing the flow rate

$$Q = \int u_x^{n+1} dydz$$

to be constant. This is done by a steepest descent iterative method. Once U_x^{n+1} and B_x^{n+1} are known, P^{n+1} , U_y^{n+1} and U_z^{n+1} can be solved from the cross-stream momentum equations (3.5) and the continuity equation (3.6) using a global iterative Uzawa scheme similar to the one used by Rønquist (1988). Due to $u_x=0$ at walls, the popular pressure Poisson equation decoupling approaches (for example Patera, 1984 and Kleiser & Schumann, 1984) are not applicable for (3.2-3.3). Preconditioned conjugate iterative methods similar to those used by Rønquist (1988) are used to deal with the resulting linear matrix problems.

Our codes are written in a cylindrical coordinate system. For ease of implementation, the computational variables for the velocities are chosen to be $\phi_r = ru_r$, $\phi_\theta = r u_\theta$ and $\phi_z = ru_z$. The streamwise direction is the azimuthal direction. All of the secondary effects caused by the streamwise curvature are treated as force terms. In order to keep the equivalence between the divergence matrices in the continuity equation and the transpose of the gradient matrices D_i^T ,

the Navier-Stokes equations are carefully arranged in the streamwise direction as

$$\begin{aligned} 2 \frac{\phi_\theta}{r^3} \frac{\partial \phi_\theta}{\partial \theta} + \frac{\partial}{\partial r} \left(\frac{\phi_r \phi_\theta}{r^2} \right) + \frac{\partial}{\partial z} \left(\frac{\phi_z \phi_\theta}{r^2} \right) + \frac{2\phi_r \phi_\theta}{r^3} - \frac{1}{Re} \frac{2}{r^3} \frac{\partial \phi_r}{\partial \theta} \\ = -\frac{1}{r} \frac{\partial \bar{p}}{\partial \theta} + \frac{1}{Re} \left[\frac{\partial}{\partial r} \frac{1}{r} \frac{\partial \phi_\theta}{\partial r} + \frac{\partial}{\partial z} \frac{1}{r} \frac{\partial \phi_\theta}{\partial z} \right] \end{aligned}$$

and in the cross-stream directions as

$$\begin{aligned} \frac{\partial}{\partial \theta} \left(\frac{\phi_\theta}{r^3} \phi_r \right) + \frac{\partial}{\partial r} \left(\frac{\phi_r \phi_r}{r^2} \right) + \frac{\partial}{\partial z} \left(\frac{\phi_z \phi_r}{r^2} \right) + \frac{(\phi_r^2 - \phi_\theta^2)}{r^3} + \frac{1}{Re} \frac{2}{r^3} \frac{\partial \phi_\theta}{\partial \theta} \\ = -\frac{\partial p}{\partial r} + \frac{1}{Re} \left[\frac{\partial}{\partial r} \frac{1}{r} \frac{\partial \phi_r}{\partial r} + \frac{\partial}{\partial z} \frac{1}{r} \frac{\partial \phi_r}{\partial z} \right] \\ \frac{\partial}{\partial \theta} \left(\frac{\phi_\theta}{r^3} \phi_z \right) + \frac{\partial}{\partial r} \left(\frac{\phi_r \phi_z}{r^2} \right) + \frac{\partial}{\partial z} \left(\frac{\phi_z \phi_z}{r^2} \right) + \frac{\phi_z \phi_r}{r^3} - \frac{1}{Re} \frac{\phi_z}{r^3} \\ = -\frac{\partial p}{\partial z} + \frac{1}{Re} \left[\frac{\partial}{\partial r} \frac{1}{r} \frac{\partial \phi_z}{\partial r} + \frac{\partial}{\partial z} \frac{1}{r} \frac{\partial \phi_z}{\partial z} \right] \end{aligned}$$

The continuity equation is

$$-\frac{\partial \phi_r}{\partial r} - \frac{\partial \phi_z}{\partial z} = \frac{1}{r} \frac{\partial \phi_\theta}{\partial \theta}$$

3.2.2 Spanwise secondary instability of spatially developing flow

Once the developing Dean vortices and Görtler vortices \mathbf{u}^0 are found from (3.1-3.3), the stability of \mathbf{u}^0 can be studied by substituting

$$\mathbf{u} = \mathbf{u}^0 + \mathbf{u}'$$

into the Navier-Stokes equations, where \mathbf{u}' is the perturbation. For small spanwise perturbations, the resulting stability equations can be linearized and \mathbf{u}' can be written as

$$\mathbf{u}' = \tilde{\mathbf{u}} \exp(i\beta z) \quad (3.7)$$

where β is the wavenumber and $\tilde{\mathbf{u}}$ is the complex eigenfunction. In some cases it is more convenient to use the non-dimensionalized wavenumber $b = \beta/\alpha$, where α is

the wavenumber of the base flow \mathbf{u}^0 . The flow pattern of the perturbation is given by the real part of (3.7).

Assuming that the perturbation \mathbf{u}' has slow streamwise variation, the terms $\frac{\partial^2}{\partial x^2}$ in the stability equations are much smaller than the other terms involving second derivatives and therefore can be neglected. This gives the parabolized stability equations. They can be written in the streamwise direction as

$$2 \frac{\partial}{\partial x} (u_x^0 \tilde{u}_x) + w_x = \frac{1}{Re} \left[\frac{\partial \tilde{u}_x}{\partial y} + \frac{\partial \tilde{u}_x}{\partial z} \right] \quad (3.8)$$

and in the cross-stream directions as

$$\begin{aligned} \frac{\partial}{\partial x} (u_x^0 \tilde{u}_y) + \frac{\partial}{\partial x} (u_y^0 \tilde{u}_x) + w_y &= -\frac{\partial \tilde{p}}{\partial y} + \frac{1}{Re} \left[\frac{\partial^2 \tilde{u}_y}{\partial y^2} + \frac{\partial^2 \tilde{u}_y}{\partial z^2} \right] \\ \frac{\partial}{\partial x} (u_x^0 \tilde{u}_z) + \frac{\partial}{\partial x} (u_z^0 \tilde{u}_x) + w_z &= -\frac{\partial \tilde{p}}{\partial z} - i\beta \tilde{p} + \frac{1}{Re} \left[\frac{\partial^2 \tilde{u}_z}{\partial y^2} + \frac{\partial^2 \tilde{u}_z}{\partial z^2} \right] \end{aligned} \quad (3.9)$$

The continuity equation is

$$-\frac{\partial \tilde{u}_y}{\partial y} - \left(\frac{\partial}{\partial z} + i\beta \right) \tilde{u}_z = \frac{\partial \tilde{u}_x}{\partial x} \quad (3.10)$$

where

$$w_i = \frac{\partial}{\partial y} (u_y^0 \tilde{u}_i + \tilde{u}_y u_i^0) + \left(\frac{\partial}{\partial z} + i\beta \right) (u_z^0 \tilde{u}_i + \tilde{u}_z u_i^0) - \frac{1}{Re} \left(2i\beta \frac{\partial \tilde{u}_i}{\partial z} - \beta^2 \tilde{u}_i \right)$$

and $i = x, y$ and z . The equations (3.8-3.10) deal with steady, spatially evolving perturbations, and are a specialization of the general parabolized stability equations explored by Bertolotti, Herbert & Spalart (1990).

The discretization of the stability equations (3.8-3.10) by the spectral-element method follows that of (3.4-3.6). In the streamwise direction, a third order Adam-Bashforth scheme is used for the w_i terms and a backward Euler scheme for the rest of the equations. The solutions of (3.8-3.10) are marched in the streamwise direction together with (3.4-3.6) by first marching the base flow \mathbf{u}^0 from step n to step $n+1$ using the equations (3.4-3.6). Then $\tilde{\mathbf{u}}_x^{n+1}$ is obtained from (3.8) and \tilde{p}^{n+1} ,

\tilde{u}_y^{n+1} and \tilde{u}_z^{n+1} from (3.9-3.10) using a strategy similar to that of (3.4-3.6). The matrix system for \tilde{p}^{n+1} is full and complex, and a direct solver from LINPACK is used.

Once the perturbation \mathbf{u}' is found, the energy growth rate σ of the perturbation can be calculated by

$$\sigma = (\ln e^{n+1} - \ln e^n) \frac{l}{\Delta x}$$

where e is the energy of the perturbation defined by

$$e = \int |\mathbf{u}'|^2 dy dz.$$

and l is the length scale used to non-dimensionalize σ . For Dean vortices, the channel half-width, $d/2$, is used. For Görtler vortices, the streamwise distance x from the leading edge is used. In cylindrical coordinates, $\Delta x = \Delta\theta(r_o - r_i)/2$ for channel flows and $\Delta x = R\Delta\theta$ for growing boundary layers. In some cases, the growth rate σ_1 defined by

$$\sigma_1 = (\ln |u_x^{n+1}|_{max} - \ln |u_x^n|_{max}) \frac{l}{\Delta x}$$

is also used. For the linear stability equations (3.8-3.10), the absolute energy level of the perturbation \mathbf{u}' is irrelevant.

There is no need to develop a new code to study the nonlinear aspects of spanwise secondary instability. Instead, once the most unstable wavenumber β is found from the linear analysis, the nonlinear development of this perturbation can be studied using the same code that produces the base flow \mathbf{u}^0 by using a computational box with a larger spanwise length which can hold n pairs of base vortices in (3.1-3.3). Here n is the minimum number which makes $n \times \beta/\alpha$ an integer. Our results show that the most unstable wavenumber for spanwise secondary instability in this study is usually $\alpha/2$. So only two pairs of vortices need to be included in a computational box in order to study the nonlinear dynamics of spanwise secondary instability.

In this study, the orders of the polynomials used for each spectral element are 8, 10, or 12. For the simulation and stability analysis of Dean vortices, usually 2 to 4 elements are used in the radial directions, depending on Re . For the simulation and stability analysis of Görtler vortices, the number of elements in the radial direction varies from 3 to 6. The computational grid extends to at least $8\delta_{.99}$ normal from the wall, where $\delta_{.99}$ is the Blasius boundary layer thickness at $u_\theta = 0.99U_\infty$. In the spanwise direction, the number of elements depends on the aspect ratio of the computational box. The minimum is two. Since most computations in this study were done on our own IBM/RISC 6000 work-stations and our access to these computers is unlimited, relatively high resolutions are used in most cases. The results presented here are also tested by using different resolutions.

3.3 Code verification

Since the numerical schemes we use to discretize and solve the parabolized Navier-Stokes equations (3.1-3.3) and the related stability equations (3.8-3.10) have never been reported before, proper code verifications are crucial. In this study, two codes are developed. The "simulation code" simulates the developing flow, while the "stability code" examines the stability of this flow.

As a first step in insuring that the spectral-element methods in our codes work properly, we set the streamwise velocity $u_x = 1$ and only consider the cross-stream momentum equations (3.2) and the continuity equation (3.3). The resulting equations are identical to the unsteady two-dimensional Navier-Stokes equations for which there are closed form solutions (Kim & Moin, 1985). The code was then tested against those solutions and found to be correct.

3.3.1 Verification of simulation code for developing flows

For channel flows, we usually start a simulation with the velocity profile for a straight channel as the initial conditions. The solution reaches a fully developed state after a certain distance downstream. In order to test the convergence of the code, artificial perturbations are also added to the initial conditions in some cases. For fully developed flow, our simulation code can accurately duplicate the velocity and pressure of the fully developed nonlinear Dean vortices given by Finlay *et al.* (1988) and Guo & Finlay (1991), regardless of what initial conditions are used to start the simulations.

The simulations of developing Dean vortices cannot be verified directly because the velocity and pressure of the developing Dean vortices depend both on the initial conditions and the streamwise location and there are no such data available. However, through the manipulation of initial flow conditions, our numerical results can be made to match the data given by Matsson & Alfredsson (1992) experimentally and by Bottaro *et al.* (1991) numerically. Another indirect verification is given by the fact that the streamwise growth of developing Dean vortices from the simulation code is accurately predicted by the stability code, i.e. both our codes give the same growth rates for linear Dean vortices (see §3.4). Since these two codes use different theories and formulations, it is unlikely that both codes have errors which make them give the same results.

With minor code changes to deal with boundary conditions, the simulation code can be applied to growing boundary layer problems. The code accurately duplicates the Blasius velocity profile for the flat plate (Schlichting, 1955). For the concave boundary layer, the growth of developing Görtler vortices is well predicted by the stability code. Spatially developing nonlinear Görtler vortices are a topic of several recent papers. The most comprehensive experimental measurements are given by Swearingen & Blackwelder (1987). The most detailed numerical simulation is given

by Lee & Liu (1992) by solving an equation set similar to (3.1-3.3) using a control volume method. The results obtained by our simulation code are in good agreement with those given by Swearingen & Blackwelder (1987) and Lee & Liu (1992). Since the detailed structure of Görtler vortices depends on the initial conditions and there is no fully developed state (unlike Dean vortices), we choose not to present the simulations of spatially developing Görtler vortices as a part of our code verification here; instead we will discuss them in Part 2 of this study (Guo & Finlay, 1992).

The simulation code duplicates fully developed Dean vortices (which are two dimensional in the cross-stream plane) and the growing flat plate boundary layer (which is a streamwise developing flow with one dimension in the cross-stream plane), and gives the same growth rates for developing Dean vortices and Görtler vortices as the stability code does. Thus we believe the numerical methods we use to deal with the three-dimensional parabolized Navier-Stokes equations are correct and the simulation code is properly implemented.

3.3.2 Verification of spanwise secondary stability code for spatially developing flows

Using the spatial stability code described in §3.2.2, we can accurately duplicate the primary instability boundary from a temporal theory (Guo & Finlay, 1991) by setting the base flow u^0 to be one-dimensional curved channel Poiseuille flow in (3.8-3.10). The growth rates given by the spatial stability code are the same as those given by our simulation code, which further verifies our simulation code. We can also accurately duplicate the results given by Matsson & Alfredsson (1990) for the primary spatial instability associated with Dean vortices.

When the base flow is set to be fully developed Dean vortices, the stability code duplicates the instability boundary of spanwise secondary instability given by Guo & Finlay (1991) using temporal theory (i.e. the "Eckhaus boundary" in their

paper). The code also gives growth rates and eigenfunctions of spanwise secondary instability of spanwise periodic flow that are symmetric in b about $b = \beta/\alpha = 0.5$, and the following relation discussed by Guo & Finlay (1991) (using the temporal theory) is still true:

$$f(b) = f(b \pm n) \quad (3.11)$$

Here $f(b)$ represents the spatial growth rate and eigenfunction at b , and $n = 1, 2, 3, \dots$. Since equation (3.11) can be derived analytically for any spanwise periodic base flow (cf. Appendix A), we believe our stability code is working properly for fully developed flows.

No comparable data are available for verification of the stability analysis of nonlinear spatially developing vortices with respect to spanwise perturbations. Instead, we will use the linear stability analysis of Görtler vortices in the spatially growing boundary layer as verification of our stability analysis of spatially developing flows with respect to spanwise perturbations. When the base flow u^0 is set to be Blasius boundary layer flow (Schlichting, 1955) in (3.8-3.10), the stability code is equivalent to the global marching method used by Hall (1983), except that no scaling is used here. First, our code confirms Hall's results that the stability boundary depends very much on how and where the initial perturbations are used to start the analysis. Further downstream, our results confirm the statement of Day, Herbert & Saric (1990) that the growth rates converge to a unique curve which does not depend on the initial perturbations.

Figure 3.3 shows the typical development of the growth rates for Görtler vortices with the wavelength parameter $\Lambda = 62$. Also given for comparison are the growth rates calculated by Day *et al.* (1990) using a local approach (Floryan & Saric, 1984) and a global marching method (Hall, 1983). In figure 3.3, x_0 is the streamwise location of the neutral point given by the local method. For $\Lambda = 62$, the neutral Görtler number from the local method is $G\ddot{o} = 0.998$. It can be seen that our neutral

points depend on the initial perturbations and locations used to start the marching. The difference between the data given by Day *et al.* and ours for $x/x_0 < 4.0$ is due to the different initial perturbations used to start the marching. Day *et al.* use the eigenfunctions from local theory as the initial perturbations. It is to be expected that the eigenfunctions from local theory converge to the 'asymptotic' curve faster than arbitrary perturbations. The fluctuations in the growth rate σ_1 of $|u_\theta'|_{max}$ are associated with the varying locations of grid points in the cross-stream plane when using the spectral-element methods. Since the integration of $|u'|^2$ over the cross-stream plane is less affected by the uneven grids, we will use only the energy growth rate σ in the rest of this paper.

A comparison of the perturbation velocity profiles is given in figure 3.4 for $\Lambda = 62$ at $x/x_0 = 4$. The agreement is reasonable. In figure 3.4, u_r' is scaled by $U_\infty x_0/\nu$. It is worth mentioning that $\partial u_r'/\partial r = 0$ at the wall and our result faithfully reproduces this fact.

3.4 Spatial primary instability and development of nonlinear Dean vortices

Having verified our codes, let us now examine curved channel flow. One purpose here is to further establish the credibility of the methods and theories developed in this study, since considerable work has been done on curved channel flows with large aspect ratio, both numerically and experimentally. All cases presented in this paper are in a curved channel with radius ratio $\gamma = 0.975$.

By setting the base flow \mathbf{u}^0 to be curved channel Poiseuille flow in the stability code (3.8-3.10), we first study the spatial primary instability of Dean vortices. Figure 3.5 shows contours of the spatial (energy) growth rate σ of Dean vortices in a curved channel for $\gamma = 0.975$. The contour line $\sigma = 0.0$ represents the neutral stability boundary. It is identical to the one from temporal theory. The contours

are in good agreement with those given by Matsson & Alfredsson (1990). For any Re beyond $Re_c = 114.16$, there exists a band of unstable wavenumbers and one of them has the largest growth rate. As Re increases, the band of unstable wavenumbers broadens and the difference between the growth rates of the most unstable wavenumber and neighboring wavenumbers becomes smaller. This suggests that at high Re the wavenumber selection mechanism of primary instability is not as strong as at low Re . We also notice that the most unstable wavenumbers from spatial theory are almost the same as those from temporal theory (Finlay *et al.* 1988).

Figure 3.6 shows the spatial development of the energy of nonlinear Dean vortices at $Re = 2.186Re_c$. Only one pair of vortices are included in the computational box and periodic boundary conditions are used in the spanwise direction. The initial velocity field used to start the simulation is $\mathbf{u}^0 = (0, u_{1D}[1.0 + \sin(2\pi\alpha z) \times 10^{-5}], 0)$, where u_{1D} is the velocity profile of curved channel Poiseuille flow and α is the wavenumber. The most unstable wavenumber at this Re is near $\alpha = 2.5$. It can be seen that the spatial growth of the vortices is essentially exponential. This confirms the experimental observations given by Matsson & Alfredsson (1992). The growth rate σ can be calculated from the slope of the energy growth curve. For example when $\alpha = 2.0$, the energy growth rate is 0.1, well predicted by spatial stability theory (see figure 3.5). Our results also show that the streamwise length needed for Dean vortices to become fully developed depends on both the growth rate and initial perturbation amplitude.

We have done many other simulations with different patterns and energy levels for the initial perturbations. The spatial growth of Dean vortices for all these cases is generally like that in figure 3.6. When the difference between the growth rates of Dean vortices with different wavenumbers is small, the wavenumber favoured by the initial perturbations can reach the fully developed state first (due to its higher initial energy) even if it has a smaller growth rate.

3.5 Spanwise secondary instability of fully developed Dean vortices

Using fully developed Dean vortices as the base flow \mathbf{u}^0 in (3.8-3.10), we can examine the spatial instability of the Dean vortices with respect to spanwise perturbations. As mentioned in §3.3, our results show that spatial theory gives the same stability boundaries as those given by temporal theory (Guo & Finlay 1991). Our further numerical results show that the growth rate and the related eigenfunction of spanwise secondary instability do not depend on the initial eigenfunctions used to start the marching of the stability code when $Re < 2.8Re_c$. They always converge to the same value and pattern regardless of the initial conditions. When $Re > 2.8Re_c$, some types of initial conditions cause the spatial oscillation of growth rates and eigenfunctions. Since Dean vortices will likely develop into wavy vortices (Finlay *et al.* 1988) and become time dependent when $Re > 2.8Re_c$, we will restrict our discussion to $Re < 2.8Re_c$.

As in the case of temporal theory, the spatial growth rate σ and the flow pattern of the perturbation (3.7) are symmetric in b about $b = 0.5$. The value $b = 0.5$ is the most unstable wavenumber for most of the region exterior to the stability boundary in the (α, Re) plane. Examinations of the perturbation reveal the same flow patterns as those given by temporal theory (Guo & Finlay 1991, figure 11). In the space of two pairs of base Dean vortices, there are three vortex pairs if the Dean vortices have small wavenumber and there is only one pair if the Dean vortices have large wavenumber. As in the case of temporal theory (Guo & Finlay, 1991), the flow pattern of the perturbation indicates that the spanwise secondary instability of fully developed Dean vortices causes two pairs of Dean vortices with large wavenumber to merge into one pair and two pairs with small wavenumbers ($\alpha < 3.0$) to split into three pairs.

To support the above arguments and understand how the spanwise secondary

instability develops nonlinearly, we performed spatial simulations using two pairs of fully developed Dean vortices as the initial conditions. Our simulations show that spanwise perturbations do grow up in the way predicted by linear spanwise secondary instability. The growths of these perturbations are basically exponential and the growth rates are well predicted by the linear secondary stability theory. As in the case of temporal theory (Guo & Finlay, 1991, figure 19), the nonlinear growth of these perturbations eventually causes two pairs of Dean vortices to split into three pairs if the Dean vortices have a small wavenumber, or merge into one pair if the Dean vortices have a large wavenumber.

Figure 3.7 shows a typical case of splitting and merging of Dean vortices at $Re = 2.0Re_c$ in a curved channel with $\gamma = 0.975$. The simulation was started with curved channel Poiseuille flow as the initial flow conditions. No artificial perturbations are introduced except numerical truncation error. For visual clarity, the curved channel is shown as a straight channel with the streamwise direction in θ (rad). In figure 3.7, four pairs of Dean vortices with $\alpha = 2.0$ reach the fully developed stage at $\theta = 10.0$. At $\theta = 15.0$, two merging events are observed simultaneously and the number of vortex pairs becomes two. Shortly afterward, a new pair of vortices begins to appear at $\theta = 20.0$. At almost the same time, the two old pairs resulting from the upstream vortex merge begin to move closer. At $\theta = 23.0$, these two pairs are merged into one pair.

There also exists a wavenumber for a given Re which has the smallest growth rate of spanwise secondary instability. This wavenumber is very close to that given by temporal theory (the "Eckhaus valley" in Guo & Finlay, 1991). In general, the growth rates of the spanwise secondary instability of fully developed Dean vortices are smaller than those of the primary instability. Table 3.1 lists typical values of these growth rates. It can be seen they are almost eight times smaller than those of primary instability in most cases. Small growth rates suggest that in order to observe the splitting and merging of Dean vortices in a finite streamwise distance,

relatively high energy levels of disturbances are needed. For example in figure 3.7 when no large disturbances are present, the first merging event takes 5.0 radians to develop. Our later simulations show that Dean vortices which are distorted due to a variety of factors are more likely to split or merge. We will discuss this issue in §3.7.

3.6 Spanwise secondary instability of spatially developing Dean vortices

The interactions that occur between developing Dean vortices are not well understood. In most experimental observations and numerical simulations, Dean vortices with a well-defined wavenumber are seen at a specific location in a channel. One myth is that the development of one wavenumber inhibits the growth of other wavenumbers so that only one wavenumber is observed at one location. To resolve this issue, we next examine the spatial instability of developing vortices with respect to spanwise perturbations by marching the base flow \mathbf{u}^0 and the eigenfunction $\bar{\mathbf{u}}$ together using both the simulation code and the stability code. In this section, all cases are presented at $Re = 2.0Re_c$ in a curved channel with $\gamma = 0.975$. The initial flow condition used to start the simulation code is $\mathbf{u}^0 = (0, u_{1D} (1.0 + \sin(2\pi\alpha z) \times 10^{-4}), 0)$; $(0, u_{1D}, 0)$ is used as the real part of the initial eigenfunction to start the stability code (the imaginary part is zero). We have tried different forms of initial eigenfunctions and found no differences in the growth rate and perturbation pattern of spanwise secondary instability.

3.6.1 Dean vortices with large wavenumber

Figure 3.8 shows the development of both the energy of Dean vortices in the base flow and the perturbation associated with spanwise secondary instability. The wavenumber of the base Dean vortices is $\alpha = 4.0$. The perturbation wavenumber

is $\beta = 2.0$ ($b = 0.5$). In figure 3.8 when $\theta < 1.5$, the growth rates of the base Dean vortices and the related perturbation are 0.071 and 0.09, which are equal to the growth rates of primary instability at $\alpha = 4.0$ and 2.0 (see figure 3.5). This suggests that when the Dean vortices in the base flow have small amplitude, the growth of each wavenumber is governed by primary instability. Different wavenumbers do not interact with each other. This is to be expected since small amplitude Dean vortices do not alter the base flow significantly and the base flow is essentially curved channel Poiseuille flow. This result can also be shown analytically using linear stability theory. When the amplitude of Dean vortices is small, the vortices can be represented as the small perturbation in (3.7) but with multiple wavenumbers. Then the stability equations can be linearized and decoupled into several sets of stability equations, one set for each wavenumber in the perturbation. The base flows in these stability equation sets are curved channel Poiseuille flow. The small vortices with one wavenumber thus do not have any influence on the stability equations for other wavenumbers. The growth of each wavelength is purely governed by primary instability.

The growth rate of the perturbation remains near 0.09 until $\theta = 1.75$, where the base Dean vortices have reached a significantly nonlinear level. When the base Dean vortices are fully developed at $\theta = 3.0$, the growth rate of the perturbation changes to 0.019. This value is very close to the one given by the spanwise secondary instability using the fully developed Dean vortices $\alpha = 4.0$ as the base flow. Thus the energy of the perturbation with $b = 0.5$, which grew initially due to a primary instability, is transferred into a spanwise secondary instability once the base vortices become strongly nonlinear (at $\theta > 2.5$ or so). In figure 3.8 we also notice that the energy of the perturbation never stops growing while the base Dean vortices are developing. This is true even when the fully developed base vortices are stable to spanwise perturbations.

For the perturbations with other wavenumbers (i.e. $b \neq 0.5$), our numerical

results are similar to those in figure 3.8. When the base vortices are linear, the growth of these perturbations is dictated by primary instability. When the base vortices enter the nonlinear stage and become fully developed, these perturbations continue to grow, at a rate given by spanwise secondary instability. This growth rate is smaller than that at $b = 0.5$. When $Re > Re_c$, there is a band of unstable base wavenumbers α which have positive primary growth rate. Thus, when the base vortices are developing, there will be a band of perturbation wavenumbers $b = \beta/\alpha$ which are unstable. These perturbations will have positive growth rate even in the nonlinear region of the base vortices. Thus, prior to fully developed, Dean vortices are always unstable to a range of perturbation wavenumbers.

Figure 3.9 shows the spatial development of the radial velocity component of the base flow and the perturbation in figure 3.8. In figure 3.9(a), the base Dean vortices become visible at $\theta = 1.76$. There are two vortex pairs in the domain because $b = 0.5$. When $\theta > 2.5$, the base vortices become fully developed. In figure 3.9(b), it can be seen that though there is always one pair of vortices in the perturbation, the shape of the perturbation begins to change at $\theta = 1.76$, where the base flow develops into nonlinear Dean vortices. From $\theta = 1.76$ to 3.0, the perturbation pattern experiences a spanwise shift. The increased density of the contour lines also indicates an increase of energy in the perturbation. By $\theta = 3.76$, the shape of the perturbation stops changing.

The flow patterns of the base flow and the perturbation at $\theta = 1.26$ and 4.26 are shown in figure 3.10 in the cross-stream plane. The grid point velocities in figure 3.10 (and all other vector plots in the rest of the paper) are shown on the grid points actually used in the computation. Figure 3.10(a) and 3.10(b) show the base Dean vortices at $\theta = 1.26$ and 4.26. There are two pairs of vortices in the domain. It is interesting to see that the flow pattern of the linear Dean vortices in figure 3.10(a) does not differ much from the nonlinear one in figure 3.10(b). The related perturbations in figure 3.10(c) and 10(d) have different flow patterns, though both

of them have only one pair of vortices in the space of two base pairs. The shape of the perturbation at $\theta = 1.26$ in figure 3.10(c) is that of a primary instability eigenfunction with $\alpha = 2.0$. The shape of the perturbation at $\theta = 4.26$ in figure 3.10(d) is quite similar to those given by Guo & Finlay (1991) using a temporal theory. Compared to figure 3.10(c), the spanwise shift of the perturbation vortices at $\theta = 4.26$ is shown clearly in figure 3.10(d). Thus the character of the perturbation changes from a primary instability eigenfunction to a spanwise secondary instability eigenfunction once the base vortices reach their saturation amplitude.

To demonstrate the effect of this type of perturbation on the base flow, 50% of the perturbation in figure 3.10(d) is superimposed on the base flow in figure 3.10(b) and the result is shown in figure 3.10(e). It can be seen that the two base vortices near $2z/a = 1.6$ and 2.4 in figure 3.10(b) are being forced together in figure 3.10(e) and become smaller. These two vortices are separated by an outflow region where the fluid flows from the convex (inner) wall to the concave (outer) wall. A similar situation is found by Guo & Finlay (1991) when a temporal method is used. In the context of temporal theory, they find that the nonlinear development of these types of perturbations leads to the merging of two vortex pairs into one pair.

3.6.2 Dean vortices with small wavenumber

Figure 3.11 shows the energy development of a flow similar to the one in figure 3.8 but with the base Dean vortices having $\alpha = 2.0$ and the perturbation having $\beta = 1.0$ ($b = 0.5$). For $\theta < 1.0$ where the energy level of the base Dean vortices is low, the growth rates of the base Dean vortices and the perturbation are 0.09 and 0.036, which are equal to the growth rates of primary instability at the wavenumbers $\alpha = 2.0$ and 1.0 (figure 3.5). For $1.0 < \theta < 1.6$ where the nonlinearity of the base Dean vortices sets in, the growth rate of the perturbation begins to increase. When the base Dean vortices reach the fully developed state at $\theta = 2.75$, the growth rate

of the perturbation switches to 0.0155, which is equal to the one given by spanwise secondary instability using fully developed Dean vortices (with $\alpha = 2.0$) as the base flow.

The spatial developments of the velocity components u_r^0 and u_r' are shown in figure 3.12. In figure 3.12(a) the base Dean vortices become visible at $\theta = 1.26$ and reach a significantly nonlinear level at $\theta = 1.5$. There are two vortex pairs in the domain. In figure 3.12(b), the related perturbation has only one pair of vortices for $\theta < 1.26$. At $\theta = 1.26$ in figure 3.12(b), two new small vortices can be seen near the concave wall. The new vortices continue to grow downstream. By $\theta = 2.76$, the flow pattern of the perturbations stops changing and there are three pairs of vortices in the space of the two base vortex pairs. The energy of the perturbation continues to grow downstream. A spanwise shift of the perturbation pattern can also be seen from $\theta = 1.26$ to 2.76.

The flow patterns of the base flow and the perturbation of figure 3.11 at $\theta = 0.76$ and 3.26 are shown in figure 3.13. At $\theta = 0.76$, the base flow has two vortex pairs (figure 3.13a) and the related perturbation has one pair (figure 3.13c). The flow pattern of the perturbation is similar to that given by primary instability at $\alpha = 1.0$. At $\theta = 3.26$, the number of vortices in the perturbation increases to three pairs (figure 3.13d) while the number of the base vortices remains at two pairs (figure 3.13b). The effect of the perturbation on the base flow is illustrated in figure 3.13(e) through the superimposition of 100% of the perturbation (figure 3.13d) on the base vortices (figure 3.13b). In figure 3.13(e) near $2z/d = 0.8$, it can be seen that a small vortex pair with an inflow region at its center is generated near the concave wall while the two old pairs with inflow regions at their centers near $2z/d = 2.4$ and 5.5 in figure 3.13(b) are squeezed together towards $2z/d = 4.0$ in figure 3.13(e). This situation is almost identical to that discussed in Guo & Finlay (1991). In Guo & Finlay (1991), the temporal simulations show that the nonlinear development of these perturbations results in the appearance of a new vortex pair.

We find a similar result for base Dean vortices with other wavenumbers. If the fully developed Dean vortices are within the stability boundary of spanwise secondary instability (i.e. they are stable and lie within the "Eckhaus boundary" in Guo & Finlay, 1991), we find that the growth of the perturbation is similar to that in figure 3.8 and 3.11 before the base Dean vortices reach the fully developed state. Once the base vortices become fully developed, the perturbation decays.

To summarize the above discussions, our study in this section shows that, when the energy level of Dean vortices in the base flow is low, the stability of each wavenumber is dictated independently by primary instability. Multiple wavenumbers can develop at the same time until a dominant wavenumber in the base flow reaches the nonlinear stage. As the dominant Dean vortices develop nonlinearly towards their fully developed state, spanwise secondary instability sets in and the perturbations associated with the wavenumber $b = 0.5$ become the most unstable and can continue to grow. The development of one wavenumber does not inhibit the development of other wavenumbers. Once the vortices are strongly nonlinear, the energy in wavenumbers other than the dominant one and its harmonics appears to be transferred from independently growing primary instability eigenfunctions into spanwise secondary instability eigenfunctions. When the dominant Dean vortices are fully developed, the perturbations will continue to grow (at a new rate) if the dominant vortices are outside the stability boundary of spanwise secondary instability.

3.7 Simulation of splitting and merging of Dean vortices

To support the arguments in §3.6, in this section we study the nonlinear aspects of spanwise secondary instability using the simulation code. The initial

flow condition used to start the simulation code is

$$\mathbf{u} = (0, u_{1D}(1.0 + (\sin(4\pi\alpha z) + \epsilon \sin(4\pi\beta z)) \times 10^{-4}), 0) \quad (3.12)$$

where α is the wavenumber of the dominant Dean vortices and β is the perturbation wavenumber. In equation (3.12), ϵ is used to adjust the energy level of the perturbation relative to the dominant vortices. Two pairs of dominant vortices are included in the computational box. The energy in spanwise Fourier modes is also monitored. The energy in spanwise Fourier mode k_z is defined by (Finlay *et al.*, 1988)

$$E(k_z) = c(k_z) \int_{r_i}^{r_o} \hat{u}(r, k_z)^2 dr$$

where $c(k) = 0.5$ for $k = 0$ and $c(k) = 1$ for $k \neq 0$; $\hat{u}(r, k_z)$ is the spanwise Fourier transform of \mathbf{u} . In the case of $b = 0.5$, before the spanwise perturbation becomes nonlinear the energy in the first mode comes mostly from the perturbation with $b = 0.5$ and the energy in the second mode mostly from the dominant Dean vortices.

3.7.1 Dean vortices with large wavenumber

Figure 3.14 shows the development of the velocity component u_r with the dominant wavenumber $\alpha = 4.0$ and the perturbation wavenumber $\beta = 2.0$ ($b = 0.5$). In this simulation, $\epsilon = 0.08$. Two pairs of the dominant Dean vortices become visible at $\theta = 2.75$. At $\theta = 3.0$, they are fully developed. A complete vortex merging event can be seen at $\theta = 4.25$ shortly after the dominant wavenumber reaches the fully developed state. From $\theta = 3.0$ to 4.0, we can see the left pair of the dominant vortices is somehow weaker than the right pair.

The energy development of figure 3.14 is shown in figure 3.15. We can see that before the energy in the second Fourier mode reaches the nonlinear state at $\theta = 2.0$, the energy growth rates in the second and first modes are 0.07 and 0.09, which

are equal to the growth rates of primary instability at $\alpha = 4.0$ and 2.0 . (These growth rates are obtained from the simulation and are the same as those in figure 3.8 obtained from the spanwise secondary instability analysis, which confirms our stability results). Before the Dean vortices in the base flow reach a nonlinear level, the growth of each wavenumber is purely governed by primary instability. When the dominant Dean vortices enter the nonlinear stage at $\theta = 2.0$, the energy growths in the second and first modes begin to slow down. When the dominant wavenumber reaches the fully developed state at $\theta = 3.5$, the energy in the first mode continues to grow from $\theta = 3.5$ to 4.0 but at the new rate 0.02 , which is close to the growth rate of spanwise secondary instability of fully developed Dean vortices $\alpha = 4.0$ (cf. figure 3.8). Further downstream, nonlinear interaction between the dominant wavenumber and the perturbation can be expected because the energy level in the first mode is comparable to that in the second mode. At $\theta = 4.25$, the sudden drop of the energy in the second mode indicates the beginning of nonlinear vortex merging.

The flow pattern of figure 3.14 is shown in cross-stream planes in figure 3.16. At $\theta = 1.51$ in figure 3.16(a), there are two pairs of vortices with outflow regions at their centers near $2z/d = 1.2$ and 2.7 . At this stage, the vortices are basically linear. Both pairs have almost the same strength. At $\theta = 3.01$ in figure 3.16(b), the dominant vortices are more or less fully developed. We can see there are some distortions on the vortex pair near $2z/d = 1.2$. We believe these distortions are due to the growth of the energy in the first Fourier mode (associated with the perturbation $\beta = 2.0$). These distortions provide high perturbation levels for the nonlinear development of spanwise secondary instability that soon follows. At $\theta = 3.76$ in figure 3.16(c), the vortex pair between $2z/d = 1.6$ and 2.4 is squeezed towards $2z/d = 2.0$ and becomes smaller, while the other vortex pair grows bigger. This development continues downstream. At $\theta = 4.81$ in figure 3.16(d), the two small vortices near $2z/d = 2.0$ in figure 3.16(c) disappear completely and there is only

one pair of vortices in the domain. The vortex merging event is completed.

Comparing figure 3.16(c) to figure 3.10(e), we can see the merging event roughly follows what is predicted by the stability theory: one vortex pair separated by an outflow region is squeezed and weakened by spanwise secondary instability, and eventually two pairs of vortices merge into one pair. From figure 3.16(b) and figure 3.16(c), we also see the flow pattern switches from distorted Dean vortices to the vortex merging pattern predicted by the secondary stability theory.

During a vortex merging event, the vortex structures can become highly asymmetric and irregular due to the nonlinear development of spanwise secondary instability and the nonlinear interactions between different wavenumbers. But when the merging event is complete, the vortex structures become symmetric again. In experiments, time-dependence of the flow will probably occur due to time-varying inlet perturbation conditions. How this will affect vortex merging process needs further study.

We can control the streamwise location of a vortex merging event by adjusting ϵ in equation (3.12). Figure 3.17 shows the development of the energy for a flow similar to that in figure 3.15, but now with $\epsilon = 0.05$. It can be seen more clearly that the energy growth rate of the first Fourier mode switches from the primary growth rate $\sigma = 0.09$ when $\theta < 2.0$ to the growth rate $\sigma = 0.02$ of spanwise secondary instability when $\theta > 3.5$. The merging event is completed by $\theta = 5.5$. Our simulations show that when small ϵ is used, the dominant Dean vortices are less distorted when their amplitude saturates and the structures of the vortices are more symmetric, like those in figure 3.7 and Guo & Finlay (1991, figure 19). In addition, the merging event takes longer streamwise distance to complete when a smaller ϵ is used.

3.7.2 Dean vortices with small wavenumber

Figure 3.18 shows the evolution of the velocity component u_r of a flow similar to that in figure 3.14, except the dominant wavenumber is $\alpha = 2.0$ and the perturbation wavenumber is $\beta = 3.0$ ($b = 1.5$) and $Re = 2.186Re_c$. In this simulation, $\epsilon = 0.25$. We choose $b = 1.5$ here instead of $b = 0.5$ because the growth rate of the primary instability at $\beta = 3.0$ is larger than that at $\beta = 1.0$ ($b = 0.5$). When the dominant wavenumber enters the nonlinear stage, the growth rate of the spanwise secondary instability is the same for both $b = 1.5$ and 0.5 (cf. equation 3.11). Thus, $b = 1.5$ will generate more perturbation energy than $b = 0.5$ will when entering the spanwise secondary instability stage (a simulation with $b = 0.5$ confirms this). In figure 3.18, it can be seen that the two dominant vortex pairs reach a fully developed stage at $\theta = 2.25$. Shortly afterwards at $\theta = 4.0$, a new vortex pair appears between the two dominant vortex pairs and the dominant pairs are pushed apart a little. For $\theta > 4.5$, the domain is filled by three pairs of vortices. This is a vortex splitting event.

The flow pattern of figure 3.18 is shown in cross-stream planes in figure 3.19. At $\theta = 2.5$ in figure 3.19(a), there are two equal strength pairs of vortices with inflow regions near $2z/d = 1.8$ and 5.8 . Downstream at $\theta = 4.0$ in figure 3.19(b), the two dominant pairs are pushed apart and a small vortex pair can be seen at $2z/d = 3.9$ near the concave wall. This new vortex pair has an inflow region at its center. As this new vortex pair grows downstream, it pushes the two dominant pairs further apart in figure 3.19(c). By $\theta = 6.0$ in figure 3.19(d), the vortex splitting event is complete and three pairs of vortices occupy the whole domain. Comparing figure 3.19(b) to figure 3.13(e), we can see that the vortex splitting pattern is well predicted by linear secondary stability theory. A small new vortex pair is generated first near the concave wall in between two dominant vortex pairs. It has an inflow region at its center. Two dominant vortex pairs are pushed apart by the new pair.

The development of the energy in spanwise Fourier modes shows a similar situation to that in figures 3.15 and 3.17, except that here the energy in the third Fourier mode is used to monitor the growth of the perturbation with $b = 1.5$. As in the case of vortex merging, the streamwise location of a vortex splitting event can be controlled by adjusting ϵ in equation (3.12). An increase in ϵ causes a splitting event to become visible earlier upstream.

When perturbations with $b \neq 0.5$ (or 1.5) are used, results similar to those in §3.6 are obtained if the perturbation energy level is much lower than that of the dominant vortices and there is no nonlinear interaction between the perturbation and the dominant vortices. In other words, before the dominant vortices become fully developed, the growth of the perturbation with low energy level is governed by primary instability. When the dominant vortices are fully developed, the growth rate of this perturbation is given by spanwise secondary instability. If the perturbation level is high and comparable to that of the dominant vortices, some energy of the perturbation with $b \neq 0.5$ is converted into perturbations with b near 0.5 due to nonlinear interactions between the dominant vortices and the perturbation with $b \neq 0.5$. As a result, the growth of the perturbation with $b = 0.5$ dominates the flow in some cases and the nonlinear vortex splitting and merging discussed early in this section occur. If the growth of the perturbation with $b = 0.5$ does not dominate the flow, vortex splitting and merging still occur but in a different (irregular) way.

Similar results are also found at other α and Re . From the above discussions we conclude that the instability of developing Dean vortices to spanwise perturbations is essential to vortex splitting or merging in curved channels. Initial perturbations at the channel entrance, as well as the growth rates of primary instability and spanwise secondary instability all play important roles in the first appearance of vortex splitting or merging.

3.8 Wavenumber selection and irregularity of Dean vortices

Our discussions in §3.4 show that the growth rates of primary instability do not vary significantly with α for a band of wavenumbers near the one with the maximum growth rate. The wavenumber selection mechanism of primary instability is not strong for this band of wavenumbers. Since the nonlinear growth of Dean vortices depends on both the growth rate of primary instability and the perturbations at the entrance of a channel, the wavenumber with the maximum growth rate is not necessarily the one that will be observed in experiments. The observed wavenumbers could be in a band near the most unstable wavenumbers, especially for high Re where the differences between the primary growth rates for different wavenumbers are small. If the perturbations have equal energy for all wavenumbers (e.g. low level broadband turbulence), then upstream of any vortex splitting or merging event, the observed wavenumber should be close to the one with the maximum growth rate. At high Re ($> 2.0Re_c$), the spatial development of Dean vortices is very sensitive to small disturbances due to a large primary growth rate. For example at $Re = 2.186Re_c$ in figure 3.6, a perturbation level less than $10^{-5}\bar{U}$ is enough to make Dean vortices visible in a streamwise distance of $\theta < 5.0$ rad. (With only numerical error as perturbation, vortices require much longer length to develop.) Thus we believe that the preference of Dean vortices for certain spanwise locations observed by Matsson & Alfredsson (1992) may be due to disturbances caused by the channel geometry.

In §3.5 and §3.6, we have shown that the developing Dean vortices are unstable to spanwise perturbations. The nonlinear growths of these spanwise perturbations cause vortex merging and splitting. As a result, the wavenumbers of Dean vortices are changed. Since the first round of vortex splitting and merging events depends on the initial perturbations at the channel entrance and the growth rates of primary

instability and spanwise secondary instability, it is difficult to predict the favoured wavenumbers which survive the first round of vortex splitting and merging. Further downstream as the splitting and merging of vortices continue to occur due to the instability of fully developed Dean vortices with respect to spanwise perturbations, the wavenumbers which have the minimum growth rate of spanwise secondary instability are more likely to be observed. More discussion on this wavenumber selection mechanism can be found in Guo & Finlay (1991).

The perturbations needed for splitting and merging of vortices to occur can also come from the interactions between vortices with different wavenumbers. Figure 3.20 shows such a case at $\gamma = 0.975$ and $Re = 2.186Re_c$. The initial perturbations used to start the simulation have a wavenumber of 2.5 for the left two vortex pairs and 3.0 for the remaining three vortex pairs. The maximum amplitudes of the initial perturbations are 0.01% of curved channel Poiseuille flow. In figure 3.20, the Dean vortices of $\alpha = 3.0$ and 2.5 reach a fully developed state at $\theta = 2.5$. Then, near the two interfaces between vortices with different wavenumbers, a merging event among the vortices with $\alpha = 3.0$ and a splitting event among the vortices with $\alpha = 2.5$ begin to develop one after another. When the same parameters are used but with only one wavenumber initially in the flow, splitting or merging events are not visible in the same length of the channel.

Since Dean vortices are unstable all the time to spanwise perturbations for $Re > 1.5Re_c$ (outside the stability boundary of spanwise secondary instability), they are constantly distorted by all other disturbances, e.g., the development of multiple wavenumbers during their linear development and vortex splitting or merging during their nonlinear development. Observation of irregular Dean vortices should be rather common.

3.9 Concluding remarks

The material presented in this chapter shows that spatially developing Dean vortices are unstable to spanwise perturbations. When the vortices are small and linear, spanwise perturbations with multiple wavelengths can coexist and grow at the same time at the rates given by primary instability. When some of these vortices grow strong enough to become the dominant wavelengths and nonlinearities set in, spanwise secondary instability becomes the dominant instability. Perturbations with twice that of the dominant wavelengths are found to be most unstable. Nonlinear growth of these perturbations distorts the dominant vortices. When the dominant Dean vortices become fully developed, their stability boundary to spanwise perturbations is a small closed loop. Outside the stability boundary, the nonlinear development of these perturbations causes two pairs of vortices with short wavelength to merge into one pair and generates a new pair of vortices between two pairs of vortices with long wavelength. The vortex splitting and merging patterns are well predicted by linear spanwise secondary instability.

The concept of spanwise secondary instability proposed in this study is a general instability of spatially developing vortices with respect to spanwise perturbations. When the vortices in the base flow are linear, spanwise secondary instability is equivalent to primary instability. When the vortices in the base flow enter the nonlinear stage, spanwise secondary instability controls the growth of the energy involved in the distortion of the dominant vortices, vortex splitting/merging, and the interactions between various wavenumbers and the dominant wavenumbers. Because spanwise secondary instability rapidly destroys vortex pairs with particularly large or small wavenumbers, this instability restricts the spanwise scale of the vortices.

Since the nonlinear development of spanwise secondary instability changes the structure of the streamwise vortices significantly, understanding how this type of

instability affects the onset of other secondary instabilities is an important step toward the understanding of transition and turbulence in a developing flow.

TABLE 3.1. The growth rates of primary instability (σ_{1D}) and spanwise secondary instability (σ_{2D}) with $b = 0.5$ are listed as a function of Re/Re_c and wavenumber α .

Re/Re_c	α	σ_{1D}	σ_{2D}
1.7	2.4	0.077	0.0124
1.9	2.4	0.091	0.0143
2.2	2.4	0.109	0.0156
2.5	2.4	0.122	0.0160
2.8	2.4	0.134	0.0180
3.0	2.4	0.140	0.0190
3.25	2.5	0.150	0.0200

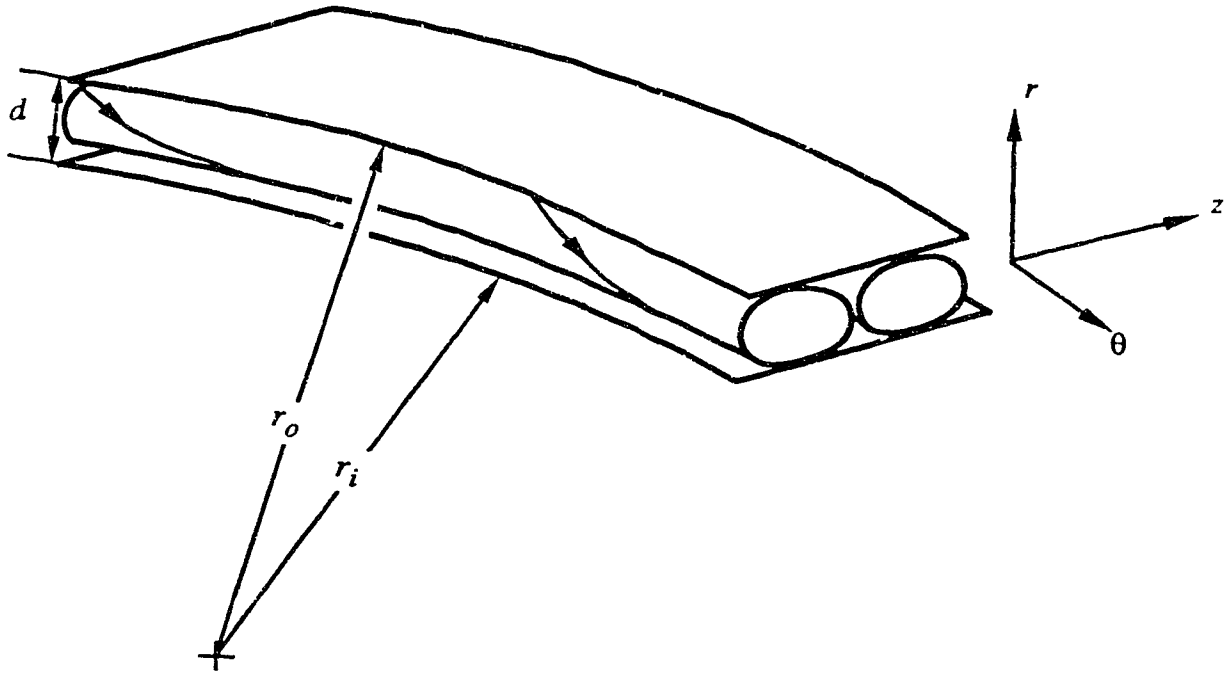


FIGURE 3.1. The geometry of curved channel flow is shown.

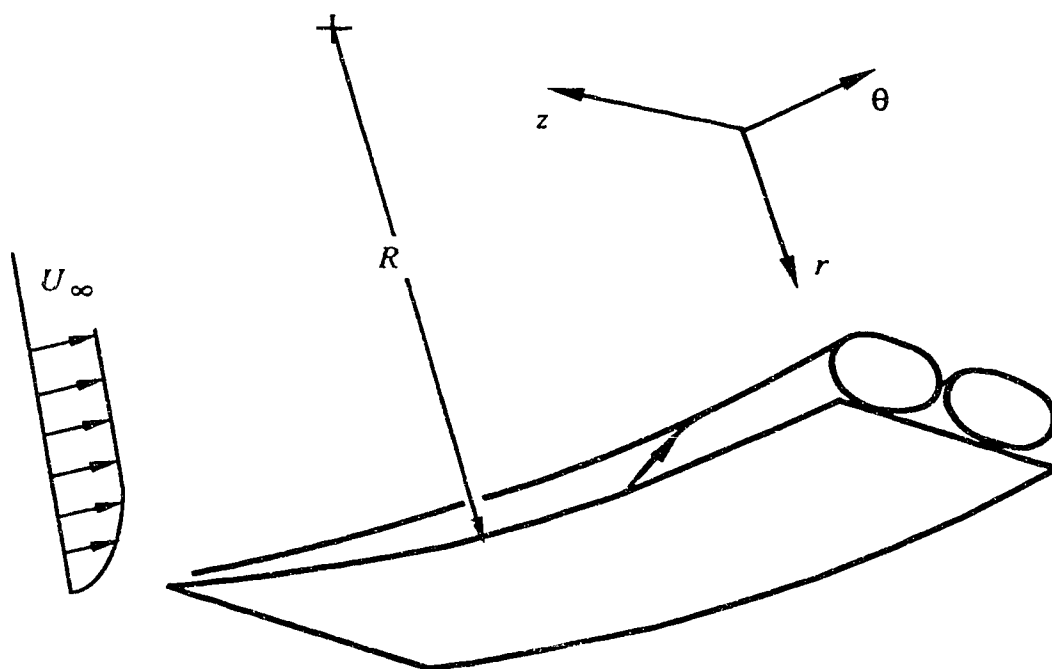


FIGURE 3.2. The geometry of boundary layer flow over a concave surface is shown. The streamwise direction is θ .

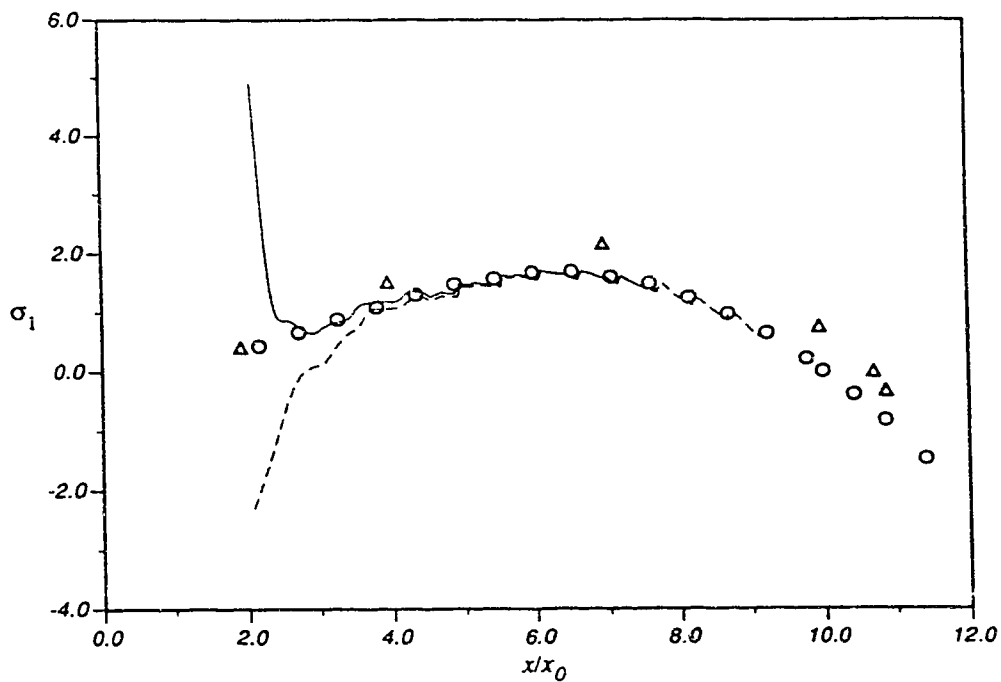


FIGURE 3.3. The growth rates σ_1 of linear Görtler vortices with $\Lambda = 62$ are shown as functions of streamwise distance from the leading edge x/x_0 , where x_0 is the streamwise location of the neutral point given by a local method. The values of σ_1 (----) are obtained with the initial eigenfunctions $(-v_B, 0, 0)$; the σ_1 (—) are obtained with the initial eigenfunctions $(0, u_B, 0)$, where u_B and v_B are the streamwise and vertical components of Blasius flow. The growth rates σ_1 obtained by Day *et al.* (1991) using a local method (Δ) and a global marching method (\circ) are also given.

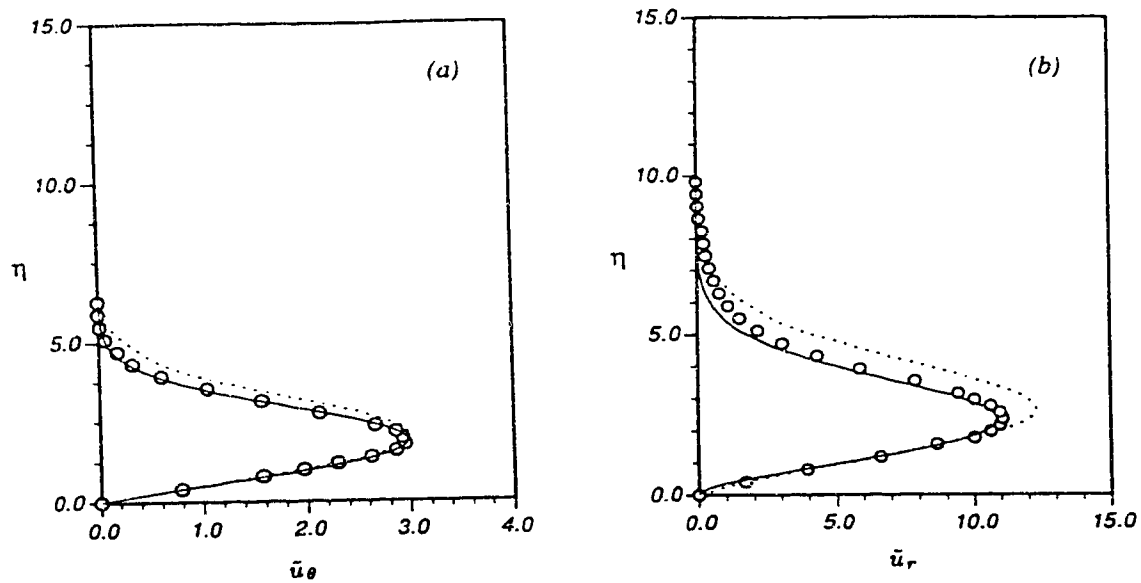


FIGURE 3.4. Comparison of the eigenfunction components (a) \bar{u}_θ and (b) \bar{u}_r of linear Görtler vortices (—) with the data obtained by Day *et al.* (1991) using a local method (.....) and a global marching method (o). Distance from the wall is $\eta = y\sqrt{U_\infty/\nu x}$, and \bar{u}_r is scaled by $U_\infty x_0/\nu$.

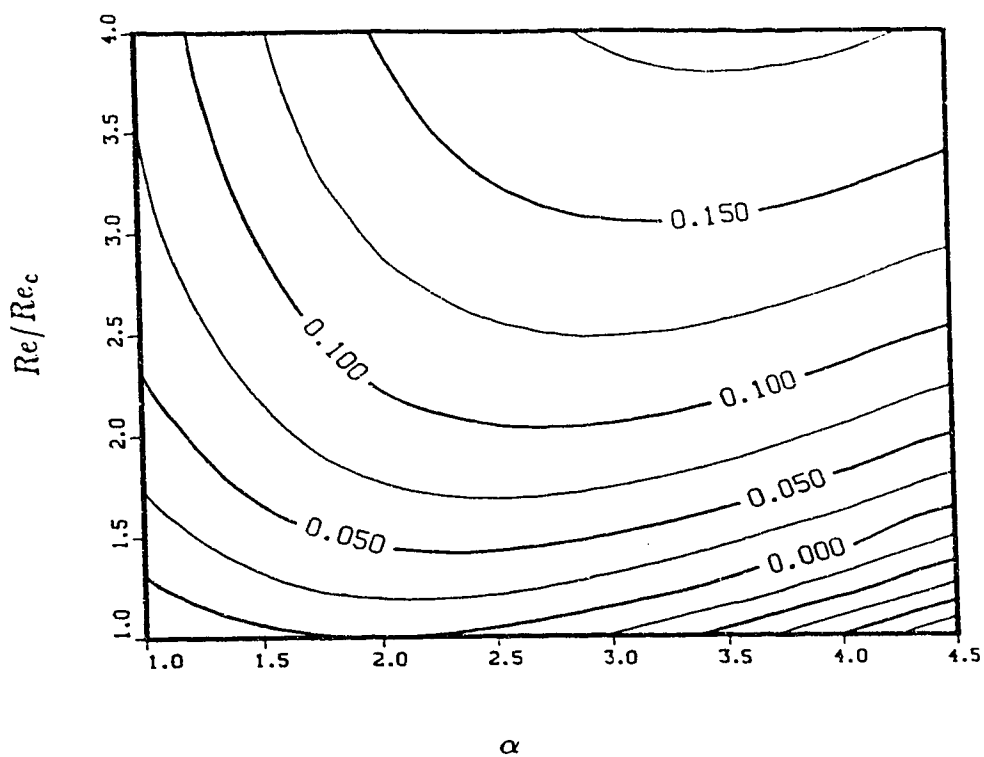


FIGURE 3.5. Contours of the spatial growth rate σ of primary instability are shown as a function of spanwise wavenumber α and Re/Re_c for a curved channel with $\gamma = 0.975$, $Re_c = 114.26$.

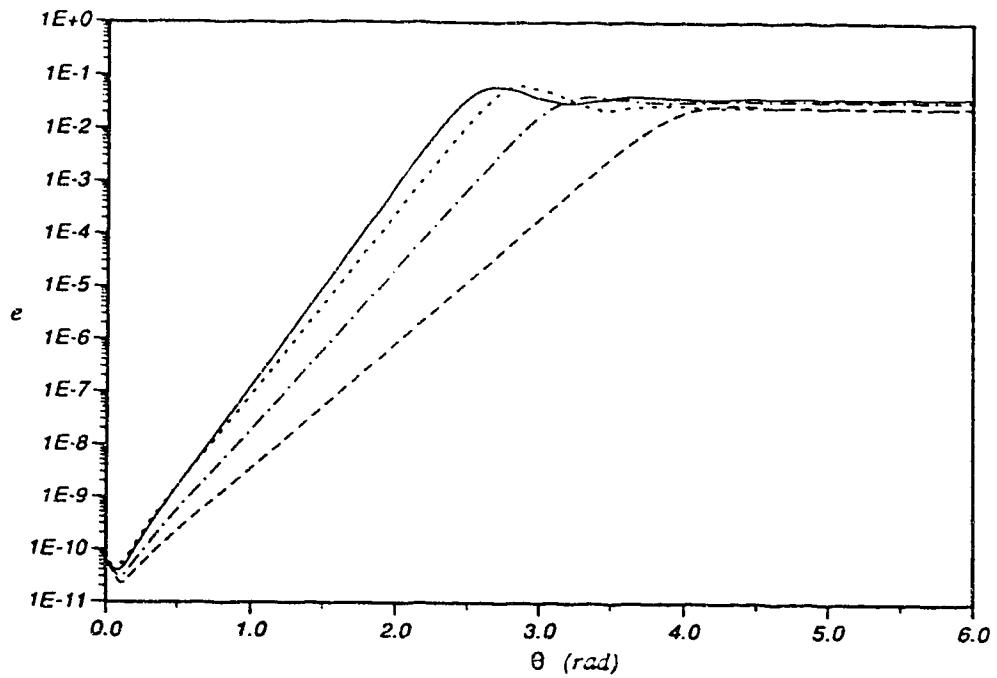


FIGURE 3.6. Spatial growth of the energy of Dean vortices with the spanwise wavenumber $\alpha = 2.0$ (.....), 2.5 (—), 4.0 (— —) and 4.5 (----) in a curved channel with $\gamma = 0.975$ at $Re = 2.186Re_c$.

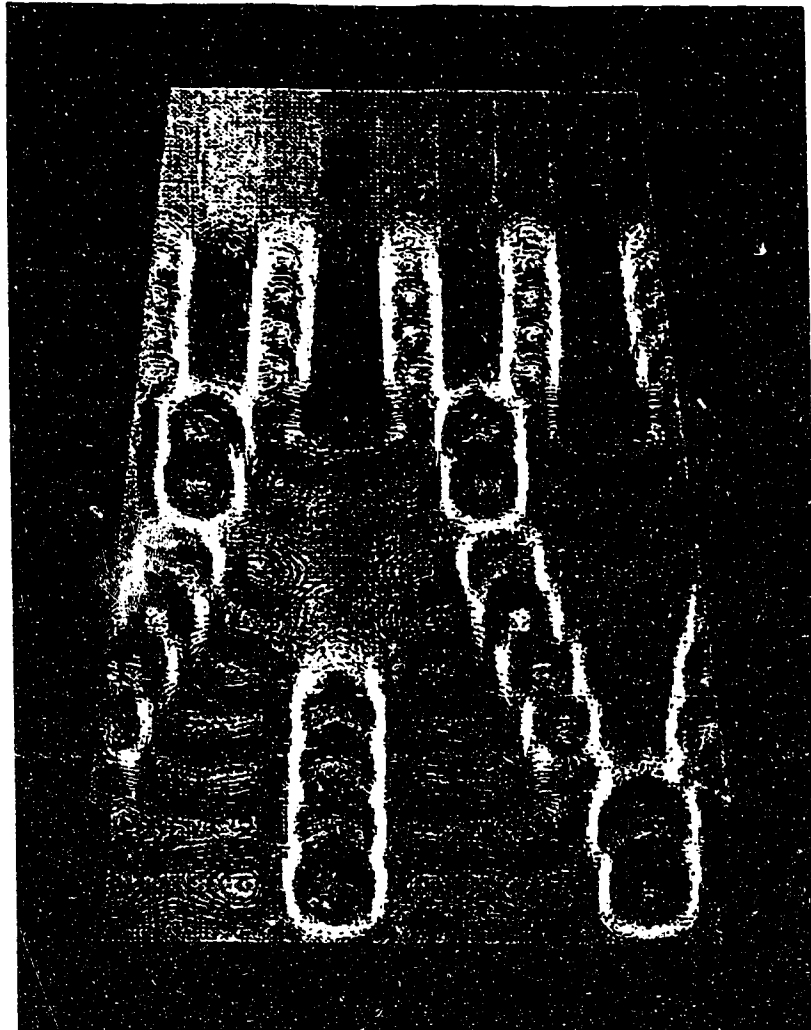


FIGURE 3.7. Contour plot of the velocity component u_r of spatially developing Dean vortices are shown in cross-stream planes from the streamwise location $\theta = 7.0$ to 24.0 rad in a curved channel $\gamma = 0.975$ at $Re = 2.0Re_c$. The inner wall is above the outer wall and the flow proceeds downstream from top to bottom.

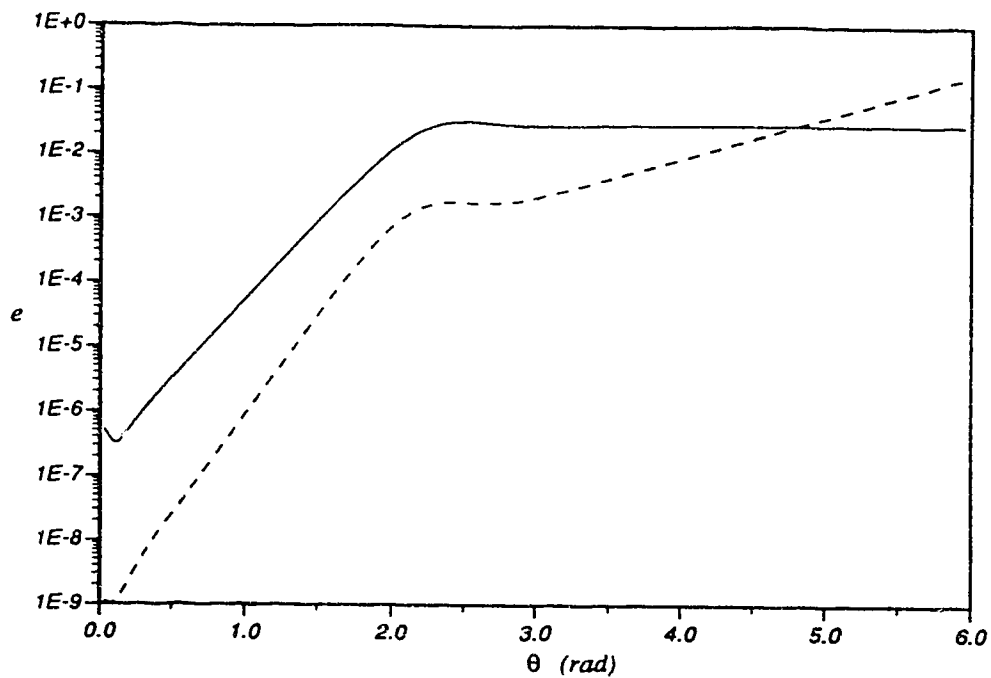


FIGURE 3.8. Spatial growth of the energy in the base Dean vortices $\alpha = 4.0$ (—) and the related perturbation $\beta = 2.0$ ($b = 0.5$) of spanwise secondary instability (---) in a curved channel $\gamma = 0.975$ at $Re = 2.0Re_c$.

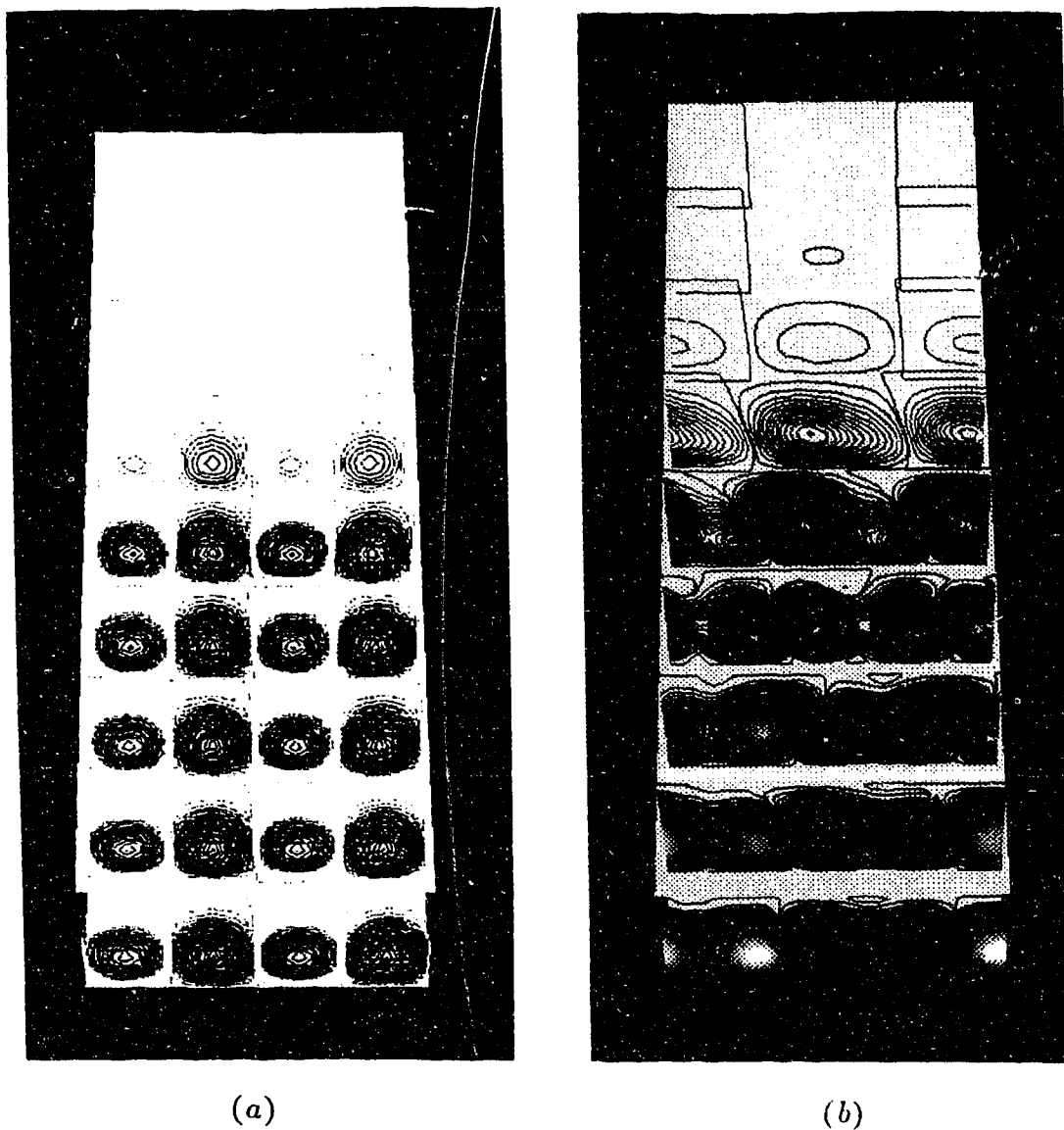


FIGURE 3.9. Contours of the velocity components (a) u_r^0 of the base Dean vortices and (b) u_r' of the related perturbation in figure 3.8 are shown in cross-stream planes from the streamwise location $\theta = 0.26$ to 4.26 rad with $\Delta\theta = 0.5$ rad. The inner wall is above the outer wall and the flow proceeds downstream from top to bottom.

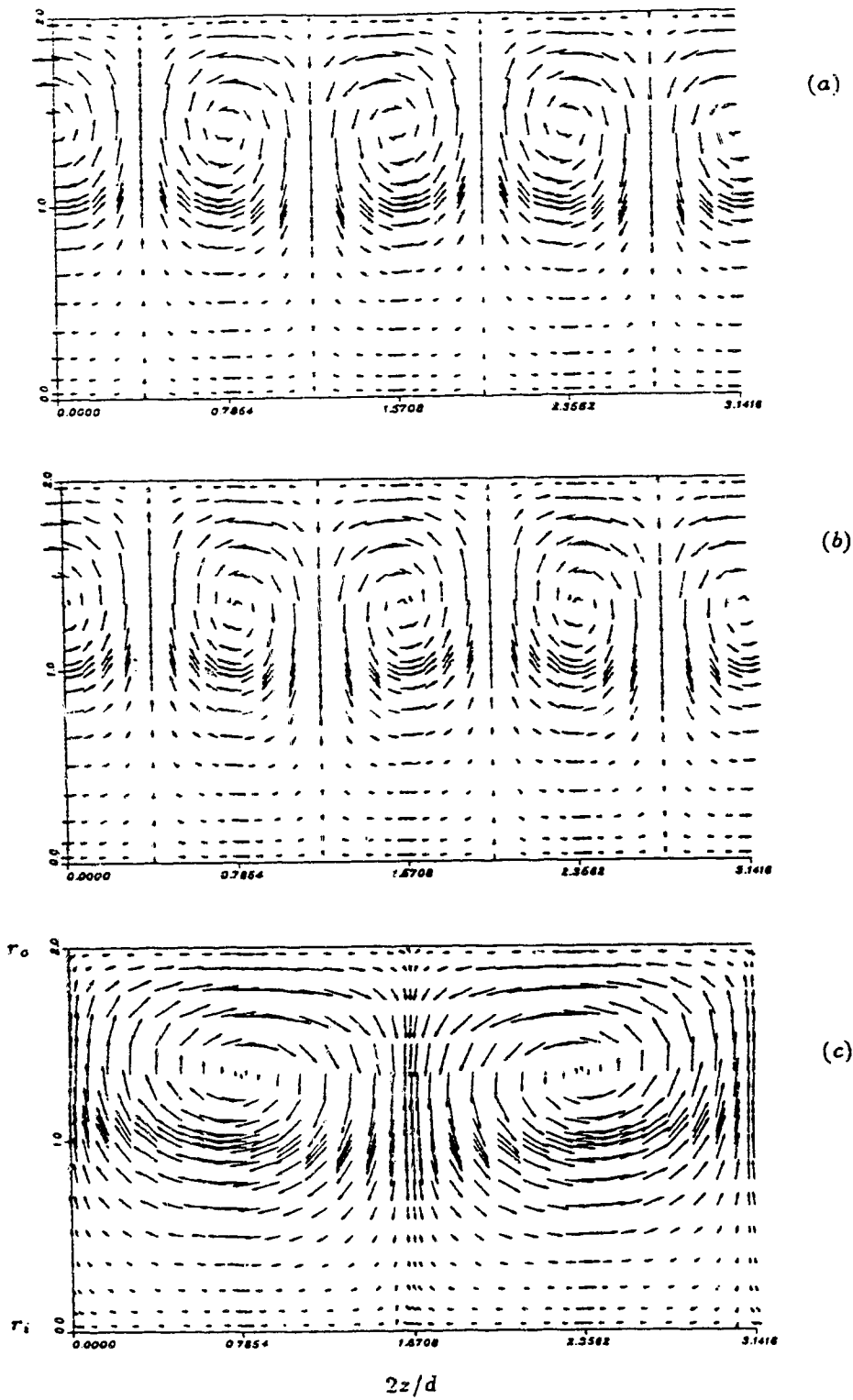


FIGURE 3.10. For caption see facing page.

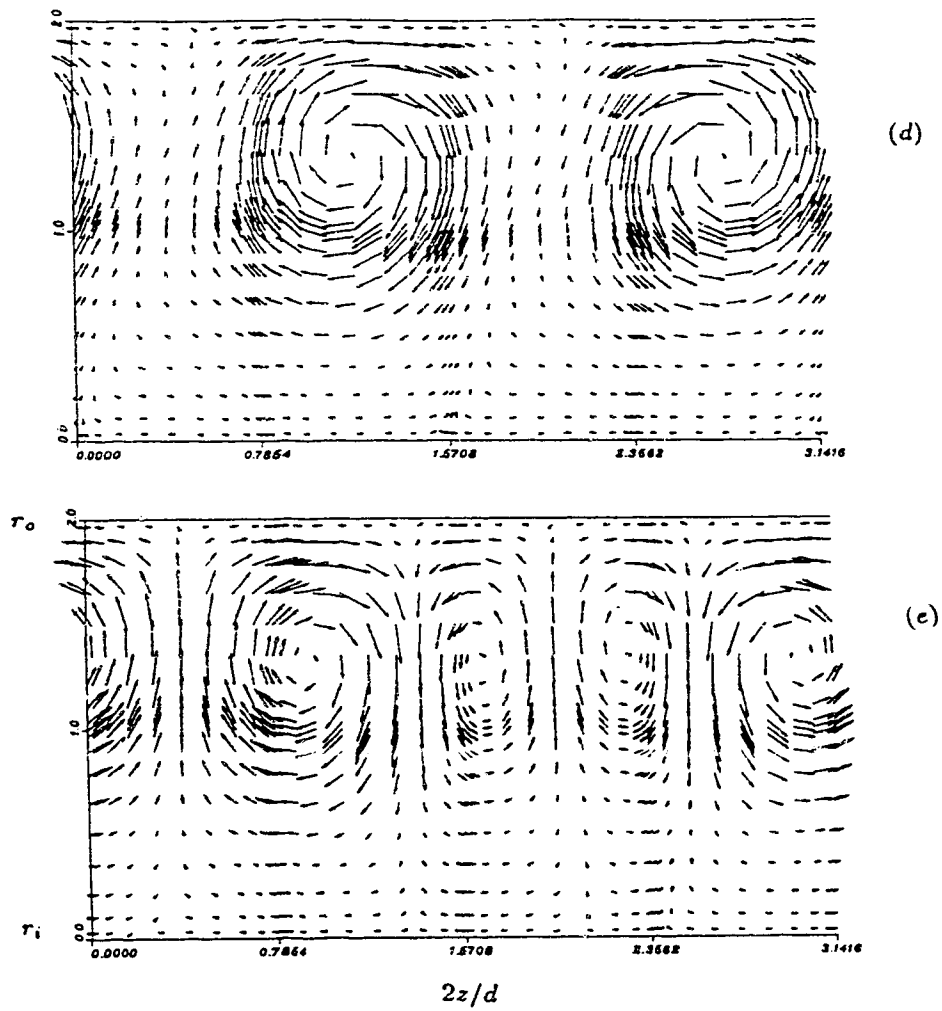


FIGURE 3.10. Base Dean vortices and the related perturbation in figure 3.9 are projected onto the $(r-z)$ plane at $\theta = 1.26$ (a & c) and $\theta = 4.26$ (b & d). (e) shows (b) +50% of (d).

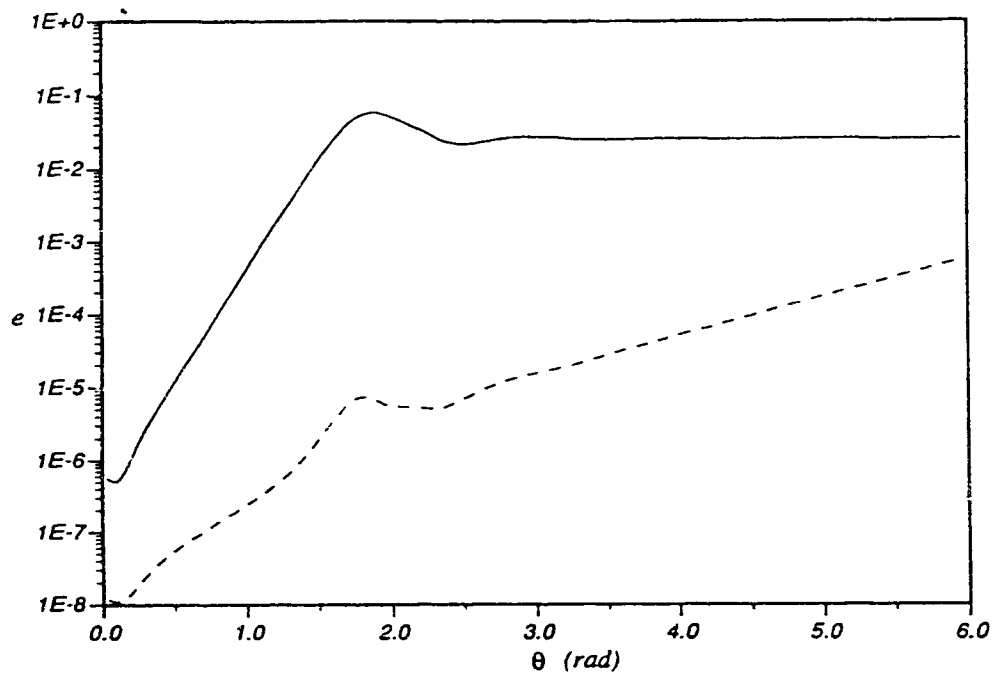
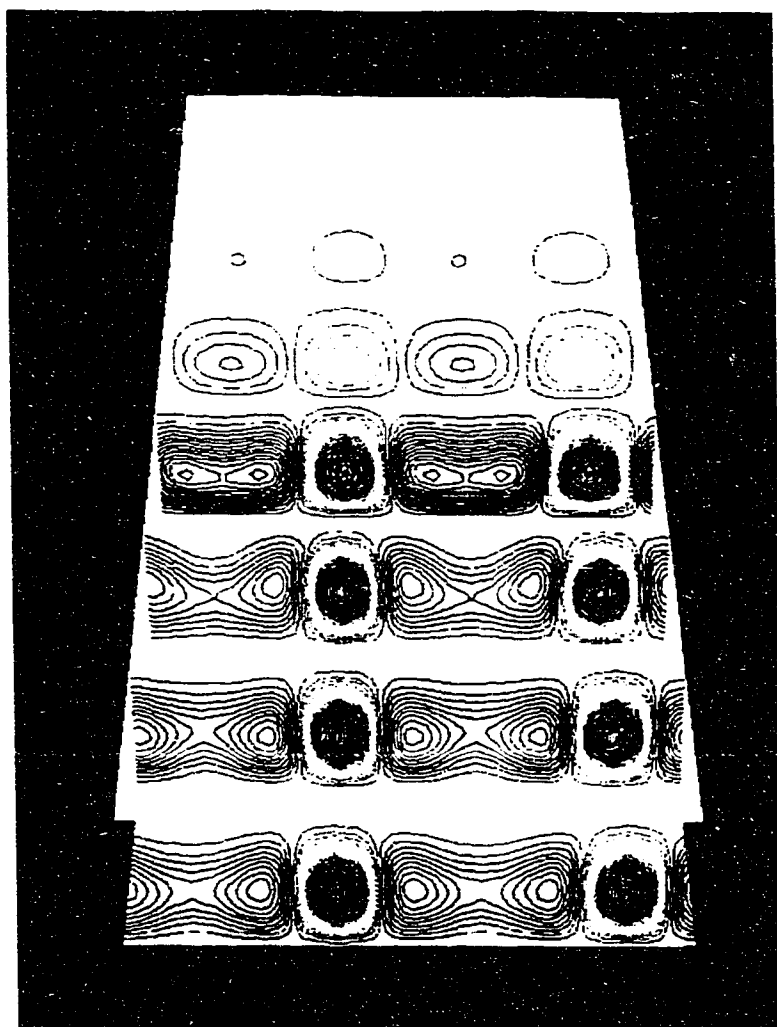
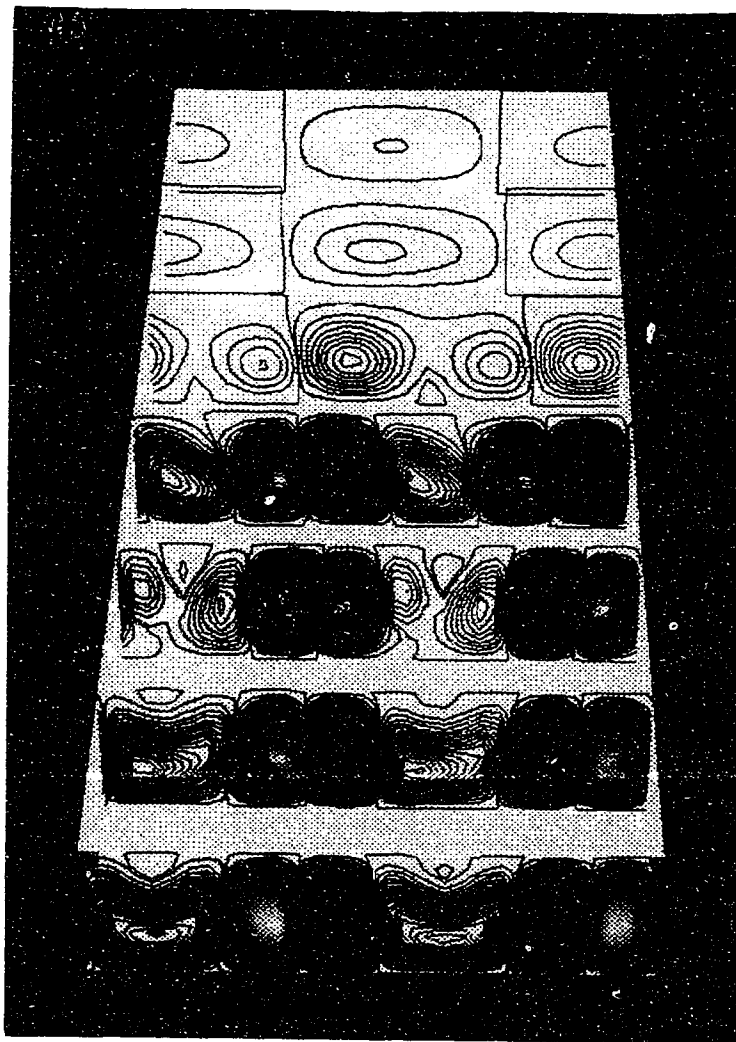


FIGURE 3.11. Spatial energy growths of the base Dean vortices $\alpha = 2.0$ (—) and the related perturbation $\beta = 1.0$ of spanwise secondary instability (----) in a curved channel $\gamma = 0.975$ at $Re = 2.0Re_c$.



(a)

FIGURE 3.12. For caption see facing page.



(b)

FIGURE 3.12. Contours of the velocity components (a) u_r^0 of the base Dean vortices and (b) u_r' of the related perturbation in figure 3.11 are shown in cross-stream planes from the streamwise location $\theta = 0.26$ to 3.26 rad with $\Delta\theta = 0.25$ rad. The inner wall is above the outer wall and the flow proceeds downstream from top to bottom.

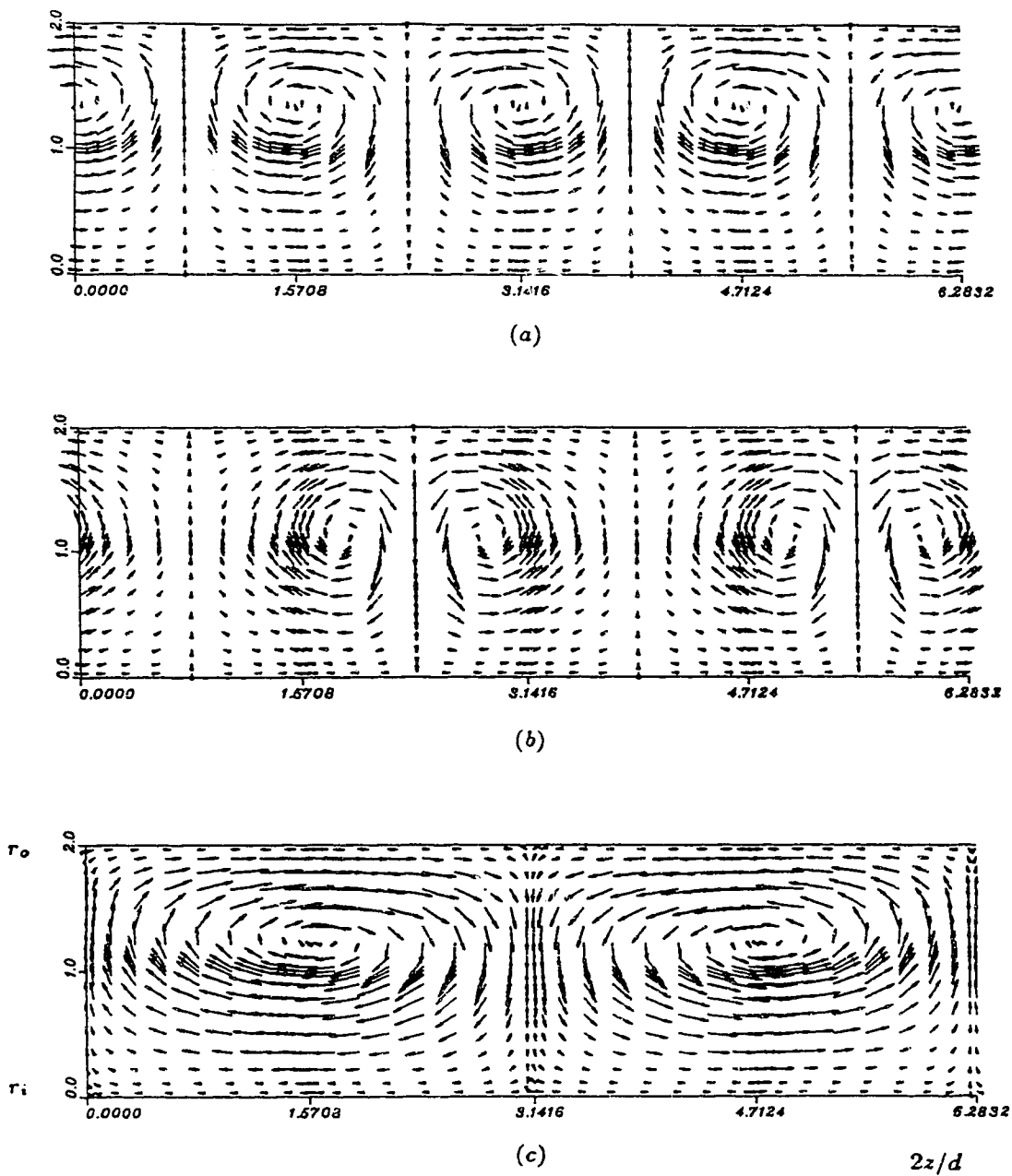


FIGURE 3.13. For caption see facing page.

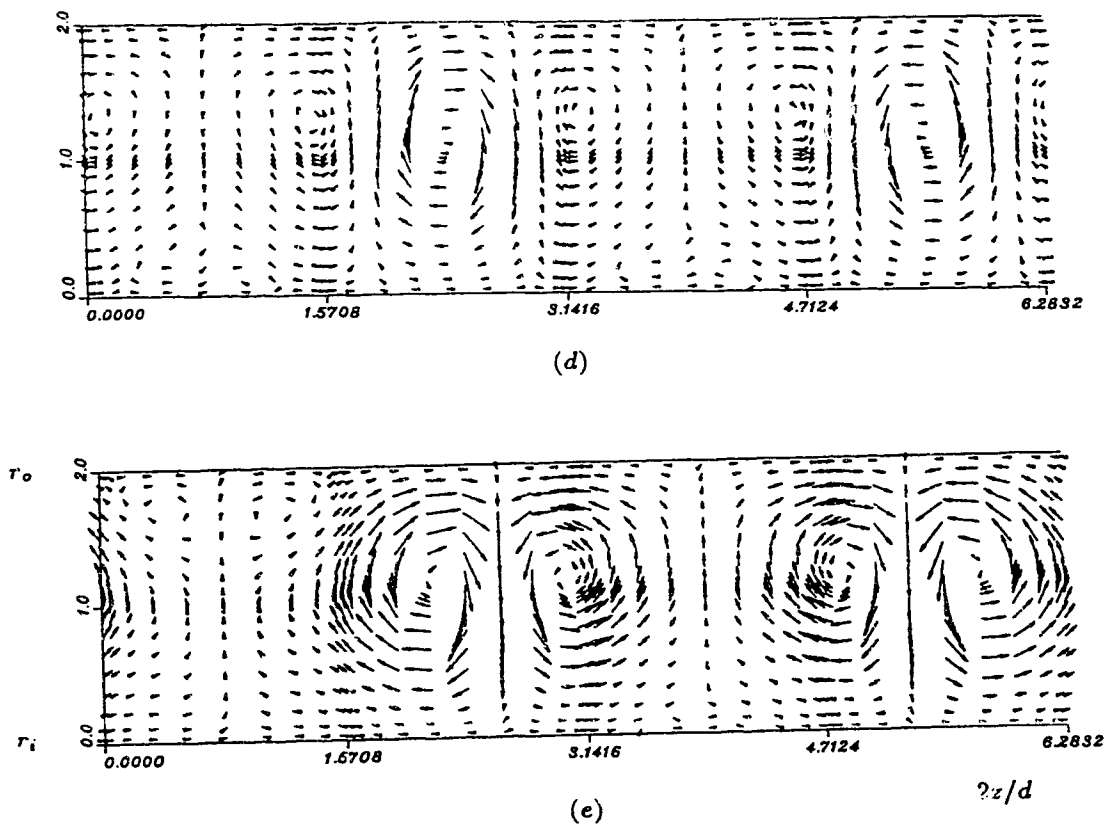


FIGURE 3.13. Base Dean vortices and the related perturbation in figure 3.11 are projected onto the $(r-z)$ plane at $\theta = 0.76$ (a & c) and $\theta = 3.26$ (b & d). (e) shows (b) +100% of (d).

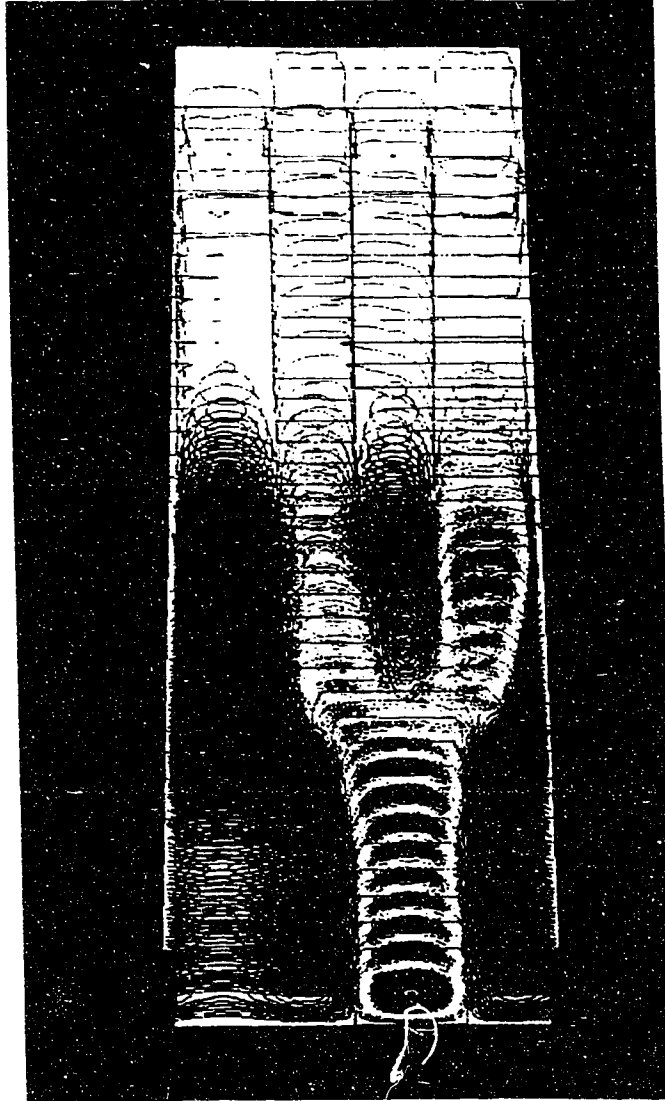


FIGURE 3.14. Contours of the velocity component u_r of developing Dean vortices is shown in cross-stream planes from the streamwise location $\theta = 0.16$ to 6 rad with $\Delta\theta = 0.15$ rad in a curved channel $\gamma = 0.975$ at $Re = 2.0Re_c$. The simulation is started with $\alpha = 4.0$, $\beta = 2.0$ and $\epsilon = 0.08$ in equation (3.12). Before the vortex merging at $\theta = 4.26$, the wavenumber of the vortices is $\alpha = 4.0$. The inner wall is above the outer wall and the flow proceeds downstream from top to bottom.

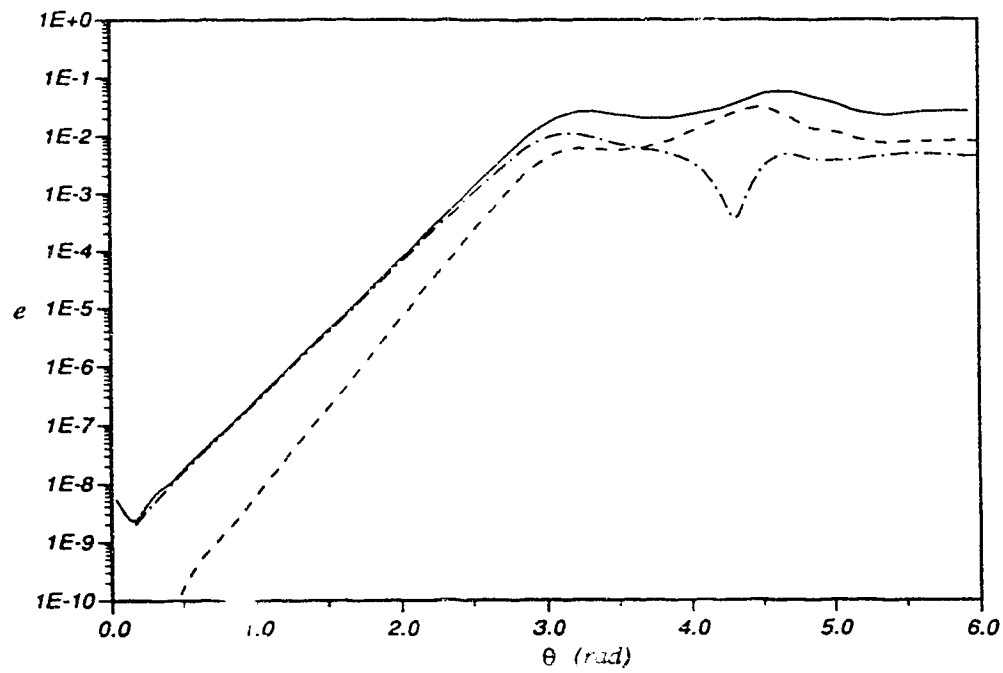
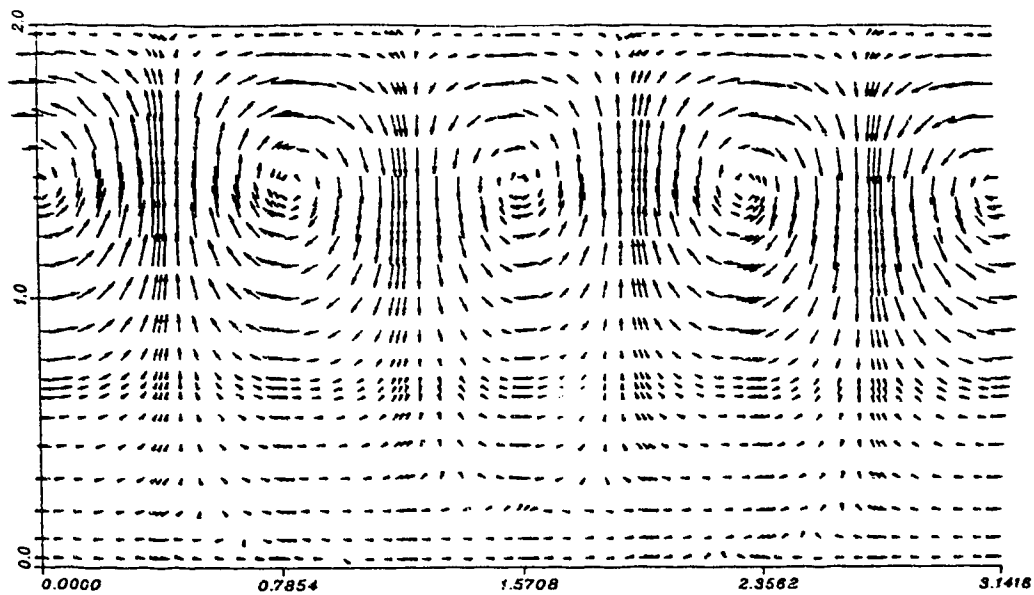
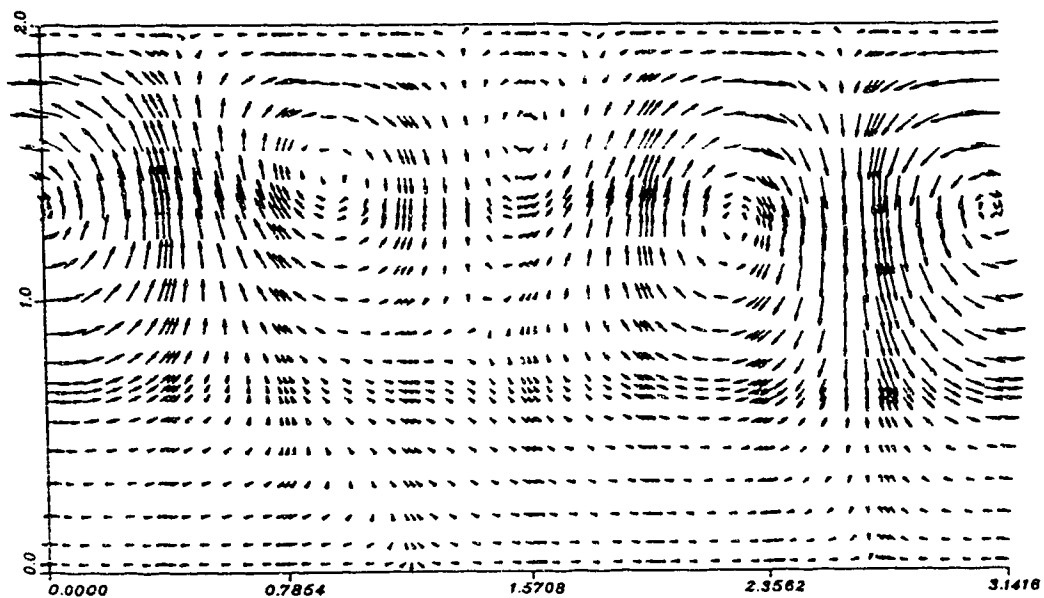


FIGURE 3.15. Spatial variation of the total energy (—) and the energy in the first (----) and the second (- · -) spanwise Fourier modes of the Dean vortices in figure 3.14.



(a)



(b)

FIGURE 3.16. For caption see facing page.

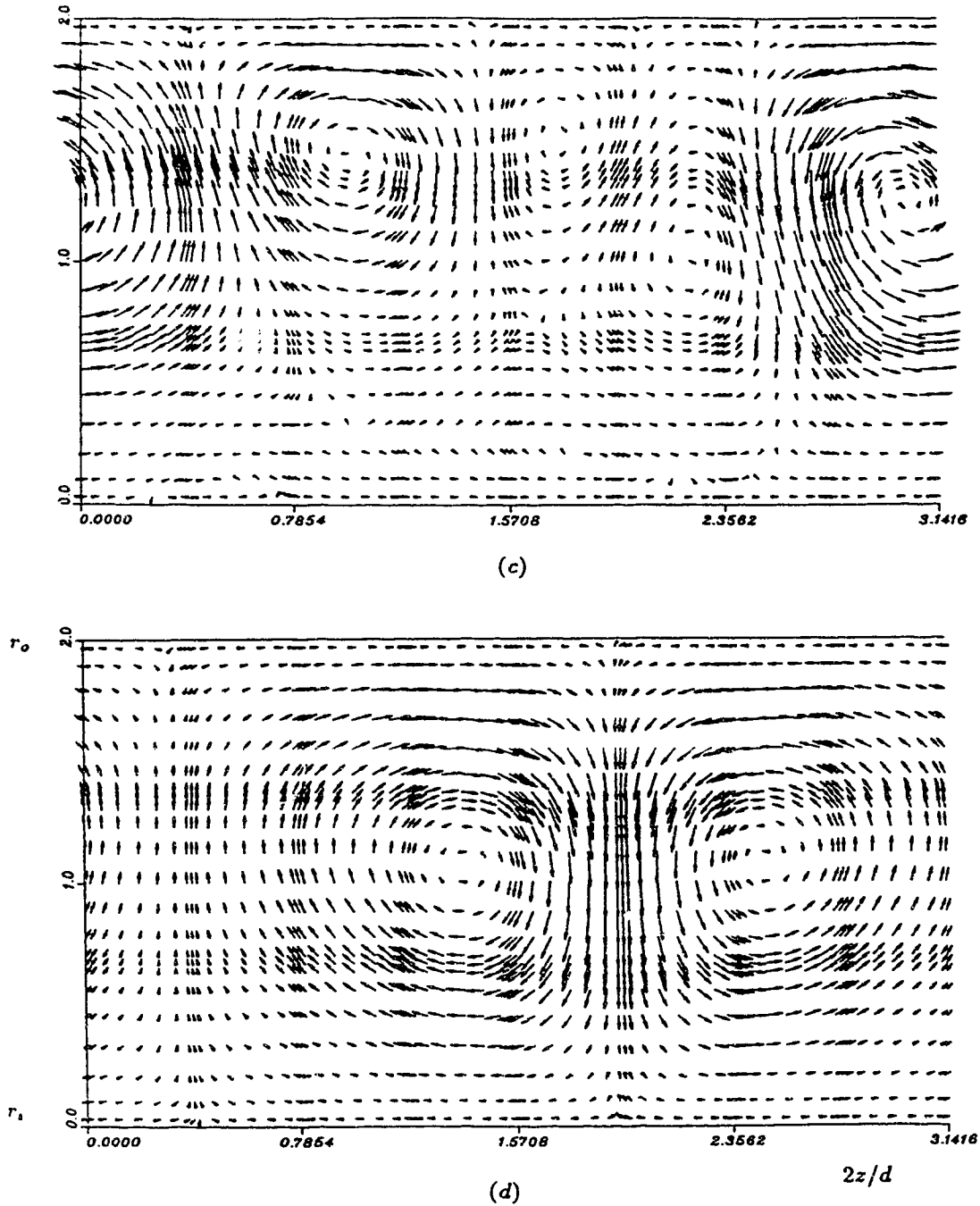


FIGURE 3.16. Dean vortices of figure 3.14 are projected onto the $(r-z)$ plane at (a) $\theta = 1.51$; (b) $\theta = 3.01$; (c) $\theta = 3.76$ and (d) $\theta = 4.81$ rad.

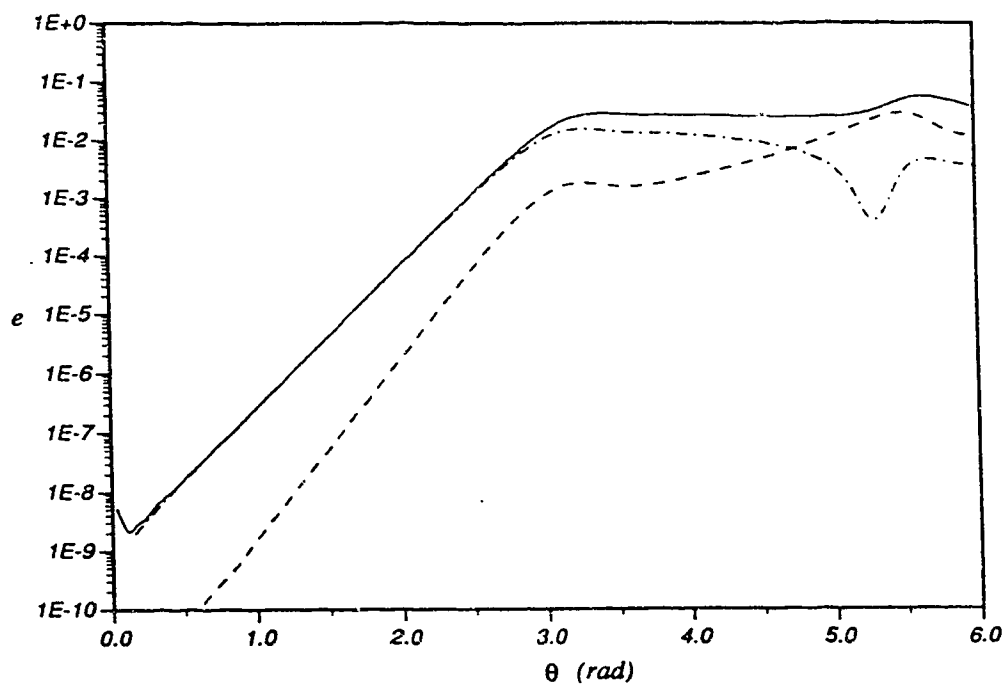


FIGURE 3.17. Energy of a flow similar to that in figure 3.15 but with $\epsilon = 0.05$ in equation (3.12).

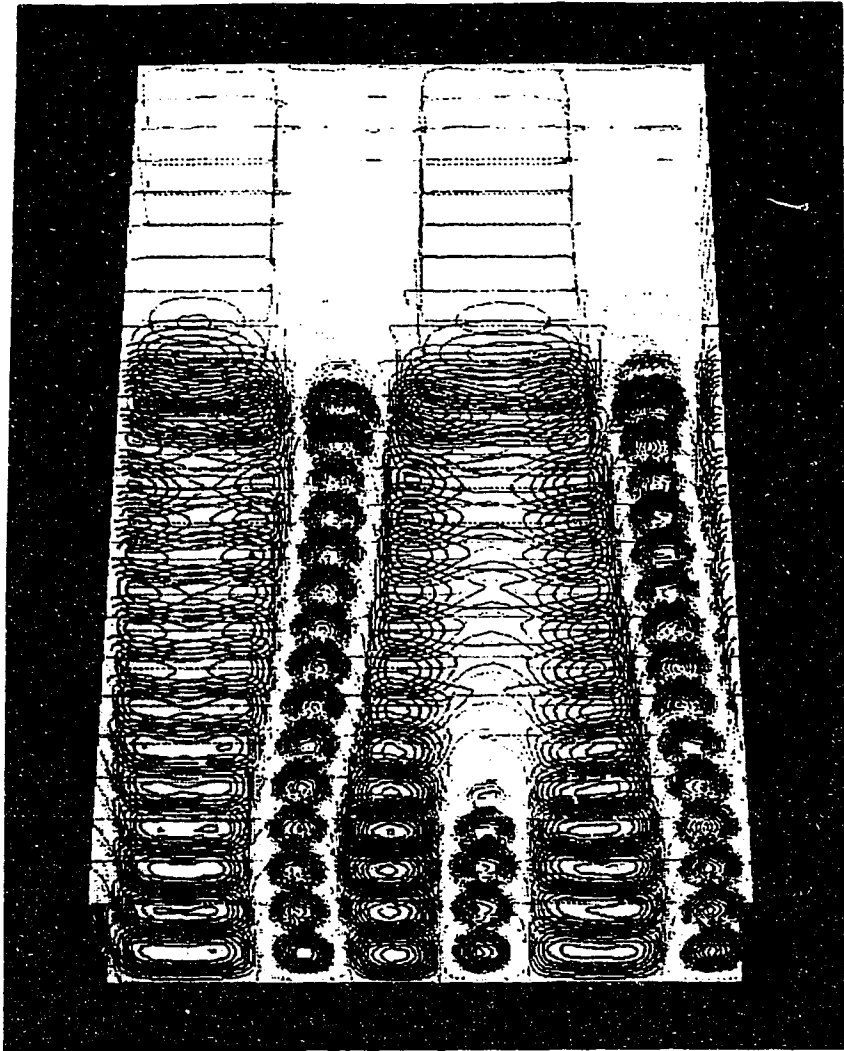


FIGURE 3.18. Contours of the velocity component u_r of developing Dean vortices is shown in cross-stream planes from the streamwise location $\theta = 0.255$ to 6 rad with $\Delta\theta = 0.25$ rad in a curved channel with $\gamma = 0.975$ at $Re = 2.186Re_c$. The simulation is started with $\alpha = 2.0$, $\beta = 3.0$ and $\epsilon = 0.25$ in equation (3.12). Before the vortex splitting at $\theta = 4.0$, the wavenumber of the vortices is $\alpha = 2.0$. The inner wall is above the outer wall and the flow proceeds downstream from top to bottom.

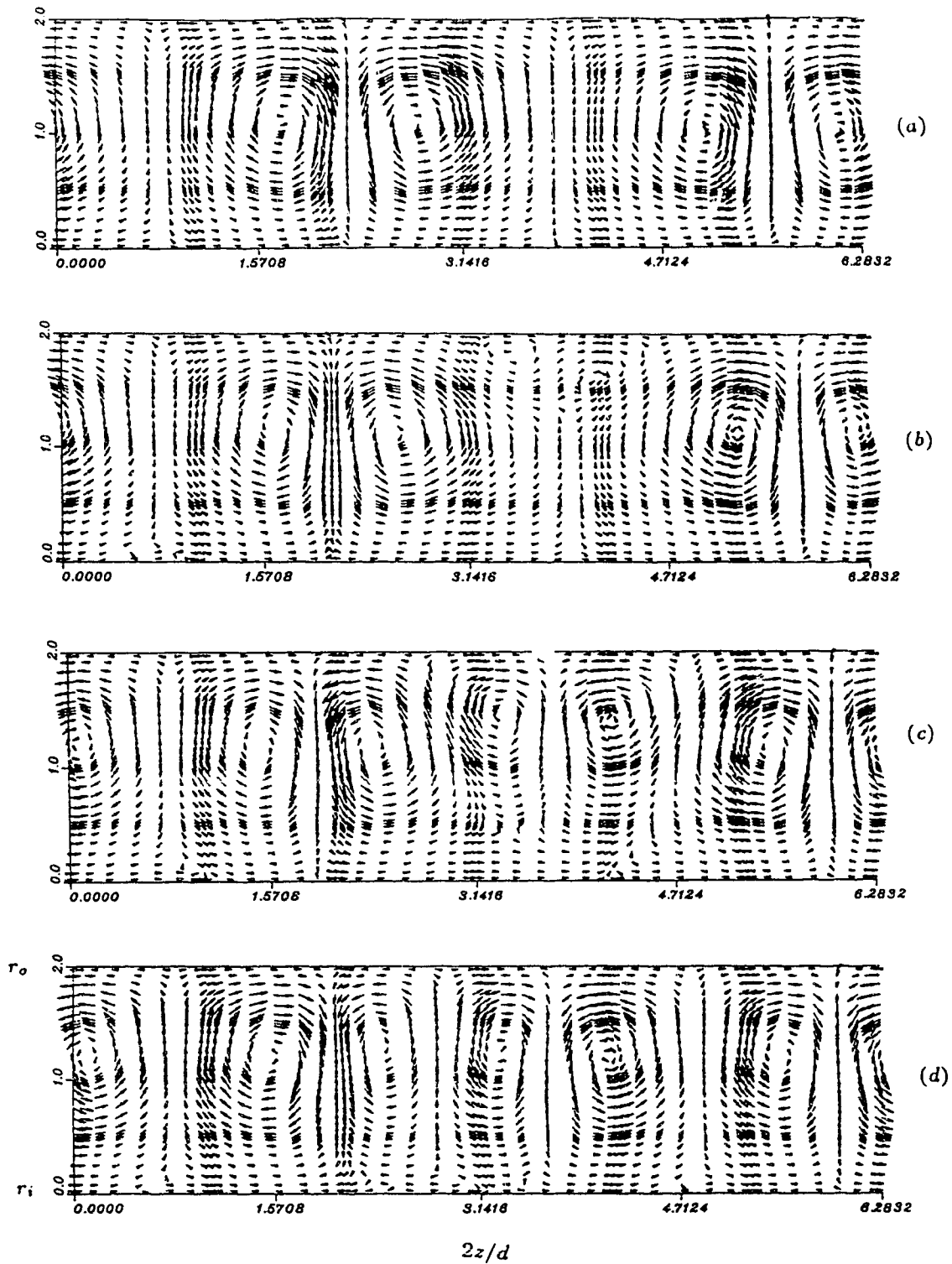


FIGURE 3.19. Dean vortices of figure 3.18 are projected onto the $(\tau - z)$ plane at (a) $\theta = 2.5$; (b) $\theta = 4.0$; (c) $\theta = 5.0$ and (d) $\theta = 6.0$ rad.

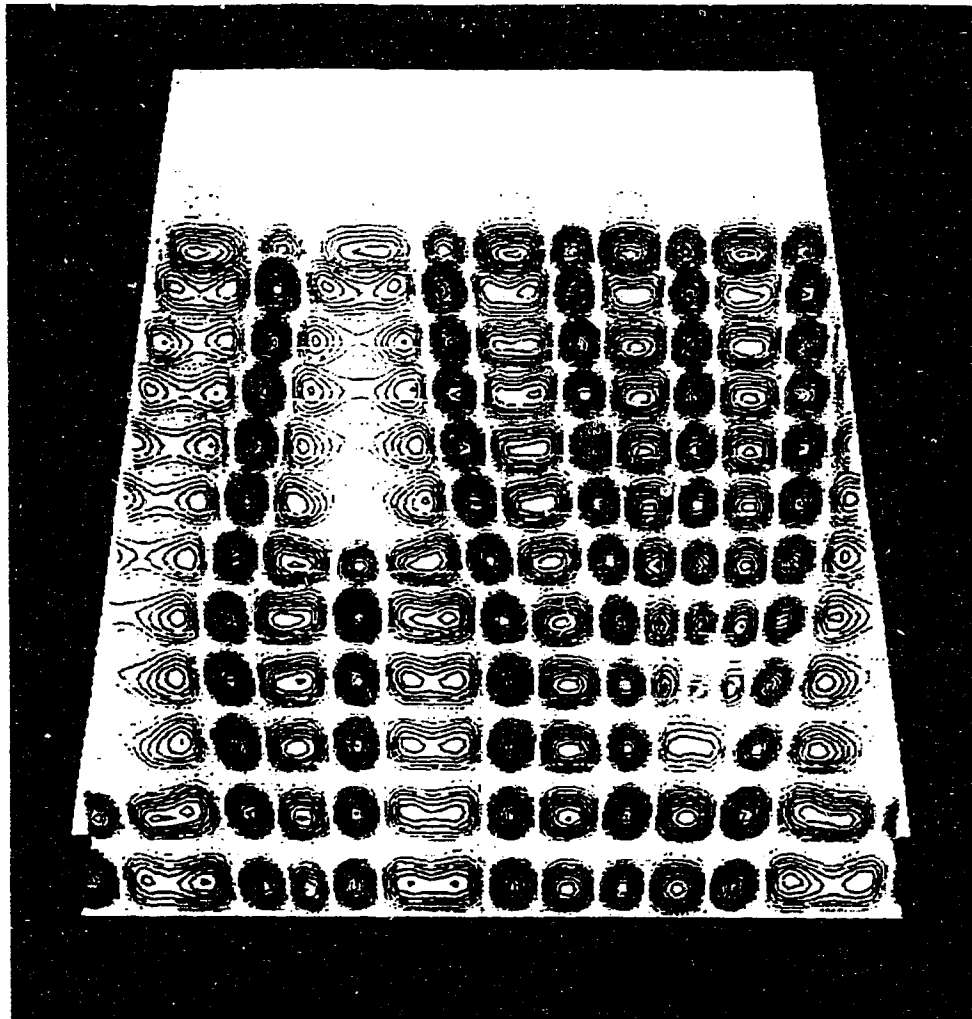


FIGURE 3.20. Contours of the velocity component u_r of developing Dean vortices is shown in cross-stream planes from the streamwise location $\theta = 0.5$ to 7.5 rad with $\Delta\theta = 0.5$ rad in a curved channel $\gamma = 0.975$ at $Re = 2.186Re_c$. The simulation is started with $\alpha = 3.0$ for the right three vortex pairs and $\alpha = 2.5$ for the left two vortex pairs. The inner wall is above the outer wall and the flow proceeds downstream from top to bottom.

References

- Alfredsson, P.A. & Persson, H. 1989 Instabilities in channel flow with system rotation. *J. Fluid Mech.*, **202**, 543–557.
- Baker, A.J. 1983 *Finite Element Computational Fluid Mechanics*. McGraw-Hill, New York.
- Bertolotti, F.P., Herbert, Th. & Spalart, P.R. 1990 Linear and nonlinear stability of the Blasius boundary layer. *J. Fluid Mech.*, submitted.
- Blackwelder, R.F. 1983 Analogies between transitional and turbulent boundary layers. *Phys. Fluids*, **26**, 2807–2815.
- Bottaro A., Matsson O.J.E., & Alfredsson P.H. 1991 Numerical and experimental results for developing curved channel flow. *Phys. Fluids A*, **40**, 1473–1476.
- Cantwell, B.J., Coles, D.E. & Dimotakis, P.E. 1978 Structure and entrainment in the plane of symmetry of a turbulent spot. *J. Fluid Mech.*, **87**, 641–672.
- Carey G.F. & Oden J.T. 1983 *Finite Elements: A Second Course*. Prentice-Hall, Inc., Englewood Cliffs, New Jersey
- Carey G.F. & Oden J.T. 1983 *Finite Elements: Fluid Mechanics*. Prentice-Hall, Inc., Englewood Cliffs, New Jersey
- Day, H.P., Herbert Th. & Saric W.S. 1990 Comparing local and marching analyses of Görtler instability. *AIAA Journal*, **28**(6), 1010–1015.
- Eckhaus, W. 1965 *Studies in nonlinear stability theory*. Springer, New York.
- Finlay, W.H., Keller, J.B. & Ferziger, J.H. 1988 Instability and transition in curved channel flow. *J. Fluid Mech.*, **194**, 417–456.
- Fletch, C.A.J. 1988 *Computational Techniques for Fluid Dynamics*, Vol. II. Springer-Verlag.
- Floryan J.M. & Saric W.S. 1984 Wavelength selection and growth of Görtler vortices. *AIAA Journal*, **22**(11), 1529–1538.

Guo Y. & Finlay, W.H. 1991 Splitting, merging and wavelength selection of vortices in curved and/or rotating channel flow due to Eckhaus instability. *J. Fluid Mech.*, **228**, 661-691.

Guo Y. & Finlay, W.H. 1992 Spanwise secondary instability of spatially develop vortices. Part 2. Irregularity and wavelength selection of Görtler vortices. *J. Fluid Mech.*, submitted.

Hall, P. 1983 The linear development of Görtler vortices in growing boundary layers. *J. Fluid Mech.*, **130**, 41-58.

Huerre P. & Monkewitz P.A. 1990 Local and global instabilities in spatially developing flows. *Annual Review of Fluid Mechanics*, **22**, 473-537.

Kim, J. & Moin, P. 1985 Application of a fractional-step method to incompressible Navier-Stokes equations. *J. Comput. Phys.*, **59**, 308-323.

Lee, K. & Liu J.T.C. 1992 On the growth of mushroomlike structures in nonlinear spatially developing Görtler vortex flow. *Phys. Fluids A*, **4**(1), 95-103.

Kleiser, L. & Schumann, U. 1984 Spectral simulation of the laminar turbulent transition process in plane Poiseuille flow, in *Spectral Methods for Partial Differential Equations*, Voigt, R.G., Gottlieb, D. and Hussaini, M.Y. (eds.). SIAM, 1984, 141.

Ligrani, P.M. 1991 private conversion.

Ligrani, P.M., Finlay, W.H., Fields, W.A., Fuqua, S.J. & Subramanian, C.S. 1992 Features of wavy vortices in a curved channel from experimental and numerical studies. *Phys. Fluids A*, in press.

Ligrani, P.M., Longest, J.E., Fields, W.A., Kendall, M.R., Fuqua, S.J. & Baun, L.R. 1992 Initial development and structure of Dean vortex pairs in a curved rectangular channel including splitting, merging and spanwise wavenumber selection. *Phys. Fluids A*, submitted.

Ligrani, P. & Niver, R.D. 1988 Flow visualization of Dean vortices in a curved

channel with 40 to 1 aspect ratio. *Phys. Fluids*, **31**,3605–3618.

Maday Y. & Patera, A.T. 1989 Spectral element methods for the incompressible Navier-Stokes equations, in *State-of-The-Art Surveys on Computational Mechanics*, ASME, edited by Noor, A.T., & Oden, J.T., 71–143.

Matsson, J.O.E. & Alfredsson, P.H. 1990 Curvature- and rotation- induced instabilities in channel flow. *J. Fluid Mech.*, **202**,543–557.

Matsson, O.J.E. & Alfredsson P.H. 1992 Experiments on instabilities in curved channel flow. *Phys. Fluids A*, *submitted*.

Patankar & Spalding 1972 A Calculation procedure for heat, mass and momentum transfer in three-dimensional parabolic flows. *Int. J. Heat Mass Transfer*, **15**, 1787–1806

Patera, A.T. 1984 A spectral element methods for fluid dynamics: laminar flow in a channel expansion. *J. Comp. Phys.*, **54**, 468–488.

Riecke, H. & Paap, H. 1986 Stability and wave-vector restriction of axisymmetric Taylor vortex flow. *Physical Review A* **33**, 547–553.

Rónquist, E.M. 1988 Optimal spectral element methods for the unsteady three-dimensional incompressible Navier-Stokes equations. *Ph.D thesis*, Massachusetts Institute of Technology.

Rubin, S.G., Khosla, P.K. & Saari, S. 1977 Analysis of Global pressure relaxation for flows with strong interaction and separation. *Computers and Fluids*, **11**, 281–306

Sabry, A.S. 1988 Numerical computation of the nonlinear evolution of Görtler vortices. *Ph.D Thesis*, Brown University.

Sabry, A.S. & Liu, J.T.C. 1991 Longitudinal vorticity elements in boundary layers: nonlinear development from initial Görtler vortices as a prototype problem. *J. Fluid Mech.*, **231**,615–663.

Swearingen J.D. & Blackwelder R.F. 1987 The growth and breakdown of streamwise vortices in the presence of a wall. *J. Fluid Mech.*, **182**, 255–290.

Yang, K.S. & Kim J. 1991 Numerical investigation of instability and transition in rotating plane Poiseuille flow. *Phys. Fluids A*, 3(4), 633–641.

CHAPTER 4

Spanwise secondary instability of spatially developing vortices.

Part 2. Irregularity and wavelength selection of Görtler vortices

4.1 Introduction

¹In Part 1 of this study (Guo & Finlay, 1992), we developed a Legendre spectral-element based numerical method to study the secondary instability of spatially developing flows with respect to spanwise perturbations (spanwise secondary instability). As an application, Dean vortices found in curved channels were studied. In Part 2 of this study, we will numerically examine the linear and nonlinear aspects of the spanwise secondary instability of spatially developing nonlinear Görtler

¹A version of this chapter has been submitted to J. Fluid Mech. for publication.

vortices and the effect of this instability on wavenumber selection and nonlinear development of these vortices.

The flow geometry for Görtler vortices is shown in figure 4.1. The streamwise and spanwise directions of the flow are given by θ and z respectively. We will restrict ourselves to the case of constant wall curvature, i.e. the radius of the wall, R , is constant. The freestream velocity is U_∞ . The Görtler number at the downstream distance $x = R\theta$ from the leading edge is defined as

$$G\ddot{o} = \frac{U_\infty \delta_m}{\nu} \left(\frac{\delta_m}{R} \right)^{\frac{1}{2}}$$

where δ_m is the momentum thickness of a Blasius boundary layer. The wall curvature can also be measured by the ratio $\gamma = (R - \delta_{.99})/R$, where $\delta_{.99}$ is the Blasius boundary layer thickness at $u_\theta = 0.99U_\infty$. In this study, the wavelength of Görtler vortices is measured by the dimensionless parameter

$$\Lambda = \frac{U_\infty \lambda}{\nu} \left(\frac{\lambda}{R} \right)^{\frac{1}{2}}$$

where λ is the dimensional wavelength in the spanwise direction. Both Λ and λ are constant in the streamwise direction.

Ever since Görtler (1940) predicted the existence of a secondary vortex-type motion in boundary layers over concave surfaces, many efforts have been made both experimentally and theoretically toward understanding these vortices. On a concave wall with small curvature, Görtler vortices provide disturbances for three-dimensional Tollmien-Schlichting waves and thus promote early transition. When the wall curvature is strong (as in this study), Görtler vortices develop significantly faster than Tollmien-Schlichting waves. The boundary layer will then be dominated by streamwise counter-rotating vortices and the transition toward turbulence will be characterized by the breakdown of these vortices. A better understanding of these vortices may lead to a better understanding of many flows including the flows near the concave surfaces of turbine blades and aerofoils. Recently, attention has been

paid to the similarity between Görtler vortices and the counter-rotating streamwise vortices found in most transitional and turbulent wall bounded shear flows (cf. Swearingen & Blackwelder 1987 for a review). Some studies suggest that these vortices may be due to a Görtler instability resulting from streamwise curvature (Cantwell, Coles & Dimotakis, 1978). Thus, Görtler vortices offer a simple model for studying the dynamics which govern the vortices in transitional and turbulent wall bounded shear layers.

A review of early theoretical works on Görtler vortices done by Hammerlin (1955), Smith (1955), Tobak (1971) and Shultz-Grunow *et al.* (1973) can be found in Herbert (1976). Due to the difficulties associated with the nonparallel nature of the problem, there is wide disagreement even among some recent works. Floryan & Saric (1984) solved the stability equations which include nonparallel effects using a local method similar to the one used by Ragab & Nayfeh (1981). Their method gives a unique neutral stability boundary. From the wavenumbers which have the largest growth rate they propose a wavenumber selection mechanism which can explain the experimental observations of Bippes (1972) well, but which has some problems with the data from Tani (1962) and Tani & Sakagami (1962). Some recent experimental observations (Winoto & Crane 1980, Swearingen & Blackwelder 1987) also show some differences from this wavenumber selection theory.

Using a global marching approach, Hall (1983) solved the same problem and proposed that the neutral stability boundary is non-unique. His results show that the location of the first neutral point depends sensitively on both how and where a boundary layer is disturbed. To clarify this issue Day, Herbert & Saric (1990) made a comparison between the local method and global marching. They conclude that although the first neutral point cannot be defined uniquely using global marching, a short distance from the leading edge the results from the global marching converge to a unique asymptotic solution which is quite close to that given by the local method.

Most of the knowledge about the nonlinear evolution of Görtler vortices and their secondary instabilities is provided by experimental observations (Aihara 1962, Tani 1962, Tani & Sakagami 1962, Tani & Aihara 1969, Bippes 1972, Aihara & Koyama 1980, Aihara *et al.* 1984). More recently, Swearingen & Blackwelder (1987) detailed these aspects of Görtler vortices using smoke-wire visualization and multiple probe hot wire rakes. Relatively fewer theoretical efforts exist and most of these rely heavily on simplifications. Among them are Aihara (1976) and Hall (1982). Recently, a more detailed theoretical and numerical picture of nonlinear Görtler vortices has begun to appear (Sabry 1988, Sabry & Liu 1991, Hall 1988, Liu & Domaradzki 1990, Hall 1990). Using a global marching method and a combination of spectral methods and a finite difference scheme, Hall (1988) was able to solve the stability equations governing the nonlinear evolutions of Görtler vortices. But neither the flow field of Görtler vortices nor a comparison with existing experimental measurements was given in his paper. In his computations, only four Fourier modes were used in the spanwise direction. From our experience with spectral methods, this resolution is not enough to provide the details of the flow pattern.

The temporal evolution of nonlinear Görtler vortices was studied by Sabry (1988) and Sabry & Liu (1991) using a temporal theory and a finite difference scheme. For the first time, the quantitative comparison of nonlinear Görtler vortices between numerical results and experimental observations (Swearingen & Blackwelder, 1987) was given. Since Sabry's study is based on temporal theory, the picture of spatial nonlinear evolution is still incomplete. Very recently, Lee & Liu (1992) studied spatially developing Görtler vortices by solving the parabolized three-dimensional Navier-Stokes equations, thus unveiling some of the nonlinear details of spatially developing Görtler vortices.

Because of the difficulties in getting accurate representations of nonlinear Görtler vortices, so far the theoretical studies of secondary instability are less convincing. For example, using the streamwise component of temporally evolving

Görtler vortices (Sabry, 1988) as the base flow, Yu & Liu (1991) presented results on the instability of Görtler vortices to streamwise perturbations which causes waviness of the Görtler vortices. The same type of instability was also studied by Liu & Domaradzki (1990) through time-dependent three-dimensional numerical simulations with the help of a parallel flow assumption. To our knowledge, no work has been done on the secondary instability with respect to spanwise perturbations. In the case of Dean vortices, this type of instability causes splitting and merging of vortices (Guo & Finlay, 1992). The study of this type of instability is essential to a better understanding of the dynamics of Görtler vortices.

In this paper, using spatial instability theories and three-dimensional numerical simulations developed in Guo & Finlay (1992), we study the spatial development of nonlinear Görtler vortices and their secondary instability with respect to spanwise perturbations on a concave wall with strong curvature. We examine the roles of primary instability and spanwise secondary instability in the wavenumber selection process and their effects on the nonlinear evolution of Görtler vortices. Since both Görtler vortices and Dean vortices are caused by streamwise curvature due to centrifugal instabilities and share various similarities, we compare and contrast the features of these two types of vortices.

We first present our results on the primary instability and spatial development of nonlinear Görtler vortices in §4.2 and §4.3. In §4.4, we present the spanwise secondary instability of spatially developing Görtler vortices. Vortex splitting and merging caused by the nonlinear development of this type of secondary instability are simulated in §4.5. A discussion on the possible forms of naturally occurring perturbations near the leading edge in some experiments and their role in the formations of Görtler vortices is given in §4.6.

4.2 Primary instability: Görtler vortices

As mentioned in Guo & Finlay (1992), when dealing with primary instability (Görtler instability), the stability theory and the methods we use in this study are equivalent to Hall's global marching method (1983). Though these types of methods do not give a unique neutral point (Hall 1983 and Day *et al.* 1990), they yield asymptotic solutions which are comparable to the results from local theory (Floryan & Saric, 1984) a short distance downstream from the leading edge. Figure 4.2 shows the typical pattern of the (energy) growth rate σ for different wavelength parameters Λ obtained by setting the base flow \mathbf{u}^0 to be Blasius boundary layer in the stability code (3.8-3.10). The growth rate σ is non-dimensionalized by the local streamwise distance x from the leading edge. All runs are started at $G\ddot{o} = 0.8256$ using $(-v_B, 0, 0)$ as the initial eigenfunctions (both real and imaginary parts), where v_B is the vertical component of Blasius boundary layer flow. For these types of initial perturbations, the growth rates σ are always positive. Different initial conditions only affect the growth rates for $G\ddot{o} < 2.8$. For a given $G\ddot{o}$, the variation of the growth rate σ with Λ is similar to that given by Floryan & Saric (1984) using a local theory. For example the most unstable Λ is the one near $\Lambda = 210$ for most $G\ddot{o}$; the growth rate σ decreases for $\Lambda < 210$ or $\Lambda > 210$, as is shown in figure 4.2, and does not differ much for $175 < \Lambda < 400$.

Over a short distance downstream from the leading edge ($G\ddot{o} < 1.5$), the growth rate σ varies considerably for different perturbations and can be very large for some forms of perturbations. However, since the streamwise distance to this location is short, the perturbations do not have enough time to develop into high energy levels. A short distance from the leading edge, the growth rate σ only depends on wavelength parameter Λ , local Görtler number $G\ddot{o}$ and the distance from the leading edge x . So we do not believe the exact location of the neutral stability boundary plays an important role in the development of nonlinear Görtler vortices

on a concave wall with strong curvature. The energy level of initial perturbations near the leading edge and the growth rate for $G\ddot{o} > 1.5$ are more important.

4.3 Spatial development of nonlinear Görtler vortices

As in the case of Dean vortices (cf. Guo & Finlay, 1992), the spatial development of nonlinear Görtler vortices depends both on the energy level of initial perturbations near the leading edge and the growth rate σ . Through the manipulation of the energy level of the perturbations near the leading edge, Görtler vortices with strength comparable to those observed by Swearingen & Blackwelder (1987) can be produced by our simulation code. Figure 4.3 shows the spatial development of the streamwise velocity u_θ of Görtler vortices with spanwise wavelength $\lambda = 1.8\text{cm}$ on a concave wall with radius $R = 3.2\text{m}$. The free stream velocity U_∞ is 5m/s and the kinematic viscosity ν is $14.5 \times 10^{-6}\text{m}^2/\text{s}$. The simulation is started at a distance $x = 8\text{cm}$ from the leading edge using the initial flow condition $\mathbf{u}^0 = (0.4v_B \sin(2\pi z/\lambda), u_B, 0)$; v_B and u_B are the vertical and streamwise components of Blasius boundary layer flow. The justification of the use of such initial flow condition will be discussed in §4.6. Different initial conditions can also give Görtler vortices of the same strength. In figure 4.3, the computational grid extends to 8cm in the r direction. In the z direction, periodic boundary conditions are used.

Swearingen & Blackwelder (1987) published experimental measurements of Görtler vortices with the same parameters as figure 4.3. The spatial development of Görtler vortices from our simulation results are quite comparable to the time averaged measurements given by Swearingen & Blackwelder (their figure 11). The contour patterns are comparable for the downstream distance up to $x = 100\text{cm}$. For $x > 100\text{cm}$, the Görtler vortices begin to develop into time dependent wavy vortices in the experiments of Swearingen & Blackwelder and the vortices breakdown shortly afterwards.

Figure 4.4 shows a comparison of the streamwise velocity u_θ at different x with data from Swearingen & Blackwelder (1987). The simulation is started at $x = 12.8\text{cm}$ with the same initial flow condition as in figure 4.3. It can be seen the agreement is good up to $x = 90\text{cm}$. For $x \geq 100\text{cm}$, poor agreement may be due to the onset of waviness in the experiments. It could also be due to the difficulty associated with locating the center of the vortices in experiments, because we can see in figure 4.3(d) and (e) that a small spanwise shift away from the centers of the vortices produces velocity profiles that are quite different.

Figure 4.5 shows the growth of $|u_\theta - u_B|_{max}$ in figure 4.4 compared with the experimental measurements of Swearingen & Blackwelder. The difference between our results and the experimental measurements are minor, especially in the growth rate (the slope) for $x < 80\text{cm}$. The maximum streamwise velocity of the Görtler vortices from our simulations is always larger than in experimental measurements. This may be associated with the difficulty in measuring $|u_\theta|_{max}$ experimentally and the time averaged method used to produce the data. By lowering the energy level of the initial perturbations and increasing λ to 2.0cm , we can match the data from Swearingen and Blackwelder.

Also given in figure 4.5 is the linear growth prediction of Görtler vortices obtained from the stability code using the same parameters. The amplitude of the linear Görtler vortices is scaled to match the simulation code (since the perturbation level in a linear analysis is irrelevant). It can be seen that the growth of the Görtler vortices from the simulation code is well predicted by the stability code before the vortices reach the strongly nonlinear stage at $x > 60\text{cm}$. The disagreement for $x < 20\text{cm}$ is caused by the different streamwise locations used to start the simulation and the stability analysis. Since it is unlikely that the two codes have errors which make them give the same growth rates, this result serves as part of the verifications of the methods and codes used in this study.

The development of wall shear $\tau_w = \partial u_\theta / \partial \theta$ is given in figure 4.6. The simulation

is started with the same parameters as in figure 4.4. Again there is reasonable agreement between our results and the experimental measurements.

Sabry & Liu (1991) and Lee & Liu (1992) give a similar comparison with the experimental observations of Swearingen & Blackwelder (1987) using a temporal theory and spatial parabolized methods. In general, their results from temporally and spatially evolving Görtler vortices are quite similar to ours. Readers are referred to Sabry & Liu (1991) and Lee & Liu (1992) for more details on the nonlinear features of Görtler vortices, since this is not the main topic of this study.

4.4 Spanwise secondary instability of spatially developing Görtler vortices

Guo & Finlay (1992) show that the spanwise secondary instability of developing Dean vortices plays an important role in the wavelength selection process. This instability distorts the developing Dean vortices before they reach the fully developed stage and provides perturbation energy for the splitting and merging of vortices, which occur shortly after the Dean vortices reach the fully developed stage. To see if similar ideas apply to Görtler vortices, we next examine the spanwise secondary stability of developing Görtler vortices.

When the base flow develops from the Blasius boundary layer to Görtler vortices, its stability can be analyzed by marching the stability code together with the simulation code. Since Görtler vortices with large amplitude can only develop on a concave wall with strong curvature, all cases presented in this paper use a concave wall with radius $R = 3.2\text{m}$, freestream velocity $U_\infty = 5\text{m/s}$ and kinematic viscosity $\nu = 14.5 \times 10^{-6}\text{m}^2/\text{s}$. These parameters correspond to strong curvature and are also used by Swearingen & Blackwelder (1987) in their experiments. The initial flow condition used for the base flow \mathbf{u}^0 is

$$\mathbf{u}^0 = (\epsilon v_B \sin(2\pi z/\lambda), u_B, 0) \quad (4.1)$$

where u_B and v_B are the streamwise and vertical components of Blasius boundary layer flow and ϵ is used to adjust the initial energy level of the perturbation in the base flow. The initial eigenfunction

$$\bar{\mathbf{u}} = (-v_B, 0, 0) \quad (4.2)$$

is used for both the real and imaginary parts of the related perturbation of spanwise secondary instability.

Our numerical results show that the most unstable wavenumber b of spanwise secondary instability is 0.5 for spatially developing nonlinear Görtler vortices. Since Görtler vortices are also a spanwise periodic flow, the relation between the growth rate, eigenfunction and b is the same as that of Dean vortices (see §3.1 in Guo & Finlay, 1992)

$$f(b) = f(b \pm n). \quad (4.3)$$

Here $f(b)$ represents the spatial growth rate and eigenfunction at b , and $n = 1, 2, 3, \dots$. Unlike Dean vortices, there is no fully developed stage for Görtler vortices. They are under constant spatial development. In addition, there is no stable region for all cases we have studied.

4.4.1 Görtler vortices with long wavelength

Figure 4.7 shows the energy of the Görtler vortices in the base flow with wavelength $\lambda = 2.13\text{cm}$ ($\Lambda = 600$) and the related perturbation of spanwise secondary instability with $\lambda_1 = 4.26\text{cm}$ ($b = 0.5$). Both the simulation code and the stability code are started at $x = 9.6\text{cm}$ with $\epsilon = 0.05$ in equation (4.1). It can be seen that the energy of the perturbation always increases. This indicates that the developing Görtler vortices, like developing Dean vortices, are not stable to spanwise perturbations.

Also given in figure 4.7 is the energy of the perturbations with $\lambda = 2.13\text{cm}$ and 4.26cm obtained by setting the base flow \mathbf{u}^0 to be Blasius boundary layer in the

stability code. For $0.4\text{m} < x < 0.8\text{m}$, the growth of the Görtler vortices in the base flow is well predicted by linear theory. When $x > 0.85\text{m}$, the Görtler vortices reach the nonlinear stage and their growth begins to slow down. As with Dean vortices, the growth of the perturbation is well predicted by the primary instability growth rate at $\lambda = 4.26\text{cm}$ for $0.4\text{m} < x < 0.7\text{m}$ where the energy level of the Görtler vortices in the base flow is low. This indicates that small amplitude vortices with varying wavelength in the base flow do not interact with each other significantly. The growth of each wavelength is purely governed by primary instability. A similar situation can be found in curved channel flow.

In figure 4.7, the disagreement for $x < 0.4\text{m}$ may partly be due to the fact that the disturbance used to start the simulation is not the most unstable solution of the parabolized Navier-Stokes equations. In general, although different initial conditions lead to different solutions, the (most) unstable (or growing) eigensolutions will grow out of the transient solution associated with a given initial condition and dominate the solution downstream, while the other components of the transient solution will decay.

When $x > 0.7\text{m}$ in figure 4.7, the nonlinearity of the base Görtler vortices sets in, and the growth of the perturbation increases. Here the spanwise secondary instability begins to play an important role. The evolution of the streamwise component u_θ^0 of the base Görtler vortices and the outflow component u_r' of the related perturbation is shown in figure 4.8. At $x = 0.52\text{m}$ and 0.68m , the patterns of the perturbation (figure 4.8*b*) are the same as the ones with $\lambda = 4.26\text{cm}$ from primary instability analysis. There is only one pair of vortices in the box. These perturbation patterns grow downstream until $x = 0.84\text{m}$ where the base Görtler vortices have reached a considerable nonlinear level (figure 4.8*a*). Then two small additional single vortices begin to appear near the wall at the bottom of the two original vortices and continue to grow downstream. Unlike in curved channels (Guo & Finlay, 1992), no spanwise adjustment of the perturbation pattern is observed.

The flow patterns of the base flow and related perturbation at $x = 0.68\text{m}$ and 1.0m are shown in figure 4.9. The grid point velocities in figure 4.9 (and all other vector plots in rest of this paper) are shown on the grids actually used in the computation. At $x = 0.68\text{m}$ where the Görtler vortices in the base flow are still in their linear stage, there are two pairs of vortices in the base flow (figure 4.9a) and one pair in the perturbation, which has $\lambda_1 = 2\lambda$ (figure 4.9c). In figure 4.9(a), we can see there is strong outflow away from the wall on the edge of the boundary layer. This reflects the reality of the growing thickness of the boundary layer. At this location, the amplitudes of the Görtler vortices are small and comparable to the outflow velocity at the boundary layer edge. At $x = 1.0\text{m}$ in figure 4.9(b), the Görtler vortices have reached the nonlinear stage. The amplitudes of the vortices become much larger than the outflow velocity on the edge of the boundary layer. The vortices also extend considerably further in the radial direction. The number of vortex pairs in the perturbation increases to three in figure 4.9(d). There are two additional vortex pairs near $z/\lambda = 0.75$ and 1.75 . The effect of the perturbation of spanwise secondary instability on the base vortices is illustrated in figure 4.9(e) through the superimposition of 100% of this perturbation on the base flow (figure 4.9b). The two vortex pairs with outflow regions (where the fluid flows away from the concave wall) near $z/\lambda = 0.25$ and 1.25 in figure 4.9(b) are pushed together towards $z/\lambda = 0.75$ in figure 4.9(e), creating space near $z/\lambda = 1.75$. Increasing the percentage of the perturbation in figure 4.9(e) to 150% causes one small pair of vortices to be produced at $z/\lambda = 1.75$ near the wall with an outflow region at its center. (Note that the definition of outflow region here is different from the one used for curved channel flow in Guo & Finlay, 1992).

Compared with Dean vortices (figure 13e in Guo & Finlay, 1992), the effects of the spanwise secondary instability on the base flow are quite similar in both cases. The two vortices separated by a region where the fluid flows towards the concave wall (near $z/\lambda = 0.75$ in figure 4.9e) are squeezed together and become smaller while

a small vortex pair is created near the concave wall in between the two dominant pairs. As will be discussed in §4.5, the nonlinear development of this perturbation causes the base flow to develop from two pairs of vortices into three pairs. We call this process the splitting of Görtler vortices.

Our numerical results show that the perturbation pattern of spanwise secondary instability is sensitive to the initial spanwise phase difference between the base vortices and the perturbation, but is relatively insensitive to the actual flow patterns of the initial conditions used for the base flow and the perturbation. Figure 4.10 shows a similar case to that of figure 4.9 at $x = 0.984m$ but with the base vortices shifted $z/\lambda = -0.25$ in the spanwise direction (figure 4.10a) relative to the phase of the perturbation eigenfunction. A cosine function is used in equation (4.1) and $\epsilon = 0.1$. Before the base vortices enter the nonlinear stage, the flow pattern of the perturbation is the same as the one in figure 4.9(c). When the base vortices become nonlinear at $x = 0.984m$, the perturbation is shown in figure 4.10(b). We can see that the perturbation pattern here is different from that in figure 4.9(d), although the total number of strong vortex pairs in figure 4.10(b) is still three. Figure 4.10(c) shows the superimposition of 100% of the perturbation on the base vortices. The overall effect of the perturbation on the base flow is similar to that in figure 4.9(e). The two base vortex pairs with outflows at $z/\lambda = 0.0$ and 1.0 in figure 4.10(a) are squeezed towards $z/\lambda = 0.5$ in figure 4.10(c). Two vortices separated by an inflow region at $z/\lambda = 0.5$ become smaller. A small vortex pair can be detected at $z/\lambda = 1.5$ near the concave wall. This new pair is closer to the vortex pair near $z/\lambda = 0.9$ than the other pair. This is different from figure 4.9(e), where the new pair is equidistant from the two dominant pairs. The energy development of the perturbation in figure 4.10 is very similar to that of figure 4.7. The difference between the growth rates of the perturbations in figures 4.9 and 4.10 is small.

Similar results are found for all $\Lambda > 500$. The larger Λ is, the stronger the extra small vortices in the perturbation are, and the more likely a new pair of vortices will

appear in the flow. Like the Dean problem, it is difficult to define a lower bound on Λ at which the perturbation changes from having three pairs of vortices to one pair (and which thus distinguishes vortex splitting from merging).

4.4.2 Görtler vortices with short wavelength

Figure 4.11 shows the development of the energy of the base Görtler vortices with $\lambda = 0.749\text{cm}$ ($\Lambda = 125$) and the related perturbation of spanwise secondary instability with $\lambda_1 = 1.498\text{cm}$ ($b = 0.5$) at the same parameters as those in figure 4.7. Also given are the energy of linear Görtler vortices from primary instability at $\lambda = 0.749\text{cm}$ and 1.498cm . A similar situation to that in figure 4.7 is found here. The growth of the base Görtler vortices is well predicted by primary instability for $0.3\text{m} < x < 0.7\text{m}$. For $x < 0.7\text{m}$ where the energy level of the base Görtler vortices is low, the growth of the perturbation is the same as the one from primary instability. When $x > 0.7\text{m}$ where the nonlinearity of the base Görtler vortices sets in, the growth of the perturbation begins to change and the spanwise secondary instability becomes visible. As in figure 4.7, the growth rate of the perturbation is always positive.

Figure 4.12 shows the evolution of u_θ^0 and u_r' associated with figure 4.11. At $x = 0.52\text{m}$ and 0.68m in figure 4.12(a), the base Görtler vortices are in the linear stage. At these two locations, the patterns of the perturbation in figure 4.12(b) are the same as the ones given by primary instability at $\lambda = 1.498\text{cm}$. Further downstream, as the base Görtler vortices become nonlinear, the shape of the perturbation begins to change. This can be seen at $x = 0.84\text{m}$ in figure 4.12(b). But there is still only one pair of vortices in the perturbation. By $x = 1.25\text{m}$, the shape of the perturbation is significantly different from that at $x = 0.68\text{m}$. The total number of vortices in the perturbation remains one. There is no significant spanwise shift of the perturbation pattern in figure 4.12(b). This is different from

Dean vortices (figure 9 in Guo & Finlay, 1992). In the Dean problem, a significant spanwise adjustment of the perturbation pattern is observed when the base Dean vortices enter the nonlinear stage. As a result, the perturbation pattern there is not sensitive to the initial spanwise phase difference between the base vortices and perturbation.

The flow patterns of the base flow and the related perturbation at $x = 0.68\text{m}$ and 1.0m are shown in figure 4.13. At $x = 0.68\text{m}$ in figure 4.13(a), the base Görtler vortices are relatively small and the outflow at the edge of the boundary layer can still be seen. The related perturbation in figure 4.13(c) has the same pattern as the one given by primary instability at $\lambda = 1.498\text{cm}$. At $x = 1.0\text{m}$ in figure 4.13(b), the base Görtler vortices become nonlinear. They have grown considerably in the radial direction and have larger amplitudes. Compared to the cross-stream velocities of the vortices, the outflow on the edge of the boundary layer have become much smaller. The flow pattern of the related perturbation changes accordingly in figure 4.13(d), although there is still only one pair of vortices in the space of two base vortex pairs. Notice that the perturbation does not grow much in the radial direction. This can also be seen in figure 4.12(b). This situation is different from that at $\lambda = 2.13\text{cm}$ in figures 4.8 and 4.9. The superimposition of 50% of the perturbation (figure 4.13d) on the base flow (figure 4.13b) is shown in figure 4.13(e). The vortices near $z/\lambda = 0.5$ and 1.0 in figure 4.13(b) are squeezed together and become smaller while the other two grow stronger and bigger. This situation is quite similar to that for Dean vortices (figure 10e in Guo & Finlay, 1992). In both cases, two vortices separated by a region where the fluid flows towards the concave surface are squeezed together by the perturbation of spanwise secondary instability and become smaller, while the other two vortices grow bigger. If this analogy with Dean vortices continues further downstream, merging of Görtler vortices would occur as a result of the instability with respect to spanwise perturbations.

Like Görtler vortices with long wavelength, the perturbation pattern of spanwise

secondary instability here is sensitive to the initial spanwise phase difference between the base vortices and perturbation. Figure 4.14 shows a case where the base Görtler vortices (figure 4.14a) are shifted $z/\lambda = -0.25$ in the spanwise direction from that of figure 4.13(b) while the perturbation is unchanged. Before the base vortices enter the nonlinear stage, the flow pattern of the perturbation looks like that in figure 4.13(c). At $x = 1.169\text{m}$ where the base vortices are nonlinear (figure 4.14a), the perturbation pattern (figure 4.14b) is quite different from that in figure 4.13(d). On top of the two vortices near the wall there are another two vortices, far away from the wall. The effect on the base vortices is illustrated in figure 4.14(c) through the superimposition of the perturbation (16.7%) on the base vortices in figure 4.14(a). For the base vortex pair with an outflow region at $z/\lambda = 1.0$ in figure 4.14(a), the lower half of the vortex pair near the wall is squeezed together by the two perturbation vortices near the wall in figure 4.14(b), so that its dimension in the spanwise direction becomes less. The upper half of this vortex pair is amplified by the two perturbation vortices away from the wall, and as a result it becomes elongated in the radial direction and grows bigger. For the base vortex pair near $z/\lambda = 0.0$ (or 2.0) in figure 4.14(a), the lower half of the vortex pair near the wall is enhanced by the two perturbation vortices near the wall (figure 4.14b) and grows stronger, while its upper half is weakened by the two perturbation vortices away from the wall. As a result, this vortex pair moves closer to the wall.

Figure 4.15 shows the energy of the base vortices and the related perturbation from figure 4.14. It can be seen that the development of the energy in the perturbation is similar to that in figure 4.11. (The energy levels of the base vortices in figures 4.11 and 4.14 are not the same). The perturbation growth rates in both cases are quite close.

The perturbations shown in figures 4.9, 4.10, 4.13 and 4.14 are four typical patterns found in most cases. In all these cases, the perturbation wavenumber $b = 0.5$ is used. When other perturbation wavelengths ($b \neq 0.5$) are used, our

numerical results show that during the linear stage of the base Görtler vortices, the perturbations grow at the rates given by primary instability at these wavelengths. When the base vortices enter the nonlinear stage, these perturbations continue to grow, but at the rates given by spanwise secondary instability. These secondary growth rates are smaller than the one with $b = 0.5$. Since the perturbation growth rate of spanwise secondary instability depends on the nonlinear development of the Görtler vortices in the base flow, which again depends on the initial perturbations used to start the simulation, it is difficult to define the growth rate of the spanwise secondary instability as a function of Görtler number $G\ddot{o}$ and wavelength parameter Λ . Other than $b = 0.5$ being the most unstable, no specific growth rate pattern is given here.

The determination of $b = 0.5$ being the most unstable wavenumber for the spanwise secondary instability of developing Görtler vortices is not trivial. Since the growth rate depends both on the initial eigenfunctions used to start the marching and the nonlinear development of the base Görtler vortices, it is difficult to compare the growth rates with different b . Only with the help of the simulations with a large spanwise computational box are we able to determine that $b = 0.5$ is the most unstable wavenumber for the spanwise secondary instability of Görtler vortices. For example, when more than three pairs of Görtler vortices are included in a computational box, the splitting and merging of vortices mostly involves two pairs of Görtler vortices and the flow patterns are similar to those in figures 4.9, 4.10, 4.13 and 4.14 predicted by superimposing the perturbations with $b = 0.5$ on the base Görtler vortices.

Using a local linear theory and a semi-analytical method, Floryan & Saric (1984) found a similar result for the interaction of the streamwise vorticity in the freestream with Görtler instability. Their results show that when there exist streamwise vortices in the freestream, the most unstable wavelength of the Görtler instability is twice that of the vortices in the freestream. In their study, they

assume the amplitude of the vortices in the freestream is much larger than that of the linear Görtler vortices. Our discussions in this section show the spanwise secondary instability sets in only when the base Görtler vortices become nonlinear. Since the nonlinear effect of the streamwise vortices in the base flow is not considered in Floryan & Saric (1984), the details of these types of interactions and how they affect the wavelength selection in their work are uncertain.

To summarize the above discussions, developing Görtler vortices are always unstable to spanwise perturbations. During the early stage of the evolution where Görtler vortices are linear, the perturbations with other wavelengths also grow, at the rates given by primary instability at these wavelengths. When the base Görtler vortices reach the nonlinear stage, perturbations with wavelength double that of the base Görtler vortices become the most unstable. These perturbations will grow at different rates with different flow patterns. There are three pairs of vortices in the perturbations for the base Görtler vortices with long wavelength ($\Lambda > 500$) and one pair for the base flow with short wavelength.

4.5 Simulations of splitting and merging of Görtler vortices

To our knowledge, the formation of naturally occurring Görtler vortices in experiments is rather irregular and it is difficult to determine if there is evidence of splitting or merging of Görtler vortices from published data. In §4.4, our linear stability analysis of spatially developing Görtler vortices predicts the existence of splitting and merging of Görtler vortices. To support those arguments, we next study the nonlinear development of spanwise secondary instability and the splitting and merging of Görtler vortices using the simulation code with a large spanwise computational box. In this section, the flow parameters used in all simulations are $U_\infty = 5\text{m/s}$, $\nu = 14.5 \times 10^{-6}\text{m}^2/\text{s}$ and $R = 3.2\text{m}$. The initial flow condition used

to start the simulations is

$$\mathbf{u} = (v_B, u_B + 0.03 u_B (\sin(4\pi z/\lambda) + \epsilon \sin(4\pi z/\lambda_1)), 0) \quad (4.4)$$

where λ is the dominant wavelength, λ_1 is the perturbation wavelength, and ϵ is used to adjust the energy level of the perturbation wavelength relative to that of the dominant wavelength. Two pairs of dominant vortices are included in the computational box since, in all cases studied, the most unstable perturbation wavenumber b is 0.5 or 1.5. The energy in spanwise Fourier modes is also monitored. The energy in spanwise Fourier mode k_z is defined by (Finlay *et al.*, 1988)

$$E(k_z) = c(k_z) \int_{r_i}^{r_0} \hat{u}(r, k_z)^2 dr$$

where $c(k) = 0.5$ for $k = 0$ and $c(k) = 1$ for $k \neq 0$; $\hat{u}(r, k_z)$ is the spanwise Fourier transform of \mathbf{u} . In the case of $b = 0.5$, before the spanwise perturbation develops nonlinearly the energy in the first mode comes mostly from the perturbation with $b = 0.5$ and the energy in the second mode mostly from the dominant Görtler vortices.

4.5.1 Görtler vortices with short wavelength

Figure 4.16 shows the flow patterns in the cross-stream plane of a simulation with the dominant wavelength $\lambda = 0.749\text{cm}$ ($\Lambda = 125$) and the perturbation wavelength $\lambda_1 = 2\lambda$ ($b = 0.5$). The simulation is started at the streamwise location $x = 0.032\text{m}$. A relatively large ϵ ($\epsilon = 0.2$) is used in equation (4.4). Figure 4.16(a) shows the flow pattern at $x = 0.556\text{m}$. There are two pairs of relatively weak vortices in the domain. It can be seen that the vortices between $z/\lambda = 1.0$ and 1.5 are smaller than those between $z/\lambda = 0.0$ (2.0) and 0.5 . When compared to figure 4.13(e), the flow pattern here is well predicted by the secondary stability theory in that a pair of vortices separated by an inflow region (at $z/\lambda = 0.75$ in figure 4.13e and $z/\lambda = 1.25$ in figure 4.16a) is made smaller than others. This is the linear

stage of vortex merging. Further downstream at $x = 0.71\text{m}$, the single vortex at $z/\lambda = 1.5$ grows bigger while the one at $z/\lambda = 1.0$ continues to stay small. The vortex pair with an outflow region near $z/\lambda = 1.75$ grows bigger in the r direction compared with the other pair centered near $z/\lambda = 0.8$. These changes are seen more clearly at $x = 0.864\text{ m}$ in figure 4.16(c). The flow patterns in figure 4.16(c) and figure 4.14(c) are quite similar. The lower half of the vortex pair near $z/\lambda = 1.75$ in figure 4.16(c) is squeezed together while the upper half is elongated in the r direction and grows bigger. The vortex pair near $z/\lambda = 0.8$ is pressed towards the wall (relative to the growing boundary layer thickness) and becomes shorter in the r direction but wider in the spanwise direction. The vortex merging pattern switches from that of figure 4.13(e) at $x = 0.556\text{m}$ to that of figure 4.14(c) when it reaches $x = 0.864\text{m}$. This vortex merging pattern continues to develop nonlinearly downstream. At $x = 1.018\text{m}$ (figure 4.16d), the vortex pair near $z/\lambda = 1.75$ is much stronger and elongated in the r direction, while the other pair near $z/\lambda = 0.8$ grows only a little in the r direction. Further downstream at $x = 1.171\text{m}$ in figure 4.16(e), as the vortex pair near $z/\lambda = 1.75$ moves away from the wall, its strength reduces. The vortex pair near $z/\lambda = 0.8$ becomes stronger again. Our simulation shows that further downstream, this vortex pair eventually occupies the whole domain and the vortex pair near $z/\lambda = 1.75$ disappears totally as it moves away from the wall.

The energy in the first and second Fourier modes of the Görtler vortices in figure 4.16 is shown in figure 4.17. Also given is the perturbation energy of spanwise secondary instability from figure 4.15. The perturbation energy level is scaled to match the energy in the first Fourier mode. It can be seen that for $x < 0.6\text{m}$, the energy in the second Fourier mode (which corresponds to the dominant wavelength) is close to the total energy. This indicates that the dominant Görtler vortices are in the linear stage and the energy in the harmonics of the dominant wavelength is negligible. When $x > 0.6\text{m}$, the energy in the second mode begins to drop (compared to the total energy) and the nonlinearity of this dominant wavelength

begins to set in. For $0.45\text{m} < x < 0.6\text{m}$, the energy growth in the first mode is well predicted by spanwise secondary instability. When $x > 0.6\text{m}$, the energy growth of the first mode begins to slow down. By $x > 0.9\text{m}$, the energy level in the first mode is quite comparable to that in the second mode. From figure 4.16(c), we know that the nonlinear development of the spanwise secondary instability begins to dominate the flow at this point, and the interactions between different wavelengths become visible.

Generally, the smaller ϵ is, the greater streamwise distance over which the prediction given by spanwise secondary instability for the energy growth in the first mode is valid. This situation is similar to that for Dean vortices (§7 in Guo & Finlay, 1992). It is not surprising that the linear prediction fails once nonlinearity sets in. When ϵ is large, nonlinearity occurs early and there are three types of nonlinearities involved: the nonlinearity of the dominant vortices, the nonlinearity of perturbations and the nonlinear interaction between the dominant vortices and perturbations. It is difficult to determine these nonlinear effects even with numerical simulations.

Figure 4.18 shows the spatial development of the velocity component u_θ corresponding to figure 4.16. When $x < 0.556\text{m}$, the contour shapes of the two vortices are almost the same. At $x = 0.864\text{m}$, the vortex merging becomes visible. The middle mushroom becomes shorter than the other one (in the vertical direction). This is seen more clearly further downstream. The nonlinear development of spanwise secondary instability thus causes one mushroom in figure 4.18 to become smaller and the other to be larger in the r direction.

Other simulations we have done show that when a cosine function is used in equation (4.4) for the dominant wavelength, the vortex merging pattern always looks like that in figure 4.14(c) and no change in the vortex merging pattern is observed. The structures of both vortex pairs are more symmetric and the vortex merging process becomes visible earlier. For example, in order to obtain a flow

pattern similar to that in figure 4.18, we use a smaller ϵ ($\epsilon < 0.1$) in equation (4.4).

When more than two pairs of the dominant vortices are included in a computational box, our simulations show that the vortex merging patterns are similar to that of figure 4.14(c) in most cases. The vortex merging pattern predicted by figure 4.13(e) is only seen during the linear stage of vortex merging.

Compared to Dean vortices (§7 in Guo & Finlay, 1992), the vortex merging process of Görtler vortices is different. In the case of Dean vortices, once a vortex pair separated by the fluid flowing towards the concave wall is squeezed together and becomes smaller, this flow pattern continues to develop until the squeezed pair totally disappears. In the case of Görtler vortices, one vortex pair is pressed towards the wall and becomes shorter in the r direction (relative to the undistorted case), while its neighboring pair is elongated in the r direction and grows bigger. Further downstream as this neighboring vortex pair moves away from the wall and becomes weaker (probably due to a reduction of the centrifugal force which drives the centrifugal instability), the remaining vortex pair begins to dominate the domain. This phenomenon is not found in Dean vortices where the vortices occupy the whole breadth of the channel and the convex wall prevents any escape. But in both Dean and Görtler vortices, the nonlinear vortex merging patterns are quite similar to those predicted by spanwise secondary instability theory.

4.5.2 Görtler vortices with long wavelength

Figure 4.19 shows a simulation similar to that of figure 4.16 but with the dominant Görtler vortices having $\lambda = 2.13$ cm ($\Lambda = 600$) and the perturbation having wavelength $\lambda_1 = 2\lambda/3$ ($b = 1.5$); the perturbation level, ϵ , is 0.8 in figure 4.19. We choose $b = 1.5$ because during the linear stage of the dominant vortices, the growth rate of the primary instability at $2\lambda/3$ is larger than at 2λ . So the perturbation with $2\lambda/3$ will grow faster and generate more disturbance energy

when spanwise secondary instability sets in. Once the dominant vortices enter the nonlinear stage, the growth rate of the perturbation is the same at $2\lambda/3$ and 2λ (cf. equation 4.3). At $x = 0.474\text{m}$ in figure 4.19(a), there are two dominant pairs of Görtler vortices with outflow regions near $z/\lambda = 0.6$ and 1.8 . There is also a small single vortex appearing near $z/\lambda = 1.25$. Downstream at $x = 0.627\text{m}$ in figure 4.19(b), while the two dominant vortices are pronounced, the small vortex near $z/\lambda = 1.25$ has not decayed, but keeps growing. This flow pattern continues to develop downstream. At $x = 0.781\text{m}$ in figure 4.19(c), we can see the structure of the dominant vortex pair near $z/\lambda = 0.6$ has been modified significantly as a result of the small vortex near $z/\lambda = 1.25$. By $x = 0.93\text{m}$ in figure 4.19(d), the small single vortex near $z/\lambda = 1.25$ in figure 4.19(c) finally develops into a small vortex pair near $z/\lambda = 1.0$. There are three vortex pairs in the domain. Compared to figure 4.10(c), the flow pattern in figure 4.19(d) is roughly predicted by the linear stability theory. In both figures, the new vortex pair is generated near the wall in between the two dominant vortex pairs in a region where the fluid flows towards the wall. This new vortex pair is closer to one dominant pair than the other.

The spatial development of the velocity component u_θ is shown in figure 4.20. The two dominant mushrooms can first be seen at $x = 0.474\text{m}$. They grow rapidly downstream. At $x = 0.627\text{m}$, a small mushroom can be detected in between the two dominant mushrooms. By $x = 0.781\text{m}$, the small mushroom is clear. It is closer to the right dominant mushroom than to the left one. Adjusting ϵ , we can control the streamwise location of the appearance of this new pair of vortices. In figure 4.20, a very large $\epsilon = 0.8$ is used. If we increase the wavelength of the dominant Görtler vortices to $\lambda = 2.5\text{cm}$, a smaller $\epsilon = 0.2$ is enough to make the vortex splitting quite visible in the same streamwise distance.

Other simulations done by us show that although most vortex splitting patterns are similar to those in figure 4.19, there are still many other forms which are not predicted by either figures 4.9 or 4.10 from the linear stability theory. For example,

when a cosine function is used for the dominant wavelength in equation (4.4) and $\epsilon = 0.6$, the resulting flow pattern at $x = 0.909\text{m}$ is shown in figure 4.21. Oddly, the flow pattern is more similar to the vortex merging pattern in figure 4.14(c). The vortex pair at $z/\lambda = 0.5$ is elongated in the r direction and moves away from the wall, while the pair at $z/\lambda = 1.5$ is pressed towards the wall and becomes larger in the spanwise direction. However further downstream, a new vortex pair is created on top of the vortex pair at $z/\lambda = 1.5$. As this new vortex pair grows downstream, it splits apart the dominant pair from above, not below.

From figures 4.18 and 4.20, we see that both splitting and merging types of nonlinear development of spanwise secondary instability significantly modify the mushroom shapes of the streamwise velocity and cause asymmetric vortex structures and irregularity. Since most Görtler vortices breakdown for $x > 1.2\text{m}$ for the flow parameters we are using (cf. Swearingen & Blackwelder, 1987), the nonlinear development of splitting and merging of vortices may not have sufficient streamwise distance to develop fully. For example, in the case of vortex merging, the Görtler vortices will probably break down before two vortex pairs develop completely into one pair. Thus, in experiments only the beginning of the merging process is likely to be observed. Because Görtler vortices are under constant spatial evolution, vortex splitting may manifest itself through the later formations of some vortex pairs in between other vortices. If we consider an observation of one vortex pair becoming smaller while its neighbor grows bigger as the signature of vortex merging, and the later appearance of some vortices in between existing vortices as the signature of vortex splitting, then experimental evidence is plentiful (cf. Bippes 1972, Aihara & Koyama 1980, Aihara *et al.* 1984 and recently Swearingen & Blackwelder 1987). Since there are severe irregularities in most experimentally observed Görtler vortices and no special attention has been given to the spanwise secondary instability of Görtler vortices, we will not elaborate on experimental evidence any further.

Compared to Dean vortices (Guo & Finlay, 1992), Görtler vortices have a smaller

growth rate of spanwise secondary instability. In order to observe vortex splitting and merging (in figures 4.18 and 4.20), a large ϵ is required. This indicates that the interactions between Görtler vortex pairs are not as strong as those between Dean vortices.

When perturbations with $b \neq 0.5$ (or 1.5) are used, our simulations give results similar to those for Dean vortices when $b \neq 0.5$ (or 1.5) (§7 in Guo & Finlay, 1992). That is, if the perturbation level is low and there is no nonlinear interaction between the perturbation and the dominant vortices, the growth of the perturbation is governed by primary instability before the dominant vortices become nonlinear; when the dominant vortices enter the nonlinear stage, the growth rate of this perturbation is given by spanwise secondary instability. If the perturbation level is high, some energy of the perturbation with $b \neq 0.5$ can be converted into perturbations with b near 0.5 due to the nonlinear interaction between the dominant vortices and the perturbation with $b \neq 0.5$. As a result, the growth of the perturbation with $b = 0.5$ dominates the flow in some cases and the nonlinear vortex splitting and merging discussed earlier in this section occur. If the growth of the perturbation with $b = 0.5$ does not dominate the flow, vortex splitting and merging still occur but in a different (irregular) way and spanwise secondary instability is still characterized by irregularities of the dominant Görtler vortices.

4.6 Wavelength selection and irregularity of Görtler vortices

Using a local method, Floryan & Saric (1984) have examined the wavelength selection mechanism of Görtler vortices. They conclude that wavelengths near $\Lambda = 210$, which have the largest primary growth rate (see figure 4.2), are likely to be observed. This theory explains Bippes' observations (1972) well. In Bippes' experiments when screens (disturbance generators) are used to generate isotropic

random disturbances, the wavelength parameters Λ of the observed Görtler vortices are near 210. But in the observations of Tani (1962), Winoto & Crane (1980) and Swearingen and Blackwelder (1987), much longer wavelengths of naturally occurring Görtler vortices are observed ($\Lambda \geq 650$).

In §4.2, we have shown that the growth rate of primary instability does not vary significantly from $\Lambda = 175$ to 400 (cf. figure 4.2). For this wavelength range, the wavelength selection mechanism of primary instability is weak. Our discussions in §4.2 also show that over a short distance downstream from the leading edge, the primary growth rate varies considerably for different forms of initial perturbations. This further widens the wavelength range favoured by primary instability, and thus weakens (and complicates) the wavelength selection mechanism of primary instability. If the perturbations near the leading edge are dominated by a wavelength within this widened wavelength range, this wavelength will have a better chance to develop into dominant vortices due to its higher initial energy level. If all wavelengths in the perturbations have equal energy, wavelengths near $\Lambda = 210$ are more likely to be observed due to their slightly higher primary growth rate in most cases.

Our simulations of nonlinear Görtler vortices in §4.3 show that the growth rates of primary instability are small compared to the streamwise length allowable for Görtler vortices to develop. Relatively high energy levels for initial perturbations (1% of U_∞) are required in our simulations in order to obtain Görtler vortices with a strength comparable with those observed by Swearingen & Blackwelder (1987). (In the case of Dean vortices, the initial perturbations are less than 0.001% of \bar{U} .) This suggests that in the experiments of Swearingen & Blackwelder, there exists a relatively high level of perturbations. According to the experimental specifications given by Swearingen & Blackwelder, these large perturbations are not in the freestream. At $x = 10\text{cm}$ from the leading edge, the disturbances they measured have amplitude 1% of U_∞ (see figure 4.5). This indicates that somewhere

in between the leading edge and $x = 10\text{cm}$, large perturbations have been generated. These perturbations cannot be produced by a Görtler instability because of its small growth rate and the short streamwise distance to this location.

Since Bippes (1972) and Swearingen & Blackwelder (1987) observed different wavelengths for naturally occurring Görtler vortices, it is useful to compare experimental devices between these two groups. In the experiments conducted by Swearingen & Blackwelder (1987), the test section is essentially a variable width curved channel. The perpendicular distance between the testing (concave) plate and the convex plate is small. This design imposes restrictions on the vertical velocity u_r near the leading edge (where u_r is of order 1% of U_∞), and will generate perturbations which reduce the value of u_r compared with a free concave wall, i.e. perturbations with $u_r' = -cu_r$ (where u_r is the vertical velocity for a single free concave wall) will be generated. In Bippes' experiments, concave plates with constant curvature are towed in a water tank. We believe this setup imposes less restriction on the vertical velocity u_r near the leading edge. This is also manifested by the fact that when disturbance generators (screens) are not used in Bippes' experiments, the naturally occurring Görtler vortices are smaller and not well defined. Another likely source of large disturbances is the misalignment of the leading edge to the direction of the freestream U_∞ . Using the configurations of Swearingen & Blackwelder (1987), our simulations show that a misalignment of half a degree in the r or z directions will generate enough disturbances for the Görtler vortices of the observed strength to develop. The common feature between the large perturbations generated by either the restriction on u_r or misalignment of the leading edge to the freestream is that these large perturbations do not vary rapidly in the spanwise direction, and they depend strongly on the experimental apparatus.

To simulate the effect of leading edge misalignment, simulation was started from $x = 0.032\text{m}$ at $U_\infty = 5\text{m/s}$, $\nu = 14.5\text{m}^2/\text{s}$ and $R = 3.2\text{m}$ with the initial flow condition $(v_B, u_B, 0.01u_B)$. This initial flow condition is intended to simulate

1% misalignment (0.6 degree misalignment) of the freestream in the z direction. The spanwise length of the computational box is 6cm. Figure 4.22 shows the development of the streamwise velocity u_θ from $x = 0.198\text{m}$ to $x = 1.293\text{m}$. Both the strength and the wavelength of the dominant Görtler vortices ($\lambda = 2\text{cm}$) are comparable to those observed by Swearingen & Blackwelder ($\lambda = 2.13\text{cm}$). The evidence of vortex splitting due to spanwise secondary instability is also manifested by the later formation of two small mushrooms in between the dominant mushrooms. When random initial perturbations or perturbations with rapid spanwise variation are used in the simulations, we find the average wavelength of the dominant Görtler vortices is very close to $\Lambda = 210$, the one with the largest primary growth rate. In Bippes' experiments, the perturbations generated by screens are of rapid variation, so the observed wavelengths of Görtler vortices are close to $\Lambda = 210$.

From the above discussions we conclude that when the perturbations near the leading edge have both rapid and slow spanwise variations, there is energy for all wavelengths and thus the wavelength selection mechanism of primary instability plays a more important role. The wavelengths of the dominant Görtler vortices are expected to be close to $\Lambda = 210$. When the perturbations near the leading edge have only slow spanwise variation, longer wavelengths will be favoured and the dominant Görtler vortices will have wavelength longer than $\Lambda = 210$.

Another important source of large perturbations is the leading edge itself. When the freestream hits the leading edge, acoustic waves will be generated and the flow near the leading edge is elliptic in nature. To determine the form and strength of disturbances generated by the leading edge, it is probably necessary to resort to a time-dependent, three-dimensional elliptical analysis. Very recently, attention has been given to the leading edge receptivity of the Görtler problem (Hall, 1990). However, since large initial disturbances strongly influence the nonlinear development of Görtler vortices on a strongly curved wall (see §4.3), the dominant wavelengths of the initial perturbations may be the most important factor in the

wavelength selection process. We will not discuss the leading edge receptivity problem in this study. Readers are referred to Hall (1990) for more details.

The study in §4.4 and §4.5 shows that developing Görtler vortices are not stable to spanwise perturbations. During the linear development of the dominant Görtler vortices, vortices with other wavelengths grow independently at the rates given by primary instability at these wavelengths. As the dominant Görtler vortices develop into the nonlinear stage, perturbations with twice the dominant wavelength continue to grow (most rapidly). The nonlinear growth of these perturbations can generate new vortices or cause some dominant Görtler vortices to disappear. Since the dominant Görtler vortices break down shortly after the onset of secondary instabilities, we do not expect splitting and merging of vortices to affect the wavelength selection process significantly. Instead, they will deform the dominant Görtler vortices significantly and produce irregular vortices. This can be seen in figures 4.18, 4.20, and 4.22.

Interactions between Görtler vortices with different wavelengths can also provide large disturbances for the nonlinear development of spanwise secondary instability. Figure 4.23 shows a simulation at $U_\infty = 5\text{m/s}$, $\nu = 14.5 \times 10^{-6}\text{m}^2/\text{s}$ and $R = 3.2\text{m}$. The simulation is started with wavelength $\lambda = 2.5\text{cm}$ for the left two vortex pairs and $\lambda = 0.833\text{cm}$ for the rest of the vortices. When $x < 0.506\text{m}$, the interactions are not obvious. The shapes of the mushrooms are relatively regular. At $x = 0.67\text{m}$, the interactions become visible on the interfaces between regions with different wavelengths. The second and third mushrooms from the left and the first mushroom from the right begin to lose their symmetries. This can be seen more clearly further downstream at $x = 0.966\text{m}$. At $x = 1.12\text{m}$, the interactions among the vortices with smaller wavelength in the right half of the domain can also be seen, causing distortions to the previously symmetric shapes.

The flow pattern of figure 4.23 at $x = 0.506\text{m}$ and 1.12m is shown in figure 4.24 in the cross-stream plane. In figure 4.24(a), the flow pattern of the vortices is

relatively regular except for the two vortex pairs near $z = 0.1\text{cm}$ and 5.5cm with outflow regions at their centers. No interactions among the vortices with smaller wavelength from $z = 1.0\text{cm}$ to 4.0cm are seen. At $x = 1.12\text{m}$ in figure 4.24(b), one vortex near $z = 0.1\text{cm}$ is pushed away from the wall by its neighbor near $z = 0.75\text{cm}$. There are some distortions on the vortex pair near $z = 5.5\text{cm}$. The interactions and distortions among the smaller vortices from $z = 1.0\text{cm}$ to 4.0cm are less severe at this stage.

Comparing to Dean vortices (figure 20 in Guo & Finlay 1992), the interactions between Görtler vortices with different wavelengths are not strong. The interactions do not change the wavelengths of the vortices significantly, but they do modify the structures of the Görtler vortices and generate irregularity.

4.7 Conclusion

This study shows that spatially developing Dean vortices and Görtler vortices share several similarities. Both of them are caused by streamwise curvature due to centrifugal instability. Both of them are unstable to spanwise perturbations. When the vortices are small and linear, spanwise perturbations with multiple wavelengths can coexist and grow simultaneously at the rates given by primary instability. When some of these vortices grow strong enough to become the dominant wavelengths and nonlinearities set in, spanwise secondary instability becomes the dominant instability. Perturbations with wavelength twice that of the dominant wavelengths become the most unstable. The nonlinear development of these perturbations can cause two pairs of the vortices with short wavelength to develop into one pair and generate a new pair of vortices between two pairs of vortices with long wavelength.

There are some differences between these two types of vortices. Considering the streamwise lengths over which the two types of vortices are allowed to develop, the growth rates of both primary instability and spanwise secondary instability

for Görtler vortices are considerably less than those for Dean vortices. In order to observe the nonlinear development of these instabilities experimentally or numerically, large perturbations are needed for Görtler vortices. Since Görtler vortices have a smaller growth rate of spanwise secondary instability, the interactions between the vortex pairs are not as strong as those for Dean vortices. Vortex merging and splitting events generally do not have enough streamwise length to become strongly nonlinear and change the wavelengths of the vortices significantly, as they do in the case of Dean vortices. Instead, distortion of the vortex structures occurs. The details of vortex merging of Görtler vortices are also different from those in Dean vortices. We believe these differences may be partially related to the fact that Dean vortices have a streamwise pressure gradient while Görtler vortices do not.

Spanwise secondary instability is an important instability for developing streamwise vortices. When the vortices in the base flow are linear, spanwise secondary instability is equivalent to primary instability. When the vortices in the base flow enter the nonlinear stage, the secondary instability controls the interactions between each vortex pair. It causes the distortion and irregularity of the vortices. If there was no spanwise secondary instability, then when vortices of a certain wavelength become nonlinear, all spanwise disturbances at other wavelengths would decay. This would result in regular, symmetric nonlinear vortices like those observed in Taylor-Couette flow. The irregular, nonsymmetric vortex structures observed in curved channel and concave boundary layer experiments would not occur if the spanwise secondary instability we have discussed in this paper did not exist.

The study done by Guo & Finlay (1991) shows that in the context of temporal theory, the streamwise vortices caused by rotation or by both rotation and streamwise curvature in channel geometries have a spanwise secondary instability (called "Eckhaus instability" in Guo & Finlay, 1991) similar to that of Dean vortices.

Whether the features of Dean and Görtler vortices found in this study exist for vortices caused by rotation in a rotating channel or on a rotating flat plate, or those caused by streamwise curvature found in transitional and turbulent wall bounded shear flows remains to be seen. Since the nonlinear development of this type of secondary instability modifies the vortex structures significantly (in both Dean and Görtler problems), the study of this type of instability and its effects on the onset of other secondary instabilities is a necessary step toward understanding the transition to turbulence.

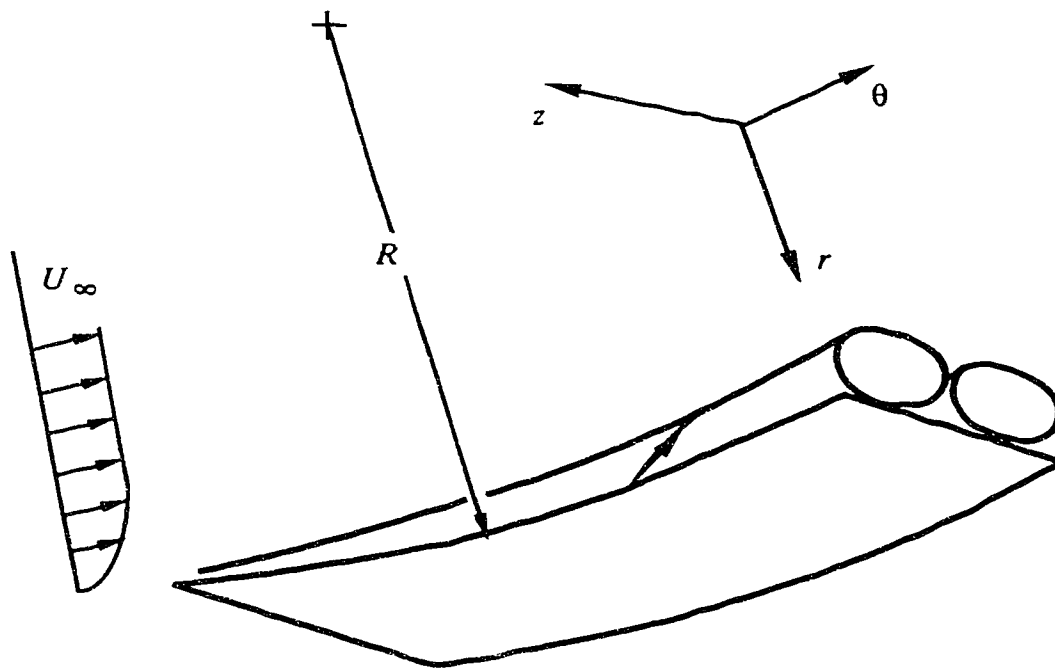


FIGURE 4.1. The geometry of boundary layer flow over a concave surface is shown. The streamwise direction is θ .

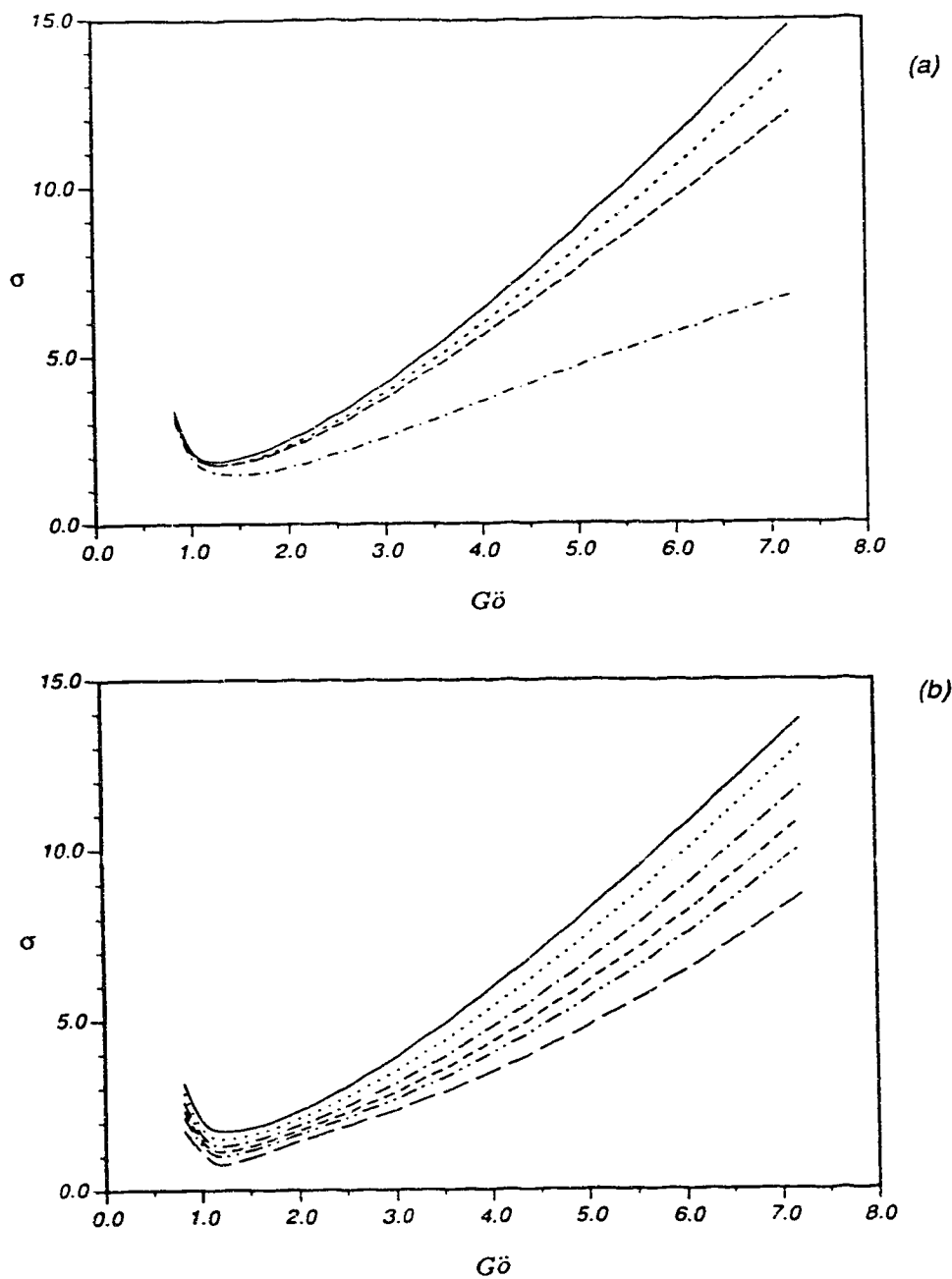


FIGURE 4.2. Energy growth rate σ is shown as a function of Görtler number $G_{\ddot{o}}$. In (a): —, $\Lambda = 210$; , $\Lambda = 175$; ---- , $\Lambda = 125$; - · - , $\Lambda = 75$. In (b): —, $\Lambda = 210$; , $\Lambda = 400$; - · - , $\Lambda = 600$; ---- , $\Lambda = 800$; - · · - , $\Lambda = 1000$; - - , $\Lambda = 1500$.

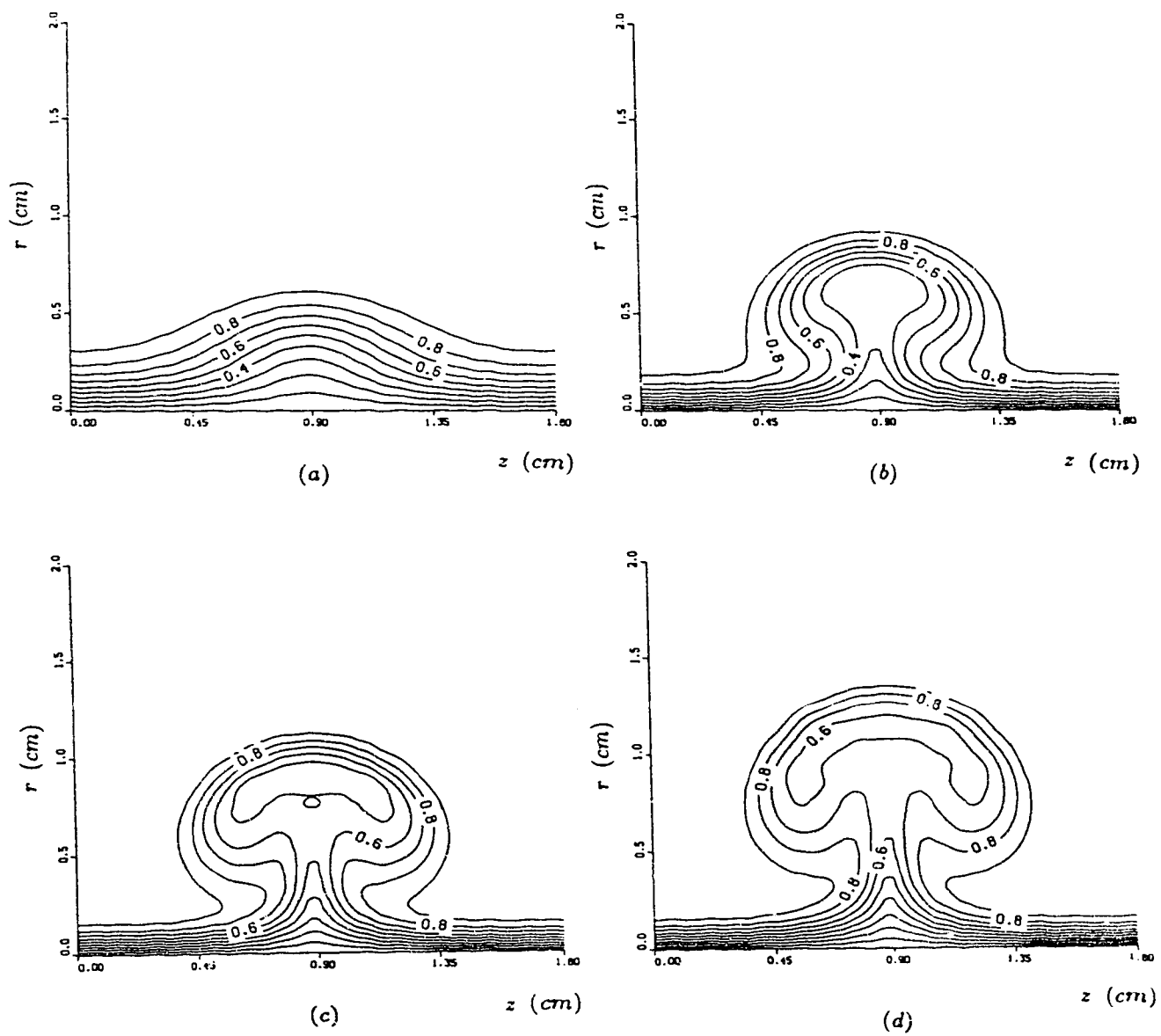


FIGURE 4.3. For caption see facing page.

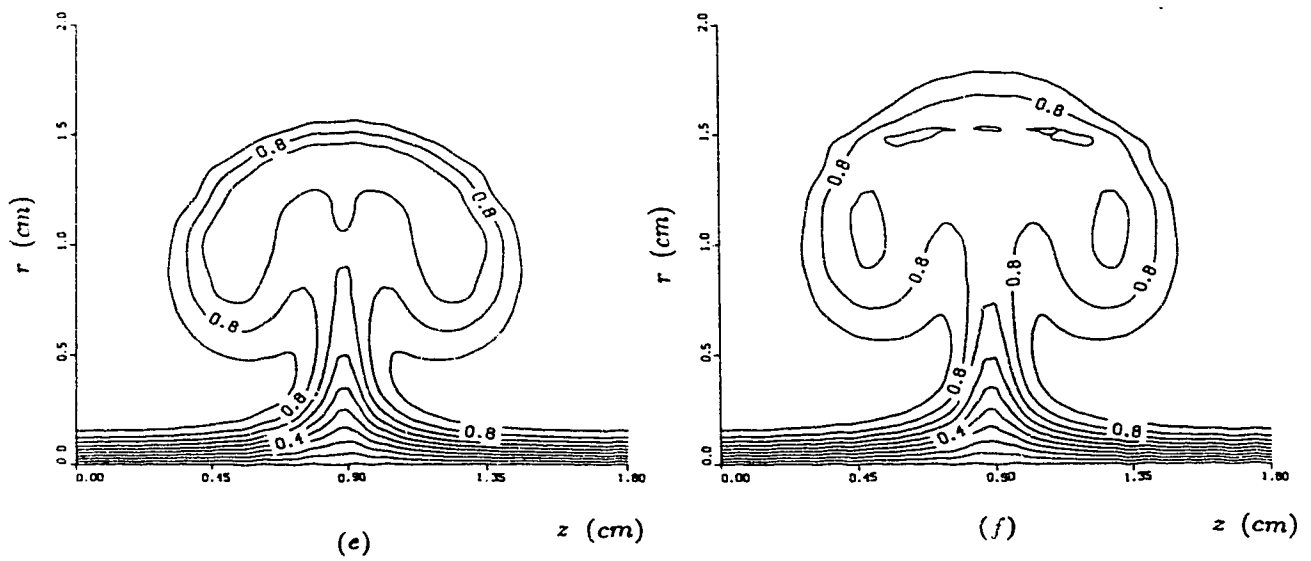


FIGURE 4.3. Contours of the streamwise velocity u_θ of Görtler vortices with $\lambda = 1.8\text{cm}$ on a concave wall (of radius $R = 3.2\text{ m}$) are shown at (a) $x = 60\text{cm}$; (b) $x = 80\text{cm}$; (c) $x = 90\text{ cm}$; (d) $x = 100\text{cm}$; (e) $x = 110\text{cm}$ and (f) $x = 120\text{cm}$. Here, $U_\infty = 5\text{m/s}$ and $\nu = 14.5 \times 10^{-6}\text{m}^2/\text{s}$.

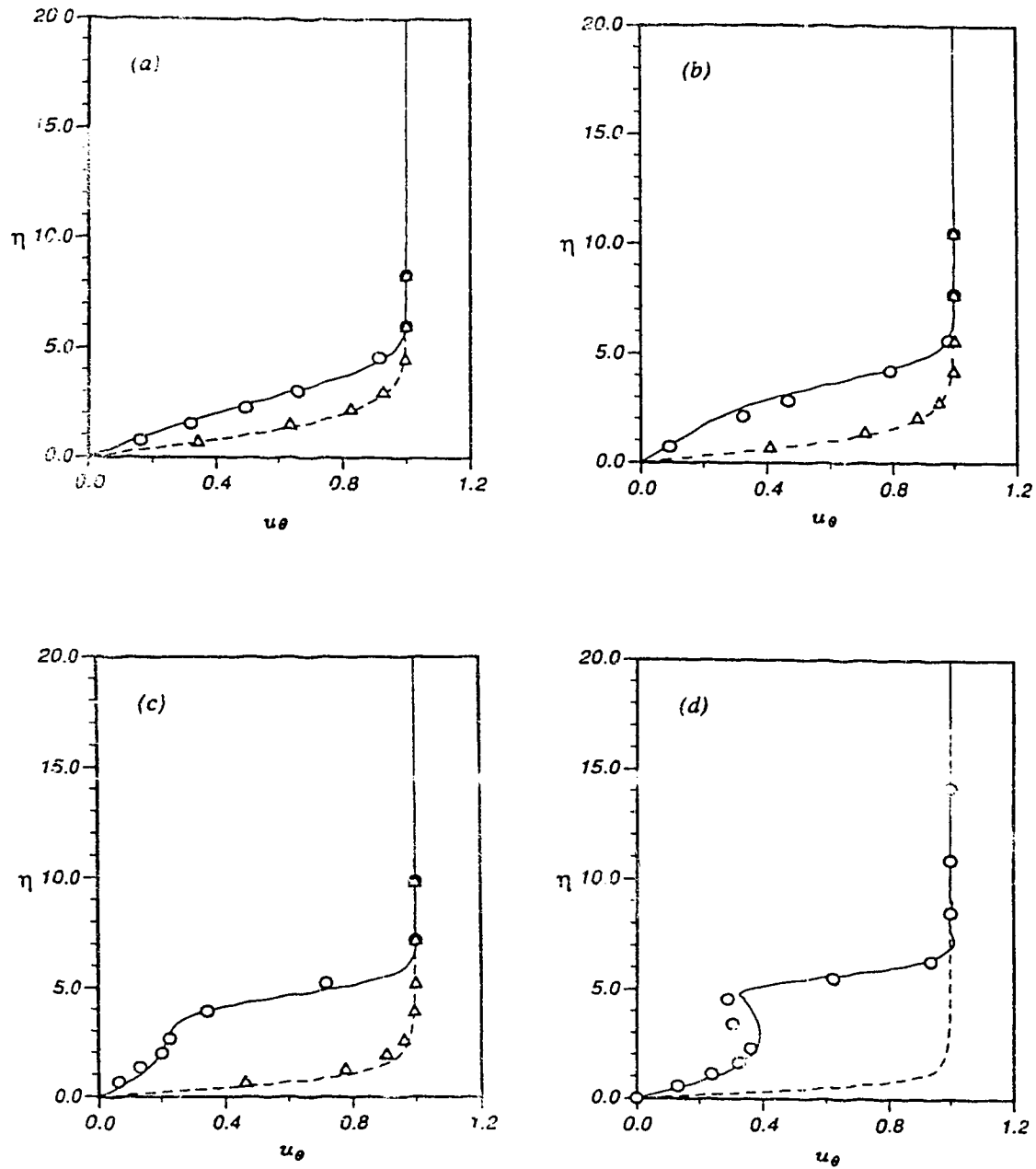


FIGURE 4.4. For caption see facing page.

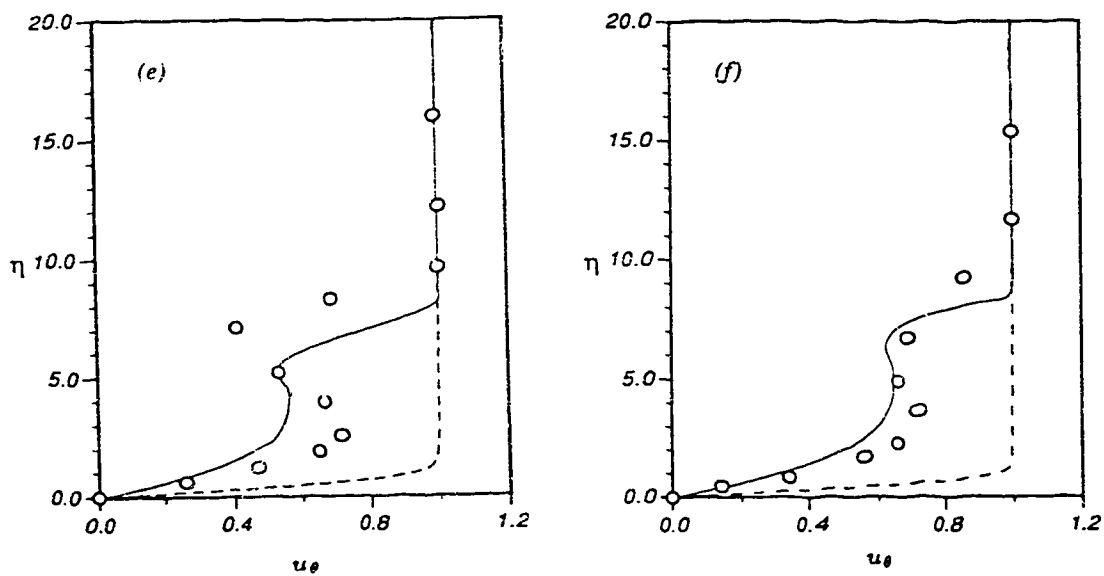


FIGURE 4.4. Velocity profile u_θ at the peak (—) and valley (----) of Görtler vortices with $\lambda = 1.8\text{cm}$ is shown as a function of $\eta = y\sqrt{U_\infty/\nu x}$ at (a) $x = 60\text{cm}$; (b) $x = 70\text{cm}$; (c) $x = 80\text{cm}$; (d) $x = 90\text{cm}$; (e) $x = 100\text{cm}$ and (f) $x = 110\text{cm}$. Here, $U_\infty = 5\text{m/s}$ and $\nu = 14.5 \times 10^{-6}\text{m}^2/\text{s}$. The data of Swearingen & Blackwelder (1987) is given as \circ (peak) and Δ (valley).

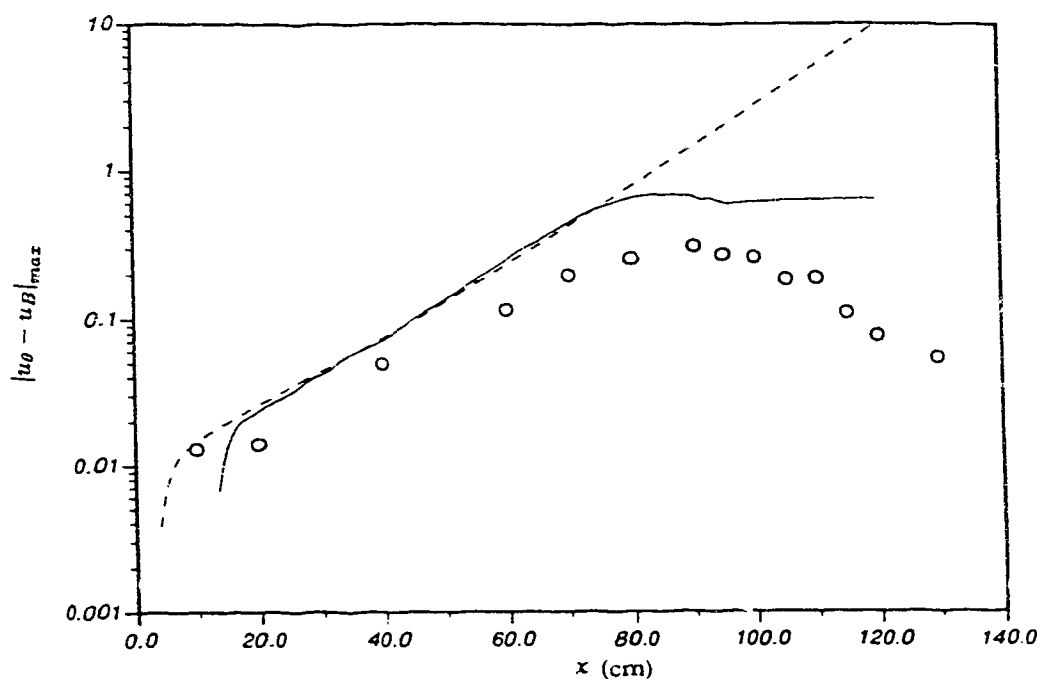


FIGURE 4.5. Spatial growth of $|u_{\theta} - u_B|_{max}$: — for the Görtler vortices in figure 4.4; ---- for the linear Görtler vortices with $\lambda = 1.8\text{cm}$ from secondary instability; \circ for the data from Swearingen & Blackwelder (1987). Here u_{θ} is the streamwise component of Blasius flow.

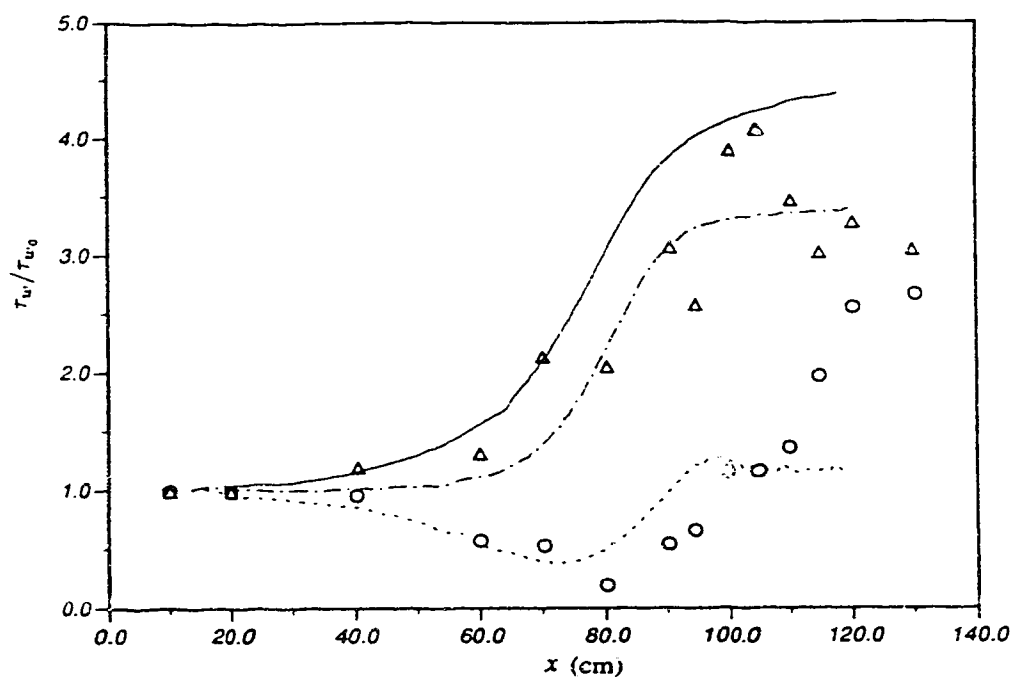


FIGURE 4.6. Spanwise averaged wall shear (— —), the wall shear τ_w at the peak (—) and valley (· · ·) of the Görtler vortices in figure 4.4 are shown as a function of x . Here, τ_{w0} is the wall shear of Blasius boundary layer; Δ and \circ are measured by Swearingen & Blackwelder (1987) at the peak and valley of naturally occurring Görtler vortices.

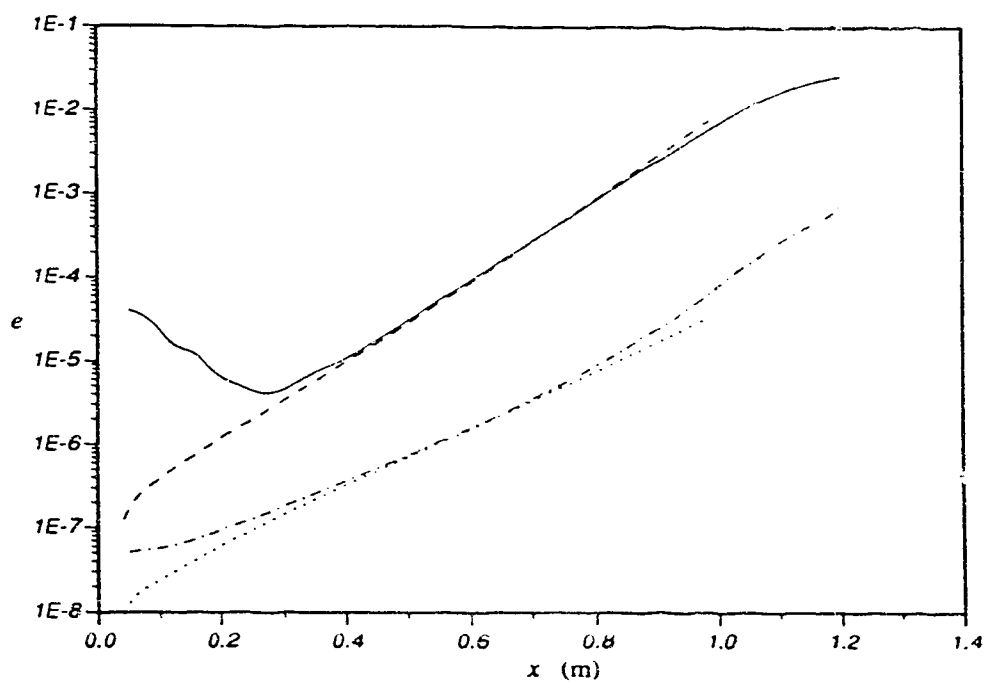
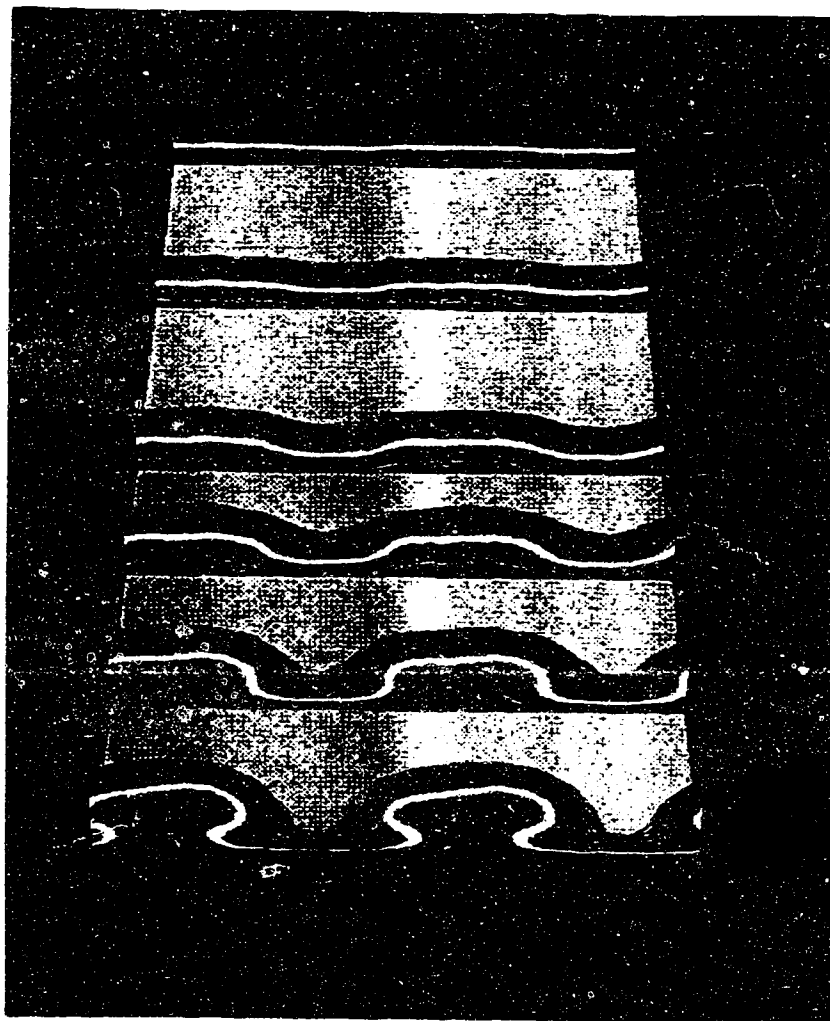
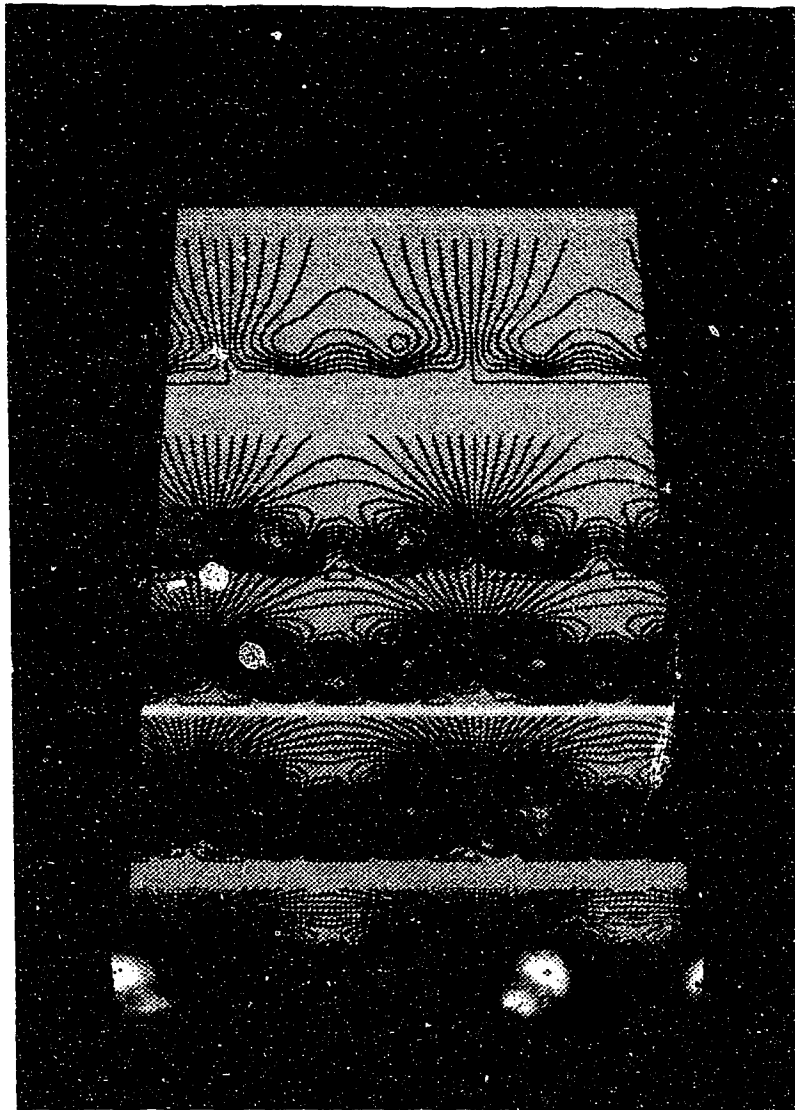


FIGURE 4.7. Energy of the base Görtler vortices $\lambda = 2.13\text{cm}$ ($\Lambda = 600$, —) and the related perturbation $\lambda_1 = 4.26\text{cm}$ ($b = 0.5$) of spanwise secondary instability (— —) at $U_\infty = 5\text{m/s}$, $\nu = 14.5 \times 10^{-6}\text{m}^2/\text{s}$ and $R = 3.2\text{m}$. The energy of linear Görtler vortices from primary instability with $\lambda = 2.13\text{cm}$ (----) and 4.26cm (.....) is also given.



(a)

FIGURE 4.8. For caption see facing page.



(b)

FIGURE 4.8. Contours of the velocity components (a) u_θ^0 of the base Görtler vortices and (b) u_r' of the perturbation in figure 4.7 are shown in cross-stream planes at $x = 0.52, 0.68, 0.84, 0.93, 1.0$ and 1.25m . The concave wall is shown as a flat plate and the flow proceeds downstream from top to bottom.

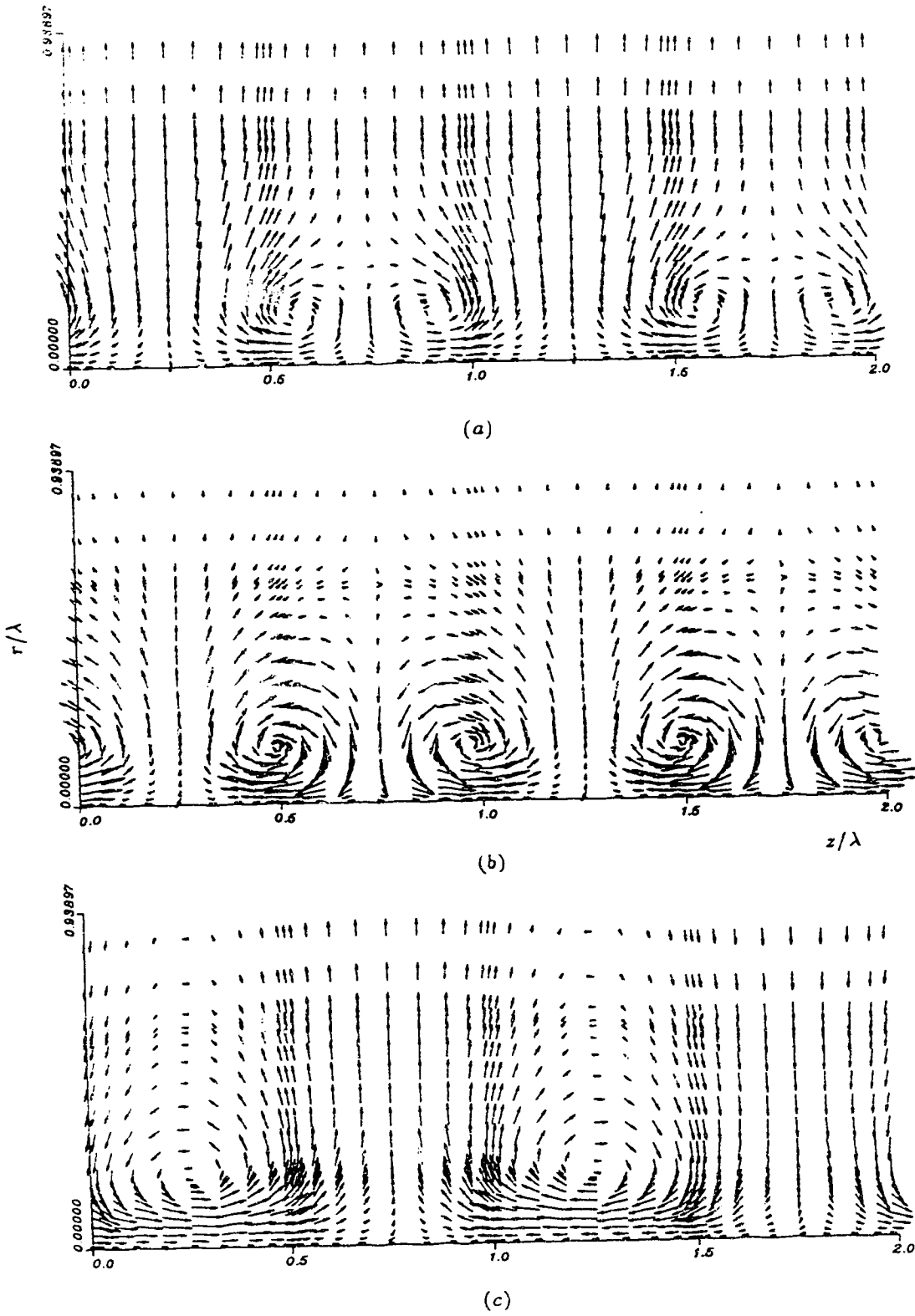


FIGURE 4.9. For caption see facing page.

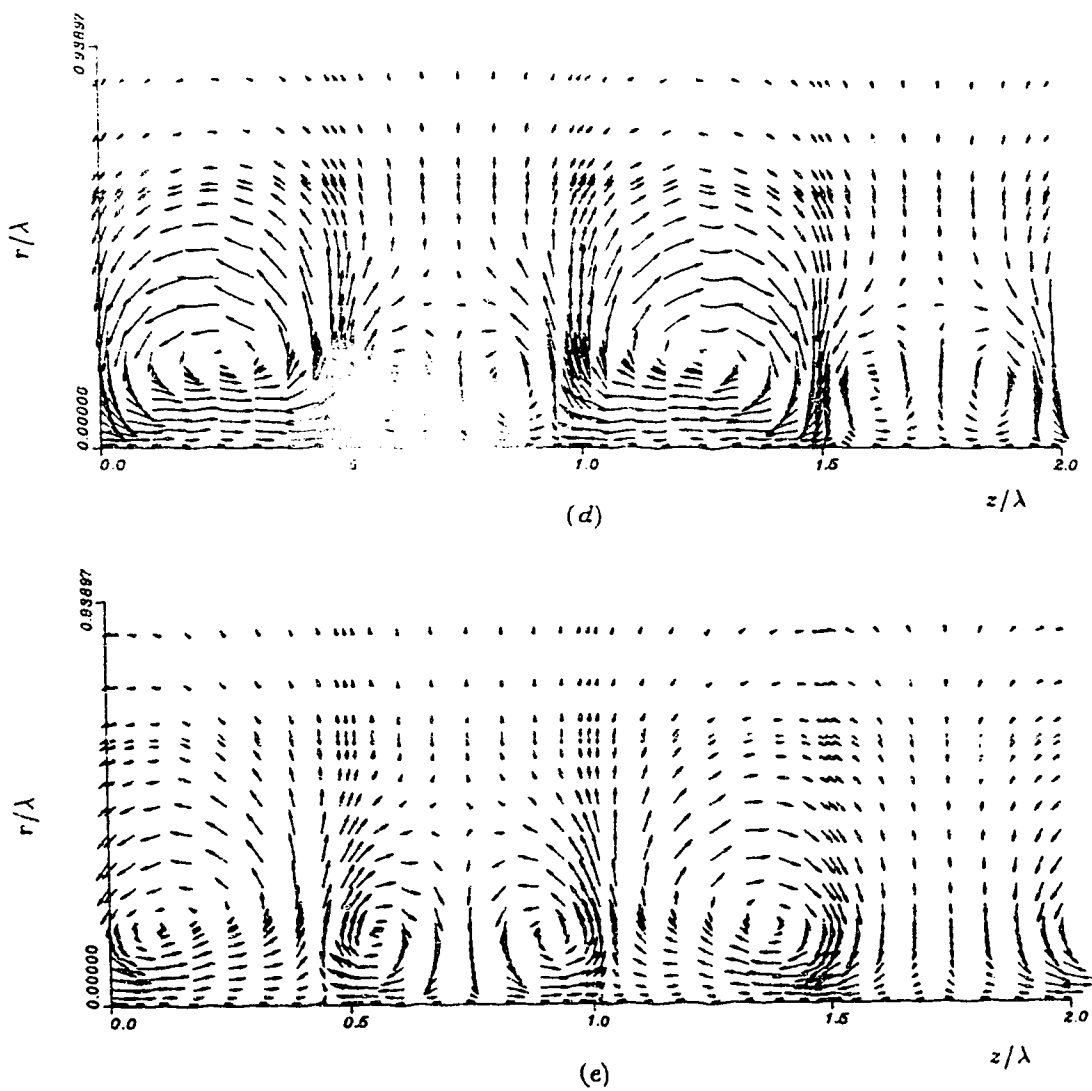
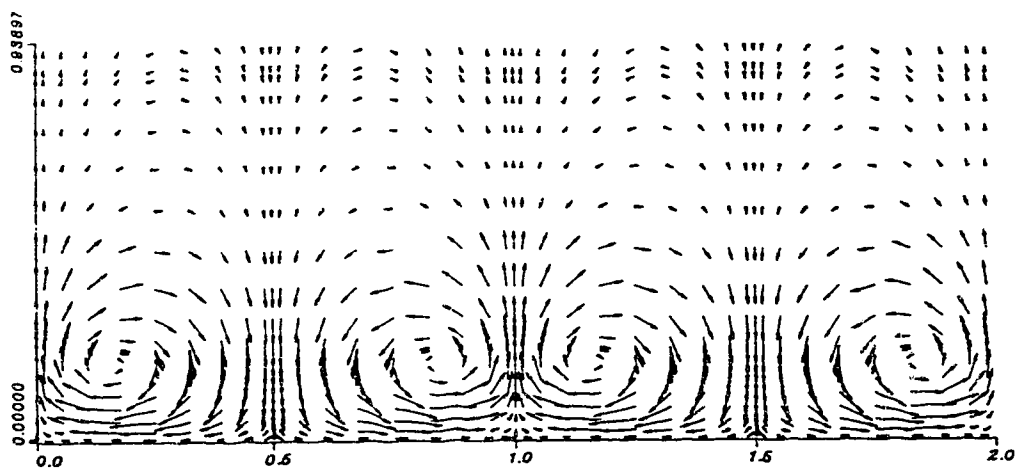
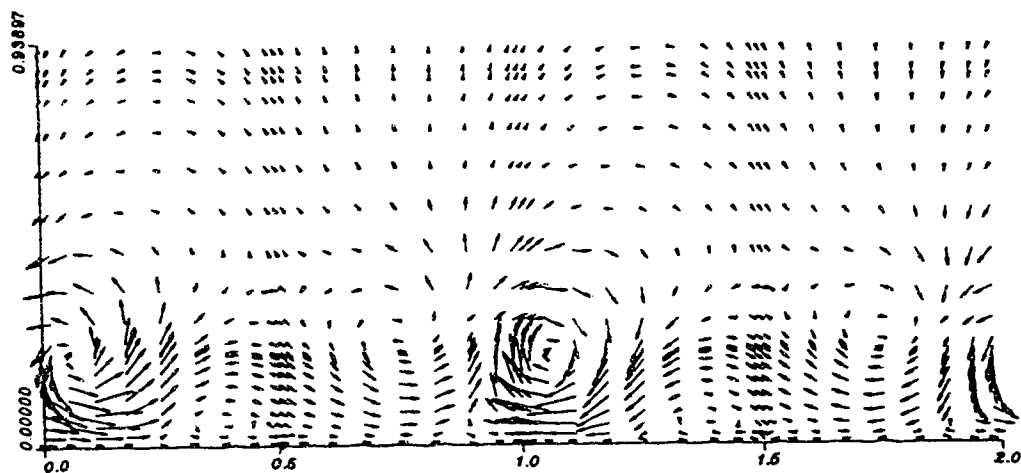


FIGURE 4.9. Base Görtler vortices and the perturbation in figure 4.7 are projected onto the $(r - z)$ plane at $x = 0.68\text{m}$ (in *a* & *c*) and $x = 1.0\text{m}$ (in *b* & *d*); (*e*) shows (*a*) + (*d*).



(a)



(b)

FIGURE 4.10. For caption see facing page.

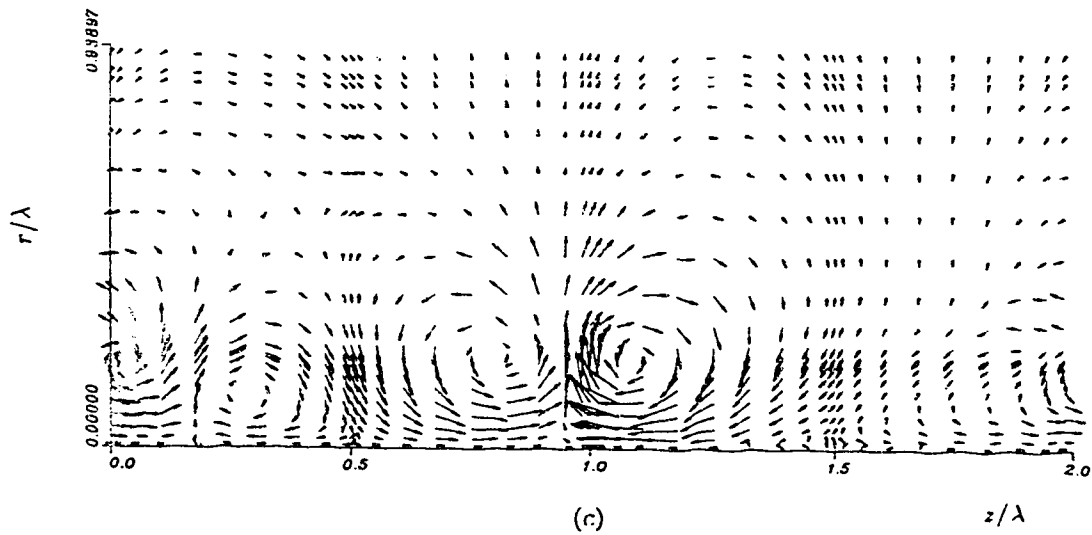


FIGURE 4.10. Base Görtler vortices and the perturbation similar to those in figure 4.8, but with $\epsilon = 0.1$ and a cosine function in equation (4.1), are projected onto the $(r - z)$ plane at $x = 0.982\text{m}$ (in *a* & *b*); (*c*) shows (*a*) + (*b*).

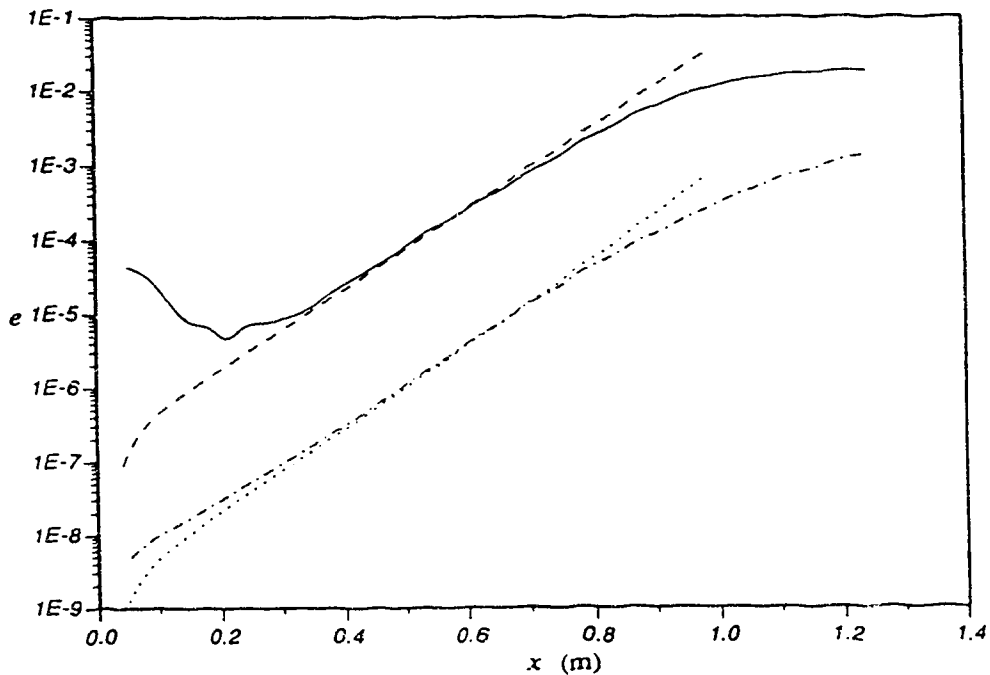


FIGURE 4.11. Same as in figure 4.7 but with $\lambda = 0.745\text{cm}$ ($\Lambda = 125$), $\lambda_1 = 1.498\text{cm}$ ($b = 0.5$).

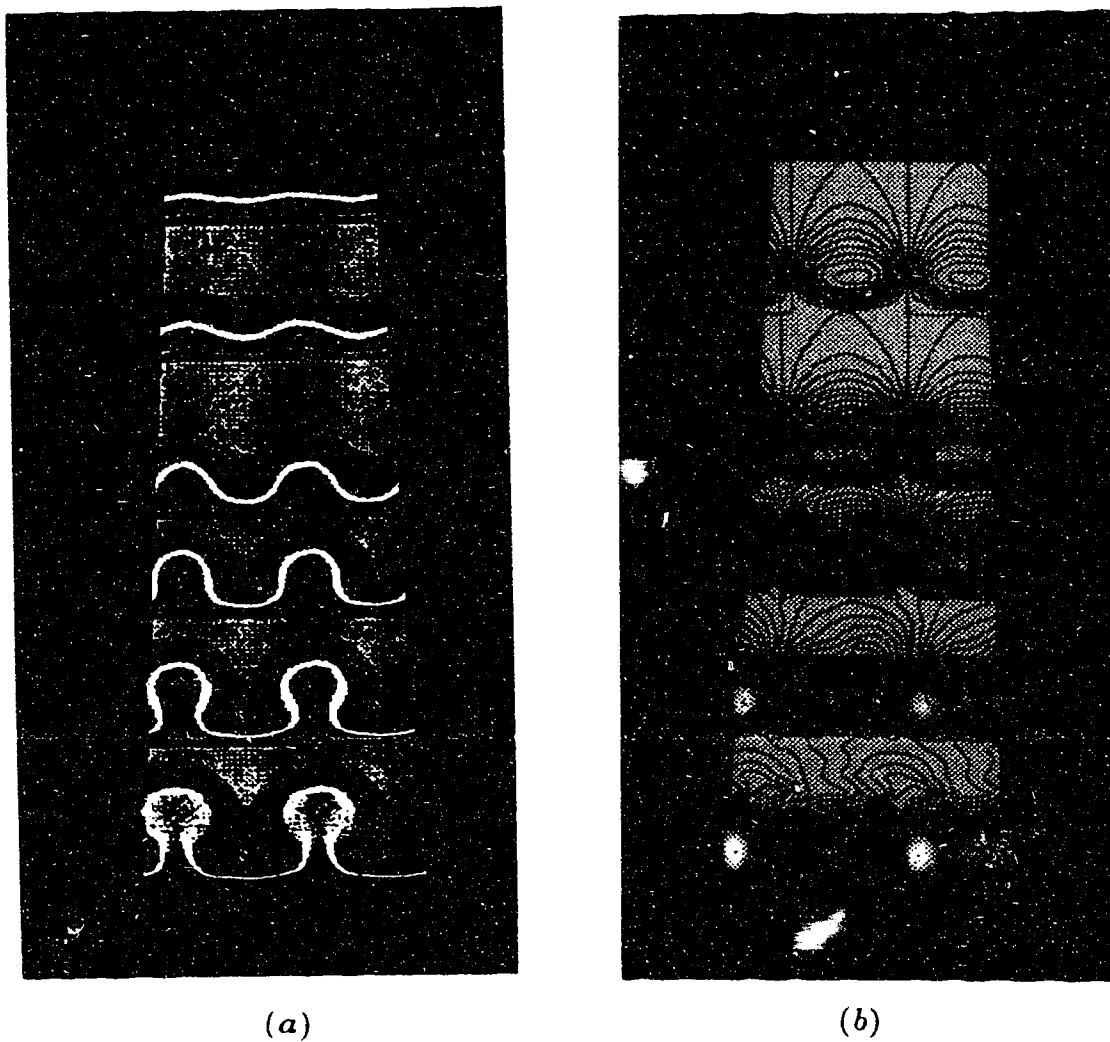
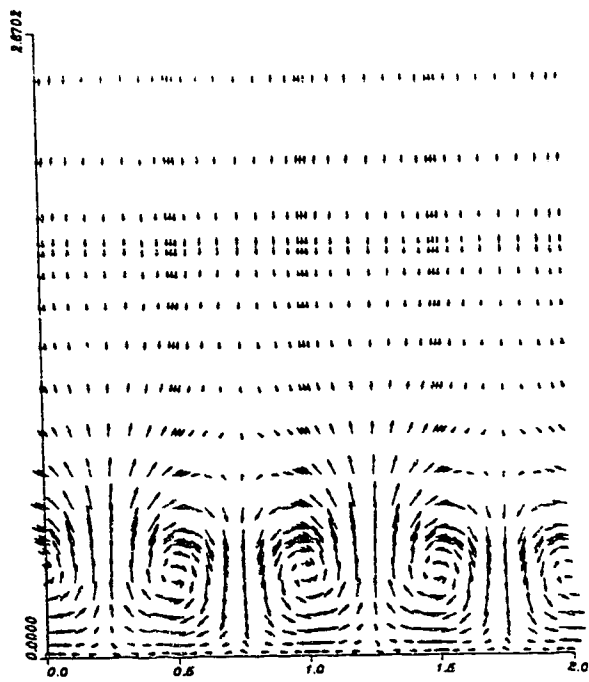
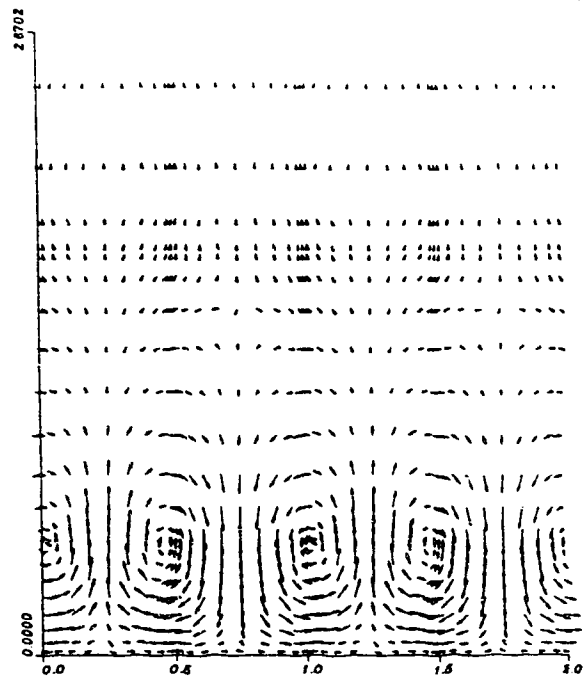


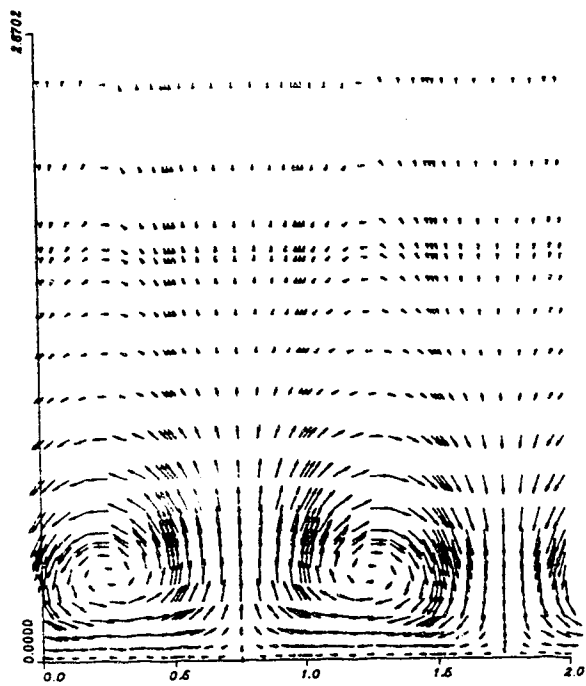
FIGURE 4.12. Contours of the velocity components (a) u_{θ}^0 of the base Görtler vortices and (b) u_r' of the perturbation in figure 4.11 are shown in cross-stream planes at $x = 0.52, 0.68, 0.84, 0.93, 1.0$ and 1.25m . The concave wall is shown as a flat plate and the flow proceeds downstream from top to bottom.



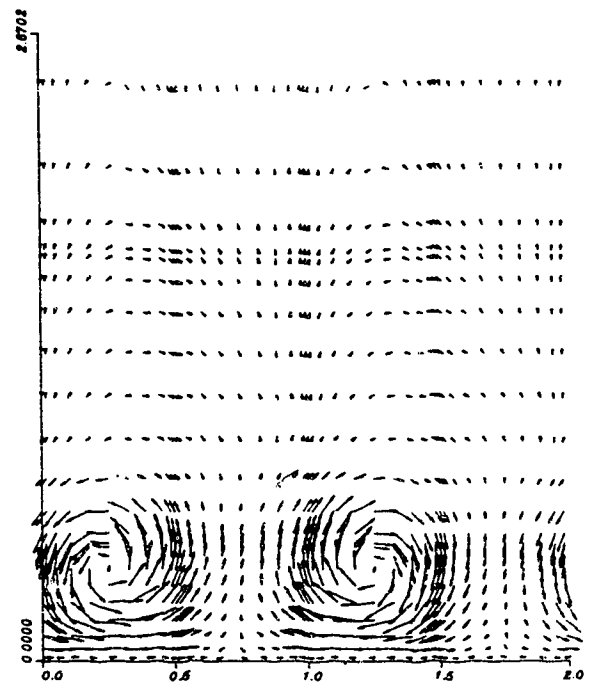
(a)



(b)



(c)



(d)

FIGURE 4.13. For caption see facing page.

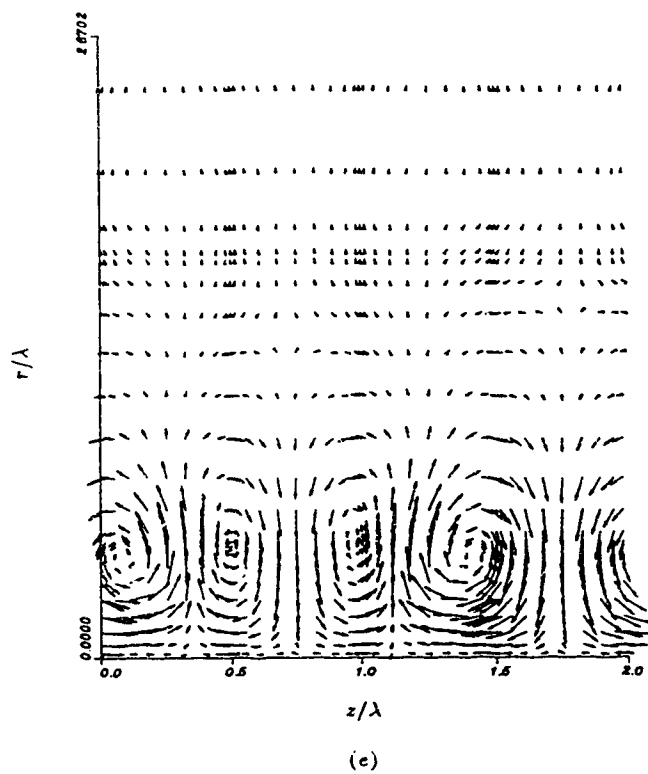
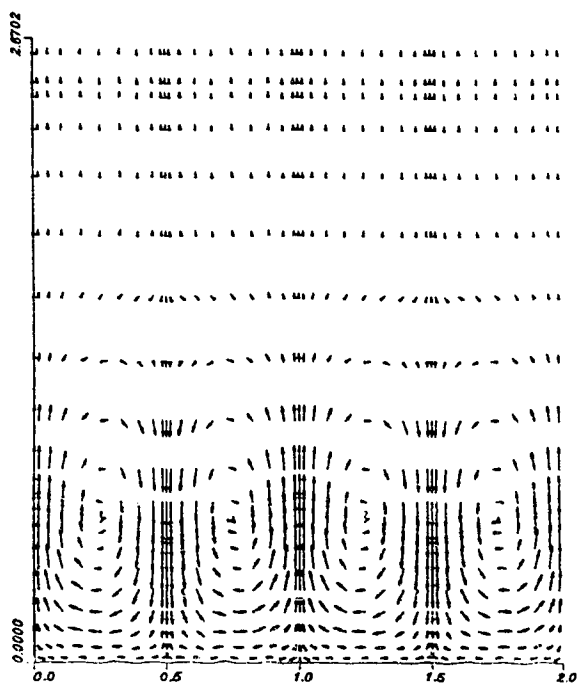
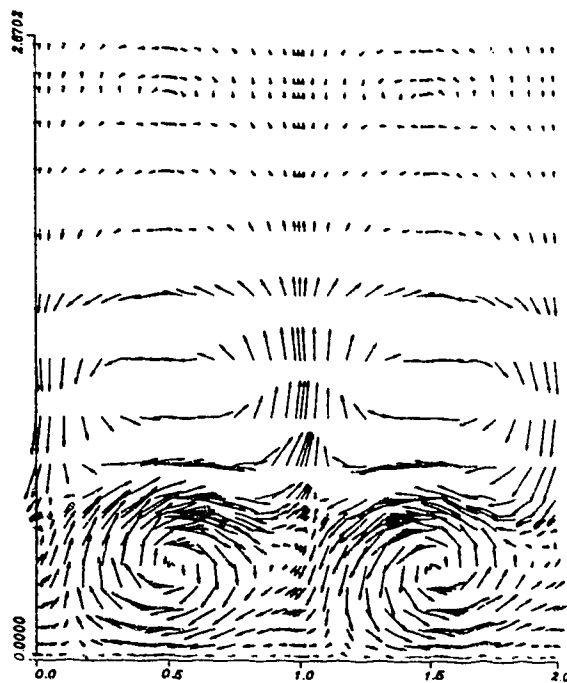


FIGURE 4.13. Base Görtler vortices and the perturbation in figure 4.12 are projected onto the $(r - z)$ plane at $x = 0.68\text{m}$ (in *a* & *c*) and $x = 1.0\text{m}$ (in *b* & *d*); (c) shows (b) +50% of (d).



(a)



(b)

FIGURE 4.14. For caption see facing page.

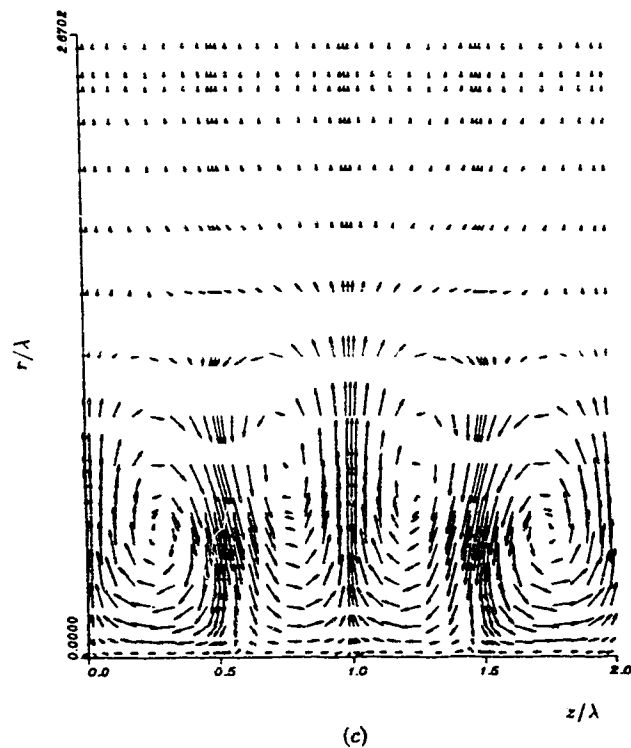


FIGURE 4.14. Base Görtler vortices and the perturbation similar to those in figure 4.11, but with $\epsilon = 0.1$ and a cosine function in equation (4.1), are projected onto the $(r - z)$ plane at $x = 1.169\text{m}$ (in *a* & *b*); (c) shows $(a) + 16.7\%$ of (*b*).

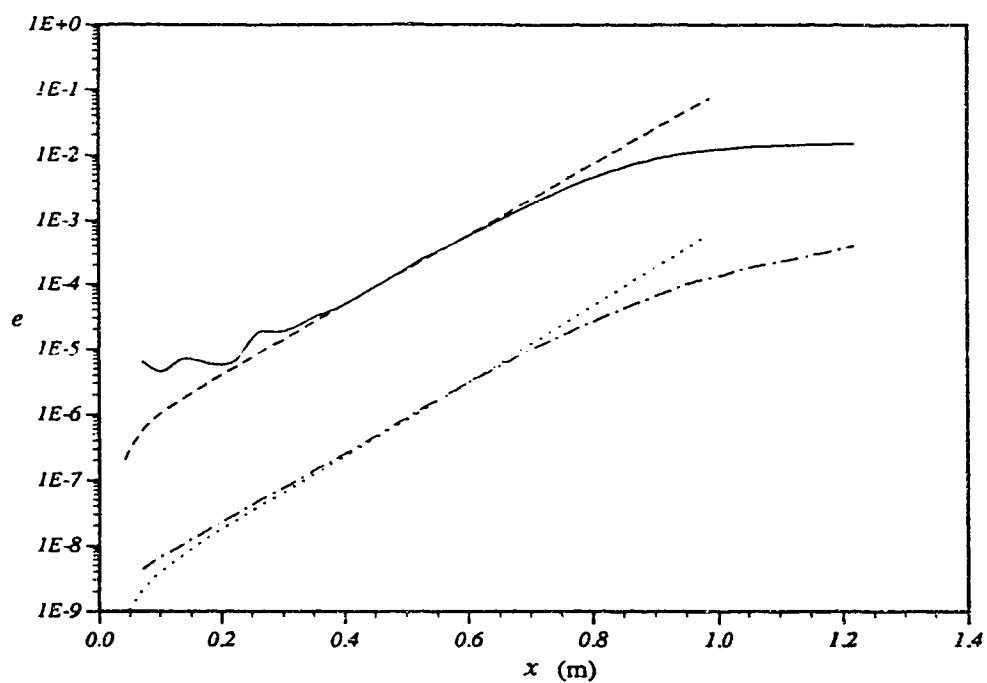
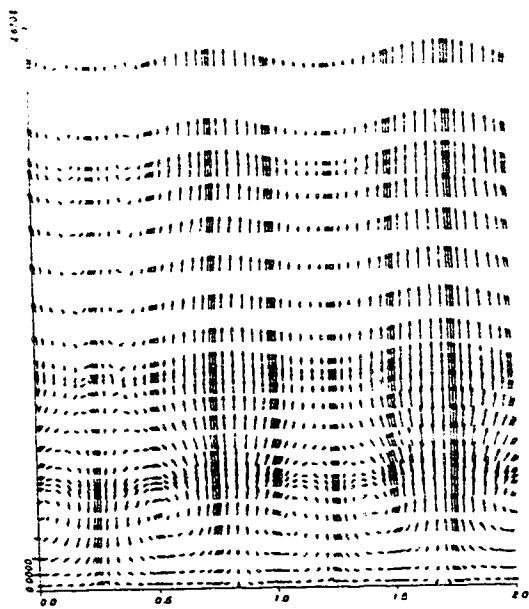
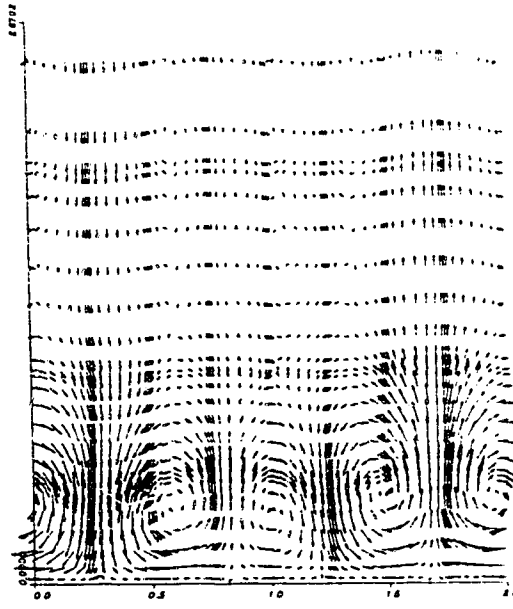


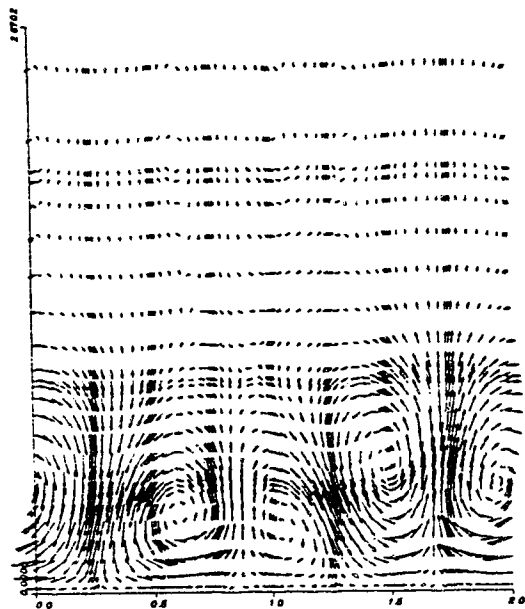
FIGURE 4.15. Energy of the base Görtler vortices (—) and the related perturbation ($b = 0.5$) of spanwise secondary instability (---) in figure 4.14. The energy of linear Görtler vortices from primary instability with $\lambda = 2.13$ cm (----) and 4.26cm (.....) is also given.



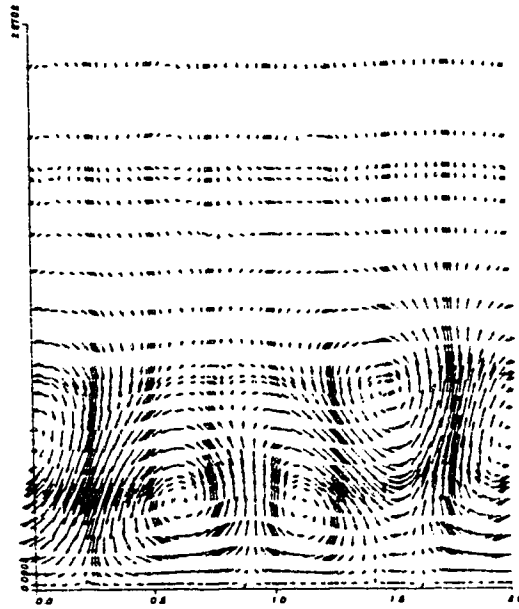
(a)



(b)



(c)



(d)

FIGURE 4.16. For caption see facing page.

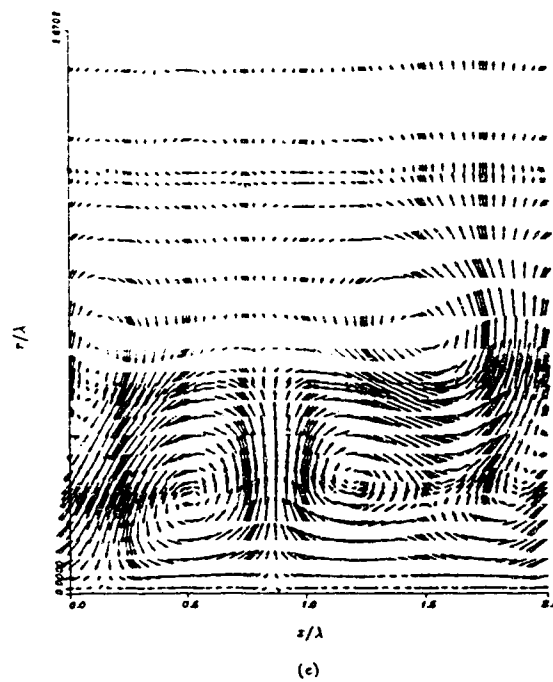


FIGURE 4.16. Görtler vortices with dominant wave length $\lambda = 0.749$ cm ($\Lambda = 125$) are projected onto the $(r - z)$ plane at (a) $x = 0.556$ m; (b) $x = 0.71$ m; (c) $x = 0.864$ m; (d) $x = 1.018$ m and (e) $x = 1.171$ m. Here, $U_\infty = 5$ m/s. $\nu = 14.5 \times 10^{-6}$ m/s² and $R = 3.2$ m. The simulation is started with $\lambda = 0.749$ cm, $b = 0.5$ and $\epsilon = 0.2$ in equation (4.4).

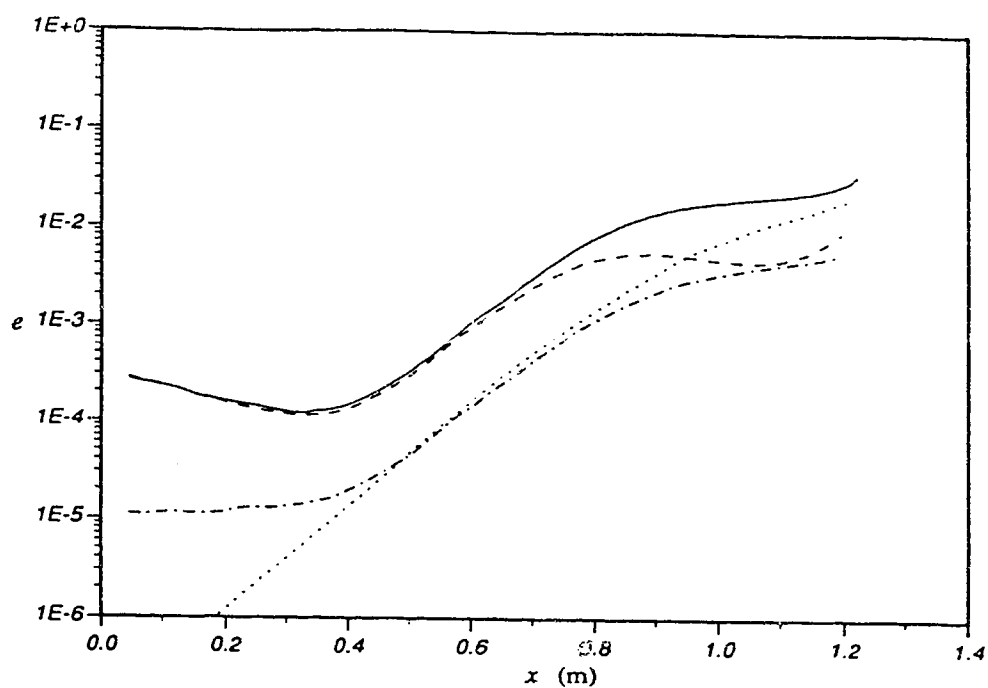


FIGURE 4.17. The total energy (—) and the energy in the first (---) and second (----) Fourier modes of the Görtler vortices in figure 4.16 are shown vs. streamwise distance. Also given is the energy of the perturbation from spanwise secondary instability in figure 4.15 (.....).

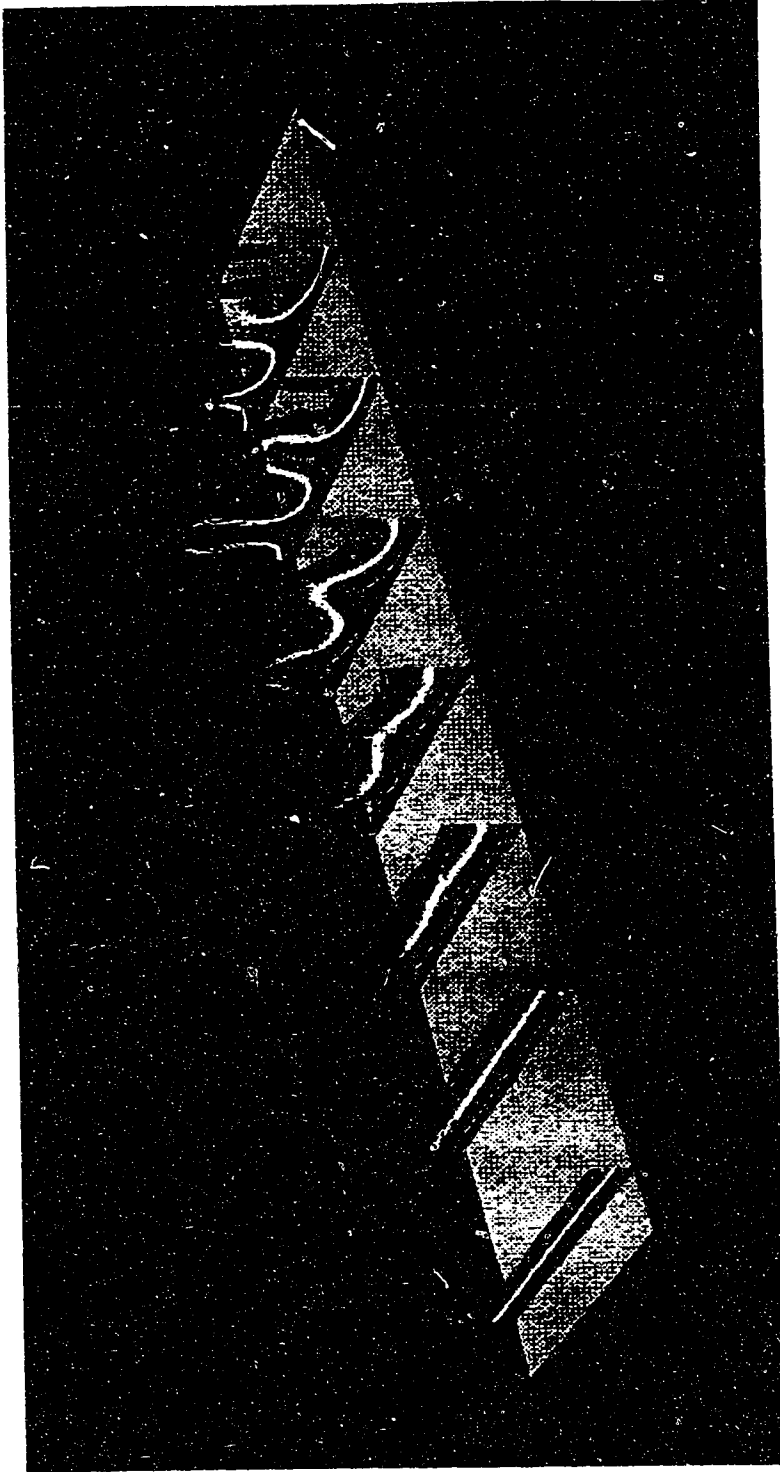


FIGURE 4.18. Contours of the streamwise velocity u_0 of the Görtler vortices in figure 4.16 are shown in cross-stream planes from $x = 0.096$ to 1.018m with $\Delta x = 0.1536\text{m}$. The concave wall is shown as a flat plate and the flow proceeds downstream from left to right.

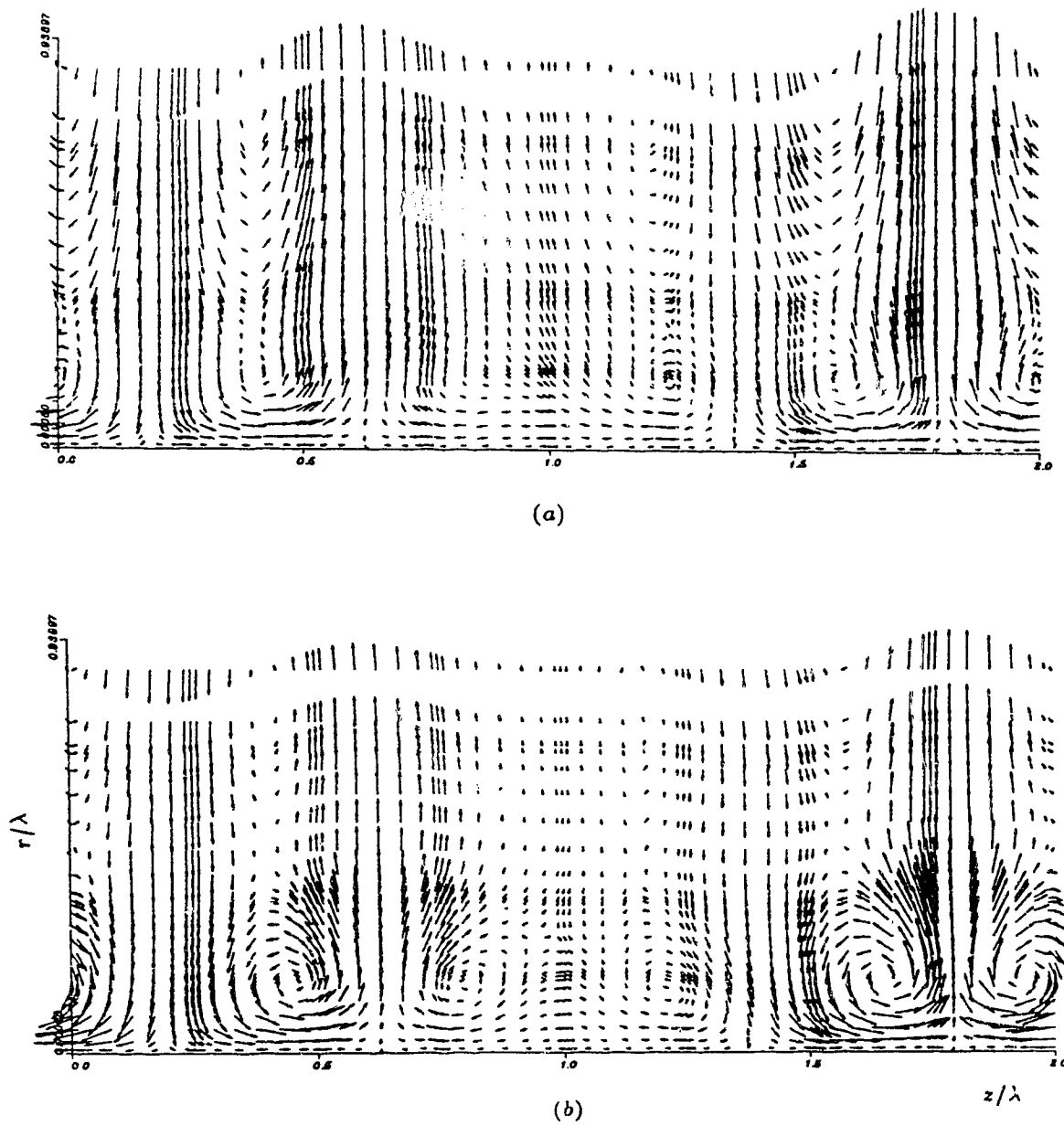


FIGURE 4.19. For caption see facing page.

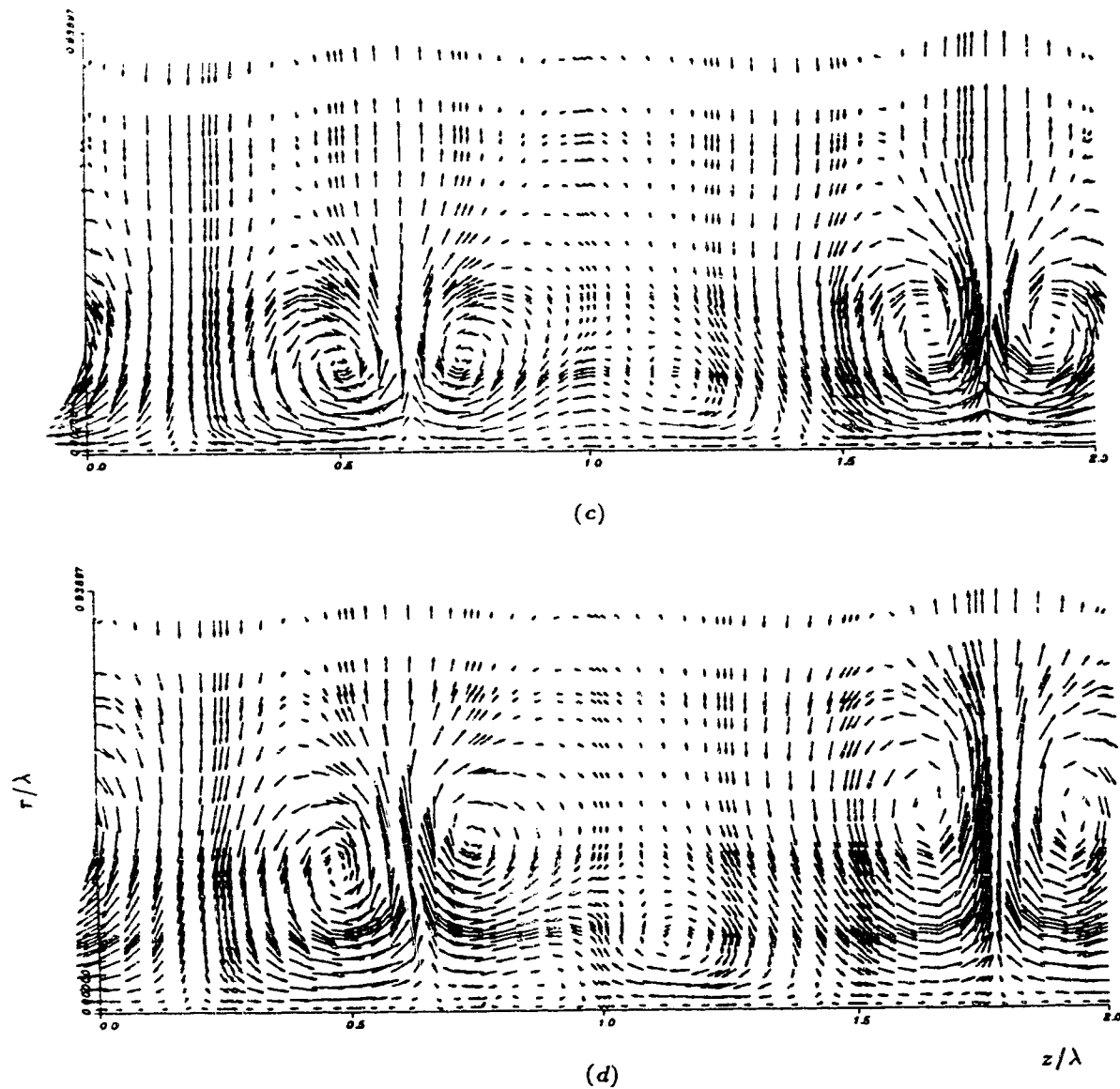


FIGURE 4.19. Görtler vortices with dominant wavelength $\lambda = 2.13$ cm ($\Lambda = 600$) are projected onto the $(r - z)$ plane at (a) $x = 0.474$ m; (b) $x = 0.627$ m; (c) $x = 0.781$ m and (d) $x = 0.934$ m. Here, $U_\infty = 5$ m/s, $\nu = 14.5 \times 10^{-6}$ m/s² and $R = 3.2$ m. The simulation is started with $\lambda = 2.13$ cm, $b = 1.5$ and $\epsilon = 0.8$ in equation (4.4).



FIGURE 4.20. Contours of the streamwise velocity u_θ of the Görtler vortices in figure 4.19 are shown in cross-stream planes from $x = 0.0384$ to 0.96 m with $\Delta x = 0.1536$ m. The concave wall is shown as a flat plate and the flow proceeds downstream from left to right.

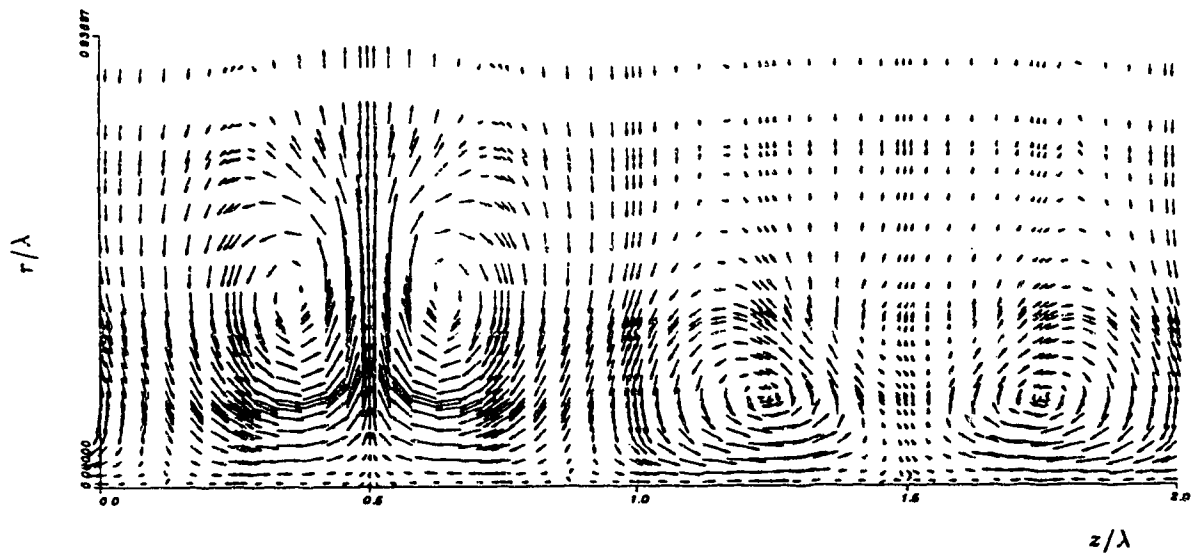


FIGURE 4.21. Görtler vortices similar to those in figure 4.19 but with $\epsilon = 0.6$ and a cosine function used for the dominant wavelength in equation (4.4) are projected onto the (r, z) plane at $x = 0.909\text{m}$.

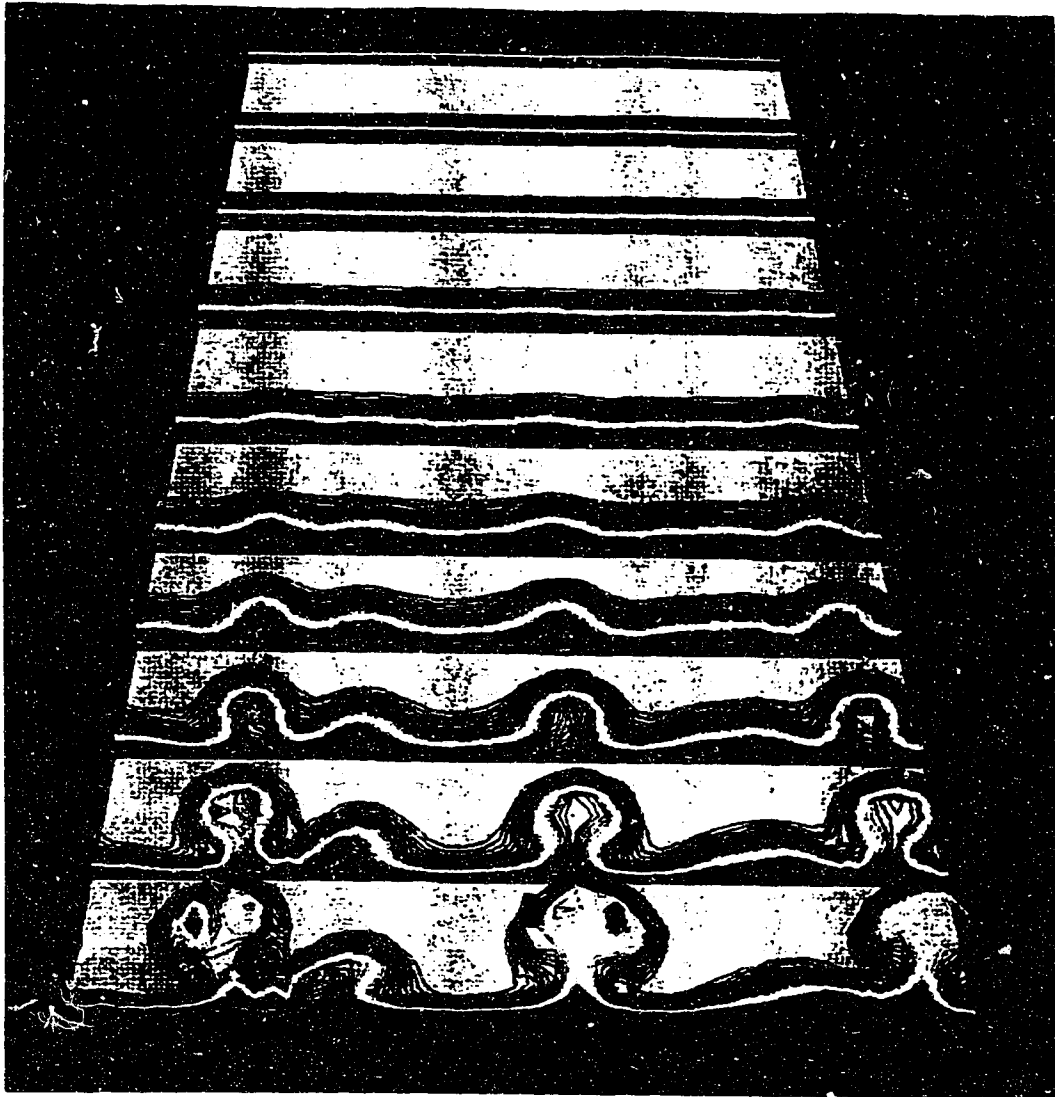


FIGURE 4.22. Contours of the streamwise velocity u_θ of the Görtler vortices at $U_\infty = 5\text{m/s}$, $\nu = 14.5 \times 10^{-6}\text{m}^2/\text{s}$ and $R = 3.2\text{m}$ are shown in cross-stream planes at $x = 0.198, 0.388, 0.518, 0.678, 0.838, 0.973, 1.078, 1.187$ and 1.293m . The spanwise length of the computational box is 6cm . The simulation is started at $x = 0.032\text{m}$ with the initial flow $(v_B, u_B, 0.01u_B)$, where v_B and u_B are the vertical and streamwise velocities of Blasius boundary layer flow. The concave wall is shown as a flat plate and the flow proceeds downstream from top to bottom.

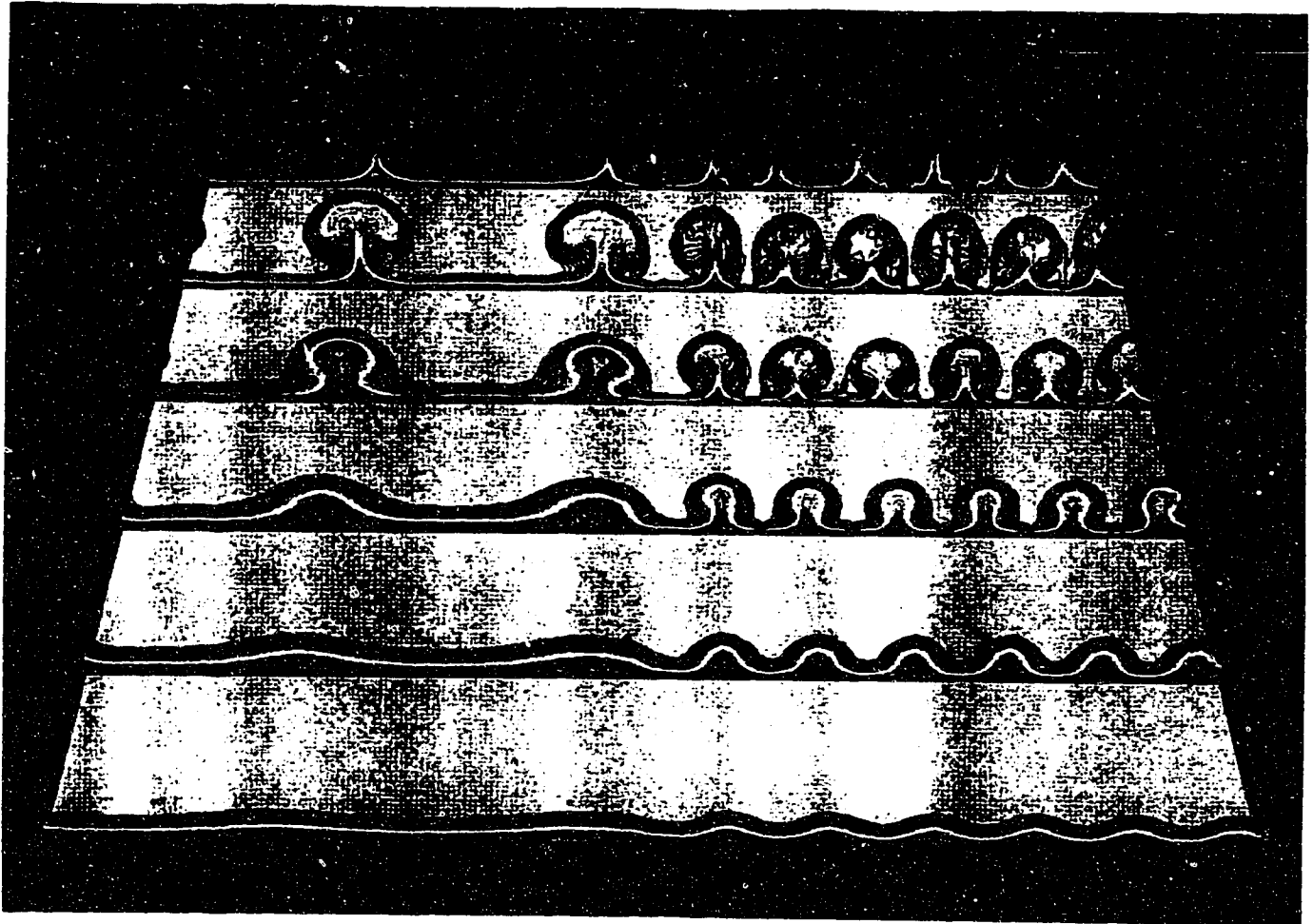


FIGURE 4.23. Contours of the streamwise velocity u_θ of the Görtler vortices at $U_\infty = 5\text{m/s}$, $\nu = 14.5 \times 10^{-6}\text{m}^2/\text{s}$ and $R = 3.2\text{m}$ are shown in cross-stream planes from $x = 0.198$ to 1.12m with $\Delta x = 0.1536\text{m}$. The spanwise length of the computational box is 10cm . The simulation is started with wavelength $\lambda = 2.5\text{cm}$ for the left two vortices and $\lambda = 0.833\text{cm}$ for the rest of the vortices. The concave wall is shown as a flat plate and the flow proceeds downstream from bottom to top.

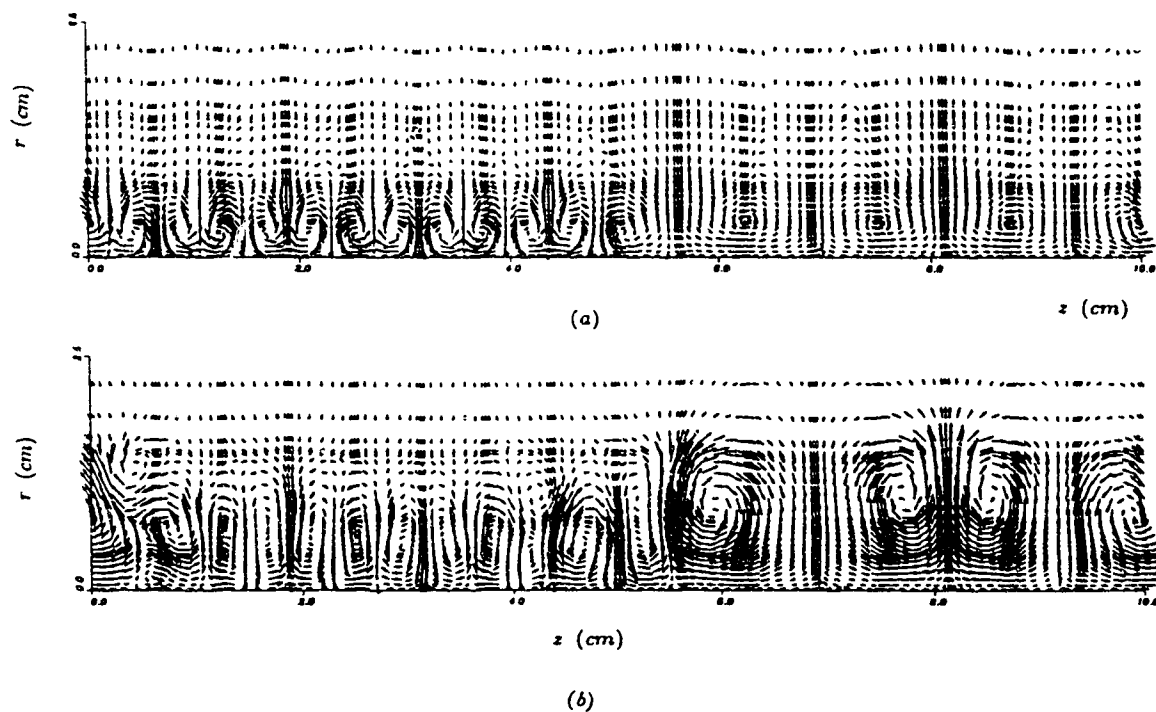


FIGURE 4.24. Görtler vortices in figure 4.23 are projected onto the $(r - z)$ plane at (a) $x = 0.506\text{m}$ and (b) $x = 1.12\text{m}$.

References

- Aihara, Y. 1962 Transition in an incompressible boundary layer along a concave wall. *Bulletin of the Aeronautical Research Institute, Univ. of Tokyo*, **3**(4), 195.
- Aihara, Y. 1976 Non-linear analysis of Görtler vortices. *Phys. Fluids*, **19**(11), 1655–1660.
- Aihara, Y. & Koyama, H. 1980 Secondary instability of Görtler vortices: formation of periodic three-dimensional coherent structure. *Trans. Japan Soc. Aero. Astron.*, **24**(64), 78–94.
- Aihara, Y., Tomita and A. Ito 1984 Generation, development and distortion of longitudinal vortices in boundary layers along concave and flat plates. *Laminar-Turbulent Transition*, IUTAM Symposium, Novosibirsk, 1984, edited by V.V. Kozlov, 447–454.
- Bertolotti, F.P., Herbert, Th. & Spalart, P.R. 1990 Linear and nonlinear stability of the Blasius boundary layer. *J. Fluid Mech.*, submitted.
- Bippes, H. 1972 Experimentelle Untersuchung des laminar-turbulenten Umschlags an einer parallel angeströmten konkaven wand. *Sitzungsberichte der Heidelberger Akademie der Wissenschaften Mathematisch-naturwissenschaftliche Klasse, 3 Abhandlung, Jahrgang 1972*, 103–180 also *NASA TM. 75243*, 1978.
- Blackwelder, R.F. 1983 Analogies between transitional and turbulent boundary layers. *Phys. Fluids*, **26**, 2807–2815.
- Cantwell, B.J., Coles, D.E. & Dimotakis, P.E. 1978 Structure and entrainment in the plane of symmetry of a turbulent spot. *J. Fluid Mech.*, **87**, 641–672.
- Day, H.P., Herbert Th. & Saric W.S. 1990 Comparing local and marching analyses of Görtler instability. *AIAA Journal*, **28**(6), 1010–1015.
- Floryan, J.M. 1986 Görtler instability of boundary layers over concave and convex walls. *Phys. Fluids*, **29**(8), 2380–2387.

Floryan J.M. & Saric W.S. 1984 Wavelength selection and growth of Görtler vortices. *AIAA Journal*, **22**(11), 1529–1538.

Görtler, H. 1940 Über eine drei-dimensionale instabilität laminarer Grenzschichten an konkaven wanden. *Math Phys*, Kl 2, 1, also *NASA TM*. 1375 (1954).

Guo Y. & Finlay, W.H. 1991 Splitting, merging and wavelength selection of vortices in curved and/or rotating channel flow due to Eckhaus instability. *J. Fluid Mech.*, **228**, 661–691.

Guo Y. & Finlay, W.H. 1992 Spanwise secondary instability of spatially develop vortices. Part 1. Theory and application to Dean vortices. *J. Fluid Mech.*, submitted.

Hall, P. 1982 On the non-linear evolution of Görtler vortices in non-parallel boundary layers. *IMA Journal of Applied Mathematics*, **29**, 173–196.

Hall, P. 1983 The linear development of Görtler vortices in growing boundary layers *J. Fluid Mech.*, **130**, 41–58.

Hall, P. 1988 The nonlinear development of Görtler vortices in growing boundary layers. *J. Fluid Mech.*, **193**, 243–266.

Hall, P. 1990 Görtler vortices in growing boundary layers: the leading edge receptivity problem, linear growth and the nonlinear breakdown stage. *Mathematika*, **37**, 151–189.

Herbert, Th. 1976 On the stability of the boundary layer along a concave wall. *Arch. Mech. Stos.*, **28**, 1039–1055.

Lee, K. & Liu J.T.C. 1992 On the growth of mushroomlike structures in nonlinear spatially developing Görtler vortex flow. *Phys. Fluids A*, **4**(1), 95–103.

Liu W. & Domaradzki J. 1990 Direct numerical simulation of transition to turbulence in Görtler flow. *AIAA Paper* 90–0114.

Ragab, S.A. & Nayfeh, A.H. 1981 Görtler Instability. *Phys. Fluids*, **24**, 1405–

1417.

Sabry, A.S. 1988 Numerical computation of the nonlinear evolution of Görtler vortices. *Ph.D Thesis*, Brown University.

Sabry, A.S. & Liu, J.T.C. 1991 Longitudinal vorticity elements in boundary layers: nonlinear development from initial Görtler vortices as a prototype problem. *J. Fluid Mech.*, **231**, 615–663.

Swearingen J.D. & Blackwelder R.F. 1987 The growth and breakdown of streamwise vortices in the presence of a wall. *J. Fluid Mech.*, **182**, 255–290.

Tani, I. 1962 Production of longitudinal vortices in the boundary layer along a curved wall. *Journal of Geophysical Research*, **67**(8), 3075–3080.

Tani, I. & Aihara, Y. 1969 Görtler vortices and boundary layer transition. *Z.A.M.P.*, **20**, 609–618.

Tani, I. & Sakagami, I. 1962 Boundary layer instability at subsonic speeds. *Proceedings of Third Congress of the International Council of Aerospace Sciences, Stockholm, 1962*, Spartan, Washington, D.C., (1964), 391–403.

Winoto, S.H. & Crane, R.I. 1980 Vortex structure in laminar boundary layers on a concave wall. *Intl. J. Heat and Fluid Flow*, **2**, 221–231.

Yu X.Y. & Liu J.T.C. 1991 The secondary instabilities in Görtler flow. *Phys. Fluids A*, **3**(8), 1845–1847.

CHAPTER 5

Final remarks

This study shows spanwise secondary instability is an important instability for spatially developing Dean and Görtler vortices. When the vortices in the base flow are linear, spanwise secondary instability is equivalent to primary instability (Dean or Görtler instability). When the vortices in the base flow enter the nonlinear stage, it becomes an instability which measures the interactions between each vortex pair. It causes two vortex pairs to develop into one pair if the wavelength of these vortices is short, and generates a new vortex pair in between two existing pairs if the wavelength is long. Spatially developing Dean and Görtler vortices are always unstable to spanwise perturbations. It will be interesting to know whether the features of Dean and Görtler vortices found in this study exist for vortices caused by rotation on a flat plate, or those caused by streamwise curvature found in transitional and turbulent wall bounded shear flows. Since the nonlinear development of this type of secondary instability modifies the vortex structures significantly, the study of this type of instability and its effects on the onset of other secondary instabilities is a necessary step toward understanding the dynamics which govern these vortices.

Appendix A

The proof of (2.7) follows. For any spanwise periodic flow, Fourier expansion can be used in the z direction for the amplitude function $\tilde{\mathbf{u}}(\tau, z)$ in (2.4). The general non-dimensional perturbation associated with spanwise wavenumber $b \pm k$ is

$$\begin{aligned} \mathbf{u} &= \sum_{n=-\frac{N}{2}}^{\frac{N}{2}} \hat{\mathbf{u}}_n(x) e^{inz} e^{st+i(dy+(\pm k+b)z)} \\ &= \sum_{l=-\frac{N}{2}}^{\frac{N}{2}} \hat{\mathbf{u}}_{l\mp k}(x) e^{ilz} e^{st+i(dy+bz)} - \sum_{l=-\frac{N}{2}}^{-\frac{N}{2}\pm k-1} \hat{\mathbf{u}}_{l\mp k}(x) e^{ilz} e^{st+i(dy+bz)} \\ &\quad + \sum_{l=\frac{N}{2}+1}^{\frac{N}{2}\pm k} \hat{\mathbf{u}}_{l\mp k}(x) e^{ilz} e^{st+i(dy+bz)}. \end{aligned}$$

For any small $\epsilon > 0$ there always exists an $m > 0$ such that when $N > m$ the following is true:

$$\left| - \sum_{l=-\frac{N}{2}}^{-\frac{N}{2}\pm k-1} \hat{\mathbf{u}}_{l\mp k}(x) e^{ilz} e^{st+i(dy+bz)} + \sum_{l=\frac{N}{2}+1}^{\frac{N}{2}\pm k} \hat{\mathbf{u}}_{l\mp k}(x) e^{ilz} e^{st+i(dy+bz)} \right| < \epsilon. \quad (\text{A.1})$$

Taking the limit $m \rightarrow \infty$ provides

$$\mathbf{u} = \sum_{l=-\infty}^{\infty} \hat{\mathbf{u}}_{l\mp k}(x) e^{ilz} e^{st+i(dy+bz)} \quad (\text{A.2})$$

Defining $\hat{\mathbf{u}}'_n(x) = \hat{\mathbf{u}}_{l\mp k}(x)$, then one obtains

$$\mathbf{u}' = \sum_{n=-\infty}^{\infty} \hat{\mathbf{u}}'_n(x) e^{inz} e^{st+i(dy+bz)}, \quad (\text{A.3})$$

which is just the perturbation associated with spanwise wavenumber b . Thus the perturbation with wavenumber b has the same growth rate as that with wavenumber $b \pm k$, but has the coefficients in the Fourier expansion shifted by $\mp k$. Since the flow pattern of a perturbation is given by (2.5), one can show the corresponding flow patterns of (A.2) and (A.3) are also the same. One can also show that $s(b) = s(-b)$ by letting $k = 0$ and reflecting the z -axis about $z = 0$.

Appendix B

Discretization of parabolized Navier-Stokes equations

For ease of illustrating our numerical formulation, the parabolized Navier-Stokes equations (3.1-3.3) are first discretized in the streamwise direction using the schemes discussed in §3.2.1, i.e. a third order Adam-Bashforth scheme for nonlinear convection terms and an implicit Euler scheme for viscous terms. Equation (3.1) then becomes

$$-\frac{1}{Re} \nabla^2 u_x^{n+1} + 2 \frac{u_x^n}{\Delta x} (u_x^{n+1} - u_x^n) = g_x - \left(\frac{\partial \bar{p}}{\partial x} \right)^{n+1} \quad (\text{B.1})$$

where

$$\nabla^2 = \frac{\partial^2}{\partial y^2} + \frac{\partial^2}{\partial z^2}, \quad g_x = - \sum_{l=0}^2 \beta_l \left\{ \frac{\partial}{\partial y} (u_y u_x) + \frac{\partial}{\partial z} (u_z u_x) - f_x \right\}^l$$

and $\beta_l = 23/12, -16/12, 5/12$ for $l = 0, 1, 2$. The equations (3.2-3.3) can be written as

$$-\frac{1}{Re} \nabla^2 \mathbf{v}^{n+1} + \nabla p^{n+1} + \frac{1}{\Delta x} (u_x^{n+1} \mathbf{v}^{n+1} - u_x^n \mathbf{v}^n) = \mathbf{g} \quad (\text{B.2})$$

$$- \operatorname{div} \mathbf{v}^{n+1} = \frac{1}{\Delta x} (u_x^{n+1} - u_x^n) \quad (\text{B.3})$$

where

$$\begin{aligned} \nabla &= \frac{\partial}{\partial y} \mathbf{e}_y + \frac{\partial}{\partial z} \mathbf{e}_z, & \mathbf{v} &= u_y \mathbf{e}_y + u_z \mathbf{e}_z, \\ \mathbf{g} &= - \sum_{l=0}^2 \beta_l \{ \mathbf{v} \nabla \cdot \mathbf{v} - \mathbf{f} \}^l, & \mathbf{f} &= f_y \mathbf{e}_y + f_z \mathbf{e}_z. \end{aligned}$$

The solutions for $u_x^{n+1}, u_y^{n+1}, u_z^{n+1}$ and p^{n+1} are sought in the domain Ω with homogeneous Dirichlet (or Neumann) velocity boundary conditions on the domain boundary $\partial\Omega$. The equation (B.1) is a two-dimensional Helmholtz equation for u_x^{n+1}

and a standard finite element formulation is used. The equations (B.2-B.3) can be viewed as a two-dimensional, unsteady, nonhomogeneous Stokes problem for \mathbf{v} and p and the equivalent variational statements are as follows: find the velocity \mathbf{v}^{n+1} in the space $H = [H_0^1(\Omega)]^2$ and the pressure p^{n+1} in the space $Q = L_0^1(\Omega)$ such that

$$\frac{1}{Re}(\nabla \mathbf{v}^{n+1}, \nabla \mathbf{w}) - (p^{n+1}, \text{div} \mathbf{w}) + \left(\frac{u_x^{n+1} \mathbf{v}^{n+1} - u_x^n \mathbf{v}^n}{\Delta x}, \mathbf{w} \right) = (\mathbf{g}, \mathbf{w}) \quad \forall \mathbf{w} \in H \quad (\text{B.4})$$

$$-(\text{div} \mathbf{v}^{n+1}, q) = \left(\frac{u_x^{n+1} - u_x^n}{\Delta x}, q \right) \quad \forall q \in Q \quad (\text{B.5})$$

where the integration (ϕ, ψ) is defined as

$$(\phi, \psi) = \int_{\Omega} \phi \psi dy dz.$$

Here the function space $H_0^1(\Omega)$ is the Sobolev space and $L_0^1(\Omega)$ is square-integrable space (cf. Carey & Oden, 1983).

In a spectral-element discretization, the domain Ω is first broken into K disjoint rectilinear elements Ω_k . The variational statements (B.4-B.5) are then required for polynomial subspaces $H^h \subset H$ and $Q^h \subset Q$ defined on the Ω_k . The spaces H^h and Q^h must satisfy certain conditions (e.g., Babuška-Brezzi conditions) in order to make the discrete problem of (B.4-B.5) well posed and behaved. Readers are referred to Maday & Patera (1988) and Carey & Oden (1983) for more details.

In a Legendre spectral-element method, the velocity \mathbf{u} and all other terms except the pressure p , are represented at the tensor-product Gauss-Legendre Lobatto points in Ω_k . For example, the velocity \mathbf{u} is expanded as:

$$\mathbf{u}_h^k(y, z) = \sum_{i=0}^N \sum_{j=0}^N \mathbf{u}_{ij}^k h_i(y) h_j(z) \quad (y, z) \in \Omega_k \quad (\text{B.6})$$

where h_i and h_j are the N^{th} order Lagrangian interpolants through the Gauss-Legendre Lobatto points in Ω_k . The pressure p is represented at the tensor-product Gauss-Legendre points in Ω_k :

$$p_h^k(y, z) = \sum_{i=0}^{N-1} \sum_{j=0}^{N-1} p_{ij}^k \tilde{h}_i(y) \tilde{h}_j(z) \quad (y, z) \in \Omega_k \quad (\text{B.7})$$

where \tilde{h}_i and \tilde{h}_j are the $(N - 2)^{th}$ order Lagrangian interpolants through the Gauss-Legendre points in Ω_k . It can be shown that the velocity is continuous across the elemental boundaries while the pressure is discontinuous.

Substituting the expansions (B.6-B.7) into (B.4-B.5) , we can generate the discrete equations of the forms (3.5-3.6) by choosing test function $w_h = h_i(y)h_j(z)$ and $q_h = \tilde{h}_i(y)\tilde{h}_j(z)$. When such test functions are used, the momentum equations are projected into the space H^h while the continuity equation into Q^h . Some basic properties of Legendre polynomials and Legendre-Lagrangian interpolants can be found in Rønquist (1988). Since the integrations in (B.4-B.5) can be carried out quite easily by Gauss quadrature formula, the derivations of the matrices in (3.5-3.6) are straightforward.

Appendix C

Discretization of stability equations

Using the numerical schemes described in §3.2.2, the spanwise stability equations (3.8-3.10) are discretized first in the streamwise direction:

$$-\frac{1}{Re} \nabla^2 \tilde{u}_x^{n+1} + \frac{2}{\Delta x} (u_x^{0n+1} \tilde{u}_x^{n+1} - u_x^{0n} \tilde{u}_x^n) = - \sum_{l=0}^2 \beta_l w_x^l \quad (C.1)$$

$$-\frac{1}{Re} \nabla^2 \tilde{v}^{n+1} + \tilde{\nabla} \tilde{p}^{n+1} + \frac{1}{\Delta x} (u_x^{0n+1} \tilde{v}^{n+1} - u_x^{0n} \tilde{v}^n) = \tilde{g} \quad (C.2)$$

$$- \tilde{\nabla} \cdot \tilde{v}^{n+1} = \frac{1}{\Delta x} (\tilde{u}_x^{n+1} - \tilde{u}_x^n) \quad (C.3)$$

where

$$\begin{aligned} \tilde{\nabla} &= \frac{\partial}{\partial y} \mathbf{e}_y + \left(\frac{\partial}{\partial z} + i\beta \right) \mathbf{e}_z, & \mathbf{v} &= u_y^0 \mathbf{e}_y + u_z^0 \mathbf{e}_z, & \tilde{\mathbf{v}} &= \tilde{u}_y \mathbf{e}_y + \tilde{u}_z \mathbf{e}_z, \\ \tilde{g} &= - \left(\frac{1}{\Delta x} (\mathbf{v}^{n+1} \tilde{u}_x^{n+1} - \mathbf{v}^n \tilde{u}_x^n) + \sum_{l=0}^2 \beta_l \mathbf{w}^l \right), & \mathbf{w} &= w_y \mathbf{e}_y + w_z \mathbf{e}_z. \end{aligned}$$

The solutions for \tilde{u}_x^{n+1} , \tilde{u}_y^{n+1} , \tilde{u}_z^{n+1} and \tilde{p}^{n+1} are sought in the domain Ω with homogeneous Dirichlet velocity boundary conditions on the domain boundary $\partial\Omega$. The equation (C.1) is a two-dimensional Helmholtz equation for \tilde{u}_x^{n+1} and the equations (C.2-C.3) can be viewed as a two-dimensional, unsteady, nonhomogeneous Stokes problem for $\tilde{\mathbf{v}}$ and \tilde{p} , so the discretization of (C.1-C.3) on the cross-stream plane follows that of (B.1-B.3). The perturbation pressure \tilde{p}^{n+1} is represented at the tensor-product Gauss-Legendre points in Ω_k as the base pressure p is in (B.7). The perturbation velocity $\tilde{\mathbf{u}}$ and all other terms are represented at the tensor-product Gauss-Legendre Lobatto points in Ω_k as the base velocity \mathbf{u} is in (B.6). The resulting discrete equations can be written in matrix form as

$$\frac{1}{Re} A \tilde{U}_x^{n+1} + \frac{2B_x^n}{\Delta x} (\tilde{U}_x^{n+1} - \tilde{U}_x^n) = - \sum_{l=0}^2 \beta_l W_x^l \quad (C.4)$$

$$\frac{1}{Re} A \tilde{U}_y^{n+1} + D_x \tilde{P} + \frac{1}{\Delta x} (B_x^{n+1} \tilde{U}_y^{n+1} - B_x^n \tilde{U}_y^n) = G_y \quad (C.5)$$

$$\frac{1}{Re} A \tilde{U}_z^{n+1} + (D_z + i\beta I) \tilde{P} + \frac{1}{\Delta x} (B_x^{n+1} \tilde{U}_z^{n+1} - B_x^n \tilde{U}_z^n) = G_z \quad (C.6)$$

$$- D_y^T \tilde{U}_y - (D_z + i\beta I)^T \tilde{U}_z = \frac{B_p^T}{\Delta x} (\tilde{U}_x^{n+1} - \tilde{U}_x^n) \quad (C.7)$$

Here the definitions of the matrices A , B_x , B_p , D_x and D_z are the same as those in (3.4-3.6). The matrix I is the identity matrix. The vectors \tilde{U}_x , \tilde{U}_y , \tilde{U}_z and \tilde{P} are constructed from the discrete perturbation velocity $\tilde{\mathbf{u}}$ and pressure \tilde{p} . It can be shown that when a global iterative Uzawa scheme is used to solve (C.4-C.7), the matrix system for \tilde{p}^{n+1} is full and complex.